Title
Defect and grain boundary engineering for enhanced performances and lifetimes of hybrid perovskite solar cells

Author
DeMarco, Nicholas Francis

Publication Date
2019

Peer reviewed|Thesis/dissertation

UNIVERSITY OF CALIFORNIA

Los Angeles

Defect and grain boundary engineering for enhanced performances and lifetimes of hybrid perovskite solar cells

A dissertation submitted in partial satisfaction of the

requirements for the degree Doctor of Philosophy

in Materials Science and Engineering

by

Nicholas De Marco

2019

ABSTRACT OF THE DISSERATION

Defect and grain boundary engineering for enhanced performances and lifetimes of hybrid perovskite solar cells

by

Nicholas De Marco

Doctor of Philosophy in Materials Science and Engineering

University of California, Los Angeles, 2019

Professor Yang Yang, Chair

As the world energy consumption increases, the necessity for clean energy proves vital and urgent as catastrophic effects of global climate change are imminent. The sun delivers more energy to Earth in just over an hour than we have consumed over the course of last year, making solar technology a most promising candidate for a sustainable future. Currently, state-of-the-art silicon-based solar technologies dominate the market owed to their maturity in processing knowledge, performance reliability, and lifetime. Despite lower costs in recent years, the levelized cost of electricity of silicon-based solar PV technologies is still much greater than conventional fossil fuel sources, providing large incentive to find more cost-effective alternative solar PV technologies. Solution-processed solar technologies are appealing as a low-cost alternative, among which, hybrid perovskites have recently risen as a high performance solution-

processed PV technology achieving laboratory scale efficiencies >23%, which are rapidly approaching those of conventional Si-based PV (~26%). However, owed to the solution-processed nature of perovskites, there are many associated defects and grain boundary regions that can adversely affect performances and lifetimes. In this dissertation, I will focus on addressing defect and grain boundary engineering, taking advantage of the wet chemical environment of perovskite thin film processing to manipulate crystallization dynamics and modulate defect and grain boundary properties.

In Chapter 4, the guanidinium molecule was first discovered for use in hybrid perovskites. It was found that inclusion of guanidinium can provide extraordinary enhancements in photoluminescent properties of the thin film and enhanced open-circuit voltage of the devices. Based on further experimental analyses and results, we believe that the guanidinium ion serves to suppress formation of defects via lattice strain relaxation and also may serve as a passivant at grain boundaries, giving rise to these impressive improvements. This work opened the door to future works throughout my Ph.D. to control crystallization and defect properties.

To further investigate the nature of controlling crystal growth and associated defect natures, a Lewis acid-base adduct approach was developed and is discussed in Chapter 5. The strength of interactios between the Lewis acid perovskite precursors and Lewis base additives were shown to greatly influence nucleation and growth dynamics. The Lewis base urea was found to provide great enhancement in crystal growth, producing larger sized grains and enhanced photoluminescent properties, alongside a greater performance and stability of the device.

Lastly, in Chapter 6, the intrinsic stability of the perovskite thin film is addressed by utilizing the compositional and dimensional tenability of hybrid perovskite materials, utilizing a hybrid 3- and 2-dimensionality of the perovskite structure to lead to even further enhanced performances and long-term lifetimes. It was found that the 2-D perovskite forms around grains (at grain boundaries) to facilitate the production of high quality 3-D grains and serve as passivating layers to grain boundaries. These works provide important future directions for hybrid perovskite PV research to realize commercial technologies with competitive efficiencies, long lifetimes, and low costs. Conclusions and future outlooks of these works are discussed in Chapter 7.

The dissertation of Nicholas De Marco is approved.

Bruce S Dunn

Jaime Marian

Richard B Kaner

Yang Yang, Committee Chair

University of California, Los Angeles

2019

To my fiancé and to my parents for their unwavering love and support.

Table of Contents

List of Figures

List of Tables

Acknowledgements

This Ph.D. would not have been what it was without the support and mentorship of others. I would like to express my deepest gratitude to those who have played an important role along this road.

I would first like to thank my advisor, Professor Yang Yang, for his continuous support throughout my Ph.D. I have learned a tremendous amount under his guidance that I believe will set me on a path for success in all my future endeavors. I learned that attitude is the most important attribute one can possess to be successful. I appreciate every discussion, story, and analogy, both in group meetings and in private, that have helped me to understand the small details that are important to find success, and that helped to shape myself and my path as a researcher. Professor Yang has also allowed me to reach my full potential by giving me higher responsibilities as I have earned his trust and respect over the years, and I would like to thank him greatly for that.

I thank my committee members for their guidance and feedback during my Ph.D that greatly helped to shape my thesis direction and to introduce me to new techniques and ideas.

I would also like to thank Dr. Huanping Zhou and Dr. Chen Qi (now both Professors in China) for their guidance at the start of my Ph.D, turning a young student from mechanical engineering into a materials scientist and engineer and pushing me to deliver upon high expectations. I would also like to thank Dr. Jinwook Lee for his great support in my latter years to further help transform me into an independent researcher.

Lastly, I would like to thank all those colleagues, as members of Prof. Yang's lab and outside, that have helped me to conduct experiments, discuss and analyze results and project directions, and ultimately to deliver high quality scientific reports to the community.

VITA

2013	Bachelor of Science, Department of Mechanical Engineering, University of California, Merced
2014	Research Assistant, University of California, Merced
2017	Engineering Intern, NAVFAC EXWC, Port Hueneme, CA
2018	Process Engineer Intern, Lam Research, CA
2014 – 2019	Graduate Student Researcher, Department of Materials Science and Engineering, University of California, Los Angeles

Selected Publications

1. Jin-Wook Lee, Zhenghong Dai, Changsoo Lee, Hyuck Mo Lee, Tae-Hee Han, Nicholas De Marco, Oliver Lin, Christopher S. Choi, Bruce Dunn, Jaekyung Koh, Dino Di Carlo, Jeong Hoon Ko, Heather D. Maynard and Yang Yang. Tuning Molecular Interactions for Highly Reproducible and Efficient Formamidinium Perovskite Solar Cells via Adduct Approach. J. Am. Chem. Soc., Article ASAP (2018)
2. Jin-Wook Lee, Zhenghong Dai, Tae-Hee Han, Chungseok Choi, Sheng-Yung Chang, Sung-Joon Lee, Nicholas De Marco, Hongxiang Zhao, Pengyu Sun, Yu Huang, Yang Yang. 2D perovskite stabilized phase-pure formamidinium perovskite solar cells. Nat Comm. Vol 9, No: 3021 (2018)
3. Jin-Wook Lee, SangHoon Bae, Nicholas DeMarco, Yao-Tsung Hsieh, Zhenghong Dai, Yang Yang. The role of grain boundaries in perovskite solar cells. Materials Today Energy (2017)
4. Lijian Zuo, Hexia Guo, Dane W. deQuilettes, Sarthak Jariwala, Nicholas De Marco, Shiqi Dong, Ryan DeBlock, David S. Ginger, Bruce Dunn, Mingkui Wang, and Yang Yang. Polymer-modified halide perovskite films for efficient and stable planar heterojunction solar cells. Sci. Adv. 2017 ; 3 : e1700106

5. Jin-Wook Lee, Sang-Hoon Bae, Yao-Tsung Hsieh, Nicholas De Marco, Mingkui Wang, Pengyu Sun, Yang Yang. A Bifunctional Lewis Base Additive for Microscopic Homogeneity in Perovskite Solar Cells. Chem, Volume 3, Issue 2, Pages 290–302 (2017)
6. Lijian Zuo, Qi Chen, Nicholas De Marco, Yao-Tsung Hsieh, Huajun Chen, Pengyu Sun, Sheng-Yung Chang, Hongxiang Zhao, Shiqi Dong and Yang Yang. Tailoring the Interfacial Chemical Interaction for High-Efficiency Perovskite Solar Cells. Nano Lett., 17 (1), pp 269–275(2017)
7. Nicholas De Marco, Huanping Zhou, Qi Chen, Pengyu Sun, Zonghao Liu, Lei Meng, En-Ping Yao, Yongsheng Liu, Andy Schiffer, and Yang Yang. Guanidinium: A Route to Enhanced Carrier Lifetime and Open-Circuit Voltage in Hybrid Perovskite Solar Cells. *Nano letters.* 2016, 16, (2), 1009-1016.
8. Lijian Zuo, Shiqi Dong, Nicholas De Marco, Yao-Tsung Hsieh, Sang-Hoon Bae, Pengyu Sun, Yang Yang. Morphology Evolution of High Efficiency Perovskite Solar Cells via Vapor Induced Intermediate Phases. J Am Chem Soc,138 (48), 15710–15716
9. Jingbi You, Lei Meng, Tze-Bin Song, Tzung-Fang Guo, Yang Yang, Wei-Hsuan Chang, Ziruo Hong, Huajun Chen, Huanping Zhou, Qi Chen, Yongsheng Liu, Nicholas De Marco, and Yang Yang. Improved Air-Stability of Perovskite Solar Cells via Solution-Processed Metal Oxide Transport Layers. *Nature Nanotechnology*. 2015
10. Qi Chen, Nicholas De Marco, Yang (Michael) Yang, Tze-bin Song, Chun-Chao Chen, Hongxiang Zhao, Zirou Hong, Huanping Zhou, and Yang Yang. Under the Spotlight: The Organic-Inorganic Hybrid Halide Perovskite for Optoelectronic Applications. *Nano Today, 10, 3, Pages 355–396.* 2015

Chapter 1. Introduction

1.1 The Sun, Energy, and need for Solar Power Generation

Energy is the fuel for life – the ebbs and flows of which are an essential part of all living organisms on Earth. The ability to access and harvest energy is the pillar of human survival and well-being. At present, our energy reliance continues to increase in a world of ever-expanding population and technological advancement.[1] In 2018, our world total energy consumption was 111,125 TeraWatt-Hours (TWh) compared to 100,914 TWh in 2010 and 54,335 TWh in 1973.[2] Historically, fossil fuels have dominated as mainstream energy sources (oil, coal, and natural gas) due to their abundance on Earth and technological simplicity for conversion into useful forms of energy (i.e. combustion). However, burning of these fossil fuels results in carbon dioxide as an unavoidable byproduct, which has led to drastic increases in carbon emissions from 15,460 Mt of CO_2 in 1973 to 32,316 Mt in 2016, and are set to reach a record-high 37,100 Mt in 2018.[2,3] This steady continuous increase of harmful carbon emissions has inevitably raised serious global environmental concerns linked to more severe climate changes seen worldwide.[4] In addition, fossil fuels are non-renewable sources of energy, which means that their supply is limited and will eventually be exhausted. The necessity for clean and renewable sources of energy proves vital and urgent as catastrophic effects of global warming are imminent, which can be seen through global efforts such as the Paris Agreement that aims to maintain the global

average temperature as close to 1.5 ºC above pre-industrial levels as possible.[5] This feat does not come without major hurdles – both in technological developments and developing grid systems capable of handling renewable sources.

As of 2017, renewable energy sources accounted for approximately 11% of the total energy consumption in the United States, amounting to approximately 11 quadrillion Btu (of 97.7 qBtu in total).[1] Among the available renewable energy sources, wind contributed to 21%, biofuels 21%, hydroelectric 25%, solar 6%, and geothermal 2%. The sun is a powerful source of energy on Earth, responsible for not only direct solar harvesting capabilities but also for all other forms of energy on Earth, aside from nuclear and geothermal, such as wind and ocean currents. The sun delivers approximately 174 PW of irradiation to the Earth, 89 PW of which is absorbed by the Earth's surfaces (lands and oceans), while the rest (~49%) is reflected or re-radiated by the Earth's atmosphere, clouds, and surfaces.[6] This equates to 782,260,000 TWh per year, and upon comparison to a 2018 world total energy consumption of 111,125 TWh, we see that the sun can provide the total energy needed for the entire year within just 1.25 hours![7] If we assume a solar panel efficiency of just 10%, that means we would need only 0.168% of Earth's surface covered in order to harvest an annual total of 15 TW global power. This equates to 858,792 km^2, which is approximately the size of Venezuela at 882,052 km^2 (calculations provided in Appendix A.1). However, we must consider the fact that we do not receive the maximum intensity of sunlight every hour of the day. If we estimate a global average of 5 hours of peak sunlight per day available to harvest, this would instead mean that it would take approximately 6 hours to receive all the energy needed for the entire year and 0.403% of the Earth's surface required to be covered by solar PV panels. If we now assume a 20% efficient panel, which is achievable with current solar PV available, this is equal to 2,061,100 km^2, roughly equal to the size of Saudi

Arabia. This is still significantly small fraction of the entire Earth. In fact, the amount of solar energy reaching Earth's surface is so vast that in one year it is about twice as much as will ever be obtained from non-renewable energy sources (i.e. coal, oil, natural gas, mined uranium) on Earth.[6] Therefore, solar is a most promising (and obvious) candidate to realize a clean and sustainable source of energy for the future of humanity.[8]

When speaking of solar energy, it is important to realize that there are several different types of solar-harvesting technologies, which includes photovoltaic, thermal, and concentrated solar. Solar photovoltaic (PV) is most appealing for implementation into electrical grid systems as this technology allows for the direct conversion of sunlight into electricity. Solar PV has blossomed over recent years, nearly doubling its total installed capacity in the U.S. from 2015-2016 and becoming the number one source of new electric generating capacity at 39% annually.[9] Moreover, the total installed capacity is anticipated to triple over the next 5 years. While the economics of the solar PV market have largely improved to allow for such large increases in installed capacity, there still is great incentive from a materials and applications standpoint to develop alternatives to current industry-leading silicon-based solar technologies.

1.2 A Brief History of Solar Photovoltaics

A timeline of the important milestones in solar PV history are provided in Figure 1-1. Solar PV dates all the way back to the 1800's and during the Industrial Revolution, when in 1839 French scientist Edmond Becquerel first discovered the fundamental process for what would be a critical component for the function of future solar PV technologies – the photovoltaic effect.[10] His experiment revealed that illuminating an electrode (Platinum, Pt) in an electrolyte (AgCl,

AgBr) could generate a photovoltage – the pillar of the solar cell function. The next important discovery towards solar PV was made between 1873-1876 by Willoughby Smith, an English electrical engineer, who observed an induced photoconductivity of selenium upon exposure to irradiation.[11] This discovery proved that solar energy can be easily harvested without the need for larger and more complicated equipment and parts, as were needed for other energy-producing technologies (e.g. coal plants). Finally, in 1883, the first solar cell was created by New York inventor Charles Fritts.[12] His cell consisted of coating a thin layer of gold onto selenium, achieving an energy conversion efficiency of 1-2%. Though it had been discovered, it was not until 1887 that the photoelectric effect was observed by Heinrich Hertz.[13] His experiment showed that upon exposure to ultraviolet light, the voltage at which sparking takes place between two metal electrodes with a voltage between them will vary, proving that the ultraviolet light could eject electrons from the metal surface. In 1918, Jan Czochralski of Poland developed a method to produce single crystal silicon,[14] called the Czochralski process, which still used to this day. However, it was not until 1953-1956 that the efficiency of solar PV became more practical when silicon was discovered at Bell Laboratories as a more efficient material than selenium for solar energy harvesting. This led to the creation of the first silicon-based solar cell that was 6% efficient.[15] This allowed enough power to be generated from a solar cell such that it could finally be used to power real devices and equipment, which paved the road for the future commercialization of silicon photovoltaics. Further development of silicon-based cells resulted in efficiencies up to 14% by Hoffman Electronics during 1960. This led to the production of modules for larger terrestrial and space-satellite applications.[12] While decent efficiencies and practical use of these solar PV cells was possible, they were still very expensive ($100-$150/W). In 1970 Exxon Corporation designed a cell to significantly cut costs down to $20/W, which

allowed solar PV to be utilized in a wider range of terrestrial applications such as navigation warning lights, lighthouses, railroad crossings, etc.[12]

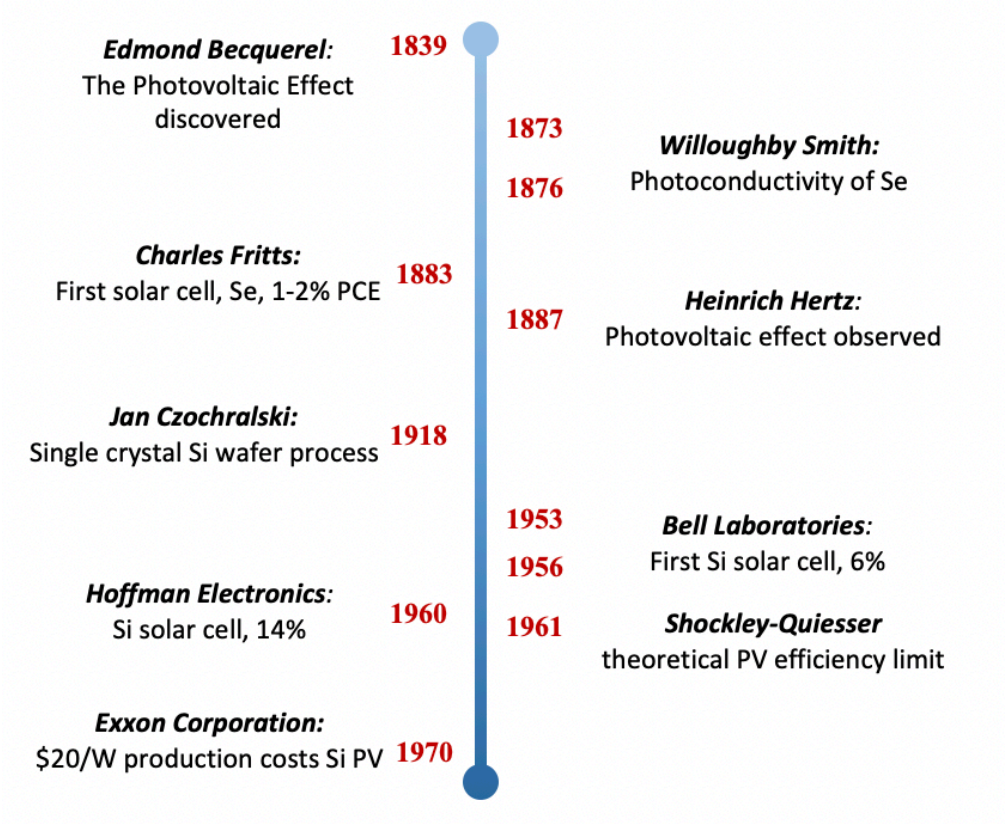

Figure 1-1: A brief timeline of history of solar PV development. (Adapted from references 10-15)

Owed to the great potential of solar PV as a major energy source, much more effort was put in to further developing the technology, both through government and industry support, with a notable opening of the National Renewable Energy Laboratory (NREL) research institute in 1977 dedicated to developing technologies to harvest solar energy. Over the next 50 years, different waves of solar PV technologies emerged as its technological promise was realized, which can be classified into the three major generations that will be discussed in the next section.

1.3 Generations of Solar PV

The three generations of solar PV technology are: wafer-based (bulk), thin film, and low-cost high-efficiency (Figure 1-2).

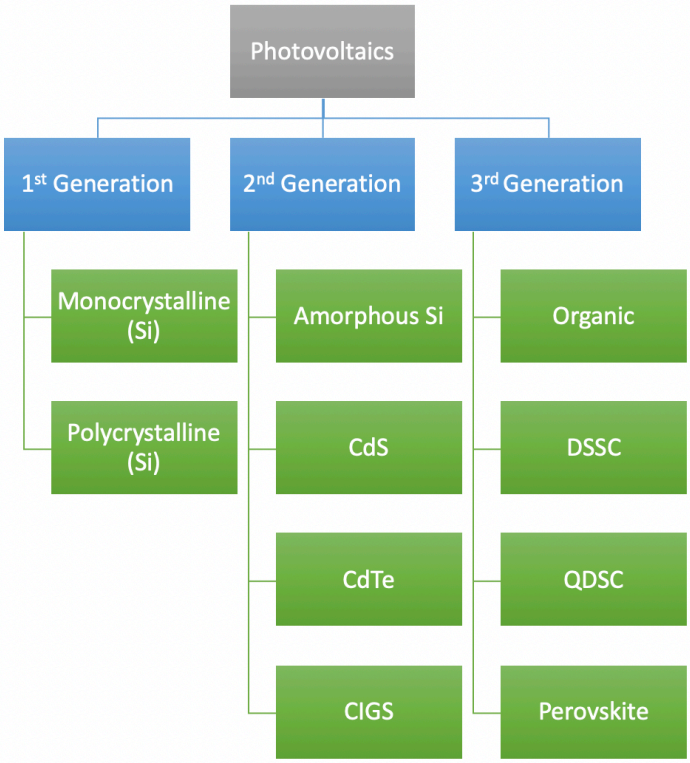

Figure 1-2: The Generations of Solar PV Technology.

The first generation pertains to what has been discussed thus far – the oldest and most conventional solar PV technology that uses silicon-based monocrystalline wafers made via the Czochralski method. Silicon is the industry standard owed to its higher efficiencies (up to 26%) than other materials, and comprises about 30% of the market. Polycrystalline silicon is also used as a first generation material, but achieves lower efficiencies than its monocrystalline counterpart (up to 21%),[16] owed to its fabrication processes where molten silicon is poured into a cast instead

of coming from a single crystal. The second generation of solar PV is known as thin film as the active layers are only a few microns thick, compared to the tens to hundreds of microns seen for bulk (first generation) silicon. This has the advantage of not only lowering material costs and supply, but opens the possibility of further applications due to the potential for flexible and lightweight packaging. The major types of second generation solar PV are: Amorphous Silicon (a-Si), Cadmium Telluride (CdTe), Copper Indium Selenide (CIS) and Copper Indium Gallium diSelenide (CIGS). a-Si is much less efficient (12%) than mono or poly, but has the advantage of a much thinner film and more simple and less expensive fabrication methods. Thin film cells typically have a top window layer that absorbs the higher energy photons, leaving the lower energy photons to be absorbed by the active material. This improves efficiency, where CdTe can reach 21.4%, CIGS 21.6%, and a-Si 11.8% as of 2016.[16] Second generation thin film solar PV also uses materials with direct band gaps, as opposed to the indirect band gaps of first generation silicon. This will be discussed in greater detail in Chapter II. The drawback with these materials, however, is that they either use rare earth elements, or toxic elements (with the exception of a-Si), which alongside higher manufacturing costs and fewer infrastructure, limits their widespread use. This leads us to the third generation of solar PV which focuses on developing low-cost, high-efficiency thin film solar cells. These types of cells are inherently different than the prior generations in that they do not rely heavily on a p-n junction for their function (described in further detail in Chapter II). Furthermore, third generation solar PV utilizes new materials and structures, such as nanomaterials, nano-structures and features, quantum effects, printable solar-absorbing inks, organic dyes, conductive plastics (polymers), etc. The first type of third generation solar PV is called the dye-sensitized solar cell (DSSC), often referred to as the Grätzel cell, which is named after its inventor Michael Grätzel. This type of solar PV device uses a

photo-absorbing dye that is coated onto a porous titania (TiO_2) layer (with high surface area such that the maximum amount of photo-absorbing dye can be loaded onto it) and a liquid electrolyte that serves as a 'shuttle' for charge carriers across the device via a redox reaction (Figure 1-3). DSSCs have the advantages of low-cost, environmental friendliness, semi-transparency, tunable color (based on the type of dye used), and ease of fabrication with efficiencies up to ~12%.[17,18] However, the most interesting advantage of DSSCs are that their efficiency enhances under lower (diffuse) light intensity and higher temperatures.[18] DSSCs are thus more ideal for unique applications such as building-integrated where they don't see the sun's full intensity. However, like any technology, DSSC do not come without drawbacks, some of which are that the use of liquid electrolytes can lead to short lifetimes due to evaporation of the organic solvent, difficulty in sealing the device that result in leakage pathways for solvents, electrode corrosion, and limited solubility of the inorganic salts.[16] The DSSC will be important as it relates to the initial operation of the hybrid perovskite solar cell.

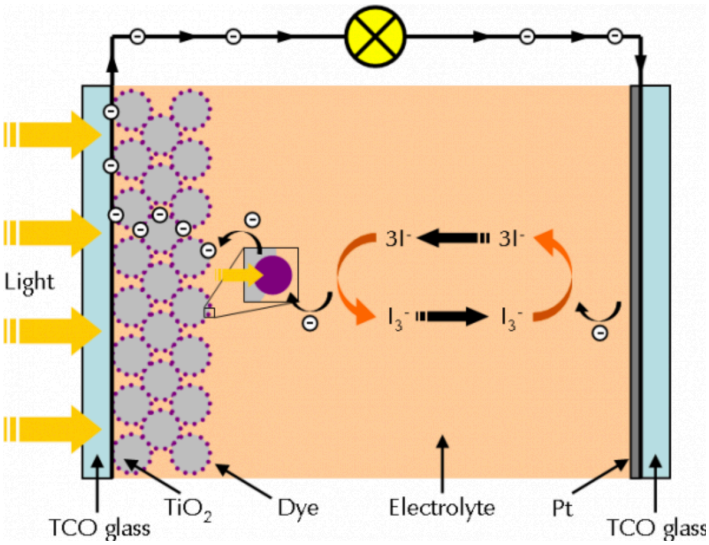

Figure 1-3: Working Principle of a Dye-Sensitized Solar Cell (DSSC). Light is absorbed by the dye (purple), followed by extraction through the electron-transporting TiO_2 scaffold to the TCO

electrode. The electron returns through the other electrode after giving off excess energy to do work, where it undergoes a redox reaction with the iodine solution. The I^-/I_3^- redox reaction serves as a shuttle for the electrons to return to the dye and maintain charge neutrality.[19]

The next type of important third generation solar PV technology is organic PV cells, where organic refers to the fact that the active layer is made from entirely organic materials, such as polymers and small molecules. Typical structures of these active layers are bi-layered or bulk heterojunction, where the active layer is comprised of donor and acceptor materials for charge separation and transport. Organic solar cells are very inexpensive, but not very efficient (current records are over 12%), which limits their use and their direction is still not clear. However, they can be manufactured using roll-to-roll printing processing, and are expected to approach $0.5/W in the near future (2020) which could rival that of conventional first and second generation solar PV technologies.[16] Some other types of third generation technologies include quantum dot/wire//well solar cells and other nanotechnologies, which are still in the fundamental research phase.

A relative newcomer to the solar PV field are a new class of materials called hybrid organic-inorganic perovskites. This family of materials shows tremendous promise in the solar PV field to achieve high efficiencies (current record over 23%), low material costs, and high throughput roll-to-roll processing capabilities. In addition, there are many interesting scientific phenomena that occur for this family of materials and associated devices not seen in other solar PV technologies, which provides much intrigue from a materials research perspective. It is this alluring family of materials that I chose to conduct my Ph.D. research on, and that will be the topic for the remainder of this thesis.

1.4 Motivation for Hybrid Perovskite Solar PV

Traditional first generation silicon-based terrestrial solar technologies, which remain firmly as the industry standard solar PV technology, are becoming less compatible with the changing nature of our society's energy requirements based on four significant limitations: (i) largely plateaued efficiencies over the last 15 years (~26% lab-scale power conversion efficiency (PCE)), (ii) high processing costs resulting from the large energy requirements to extract pure silicon from the strongly covalently bonded silicon dioxide (~1500-2000 °C via arc furnace), (iii) production of toxic pollutants and greenhouse gases during processing of silicon from silicon dioxide (SiO_2), and (iv) high weight and rigidity that result in high installation costs and limit applications to rooftops and traditional solar farms.[20] These factors provide large incentives to develop new technological breakthroughs in photovoltaic materials and devices that can reduce costs and increase performances of solar PV, ultimately alleviating current constrictions on implementing solar into our country's energy portfolio.

Recently, the organic-inorganic hybrid perovskite thin film solar cell has emerged a promising candidate to replace crystalline silicon as a terrestrial photovoltaic standard due to its high efficiencies, which have soared to reach over 23% in just 8 years[17] with low solution-based processing costs. The exceptional and unprecedented optoelectronic properties of perovskites have resulted in a calculated maximum theoretical power conversion efficiency (PCE) limit of ~31%,[21] which is close to the theoretical efficiency limit (33%) for a single junction solar cell[22] and is well beyond the current plateaued efficiency of silicon-based cells (~26%). Arguably some of the most intriguing features of hybrid perovskites from a manufacturing and applications standpoint are their flexible and light-weight thin film nature with the potential to reach high

specific powers (the ratio of power to device weight, ~1.59 kW/kg), transparency tunability, and facile high-throughput solution-processing capabilities, which have opened the door to a myriad of unique solar applications from building-integrated photovoltaics to unmanned aerial vehicles, portable micro-grid capabilities, and more. From a materials science standpoint, this family of materials exhibits a myriad of properties ideal for PV applications, such as a high dual electron and hole mobility, large absorption coefficients, a favorable band gap, a strong defect tolerance and shallow point defects, benign grain boundary recombination effects, and a reduced surface recombination.[23] It is for these reasons that hybrid perovskites are among the most highly researched field in recent years and have great potential to alleviate the restrictions of silicon-based photovoltaic technologies to pave the way towards a feasible solar-driven sustainable future.

References:

1. U.S. EIA. International Energy Outlook 2017. (2017).

2. Key World Energy Statistics 2018 - en - OECD. Available at: http://www.oecd.org/publications/key-world-energy-statistics-22202811.htm. (Accessed: 9th January 2019)

3. Carbon emissions will reach 37 billion tonnes in 2018, a record high. Available at: https://phys.org/news/2018-12-carbon-emissions-billion-tonnes-high.html. (Accessed: 9th January 2019)

4. EPA. Climate Change: Basic Information.

5. Paris Agreement. (2015).

6. Kolev, B. & Todorieva, V. Solar electricity power station building. A preliminary project investigation for "PIRIN TEX LTD." - Gotze Delchgev using. (2009)

7. Tsao, J., Lewis, N. & Crabtree, G. Solar FAQs. (2006).

8. Cass, S. Solar Power Will Make a Difference--Eventually. *MIT Technology Reviews - Sustainable Energy* (2009).

9. U.S. Solar Market Has Record-Breaking Year, Total Market Poised to Triple in Next Five Years.

10. Jewell, W. T. & Ramakumar, R. The history of utility-interactive photovoltaic generation. *IEEE Trans. Energy Convers.* **3**, 583–588 (1988).

11. Smith, W. The action of light on selenium. *J. Soc. Telegr. Eng.* **2**, 31–33 (1873).

12. Office of Energy Efficiency & Renewable Energy. The History of Solar. (2018).

13. History of Solar Cells: A Technology Evolving. *Solar Power Authority* (2016). Available at: https://www.solarpowerauthority.com/a-history-of-solar-cells/. (Accessed: 8th January 2019)

14. Czochralski, J. Ein neues Verfahren zur Messung der Kristallisationsgeschwindigkeit der Metalle. *Z. Für Phys. Chem.* **92U**, 219–221 (1918).

15. Perlin, J. The Silicon Solar Cell Turns 50. (2004).

16. Ranabhat, K. *et al.* An introduction to solar cell technology. *Istraz. Proj. Za Privredu* **14**, 481–491 (2016).

17. NREL 2017. *Res. Cell Effic. Rec. NREL Httpwwwnrelgovncpvimagesefficiencychartjpg* (2017).

18. Hagfeldt, A., Boschloo, G., Sun, L., Kloo, L. & Pettersson, H. Dye-Sensitized Solar Cells. *Chem. Rev.* **110**, 6595–6663 (2010).

19. Dye Sensitized Solar Cells-Dye Solar Cells-DSSC-DSC. Available at: https://www.gamry.com/application-notes/physechem/dssc-dye-sensitized-solar-cells/. (Accessed: 9th January 2019)

20. Solar power has big limitations. This wonder material could change that. *World Economic Forum* Available at: https://www.weforum.org/agenda/2016/06/perovskite-solar-cells/.

21. Sha, W. E. I., Ren, X., Chen, L. & Choy, W. C. H. The efficiency limit of CH3NH3PbI3 perovskite solar cells. *Appl. Phys. Lett.* **106**, 221104 (2015).

22. Shockley, W. & Queisser, H. J. Detailed Balance Limit of Efficiency of p-n Junction Solar Cells. *J. Appl. Phys.* **32**, 510–519 (1961).

23. Chen, Q. *et al.* Under the spotlight: The organic–inorganic hybrid halide perovskite for optoelectronic applications. *Nano Today* **10**, 355–396 (6).

Chapter 2. Fundamentals of Semiconductors and Solar Cells

(This chapter is based on fundamentals concepts from Solymar & Walsh, *Electronic Properties of Materials*; and Nelson, Jenny, *The Physics of Solar Cells*)

2.1 Semiconductors

Semiconductors are the stronghold of modern electronic circuits and devices. While metals are highly electronically conductive and certainly play an important role in electronic devices, semiconductors are equally if not more important because they allow for *control* over the flow of electrons through a material. This characteristic is essential for the function of electronic devices, which require frequent switching (on/off) between components to communicate in binary language and controlling current flow to occur in one direction (e.g. a diode). Semiconductor materials also allow for detection of various sources of energy (e.g. sensors, detectors), generation of light (LEDs, LASERS), and capturing of light (photovoltaics). One feature of that has allowed for the great successes of semiconductors in these applications is the capability to control the density of electrons within the semiconducting material, known as *doping*, which will be discussed further in this section. While a discussion on semiconductors could extend far into many other fields such as microelectronics, here we will focus on semiconductor fundamentals as they pertain to photovoltaics.

2.1.1 The band gap

A semiconductor is a material that has a conductivity somewhere between a metal, such as silver, gold, copper, or aluminum, and an insulator, such as glass. Semiconductors can be broken down categories based on the elements of which they are comprised. First, there are elemental semiconductors made up of Group IV elements, such as silicon and germanium, hence the name elemental as they can be made solely from one element. However, these can form compound semiconductors as well, which are still comprised of two Group IV elements, such as SiGe. Next, there are III-V semiconductors, such as GaAs, InP, GaP, GaN, that are made up of elements from Group III and Group V of the periodic table. Similarly, there are II-VI semiconductors, such as ZnO, CdTe, ZnTe, and so on.

There are two models I wish to provide that each give different, yet important, perspectives. The first is more intuitive, stemming from the well-known molecular orbital theory (MOT). MOT is a method for describing the electronic structures of molecules, and can be extended to that of bulk materials for our discussion, known as the *band model*. The basis behind this model is that the characteristic orbitals for the bulk material are obtained as linear combinations of the individual atomic orbitals. Let us first look at the case for metals. Using lithium (Li) as an example, we can first see what happens in the case of two Li atoms coming together to form Li_2. Figure 2-1a depicts the energy level diagram for this scenario consisting of Li 1s and 2s orbitals, where the 1s orbital is completely-filled and the 2s orbital half-filled. When these two single atoms are brought together to form diatomic lithium, we get an energy level splitting of both the 1s and 2s orbitals per the Pauli Exclusion Principle that creates a lower energy bonding ($\boldsymbol{\sigma}$) and higher energy anti-bonding ($\boldsymbol{\sigma}^*$) level to prevent two equivalent energy states from occurring. This creates a slight energy 'gap' between the two levels. As we increase the length of the chain,

taking Li_4 as a hypothetical example, the degree of splitting of the 2s states increases, where the number of states always equals the number of atoms. This occurs when the lithium chains are increased in length and also placed on top of one another, until eventually we obtain a bulk Li crystal. In this case there are a great number of Li atoms (one gram of Li has approximately 10^{23} atoms) and we form what are called energy bands (e.g. 2s band). These bands are bounded by an upper and lower limit that separate them from the prior and subsequent bands (1s, 2p bands) by a significant energy gap. The electronic states are filled sequentially with the lowest states filled first (per the Aufbau principle) such that for Li the electronic states of the 2s band are exactly half-filled. Half-filled bands are characteristic of metals, and is what give them their conductive properties. In this case, charge carriers (electrons or holes) can move up these energy levels with relative ease as the energy gap between their spacing is relatively small (on the order of $\sim 10^{-20}$ eV). We call the filled portion of the band the valence band (VB), and the empty band the conduction band (CB). For this reason, we commonly describe metals as having a 'sea of free electrons' that can flow with relative ease (conductive). Furthermore, different metal atoms with the same valence, i.e. from the same group of the periodic table, can often replace each other with relative ease because the width of each energy band, which relates to the overlap of electron $\boldsymbol{\psi}$ functions, is a function of the crystal structure and determines the number of nearest neighbors. Therefore, metals can form heterogeneous solid solutions, or alloys. On the other hand, not all metals have the same mechanism as Li as it depends on the electronic structure. Taking Mg for example, it has its 3s band filled, which at first would seem non-conductive since the band is already filled (no conduction states in the 3s band). However, Mg obtains its electrical conductivity through a partial overlap of the filled 3p and empty 3s bands, therefore allowing electrons to be excited into the empty 3p band states for conduction.

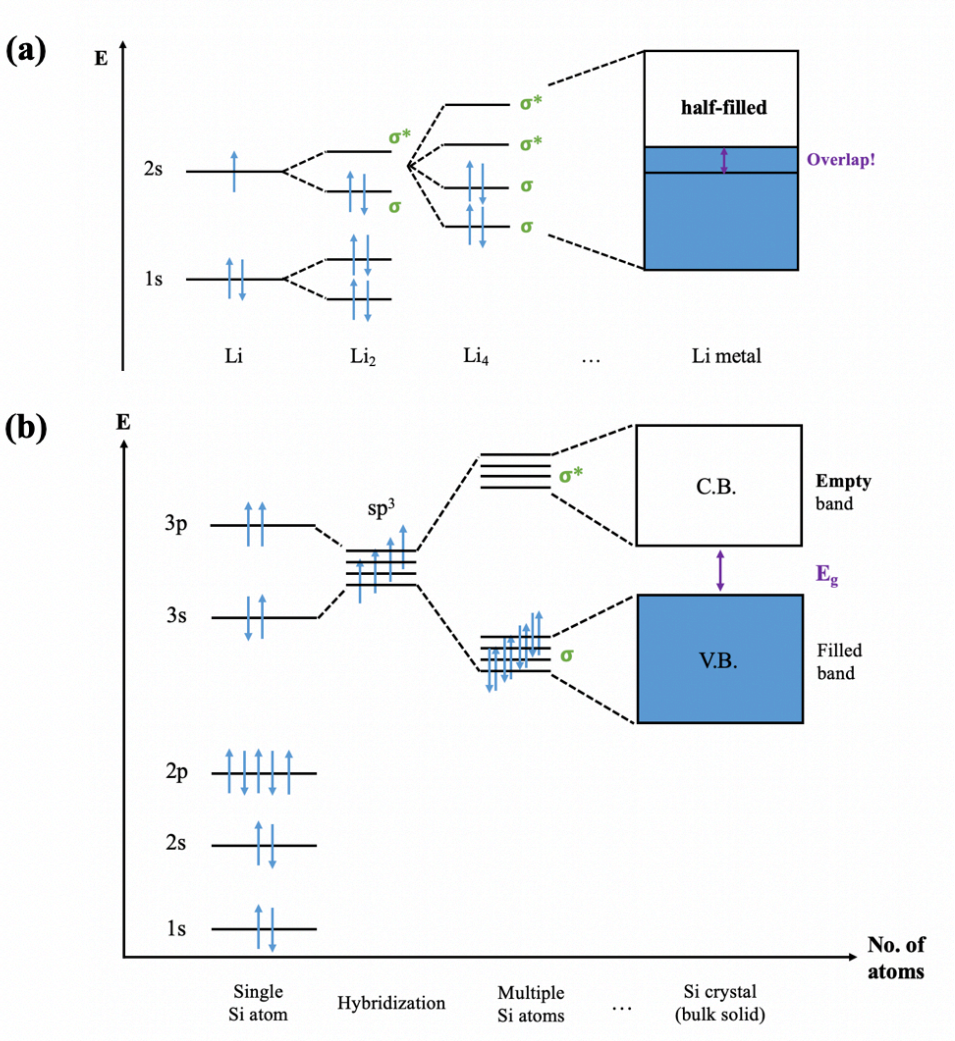

Figure 2-1: Evolution of band structures. (a) for a metal: Li. Orbital splitting occurs upon bonding of two Li atoms. Further splitting of these bonding and non-bonding orbitals leads to a continuum of closely-spaced energy bands that are half-filled - characteristic of metals. (b) for a semiconductor: Si. Hybridization of 3s and 3p orbitals occurs for Si that split into bonding and anti-bonding states. After many atoms come together into a bulk solid form, significant energy gaps form between the bonding and non-bonding bands, forming what is known as a *band gap*.

For insulators and semiconductors, the situation changes. For instance, in diamond, the bonding molecular orbitals that constitute the VB forms at a much lower energy, and the antibonding molecular orbitals that make up the CB form at a much higher energy. In addition, because each atom contributes four orbitals and four electrons, the bonding orbitals are completely filled and the only empty orbitals are those in the higher energy antibonding band. Thus, there remains a rather large energy *band gap* between the VB and CB (5.47 eV) that electrons cannot cross over.

Turning to semiconductors, we can look at the case for Si (Figure 2-1b). In a single Si atom, the 3p band is incompletely filled. At first, it may seem as though when combining two Si atoms, they would bond perfectly and completely fill the shell. Then, how does the conduction band arise? To answer this, we must first ask another question. How can Si (like C) form four bonds, when it only has two valence electrons? The answer lies in molecular orbital theory, called hybridization. Though the 3s state is initially completely-filled, the 3p state has one level completely empty and two half-filled. Thus, it is more favorable to form 'hybridized' orbitals of partial s and p components, so that each orbital is degenerate (the same) and there is symmetry of the energy distribution. Upon bonding, hybridization of its orbitals occurs and forms four sp^3 orbitals, which are then half-filled, allowing for the formation of four bonds, similarly to that of diamond, which is partly why silicon takes on the diamond crystal structure. These hybridized orbitals are then split into bonding and non-bonding states with an energy gap between them, as in the case for diamond, however the degree of splitting is less than the case of diamond. An energy band gap is still formed, however, at a much lower value (1.1 eV). This energy is low enough that even at room temperature there is a probability of electrons being thermally excited into the conduction band. Diamond has a larger band gap than Si simply because its occupied

electron levels are lower (1s, 2s, 2p versus up to 3p for Si). Thus, in Si the electrons in the outer-most shell are held less tightly than those in diamond, constituting a larger σ-σ* split, and consequently a larger band gap. Furthermore, using a technique called doping, we can introduce extra charge carriers into the material to create mid-gap states and make the semiconductor more conductive. This will be explained in the later section pertaining to doping effects in semiconductors (Section 2.1.3). Figure 2-2 shows the comparison of band diagrams for a metal, semiconductor, and insulator, and Table 2-1 lists bandgap values for common materials.

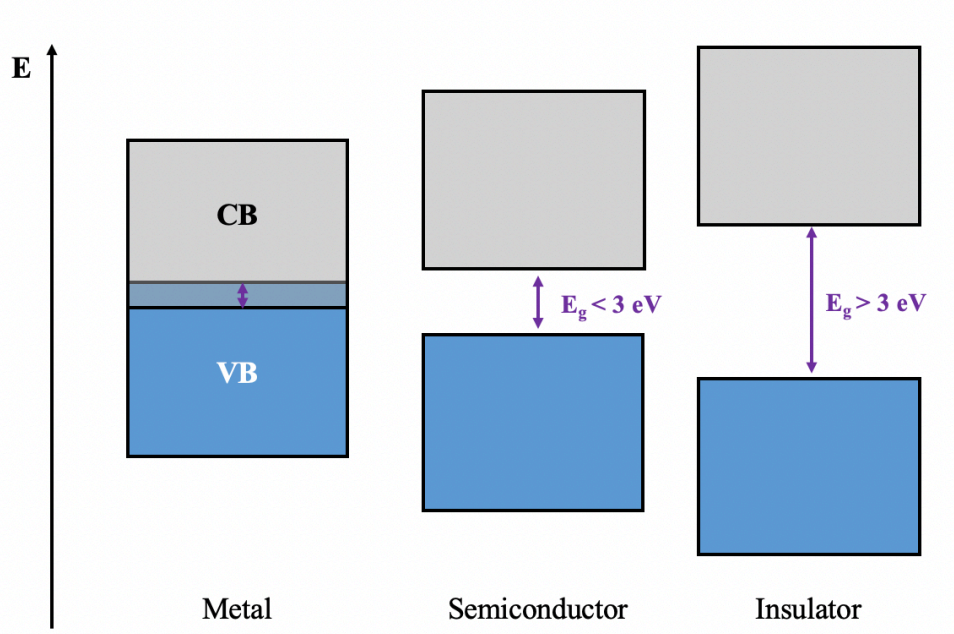

Figure 2-2: Characteristic band diagrams for metals, semiconductors, and insulators.

Table 2-1: List of common materials and associated band gaps.[1]

Material	Abbreviation	Band Gap [eV]	Type
Silicon Dioxide	SiO_2	9	Insulator
Aluminum nitride	AlN	6	Insulator

Diamond	C	5.5	Insulator
Silicon Nitride	Si_3N_4	5	Insulator
Gallium Nitride	GaN	3.4	Semiconductor
Gallium Phosphide	GaP	2.26	Semiconductor
Gallium Arsenide	GaAs	1.43	Semiconductor
Silicon	Si	1.1	Semiconductor
Germanium	Ge	0.67	Semiconductor
Lead (II) Sulfide	PbS	0.37	Semiconductor

In addition to the MOT-based band model, we can take a physics perspective to derive and plot the entire band structure. Naturally, this model starts from solving the infamous Schrödinger equation to obtain the allowable electron energy states, 1s, 2s, 2p, 3s, 3p, etc, of which are energies as a function of the wave vector (k), E(k). Bloch's theorem states that the wavefunction solution of the Schrödinger equation when the potential is periodic (this gives us Schrödinger's in terms of k-space), can be written as:

$$\psi(x) = e^{ikx} \cdot u(x) \tag{2.1}$$

where u(x) is a periodic function that satisfies u(x+a)=u(x). Essentially, this is the solution to Schrödinger's infinite potential barrier, but instead with a finite potential barrier and a periodicity term. To solve the periodic potential, we use a model called the Kronig-Penny (KP) model to solve for the allowed and forbidden k values in a periodic potential, from which an E-k plot can be constructed. This E-k plot, is essentially our band structure and tells us where the energy bands lie and what the forbidden energy levels are, i.e. *band gaps*. E-k diagrams vary based on crystallographic direction and are typically constructed for the most significant directions within

a given material/crystal structure. The E-k diagram varies from 0 to π/a, where a is the atomic spacing of the crystal structure along a given direction. Since these functions are waves, and therefore periodic in nature, the boundary of an allowed band corresponds to cos(ka)=$\pm$1, that is, k=nπ/a ; n=1, 2, 3, etc, which is the physical origin the band gap. This means that the energy distribution repeats in intervals of k=π/a, and the areas within these boundaries can be described as Brillouin Zones, where the first Brillouin Zone boundary is that of k=π/a, corresponding to when maximum or minimum energy is reached on the periodic E-k wave (slope equal to zero). In fact, what allows us to use the Bloch wavefunction to completely describe all relevant k values is that it defines all k within our First Brillouin Zone, where those k outside of the FBZ can be represented as integer multiples of those k values within the FBZ. Figure 2-3a represents an E-k diagram constructed by solving the KP model, from which band gaps and energy bands are clear for each k=π/a interval. Figure 2-3b depicts the energy band diagrams for metals, insulators, and semiconductors. The shading indicates the filling of electron states within the bands. Darker signifies a more filled band, whereas lighter that the states within the band are empty. To provide perspective the positions of the energy bands are all relative to a common energy level, called the Fermi level (E_F), which is a very important parameter, and will be discussed further in the next section.

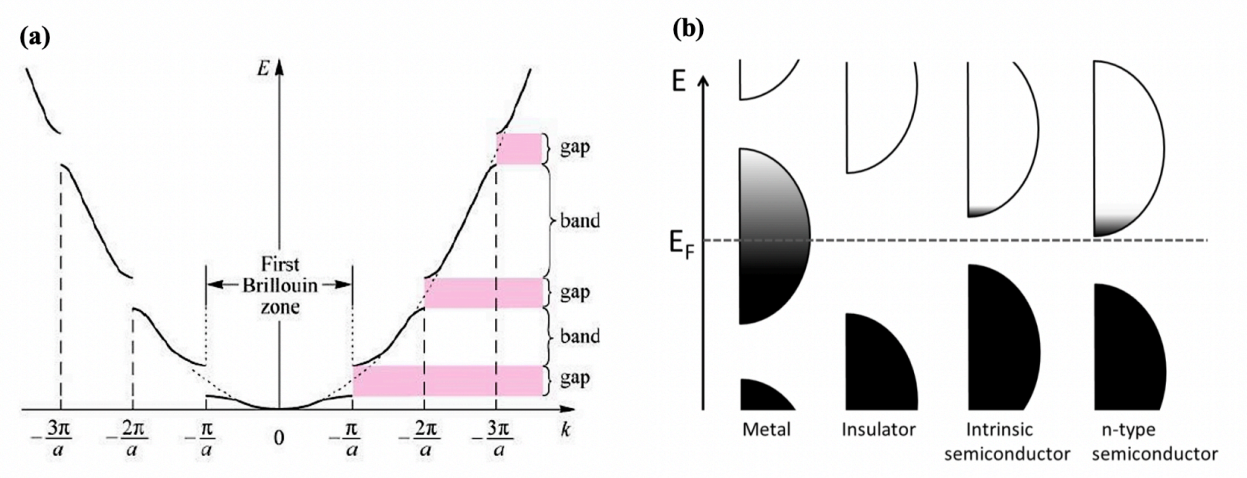

Figure 2-3: (a) E-k diagram solutions to KP model indicating Brillouin zone boundaries, allowed and unallowed E and k values (bands and band gaps). (b) Representative energy band diagram comparisons for metals, insulators, and semiconductors. The y-axis represents energy and the shading indicates the filling of electron states within the band, where darker indicates more filling and lighter less. Band positions are relative to a common Fermi level to provide perspective.[2,3]

2.1.2 The Fermi Level

The Fermi level is a measure of equilibrium. It is equivalent to the chemical potential of charge carriers (i.e. electrons) within a material. A strong understanding of the Fermi level, i.e. how it relates to electronic band structure, current and voltage, is essential to understanding solid state physics and devices, especially solar PV. Formally, the Fermi level is defined as an actual or hypothetical energy of an electron such that at thermal equilibrium it would have 50% probability of being occupied at any given time. For a metal, the Fermi level lies within the CB/VB, since there is an overlap of the two bands. However, for insulators and semiconductors, the Fermi level lies between the CB and VB, where at thermodynamic equilibrium (0K) it is

precisely at the center, meaning that no electron has an energy greater than this level. No states above the Fermi level are filled. As the temperature increases, E_F shifts upwards and offsets from the exact center, however, the amount is very small such that its shift is hardly distinguishable. This follows the Fermi-Dirac distribution function, which provides the probability that an energy level at energy, E, in thermal equilibrium with a large system, is occupied by an electron, given by the relationship:

$$f(E) = \frac{1}{1+\exp\left(\frac{E-E_F}{k_0 T}\right)} \tag{2.2}$$

The system is characterized by its temperature, T, and its Fermi energy, E_F. As temperature increases, the probability of occupation increases gradually, as shown in Figure 2.4.

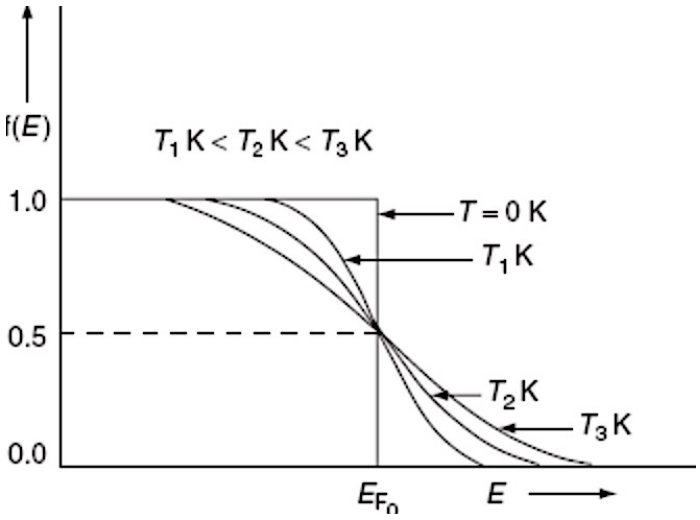

Figure 2-4: The Fermi-Dirac distribution function. As temperature increases, the slope gradually decreases, thereby increasing the probability of occupancy.

Since the Fermi level is derived from the condition that at T>0, there is some finite probability per the Fermi-Dirac (FD) distribution that some of the electrons are excited into the CB. Consideration of charge neutrality requires that the number of electrons equal the number of holes to within the semiconductor, i.e. N_e=N_h. Using the derived expressions for N_e and N_h yields:

$$E_F = \frac{E_c+E_v}{2} + \frac{3}{4}kTlog\frac{m_h^*}{m_e^*} \quad (2.3)$$

where E_c and E_v are the conduction and valence band energy levels, and m_h^* and m_e^* are the electron and hole effective masses (described in further detail shortly). Thus, we can see that if T=0K, E_F lies within the middle of the gap. Therefore, it effectively represents the chemical potential of the semiconductor, where the middle is equilibrium, and as electrons are excited to the conduction band it shifts in accordance. Electrons can be excited into the CB in several ways, such as thermally, by absorbing light, or essentially by any means so long as it has enough energy to overcome the bandgap. When electrons are excited into the CB, they leave behind a vacant site, which we refer to as a *hole*. These holes can move down in energy through the VB in a similar manner as electrons move up through the CB, because a moving hole is essentially an electron moving upwards to fill a vacant position, and in the end we still get the movement of charge carriers. Consequentially, we commonly use the term charge carriers to describe the use of either electrons or holes as the majority carrier.

The effective mass, commonly denoted by m^*, is essentially the mass that a charge carrier 'sees' due to its interaction with the periodic electric potential of the crystal lattice as it moves within, as opposed to the mass an electron sees within vacuum (with no external forces acting upon it as it moves). In other words, it is a way to represent that an electron can propagate faster than

normal in a periodic potential. The effective mass is related to the E-k diagram according to the following relationship:

$$m^* = \frac{\hbar^2}{\frac{\partial^2 E(k)}{\partial^2 k}} \quad (2.4)$$

where the term in the denominator is the second derivative of the E-k diagram, i.e. the *curvature*. Thus, a higher curvature leads to a lower effective mass, which means the electron sees a lower mass than normal and can propagate more easily within the periodic potential. This is an important concept because it relates to the *dispersion* of band diagram, which describes how an electron responds to a force, e.g. the force on the electron from the periodic potential resulting from the band structure. Dispersion is given by the relation:

$$E = \frac{\hbar^2 k^2}{2m^*} \quad (2.5)$$

A higher dispersion means that E varies more greatly for each k value increase, i.e. the difference between the lowest and highest energy levels within the band (range of k values). Referring to Figure 2-3a, the higher bands would have higher dispersion, such as bands in the k-value ranges from 0 to k=π/a vs k=$2\pi/a$ to k=$3\pi/a$. Dispersion in an important concept relating the density of states and absorption properties in photovoltaic absorbers, which will be discussed in the coming sections.

2.1.3 Doping of semiconductors

The conductivity of semiconductors can be influenced by shifting the E_F within the bandgap. This can be accomplished via a technique known as *doping,* where impurities with a

slightly different number of valence electrons are intentionally incorporated into the bulk crystal in a known quantity. This alters the bond energy between the host and impurity atoms, thereby allowing for charge carriers (either electrons or holes) to more readily free from their bonds and become a free electron, in other words, contribute towards conduction either in the CB or VB for electrons or holes, respectively. There are two types of doping: n-type and p-type doping. N-type represents introducing extra electrons and p-type signifies extra holes as the majority charge carrier type. Each impurity atom can donate one extra charge carrier (either an electron or hole). This is accomplished by introducing an impurity atom from the immediate neighbor group on the periodic table. For instance, Si can be doped n-type with phosphorous (group V) and p-type with boron (group III). N-type doping shifts the E_F closer to the CB, known as a donor impurity, while p-type doping shifts the E_F down towards the VB, known as an acceptor impurity. Figure 2-5 displays the schematic for n- and p-type doping of Si and the corresponding band diagrams. Notice the E_F shift on the band diagram lies between the newly introduced impurity states and the closest band (CB/VB). This is because the introduced carriers are not bound and therefore higher in energy as they freely move throughout the material. Typical doping densities of semiconductors are on the order of 10^{13}-10^{18} atoms/m^3 and 10^{22} atoms/m^3 for a heavily doped semiconductor, and since there is 1 carrier per atom, atoms/m^3 is equivalent to electrons or holes/ m^3.

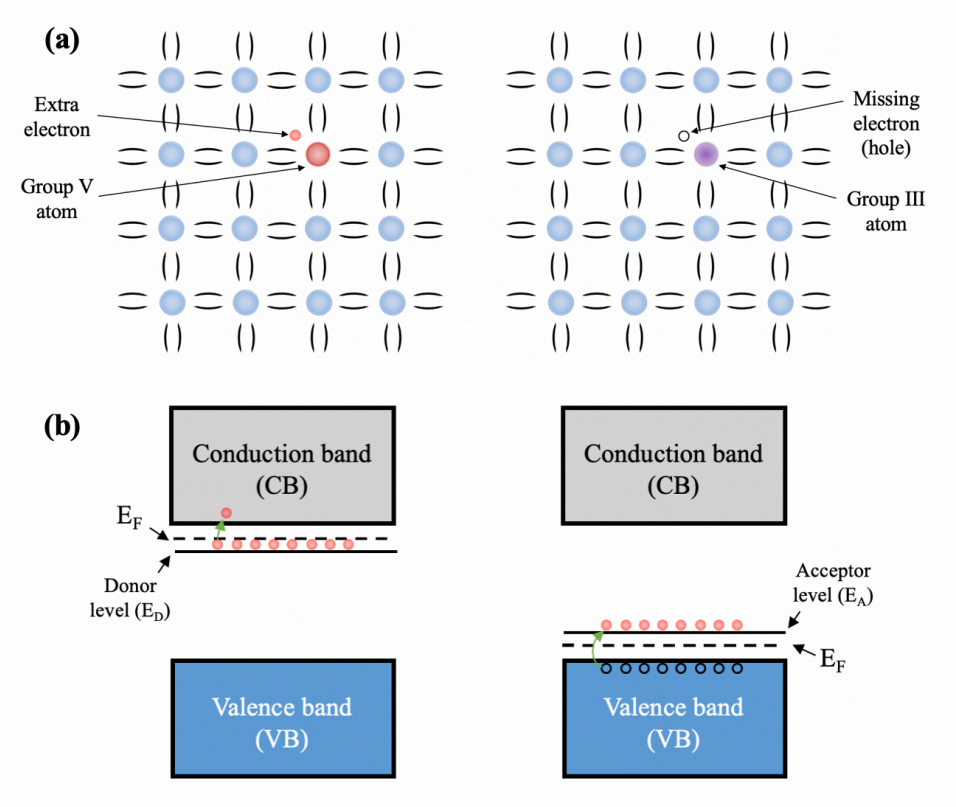

Figure 2-5: (a) n-type (left) and p-type (right) doping of a semiconductor. An impurity atom with either one extra or one less electron substitutes a host atom to introduce an extra charge carrier (electron or hole) into the system. (b) Corresponding band diagrams for n-type (left) and p-type (right) of typical high density doping of semiconductors. Figure depicts the acceptor and donor levels with associated Fermi level changes, and electron and hole charge carrier introduction via doping.

However, here it is important to note that before we can calculate the actual density of charge carriers within out material, we must find the number of states available at each energy per volume within the band. This leads us to the *density of states* (DOS), which is defined as the the number of states per unit energy per unit volume, given by:

$$g(E)dE = g(k)dk = \left(\frac{k}{\pi}\right)^2 dk \tag{2.6}$$

And since E and k are related by equation 2.5, the number of solutions to Schrodinger's equation are given by:

$$(2.7) \qquad k_x = \frac{n\pi}{L}$$

where n = 1, 2, 3, etc are the allowable quantized levels. If this is expanded to include three dimensions along the y- and z-axis, this corresponds to a cube in k-space with size n/L. Accordingly, we obtain the relationship:

$$(2.8) \qquad g(E) = \frac{1}{2\pi}\left(\frac{2m^*}{\hbar^2}\right)^{3/2} E^{1/2} \qquad \text{or} \qquad g(E) = \frac{8\pi\sqrt{2}}{h^3}(m^*)^{3/2}E^{1/2}$$

Multiplying the DOS by the probability of a state being occupied by an electron (Fermi-Dirac function), we obtain the number of electrons at each energy level:

$$(2.9) \qquad n(E) = g(E)f(E) = \frac{1}{2\pi}\left(\frac{2m^*}{\hbar^2}\right)^{3/2} \int_{-\infty}^{\infty} \frac{E^{1/2}}{1+\exp\left(\frac{E-E_F}{k_0 T}\right)} dE$$

This is typically calculated as the number of states per energy per unit volume, since the number of energy states within a material is very large. The DOS is a very important concept because it responsible for determining several important properties of semiconductors, as will be discussed.

2.1.4 Conductivity, mobility and carrier concentration

To further understand the effects and implications of doping, we should take a step back and look deeper into several important parameters that are of interest for metals and semiconductors, namely, conductivity, mobility, and carrier concentration. Conductivity is the degree to which a

material conducts electricity, or how well it transports electrons, which for metals is given by the general equation:

$$\sigma = \mu_e(N_e e) \tag{2.10}$$

where N_e is the charge carrier concentration, e is the fundamental charge of an electron, and μ_e is the mobility of the electron. We have just discussed doping as the mechanism behind controlling carrier concentrations within semiconductors, and for metals the carrier (electron) concentrations are typically very high around 10^{28} free electrons/m^3. There is no doping mechanism available for metals because (i) they do not have a band gap so doping would be ineffective and (ii) it is not needed because metals already have a high number of free electrons. For semiconductors, with both types of charge carriers, the equation for conductivity becomes:

$$\sigma = e(n\mu_e + p\mu_h) \tag{2.11}$$

where e and n designate that for electrons, and h, p represent values for holes. For n- and p-type semiconductors, this equation reduces to that of solely the dopant majority charge carrier type:

$$n - type: \ \sigma_e = e(n\mu_e) \tag{2.12}$$

$$p - type: \ \sigma_h = e(p\mu_h) \tag{2.13}$$

The mobility, μ, characterizes how fast a charge carrier (electron or hole) can propagate through a medium, such as a metal or semiconductor in response to an electric field, which is represented by its drift velocity, v_d:

$$v_d = \mu E \tag{2.14}$$

where E is the electric field potential. The mobility of the electron is given by:

$$\mu = \left(\frac{q}{m^*}\tau\right) \tag{2.15}$$

where τ is the average time between collisions, m^* is the effective mass of the carrier (either electron or hole), and q is the elementary charge.

Ultimately from these sets of equations, we can see that conductivity depends on three major parameters: carrier concentration, average time between collisions, and effective mass. Thus, there is a tradeoff between increasing carrier concentration by doping, and reducing the average time between collisions as impurity scattering centers are added through doping that increases the mobility. The effective mass will also be dependent on the type of material being used, as it depends on the nature of the periodic potential and thus the band structure of the material. That being said, conductivity and mobility are more relevant when discussing semiconductors, as these properties are directly measurable and more practical. Conductivities are measured in $(\Omega m)^{-1}$, where typical values for metals are on the order of $>10^7$ $(\Omega m)^{-1}$, semiconductors 10^{-4}-10^6 $(\Omega m)^{-1}$, and insulators 10^{-10}-10^{-20} $(\Omega m)^{-1}$. Mobility is measured in cm^2/Vs, where metals are typically in the range of 10^{-3}-10^{-4} cm^2/Vs, and for semiconductors, the mobility falls into the range of 10^3-10^4 cm^2/Vs for electrons and 10^2-10^3 cm^2/Vs for holes. Table 2-2 summarizes the conductivity, mobility, and carrier concentrations for metals, semiconductors and insulators.

Table 2-2: Common approximate values of conductivity, mobility, and carrier density for metals, semiconductors, and insulators.

Material Type	Conductivity [$(\Omega m)^{-1}$]	Mobility [cm^2/Vs]	Carrier Density [m^{-3}]
Metal	$>10^7$	10^{-3}-10^{-4}	10^{-28}
Semiconductor	10^{-4}-10^6	10^3-10^4 (n) 10^2-10^3 (p)	10^{13}-10^{18}
Insulator	10^{-10}-10^{-20}	$\sim 10^4$ (i)	N/A

At equilibrium, the number of carriers in the CB and VB is called the equilibrium carrier concentration, and the product of the minority and majority carriers is a constant following the of the Law of Mass Action:

$$n_o p_o = {n_i}^2 \tag{2.16}$$

where n_o and p_o are the electron and hole equilibrium carrier concentrations, and n_i is the intrinsic carrier concentration. This implies that upon doping, the minority carrier concentration must decrease if the majority carrier concentration is to increase upon further doping. The majority and minority carrier concentrations are:

$$\text{for n} - \text{type:} \quad n_o = N_D, \; p_o = \frac{{n_i}^2}{N_D} \tag{2.17}$$

$$\text{for p} - \text{type:} \quad p_o = N_A, \; n_o = \frac{{n_i}^2}{N_A} \tag{2.18}$$

For instance, in an n-type material some of the added electrons upon doping will occupy some of the holes present intrinsically within the VB, and thus not contribute as a majority carrier, lowering the number of holes present at equilibrium.

2.1.5 Carrier transport

There are two important carrier transport processes that occur within semiconducting materials: *diffusion* and *drift*. In the absence of any external driving force or stimuli, carriers will move at a constant velocity along a random direction until their path is impeded, and will then continue along a new direction after being redirected by a collision. Diffusion occurs when there is a concentration gradient within the semiconductor, for instance, when doping to introduce an excess of free carriers. Diffusion is a thermodynamically-driven process that essentially seeks a homogenous distribution of carriers within the material, i.e. carriers will diffuse from regions of high concentration to lower concentration to seek equilibrium. Drift, on the other hand, is the migration of charge carriers in a net direction in response to an applied electric field, i.e. an electrical bias. The carriers will accelerate in the direction or in the opposite direction, if the carrier is a hole or electron, respectively, of the applied electric field, where the net carrier movement is dictated by the mobility within the material. Drift is equivalent to the equation for drift velocity that we saw in the prior section. These two parameters will become important when discussing p-n junctions in the next section as well as for solar cell operation.

2.1.6 Recombination in semiconductors

Before proceeding to a discussion on how semiconductor devices are formed, namely, the p-n junction, we must first define and understand several important parameters: the charge carrier diffusion length and charge carrier lifetime. The diffusion length is the average distance a carrier can travel before recombining with the opposite carrier species (electron or hole), given by:

$$L_D = \sqrt{D\tau} \quad (2.19)$$

where τ is the charge carrier lifetime and D is the diffusivity given by the Einstein relation as:

$$D = \frac{\mu kT}{q} \quad (2.20)$$

where μ is the carrier mobility, k is Boltzmann's constant, T is temperature and q is the elementary charge. Thus, we can see that the diffusivity is related to the mobility, which is in turn related to carrier scattering. The charge carrier lifetime is an important parameter that describes the average time it takes a minority carrier to recombine with a majority carrier. The total bulk carrier lifetime is the sum of the lifetimes determined by three major recombination mechanisms: band-to-band, Shockley-Read-Hall (SRH), and Auger (Figure 2-6), given by the equation:

$$\frac{1}{\tau_{bulk}} = \frac{1}{\tau_{rad}} + \frac{1}{\tau_{auger}} + \frac{1}{\tau_{SRH}} \quad (2.21)$$

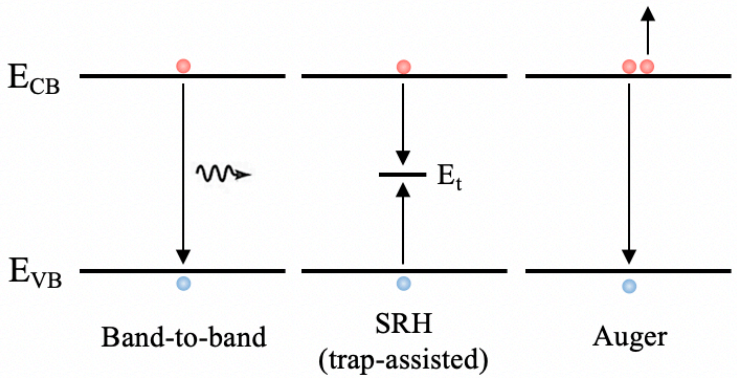

Figure 2-6: Schematic showing the three major recombination mechanisms: band-to-band (or radiative) recombination, Shockley-Read-Hall (or trap-assisted recombination), and Auger

Band-to-band recombination, also known as radiative recombination, occurs when an excited electron falls back down to the VB as it loses its energy when recombining with a hole to give off radiative energy (a photon). Auger recombination occurs when that excess energy produced when an electron drops back down to recombine with a hole is given to a third carrier, or another electron, that is then excited. This type of recombination is independent of any impurity density and unavoidable, but inversely proportional to carrier density, and thus is typically more pronounced at higher carrier densities. SRH, on the other hand, is the most important recombination mechanism for semiconductors because it is related to defect states within the material. It is a defect-mediated, monomolecular, or trap-assisted non-radiative recombination mechanism, given by the overall equation:

$$U_{SRH} = \frac{pn - {n_i}^2}{p + n + 2n_i \cdot \cosh\left(\frac{E_i - E_t}{kT}\right)} \cdot N_T v_{th} \sigma_t \tag{2.22}$$

where N_T is the trap density (or impurity/defect concentration), v_{th} is the thermal velocity, p and n are the hole and electron concentrations, E_t and E_i are the trap and intrinsic energy levels, σ_t is the trap capture cross-section. The minority carrier lifetime in a heavily doped material is related to the rate of trapping of carriers at recombination centers (trap states), and thus is also a function of the doping concentration because additional trap states are created at high doping levels. A more convenient form of this equation defines the lifetime for electrons and holes captured by the trap:

$$U_{SRH} = \frac{pn - {n_i}^2}{\tau_{n,SRH}(p + p_t) + \tau_{p,SRH}(n + n_t)} \tag{2.23}$$

where the lifetimes for electrons and holes under low-injection conditions are given by:

$$\tau_{n,SRH} = \frac{1}{v_n \sigma_n N_t} \qquad \tau_{p,SRH} = \frac{1}{v_p \sigma_p N_t} \tag{2.24}$$

and n_t and p_t are the values of the electron and hole densities when the Fermi level is equal to the trap level, i.e. the occupancy of trap states:

$$n_t = n_i e^{(E_i - E_t)/kT} \quad and \quad p_t = n_i e^{(E_i - E_t)/kT} \tag{2.25}$$

From this model, we can see that to reduce SRH recombination requires defect levels far from mid-gap, low capture cross-sections, and most notably, the density of trap states. Operating in high injection conditions is beneficial because carrier concentrations are much greater than the background defect density, and thus the greater influx of free carriers leads to a lower percentage of lost carriers to SRH recombination.

For heavily-doped semiconductors, the SRH recombination rate simplifies to:

$$U_{n,SRH} = \frac{(n - n_0)}{\tau_{n,SRH}} \quad and \quad U_{p,SRH} = \frac{(p - p_0)}{\tau_{p,SRH}} \tag{2.26}$$

However, this is only valid when these parameters for n and p do not differ by orders of magnitude, and SRH recombination is strongest when n and p are of similar magnitude. The largest contribution from traps is from those states located closest to the center of the band gap, where n≈p, known as deep lying trap states. These deep-lying states are detrimental to semiconductor performance, and typical of most semiconducting materials, however, as we will see they are not as prominent in hybrid perovskite materials.

For certain materials that have dielectric behaviors, the relative static permittivity, or dielectric constant ε_r, because it can provide charge-screening effects of the capture cross-

section σ_t. A capture event will occur when the potential energy for a charged defect is greater than the thermal energy at a specific radius, given by:

$$\sigma_t = \frac{q}{16\pi(\varepsilon_r \varepsilon_0 kT)^2} \quad (2.27)$$

where q is the elementary charge and ε_r is the permittivity in vacuum. We can see an inverse-square dependence of capture cross-section on dielectric constant of the material, and therefore higher dielectric constants can realize high amounts of dielectric screening.[4]

Another important type of recombination is surface recombination, which is similar to trap-assisted with the only difference being that it depends on the number of surface states (two-dimensional) rather than trap states within the bulk:

$$U_{SRH} = \frac{pn - {n_i}^2}{p + n + 2n_i \cdot \cosh\left(\frac{E_i - E_{st}}{kT}\right)} \cdot N_{t,s} v_{th} \sigma \quad (2.28)$$

In real semiconductor materials, defects are much more likely to occur at surfaces and at interfaces than within the bulk. Localized states at surfaces and interfaces include crystal defects owed to broken bonds or terminated surfaces, and extrinsic impurities which are deposited onto the surface from the surrounding environment, or which are concentrated at surfaces during growth. Surface and interface defects are critical for electronic devices and solar cells.

2.1.7 The p-n junction

A p-n junction is of paramount importance for the function of the majority of electronic devices. P-n junctions are formed by joining p- and n-type semiconducting materials. Owed to

the extra electrons in the n-type region and the extra holes in the p-type region, upon joining of the two materials the electrons will diffuse to the p-type side while holes will diffuse to the n-type side to attempt to homogenize. If there were no charges involved, this process would continue until it did reach homogenization. However, when electrons or holes move across the junction to the other material, they leave behind a positive or negative ion core, which is fixed within the crystal lattice unable to move because the crystal must be electrically neutral, that is, the net charge density must be zero. This creates an internal electric field due to the opposing positive and negative ion core regions, which we call the *depletion region*, since it is depleted of carriers (Figure 2-7).

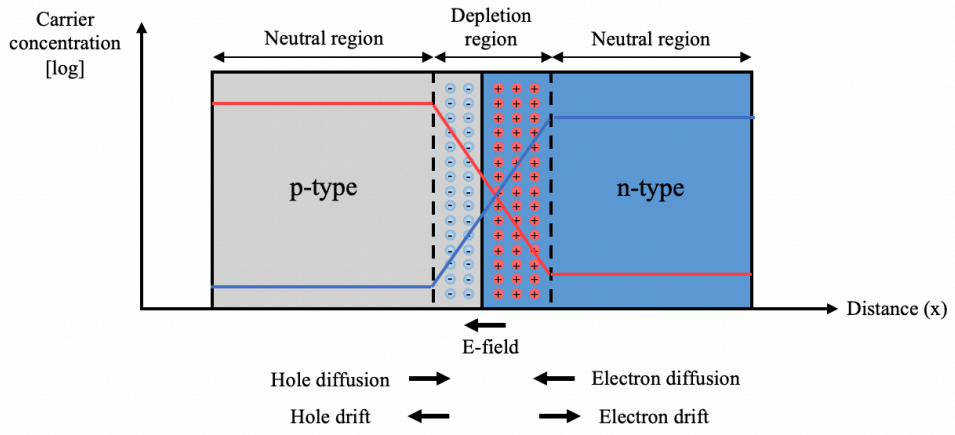

Figure 2-7: A p-n junction occurs when a p- and n-type material are placed into contact. The electrons diffuse to the p-type side, and the holes to the n-type side in an attempt to equilibrate. This leaves behind positive and negative ion cores, the create a 'depletion region' and a corresponding built-in bias the prevents further carriers from crossing the junction.

Consequentially, a built-in potential is formed across the junction, which is determined by the differences in work functions of the n- and p-type materials, and ultimately relates to doping and free carrier densities:

$$V_{bi} = \frac{kT}{q} ln\left(\frac{N_d N_a}{{n_i}^2}\right) \tag{2.29}$$

The depletion width is can be found using the following equation:

$$w_{depl} = w_p + w_n = \sqrt{\frac{2\varepsilon_s}{q}\left(\frac{1}{N_a} + \frac{1}{N_d}\right) V_{bi}} \tag{2.30}$$

where ε_s is the permittivity of the semiconductor, q is the elementary charge, N_a and N_d are the doping density of acceptors and donors, respectively, and V_{bi} is the built-in voltage. w_p and w_n are the individual depleted widths of the p- and n-type regions, given by:

$$w_p = \frac{1}{N_a}\sqrt{\frac{2\varepsilon_s V_{bi}}{q\left(\frac{1}{N_a}+\frac{1}{N_d}\right)}} \tag{2.31}$$

$$w_n = \frac{1}{N_d}\sqrt{\frac{2\varepsilon_s V_{bi}}{q\left(\frac{1}{N_a}+\frac{1}{N_d}\right)}} \tag{2.32}$$

Thus, we can see that it is not possible to have both a wide depletion region (which assists in collection of carriers) and high doping levels (which aids with increasing voltage).

Once an equilibrium is reached, the depletion region reaches relatively constant width. However, this equilibrium is dynamic, meaning that there are still a small number of carriers that diffuse across the junction despite the being impeded by the built-in electric field. This is directly related to the equation for the law of mass action that we discussed in the previous section, where

electron-hole pairs are constantly created and annihilated and there is an equilibrium when the rate of annihilation equals that of generation. This is because, statistically speaking, there is some probability that carriers obtain sufficient velocity to overcome the energy barrier imposed by the depletion region. Once a carrier crosses the junction, it becomes a minority carrier and will continue to travel a distance equal to its diffusion length. In the next section, we will look at how p-n junctions operate within devices and, in particular, solar cells.

2.2 The Physics of Solar Cells

A solar photovoltaic cell is a device that directly converts optical energy into electrical energy in a one-step process via the photovoltaic effect. Light interacts with a PV cell to produce both a current and a voltage to generate electrical power. Photons can interact with what we call an absorber material, or a photoactive material, where it can give its energy to excite an electron within that material. This depends on the energy of the photon, i.e its frequency (or color), and whether or not it is sufficient enough to excite electrons across the band gap into the conduction band. The direct conversion of light energy to electrical energy is an ideal means of harvesting solar power. The basic steps for the operation of a solar cell are:

1. absorption of light, generation of carriers
2. separation and collection of carriers to generate an electrical current
3. generation of a large voltage across the solar cell
4. extraction of carriers and power dissipation to load

This section will discuss the essential parameters, requirements, and structures of a solar PV cell.

2.2.1 The Photovoltaic Effect

When light is absorbed by a material, photon energies are given to an electron to excite it into a higher energy state within the material. Due to this separation of charge, an electrical potential, or *voltage*, is created. Consequentially, this is known as the photovoltaic effect. In a typical material, the excited electrons decay back down to their original ground energy state very rapidly giving off that energy as either radiation or heat. In a photovoltaic device, on the other

hand, there is a built-in asymmetry that sweeps the excited electrons away before they are able to recombine. This creates a potential difference, or electro-motive force, within the device due to the separation of charges, which forces the electrons through an external circuit where it can do electrical work. The photovoltaic effect is based on the principles of the photoelectric effect, however, the distinction is that the photoelectric effect ejects an electron upon exposure to light (typically UV light), whereas the photovoltaic effect produces a photo-induced voltage (typically visible light).

2.2.2 Absorption and Generation

To understand absorption processes within PV cells, it is important that we understand the properties of light and the nature of the radiation coming from the Sun. The Sun produces light with a wide range of different energies, and therefore has its own solar emission spectrum (Figure 2-8). There are two important things to take into consideration: (i) the wavelengths of light being emitted by the sun, and (ii) the intensity of each wavelength of light being emitted. The wavelength of a photon is inversely proportional to its energy according to the famous equation:

$$E = mc^2 \quad \text{or} \quad E = \frac{hc}{\lambda} \tag{2.33}$$

Thus, we can see that energy is inversely related to wavelength. This is important because it means that the lower wavelengths of light carry more energy than the higher wavelengths. However, typically this does not matter so long as the energy of the photon is greater than the band gap as any energy greater than the band gap the photon carries will typically be lost very

rapidly as heat during thermalization, except for a device concept called ‘hot carrier’ devices that in principle are able to harness this excess energy.

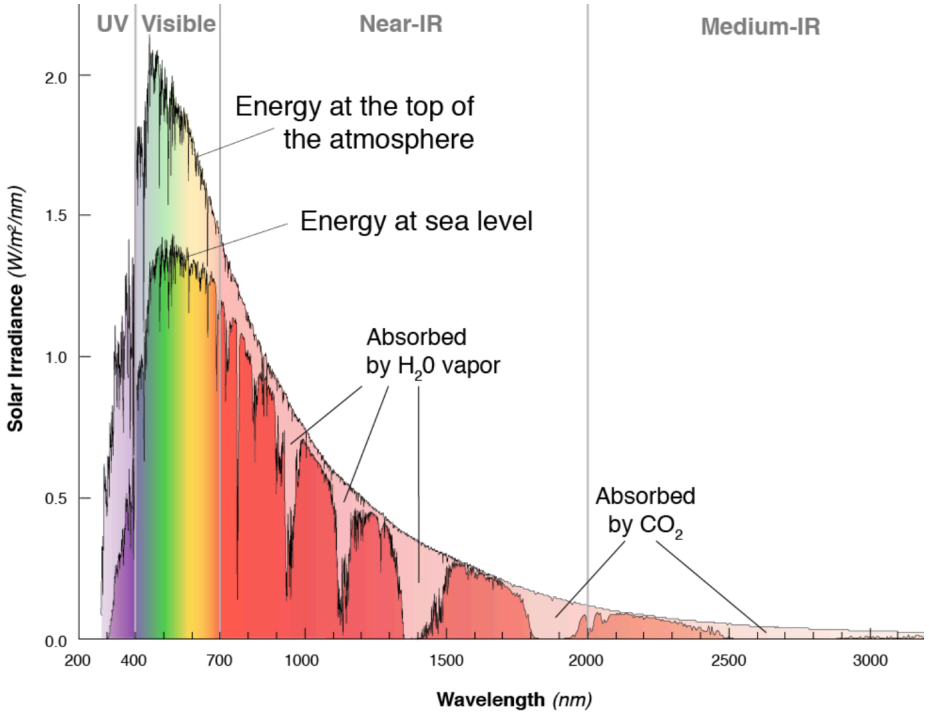

Figure 2-8: The Sun's solar irradiance spectrum.[5]

The second important point is the intensity at each wavelength (the spectrum). The higher the intensity, the more carriers can be generated. As we have learned, the intensity of the sun’s rays are attenuated by the Earth’s atmosphere. We can measure a parameter called the air mass (AM), which is the ratio of the optical path length to the Sun over the optical path length if the Sun is directly overhead, to define the optical path length through the Earth’s atmosphere. While the irradiances vary based on location, season, and time of the day, a standardized AM value called AM 1.5 G (G stands for ‘global’), which is equivalent to 1000 W/m^2. It is the standardized value for the characterization of solar cells, and is commonly referred to as the *1 sun* condition because

it is equivalent to the condition when the sun is directly overhead (shortest path length) on a clear day (no path interruption).

Like the sun's emission spectrum, a semiconductor material will have its own unique absorption spectrum. When light shines onto a photovoltaic cell, the it may either be reflected, pass through, or absorbed. The condition for absorption is that the energy of the incoming photon must be greater than or equal to the band gap of the semiconductor ($E_\lambda \geq E_g$) for the electron to cross the band gap into the CB. If the energy is less than the band gap ($E_\lambda \leq E_g$), it will transmit through the material and not be absorbed, i.e. the material is transparent to that wavelength of light.

The *absorption coefficient* is a parameter used to determine how far a photon will travel within a material before it is absorbed. A material with poor absorption will have a low absorption coefficient value, while that with good absorption will have a high value. The absorption coefficient is a material-dependent property that is also a function of the wavelength of incident light. It is related to the band structure of the material, since its energy dependence necessarily requires a relationship to the density of VB and CB states, and can be modelled based on Fermi's Golden Rule, which states the transition probability per unit time from an initial filled state to a final empty state, differing in energy by a value E. The derivation yields:

$$\alpha(h\omega) = \frac{2\pi}{\hbar}\left|\langle v\left|\widehat{H}\right|c\rangle\right|^2 \int \frac{2}{8\pi^3}\delta(E_c(\vec{k}) - E_v(\vec{k}) - h\omega)d^3k \tag{2.34}$$

where $\langle v\left|\widehat{H}\right|c\rangle$ is the transition matrix from states in the VB to the CB and the second term is the joint density of states (JDOS) which is a function of energy ($h\omega$). Therefore, the absorption coefficient is determined fundamentally by the transition matrix and the JDOS.

A simplified expression where the transition matrix and other constants are lumped into a constant, leaving the absorption coefficient in terms of the band gap energy, is given by.

$$\alpha(h\nu) = A\left[h\nu - E_g\right]^n \tag{2.35}$$

where $h\nu$ is energy of the incident photon, E_g is the band gap of the material, and A is a constant that is a function of several parameters, most notably including the effective masses of electrons and holes, the refractive index of the material, its permittivity, and a matrix element of the momentum operator. n, on the other hand, depends on the type of transition across the band gap. There are two very important types of band gaps, namely, *direct* or *indirect* band gaps. The difference is best understood by examining the E-k diagram (Figure 2-9).

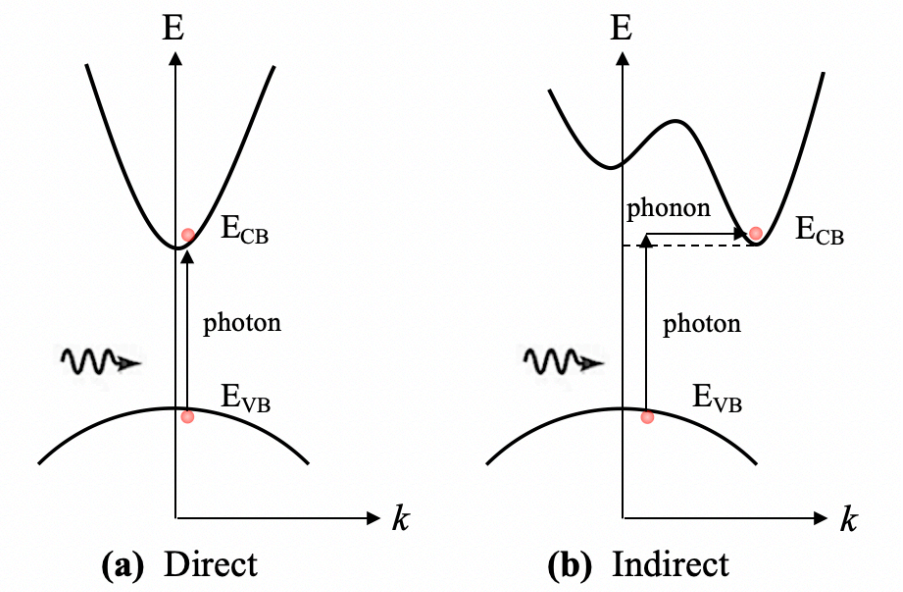

Figure 2-9: Electronic transitions in (a) a direct band gap and (b) an indirect band gap. An indirect band gap lies has a shift in k value for the CB of its band structure relative to that of its VB, which requires a phonon (momentum) to make the transition.

A direct band gap has its VB maximum (VBM) and CB minimum (CBM) at an equivalent k value. This means that for an electron to make a transition on an E-k plot requires a purely vertical transition, i.e. only E, which equal to that of the band gap between the VBM and CBM ($E_{photon}=E_g$). On the other hand, a direct band gap has its VBM and CBM offset by some value of $\boldsymbol{k}$, which means that an electronic transition requires not only an energy input but that relating to $\boldsymbol{k}$. According to De Broglie relations in terms of $\boldsymbol{k}$, we obtain a relationship for momentum as:

$$\boldsymbol{p} = \hbar\boldsymbol{k} \tag{2.36}$$

Since a photon does not have mass, this transition is not possible without the aid of a *phonon*, which is an important concept in quantum-mechanics. A phonon is a quantum of vibrational energy or quasiparticle within a crystal lattice oscillating at a single frequency. And because a phonon contains mass, it carries momentum, which allows it to make the $\boldsymbol{k}$ transition to the CB. This is an important implication because phonons must be generated within the crystal lattice with proper momentum in order for this transition to occur. As a result, the transition probability and rate are reduced in indirect band gap materials, which is disadvantageous for a PV absorber material. An example of an indirect band gap material is silicon, which is why monocrystalline silicon PV cells require large thicknesses because a poor absorption results from the necessity to create phonons to accompany the electronic transition. As a result, n=1/2 for direct band gaps and n=2 for indirect band gaps, yielding:

$$\alpha_{dir}(hv) = A\left[hv - E_g\right]^{1/2} \tag{2.37}$$

$$\alpha_{indir}(hv) = A\left[hv - E_g\right]^{2} \tag{2.38}$$

Direct band gaps correspond to sharp absorption onsets at wavelengths equivalent to the band gap energy, meaning absorption takes place immediately at a specific wavelength once the energy threshold is overcome, whereas indirect band gaps are associated with gradual absorption onsets due to the additional necessity of phonon generation. If one was to plot $\alpha(hv)^{1/n}$ vs hv and obtained a straight line, the intercept at $\alpha(hv)^{1/n} = 0$ would give the value of E_g, corresponding to the n values for direct and indirect. Figure 2-10 displays absorption coefficient versus wavelength plots for several common semiconductor materials. We notice that both Si and Ge (the elemental semiconductors) have indirect band gaps per their gradual onsets of absorption. A quick estimate to the band gap can be made by observing the intersect of the tangent to the onset of absorption with the x-axis, then using the relationship of energy and wavelength one can calculate the band gap energy.

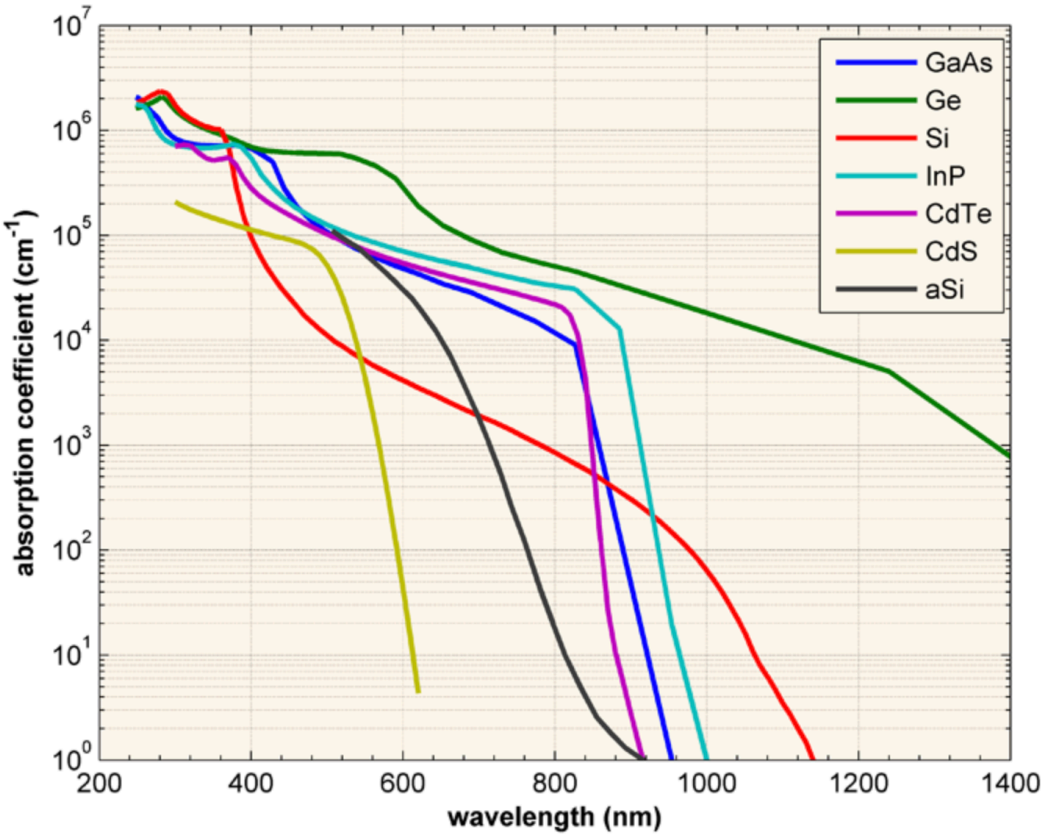

Figure 2-10: Absorption coefficient versus wavelength for several common semiconducting materials used in as absorbers in PV cells. A steep onset corresponds to a direct band gap, whereas a gradual onset indicates an indirect band gap.[6]

The absorption coefficient is also related to the extinction coefficient, κ_s, which is the imaginary part of the equation for the dielectric constant, represents the amount of attenuation of an electromagnetic wave as it propagates through a medium (material). In this case, the absorption coefficient can be related by the following equation:

$$\alpha = \frac{4\pi\kappa_s}{\lambda} \quad [nm^{-1}] \tag{2.39}$$

where κ_s is also wavelength dependent. Thus, the dependence of absorption coefficient on wavelength seen from this expression indicates that different wavelengths of light can penetrate

to different depths within the material. The absorption depth is the inverse of the absorption coefficient, α^{-1}, with units of nm, which gives the distance into the material at which the light intensity drops by a factor of $1/e$. Since the wavelength is related to energy, the higher energy photons, such as blue light, have a larger absorption coefficient and are thus absorbed at much shallower levels than a lower energy light, (e.g. red light), which is absorbed less strongly and thus penetrates deeper into the material. In fact, all of the red light is not absorbed in silicon up to 100 μm depths.

The amount of light absorbed in the material (neglecting reflection), or the absorption coefficient if the amount of light absorbed is measured, can be determined via the following equation:

$$I = I_0 e^{-\alpha x} \tag{2.40}$$

where α is the absorption coefficient, x is the distance into the material (thickness), and I_0 is the intensity at the top surface (initial intensity). If we assume that the loss in light intensity is directly related to the generation of an electron-hole pair, then the generation can be calculated by determining the change in light intensity across the material, which is the derivative of the previous equation, yielding:

$$G = \alpha N_0 e^{-\alpha x} \tag{2.41}$$

where N_0 is the photon flux at the surface. This equation further illustrates that generation is highest at the surface and decreases exponentially throughout the material (which is also dependent on wavelength since $\alpha(hv)$).

As a last piece to this section, I would like to briefly discuss the relationship between reflection and refraction. Light can also be reflected off the surface of the device, thus preventing even the possibility of absorption occurring. Reflection is dependent on the index of refraction of the material and its 'smoothness,' or surface roughness. The refractive index of a material describes how fast light propagates through a material, and is given by:

$$n = \frac{c}{v} \tag{2.42}$$

where n is the refractive index, c is the speed of light, and v is the phase velocity of light in the medium. At the atomic scale, an electromagnetic wave's phase velocity is attenuated within a material due to its interaction with the electric potential field within the material. As the electromagnetic wave cause the electric fields within the material to oscillate, the charges within the material begin to oscillate at the same frequency and radiate their own electromagnetic wave, but usually with a phase delay with respect to the incident electromagnetic wave. The overall wave travelling within the material medium is the sum (superposition) of all contributing waves, i.e. the original wave (which is typically modified via the interaction with the charges within the material) and charge-radiated waves. This wave tends to have a shorter wavelength (but same frequency) as the original wave, thus resulting in a slower phase velocity within the medium. Relating to the index of refraction, the probability of reflection, if the incident light is normal to the surface of the material, is equivalent to:

$$R = \left(\frac{n_0 - n_s}{n_0 + n_s}\right)^2 \tag{2.43}$$

where n_0 is the refractive index of the first medium (air if light is directly hitting the surface of the semiconductor material) and n_s is the refractive index of the material medium. If the incident

light is not normal to the surface, the equation then depends on the polarization of light (s- or p-polarization) as well as the angle, and becomes:

$$R = \left(\frac{\eta_0 - \eta_s}{\eta_0 + \eta_s}\right)^2 \quad (2.44)$$

and

$$\eta_s = n_s \sec(\theta_s) \text{ for p-polarized light} \quad (2.45)$$

$$\eta_s = n_s \cos(\theta_s) \text{ for p-polarized light} \quad (2.46)$$

where θ_s is the angle made by the transmitted ray (of incident ray angle θ_0). Snell's Law relates θ_0 and θ_s through:

$$\eta_0 \sin(\theta_0) = \eta_s \sin(\theta_s) \quad (2.47)$$

From Snell's law, we can derive the critical angle, θ_c, for which light will be reflected by the surface to the original medium, rather than refracted within the new medium:

$$\theta_c = \sin^{-1}\left(\frac{n_0}{n_s}\right) \quad (2.48)$$

Any reflected light is energy that cannot be absorbed by the PV cell, therefore, it is important to understand these fundamental relationships and properties of light within various mediums. Moreover, the development of antireflection coatings has been realized by manipulating these properties, and by texturizing surfaces to change incident angles and direct light into the bulk semiconductor medium.

2.2.3 Solar PV cell operation

The p-n junction is the basis of operation for a PV cell. We have already seen what happens when a p-n junction is formed – a depletion region is created and a dynamic equilibrium is established. The solar cell structure consists of a p-n junction and metal electrodes on either side that are connected to an external circuit to extract the photo-generated charge carriers (Figure 2-11). Now, we will analyze what happens when we apply a bias to the junction, then add on the effect of shining light onto the material, which the basis for operation of a PV cell.

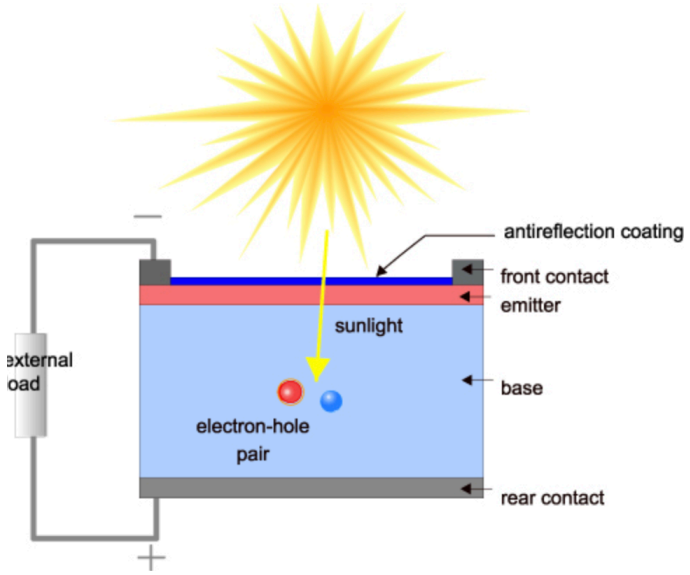

Figure 2-11: Components and basic operation of a PV cell. Sunlight creates an electron-hole pair that then separate into individual free carriers and diffuse to their selective contacts where they can be extracted outside of the cell to do work at the external load.[7]

Starting from the beginning of p-n junction formation, we can see how the band alignments change as the p- and n-type materials come into contact (Figure 2-12a). It is important to analyze not only the physical schematic of the p-n junction, but also the band structure, which is provided just below. Prior to contact, the CB and VB levels are at identical

levels because the host material is the same (e.g. Si), where the only difference is the Fermi level position that corresponds to the doping type (n- or p-). As these two materials are brought into contact (Figure 2-12b), their Fermi levels shift to align as a dynamic equilibrium is established and depletion region formed, identical to what we discussed in the previous section. Now, let's look at what happens when we apply a bias. Figure 2-12c depicts applying a reverse bias to the junction, which enhances the electric field, thereby shifting the dynamic equilibrium by forcing more of the n-type carriers to the p-type side and vice-versa until a larger depletion region is formed. This creates a larger energy barrier for diffusion to occur, and the diffusion current is reduced, which is represented on the band diagram. The Fermi levels of the individual n- and p-type regions, which we call the *quasi-Fermi levels*, split such that $E_{F,p}$ shifts upwards and $E_{F,n}$ downwards with respect to each other (and the original aligned position). The drift current is unchanged with respect to bias because it is not dependent on crossing the depletion region as is diffusion. Now, if we flip the bias, we create what is called a forward bias condition (Figure 2-12d). In this situation, the applied bias counteracts the built-in electric field to reduce the net overall field within the device, thereby shrinking the depletion region. The Fermi levels this time shift in opposite directions (due to reversal of the applied voltage), thus lowering the energy barrier for diffusion of carriers across the depletion region.

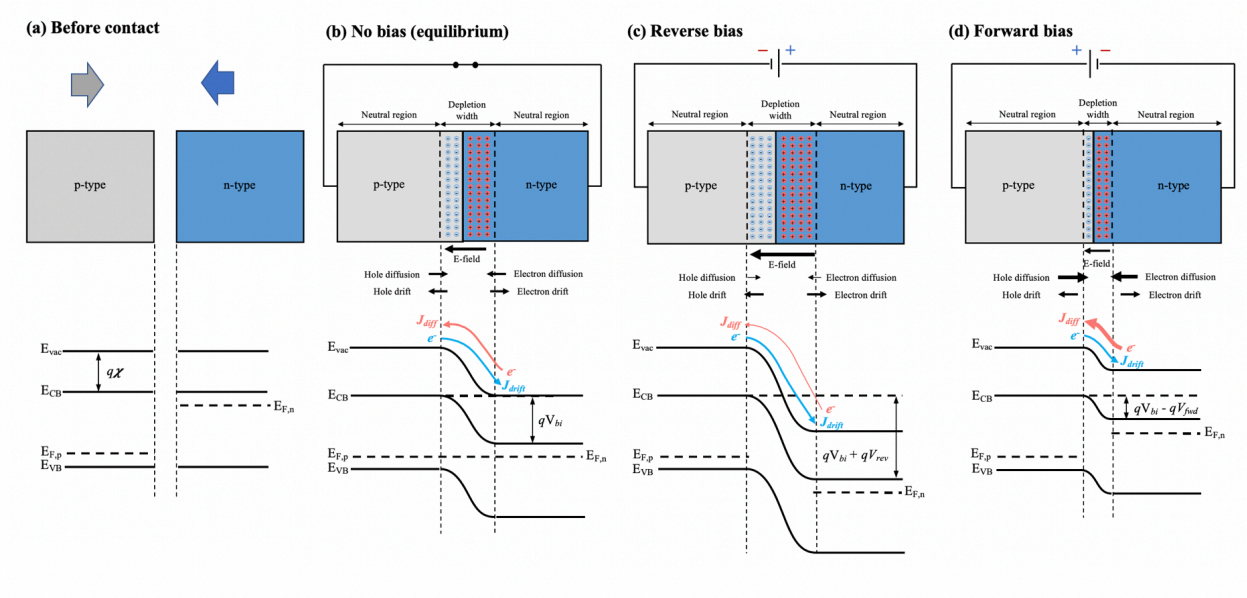

Figure 2-12: Biasing of a p-n junction (both p- and n-type are the same host materials). (a) before contact, the individual Fermi levels are shown. (b) as the two come into contact, a dynamic equilibrium is established and band bending occurs to match the Fermi levels of the p- and n-type materials. (c) upon applying a reverse bias, the depletion region enhances, lowering the diffusion current across it. (d) with a positive bias applied, the depletion region shrinks, thus allowing for a higher diffusion current across it.

Let us know look at what happens when we shine light onto the p-n junction (Figure 2-13). When a photon impinges upon a PV cell, if conditions for absorption are satisfied, an electron will absorb the photon energy and transition to an excited state from the VB to CB, and creating a corresponding hole. These excitations occur all throughout the material, following the same principles we discussed about the absorption depth. However, once an electron-hole pair is created, the two carriers must be separated. This occurs with a much higher probability within or near the junction, since the junction is void of carriers and has an electrical potential gradient that

can help to sweep the newly generated carriers out and to their respective sides of the junction (Figure 2-13b,c). This will cause a quasi-Fermi level separation owed to shift away from equilibrium, i.e. a change in chemical potential ($\Delta\mu$) due to a change in carrier concentration.

There are two extreme conditions that are very important metrics for PV cells. The first is the short-circuit condition, where the p-n junction is illuminated and the terminals of the external circuit connected (Figure 2-13b). In this case, the extra generated carriers are allowed to flow continuously around the circuit and recombine with their counterpart, resulting in an increase in drift current, which we call the *short-circuit current density*, J_{sc}, given by:

$$J_{sc} = q\int_{\lambda_{min}}^{\lambda_{max}} b_s(E)\cdot QE(E)dE \tag{2.49}$$

where b_s is the incident spectral photon flux density from within the range of wavelengths that the material absorbs, and QE is the solar cell's *quantum efficiency*, or the probability of converting one photon to one excited electron through the external circuit. The QE depends on the material's absorption coefficient, as well as the efficiency of charge separation and collection, given by the photocurrent density delivered to the circuit divided by the photon flux that strikes the cell:

$$IPCE = \frac{J_{sc}(\lambda)}{e\cdot b_s(\lambda)} = \frac{J_{sc}(\lambda)[A\ cm^{-2}]}{\lambda\ [nm]\cdot P_{in}(\lambda)[W\ cm^{-2}]} \tag{2.50}$$

Because the carriers can flow freely through the external circuit, there is no voltage buildup and therefore the depletion region, as well as the diffusion current, are unchanged. The diffusion current is commonly referred to as the *dark current*, J_{dark}, because it is the 'leakage' current through the depletion region present without illumination.

$$J_{dark} = J_0\left[e^{\left(\frac{qV}{kT}\right)} - 1\right] \tag{2.51}$$

where k is the Boltzmann's constant, and T is temperature in degrees Kelvin and J_0 is the dark saturation current (a constant) that depends on the material properties. J_0, the saturation current, is a very important parameter to differentiate one diode from another. It is a measure of recombination within the device, i.e. a diode with a larger recombination has a higher J_0, which increases with T and decreases as material quality increases. The saturation current results from the diffusion of minority carriers into the depletion region and is independent of bias voltage, but dependent on temperature since it is driven by thermal excitation of e-h pairs (per Fermi-dirac):

$$J_0 = q\left[\sqrt{\frac{D_p}{\tau_p}}\frac{{n_i}^2}{N_D} + \sqrt{\frac{D_n}{\tau_n}}\frac{{n_i}^2}{N_A}\right] \quad \text{or} \quad J_0 = \left(\frac{qD_p}{L_p N_D} + \frac{qD_e}{L_e N_A}\right){n_i}^2 \tag{2.52}$$

where D_p and D_n are the diffusivity, τ_p and τ_n the carrier lifetimes, and L_p and L_e the diffusion lengths of holes and electrons, respectively. J_0 is identical to the reverse saturation current, I_0, but per unit area ($I_0 = J_0 A$). Under normal operational conditions, the total current flowing through the solar cell is thus the difference between J_{sc} and J_{dark}:

$$J(V) = J_{sc} - J_{dark}(V) = J_{sc} - J_0\left[e^{\left(\frac{qV}{kT}\right)} - 1\right] \tag{2.53}$$

The next condition is called the open-circuit condition (Figure 2-13c), which is when the two terminals are not connected and no current is allowed to flow. In this scenario, the photo-generated carriers cause a further buildup of charge and thus a voltage is produced. This voltage counteracts that of the depletion region, thus shrinking the depletion region width and allowing for an increase in J_{dark}. The corresponding energy diagram has a reduced energy barrier for the J_{dark}. This is equivalent to when $J_{sc} = J_{dark}$, which yields:

$$V_{oc} = \frac{kT}{q}\, ln\left[\frac{J_{sc}}{J_0} + 1\right] \tag{2.54}$$

This shows that the V_{oc} increases logarithmically with light intensity, and we can see that a photo-voltage is produced under forward bias conditions (V>0). Referring to the equation for J_0, it is also clear that a larger doping level is needed for a higher V_{oc}, but not too high, which will increase carrier recombination and reduce carrier mobility.

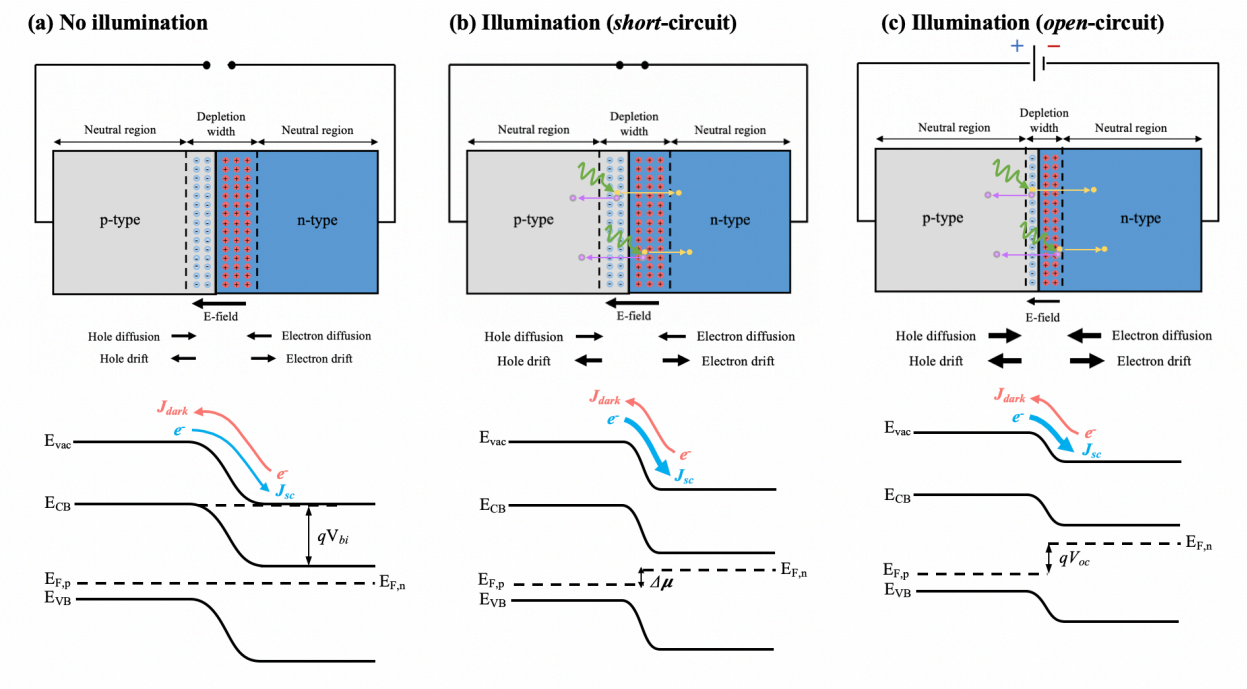

Figure 2-13: p-n junction under illumination. (a) no illumination, (b) illumination, short-circuit conditions, (c) illumination, open-circuit conditions.

The most important metric of a PV cell is its performance, or efficiency, which represents how well it harvests light and transports charge carriers outside of the cell to do electrical work. The *power conversion efficiency* (PCE) of a solar cell is given as:

$$PCE\ (\eta) = \frac{P_{max}}{P_{in}} = \frac{\text{the maximum voltage and current attainable for the cell}}{\text{power incident to the cell (1 sun)}} = \frac{V_{oc} \cdot J_{sc} \cdot FF}{1000\ \text{W}/m^2} \quad (2.55)$$

The V_{oc} and J_{sc} are the open-circuit voltage and short-circuit current density that we defined in the previous section. It is worth reiterating that the current density (J) is simply the current per area (typically cm^2), and thus I can be obtained by dividing J by the active area of the cell under analysis. The Fill-Factor (FF) is another important parameter defined as:

$$FF = \frac{V_{max} \cdot J_{max}}{V_{oc} \cdot J_{sc}} \tag{2.56}$$

These parameters can be best represented by a *current-voltage* (I-V) curve (Figure 2-14a).

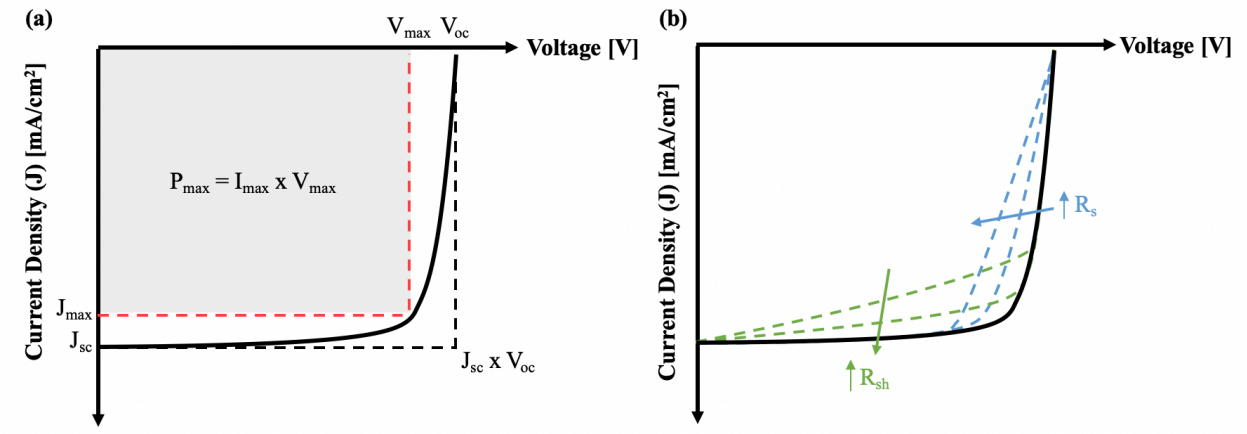

Figure 2-14: (a) an I-V (J-V) curve of a PV cell. (b) I-V curve shifts due to increase in series and shunt resistances.

The maximum power point can be represented by the shaded area, which is the product of the current and voltage that produce the maximum power within the device. Here it is worth noting that 'max' for I and V does not indicate the maximum voltage and current obtainable, but the current and voltage that produce the maximum power within the device. The FF is a direct representation of the maximum obtainable power, and is often referred to as the 'squareness' of the I-V curve as it represents how close the curve is to fitting the square provided by the J_{sc} x V_{oc}. In Figure 2-14b, we can look at the effects of *series* and *shunt* resistances. The series

resistance is related to the contact resistances at interfaces between adjacent (charge transporting) layers and how effectively current moves throughout the p- and n-type regions. Therefore, its main effect is to reduce the FF and is represented on the I-V curve as a reduction in slope near the V_{oc} location, as shown in Figure 2-14b. If excessively high, the series resistance can also impact the J_{sc}. The shunt resistance is related to the leakage current, which is typically a result of poor device manufacturing or defects rather than poor solar cell design. A low shunt resistance allows for current to take alternative paths via defects or other means, thus reducing the open-circuit voltage of the solar cell. It can be estimated by the slope of the I-V curve near the J_{sc}, as shown in Figure 2-14b, and is most prominent at low light intensity levels where there are less photo-generated charge carriers present.

A PV cell can also be represented as an equivalent circuit, as shown below in Figure 2-15. Here we can see all the factors discussed such as the photo-generated current, represented as I_{sc}, D as the diode, R_s and R_{sh}, and I_{sh} as the shunt current.

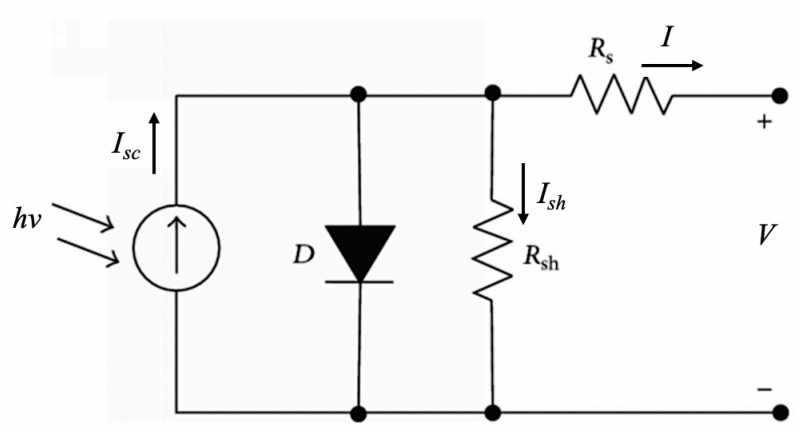

Figure 2-15: Equivalent circuit of a PV cell.

The p-n junction is standard for understanding how a PV cell works, however, there are several other types of junctions that are able to realize photovoltaic effects, such as a p-i-n junction, p-n heterojunction, electrochemical junction (such as for a DSSC), and a bulk heterojunction (such as for OPV), to name a few. Here we will discuss only the p-i-n junction as it is the type of structure used for hybrid perovskite solar cells. A p-i-n junction is the same as a p-n junction except there is an intrinsic, or undoped, (i) material sandwiched between the p- and n-type materials. In this case, the built-in electric field extends over a wider region, i.e., the intrinsic region. Intuitively, this is ideal when the minority carrier diffusion lengths are short because carriers have a greater chance to be photo-generated in the larger *i* region and can travel further within this region than the doped regions. However, this comes at a cost of lower conductivity (due to lower carrier concentration) that may introduce series resistance, and a higher probability of recombination at forward bias conditions. A discussion on the p-i-n structure will be provided in reference to perovskite solar cells in the subsequent section.

2.2.4 The Shockley-Quiesser Limit

Essential to developing PV technologies is to gain an understanding of the fundamental limitations on cell efficiency. This was first accomplished by Shockley and Quiesser in 1961 where the maximum efficiency of a single p-n junction solar cell was calculated, which was coined the Shockley-Quiesser (SQ) Limit.[8] The fundamental limit is determined based on the principle of detailed balance, which represents the principle of unavoidable losses occurring within a PV cell. While a PV cell absorbs solar radiation, it also unavoidably exchanges thermal radiation with its surroundings. Both the cell and surrounding environment radiate based on their

temperature, and the rate of emission of photons by the cell must be matched by the rate of photon absorption such that in steady state the concentration of electrons within the material remains constant. This is called the principle of detailed balance, and imposes a fundamental limit on the maximum obtainable efficiency. The SQ limit is determined by calculating the amount of extractable electrical energy per photon of incoming light. It considers limitations imposed by blackbody radiation requirements (as already discussed), recombination requirements, spectrum losses due to the band gap of the material limiting the portion of the spectrum that photons can be absorbed, and impedance matching to maximize the extractable power (which is related to the FF). The assumptions for the SQ limit are (i) only radiative recombination occurs. (ii) there is no concentrated light, (iii) for photons with greater energy than the band gap, the difference generates heat, (iv) only one electron-hole pair is generated per incoming photon, and (v) there is a single p-n junction per cell. These are requirements to maintain detailed balance and maximize PV cell efficiency. The limit is determined to be 33.7% PCE for a 1.34 eV band gap material. A plot of the efficiency limit versus band gap can be seen in Figure 2-16, with common PV absorber materials plotted for perspective.

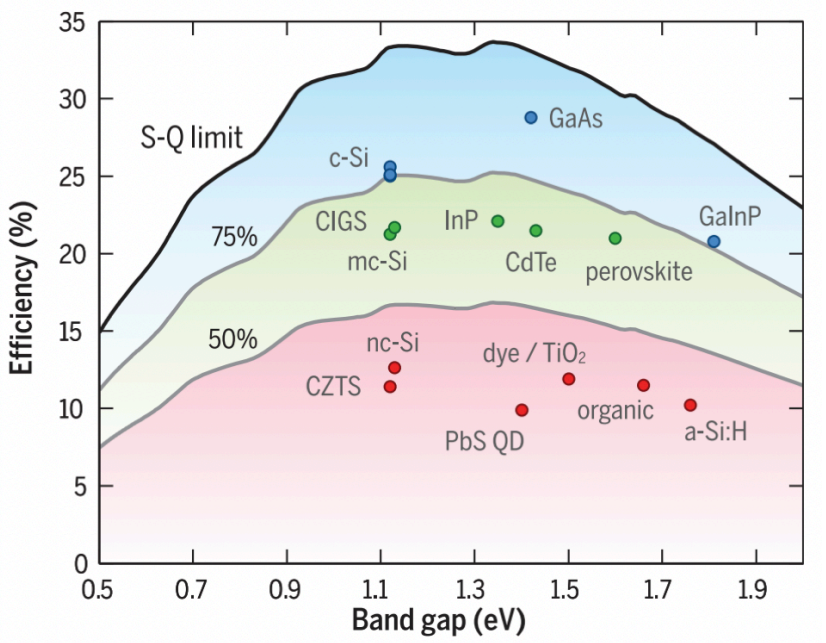

Figure 2-16: The Shockley-Quiesser Efficiency Limit for a single junction PV cell versus band gap of the material. Common PV absorber materials are plotted accordingly.[9]

However, there are other considerations not included in the SQ limit, such as mobility limitations where mobilities can vary for electrons and holes and also between different materials, thus limiting the extractable current. Moreover, non-radiative (SRH) recombination is not considered in the SQ limit and can greatly impact the overall efficiency of the PV cell.

There are also ways to overcome these limitations, such as creating multi-junction devices with multiple absorber materials, concentrating light onto the solar cell, hot carrier capturing, multiple-exciton formation, etc. These topics are not within the context of this thesis and are thus left for the reader to explore.

References:

1. Band gap. *Wikipedia* (2019).
2. Hamza El-Saba, M. Energy Band Theory & Classification of Solids. (2015).
3. Fermi level. *Wikipedia* (2019).
4. Brandt, R. E., Stevanović, V., Ginley, D. S. & Buonassisi, T. Identifying defect-tolerant semiconductors with high minority-carrier lifetimes: beyond hybrid lead halide perovskites. *MRS Commun.* **5**, 265–275 (2015).
5. Rosen, J. & Egger, A. E. Factors that control Earth's temperature. **EAS-3**, (2016).
6. Absorption Coefficient | PVEducation. Available at: https://www.pveducation.org/pvcdrom/pn-junctions/absorption-coefficient. (Accessed: 16th April 2019)
7. Pukhrem, S. How Solar Cells Work — Components & Operation Of Solar Cells. *Solar Love!* (2013). Available at: https://solarlove.org/how-solar-cells-work-components-operation-of-solar-cells/. (Accessed: 16th April 2019)
8. Shockley, W. & Queisser, H. J. Detailed Balance Limit of Efficiency of p-n Junction Solar Cells. *J. Appl. Phys.* **32**, 510–519 (1961).
9. Polman, A., Knight, M., Garnett, E. C., Ehrler, B. & Sinke, W. C. Photovoltaic materials: Present efficiencies and future challenges. *Science* **352**, (2016).

Chapter 3. Fundamentals of Hybrid Perovskites

Optoelectronic materials are typically categorized as either organic or inorganic, according to their chemical compositions, which yields strikingly different property trends. In general, organic materials are simpler to process, cheaper, and can utilize a wide variety of organic molecular components. Inorganic materials typically possess higher mobility and are more stable, both thermally and mechanically, as a result of their tight ionic and covalent bonding. The hybrid nature of the organic-inorganic perovskite combines the advantages of both the organic and inorganic natures to exhibit exceptional and unprecedented properties, alongside some new and intriguing challenges. In this section, we will discuss the fundamental knowledge of hybrid perovskites to-date, including the unique structure-property relationships seen for this class of materials.

3.1 The Perovskite Family of Materials

Perovskites are a large family of compounds that share the chemical formula ABX_3. 'A' and 'B' denote cations, where A is much larger than B, and 'X' an anion. Historically, oxide-based perovskites (X=O) have been most actively studied as they possess a unique multifunctional nature. Studies of the perovskite crystal chemistry date back to 1920, conducted by Goldschmidt, that revealed the significance of relative radii sizes to polyhedral packing that ultimately led to the ever-important tolerance factor, which will be discussed later in this section. Eventually, it was revealed that with proper tuning of composition a wide variety of electronic properties

including capacitive, ferroelectric, piezoelectric, superconductive, metallic, catalytic, and magnetic could be achieved.[1] While ferroelectric properties have recently shown beneficial effects in photovoltaics, the wide band gaps of oxide perovskites limit their use in solar applications as they utilize a mere 8-20% of the solar spectrum. Lead halide perovskites, as the name implies, employ an inorganic halide (I^-, Cl^-, Br^-) to replace the oxygen anion (O^{2-}) of oxide-based perovskites, an organic or inorganic monovalent A^+ cation and a divalent B^{2+} metal cation (which is typically lead, Pb). In this section we will discuss the unique structural and compositional flexibility of hybrid perovskite materials.

3.1.1 Crystal Structure, Composition, and Dimensionality

Hybrid organic-inorganic halide perovskites have a crystal structure adopting the formula ABX_3, where A, B, and X are most commonly a monovalent organic (or inorganic) cation, divalent metal cation, and halide anion, respectively. The unit cell for perovskite is shown in Figure 3-1a,[1] however, a common alternate representation of the crystal is as infinitely repeating corner-sharing BX_6^{4-} octahedra, as shown in Figure 3-1b. The first hybrid perovskite material discovered to have solar harvesting capabilities was methylammonium ($CH_3NH_3^+$) lead triiodide ($MAPbI_3$). Shortly after, formamidinium ($HC(NH_2)_2^+$) lead triiodide ($FAPbI_3$) was discovered as another promising PV material. One of the unique aspects of hybrid perovskites is that so long as charge neutrality is conserved, and the relative sizes of its constituents are appropriate, this structure can form a wide range of compositions, thus allowing for a large degree of *compositional* tunability. In this regard, size effects are an important consideration as they determine the dimensionality of the crystal structure. As the A-site cation increases in size, it can

cause distortion of the crystal lattice known as octahedral tilting (Figure 3-1c). Furthermore, if the A-site cation is too large, 3-D symmetry is lost and 2-D layered structures are formed since the cation is too large to fit within the A-site cavity of a 3-dimensional crystal structure. Fortunately, a metric to predict the tolerated sizes of relative constituents was developed, coined the Goldschmidt tolerance factor, that can be equated using the following relationship between atomic/molecular ionic radii:

$$t = \frac{(R_{A,eff}+R_X)}{(R_B+R_X)} \quad (3.1)$$

where R_B, R_X are the ionic radii of B and X, respectively. $R_{A,eff}$ is the effective ionic radius of the organic molecule, a modification of the tolerance factor specific to hybrid perovskites owed to the difficulties in accurately estimating the radius of a molecule.[2] Cubic structures provide the highest degree of bonding, and occur for $0.85< t<1$. If the components do not correlate to fit within this tolerance range, distortions may arise resulting in lower degrees of bonding that can affect the optoelectronic properties and stability of the resultant structure. In fact, recently the tolerance factor has been shown to be a good indicator of intrinsic thermodynamic stability of the perovskite structure,[2] which will be discussed further in Section 3.6.

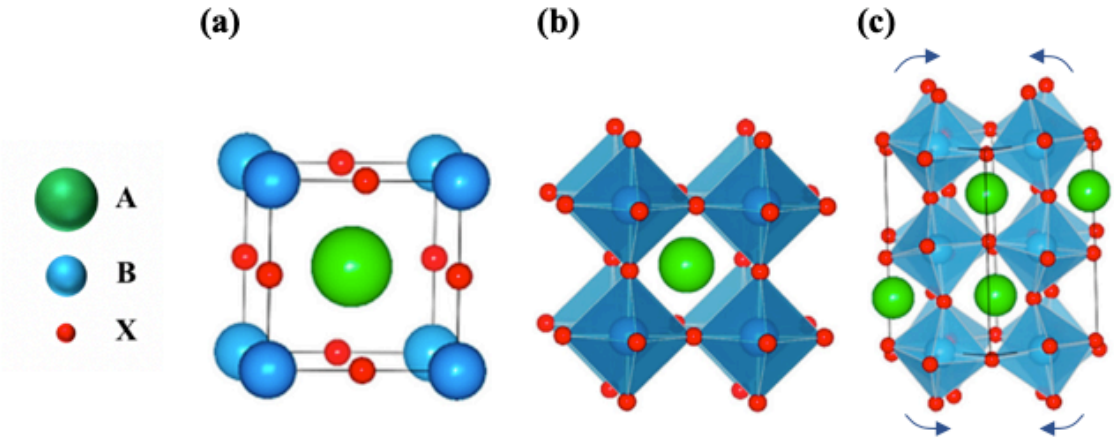

Figure 3-1: (a) Perovskite unit cell. (b) equivalent structure showing BX_6^{4-} octahedral surrounding an A-site cation. (c) tilting of the octahedra due to a tolerance factor off-unity.[1]

The second unique attribute of hybrid perovskites is their *dimensional* flexibility. So far we have discussed the requirements for the formation of 3-dimensional (3-D) perovskite crystals. However, if the size of one of the constituents is too large, and the tolerance factor exceeds unity, the symmetry can be broken and a layered two-dimensional structure forms (Figure 3-1d). This has very important implications in terms of the formation energy, resulting optoelectronic properties, and long-term stability of the crystal, which will be discussed in the coming sections.

3.2 Unique Electronic Structure and Origin Photo-physical Properties

The remarkable performances of hybrid perovskite solar cells can be attributed to their outstanding characteristic properties such as very long carrier diffusion lengths and lifetimes (1 μm, 1μs), extremely high optical absorption coefficients (10^5 cm^{-1}), balanced electron and hole

mobilities (25-100 cm^2/Vs), low trap densities (10^{15} – 10^{16} cm^{-3}), small exciton binding energies (14 – 25 meV), and very small Urbach energies (12.6 meV).[3,1] These properties are tied to the unique electronic structure of the hybrid perovskites, that is, the nature of the Pb $6s^2$ lone-pair that gives rise to an antibonding/bonding VBM/CBM and the heavy Pb atom that provides strong spin-orbit coupling (SOC) effects.[3] In this section, we will discuss the nature of the electronic band structure of hybrid perovskites and associated attributes in greater detail.

3.2.1 The Electronic Structure of Hybrid Perovskites

The hybrid perovskite crystal is dictated by the B-X bond, where the electronic energy levels consist of an antibonding (σ^*) and non-bonding (σ^0) hybrid state between the B(p)-X(p) and B(s)-X(p) orbitals that determine the valence band maximum (VBM) and conduction band minimum (CBM), respectively.[1] Figure 3-2a displays the band gap formation for PbI_6 octahedra, as in $MAPbI_3$.[4,5,1] Due to the ionic nature of hybrid perovskites, the covalent antibonding coupling between Pb p and I p is not strong. Consequentially, the CBM ought to not be much higher than the atomic Pb p state, and is thus not large. The VBM is formed via a strong s-p antibonding coupling from the Pb-6s lone pair and I-5p states that forms a Pb(6s)-I(5p)* antibonding band at the edge of the VB, a non-bonding I(5p) band, and a bonding Pb(6s)-I(5p) band deeper within the VB. This results in a pushing up of the VBM to a higher level residing *across* the bandgap rather than below, as in conventional compound semiconductors. We can see the Pb(6p)-I(5p) bonding states lie beneath the Pb(6s)-I(5p)* states, which is opposite to that of conventional compound semiconductors, which typically have bonding states that make up the VBM. This can be observed in Figure 3-2b,c, which shows the difference in bonding nature

between PVSK and conventional semiconductors, such as GaAs. The Pb having an s lone pair is necessary for this band structure to form with such antibonding VBM nature, and is thus only seen for those compound semiconductors with s lone pairs. This significant s-p hybridization owed to the Pb lone pair creates a very large dispersion of the VBM, which again is unique compared to conventional semiconductors where the VBM is composed of bonding states that are less dispersive. This is important in terms of band structure characteristics that give rise to important properties such as high optical absorption, large carrier diffusion lengths, and a defect-tolerant nature, which will be discussed in greater detail in the following sections.

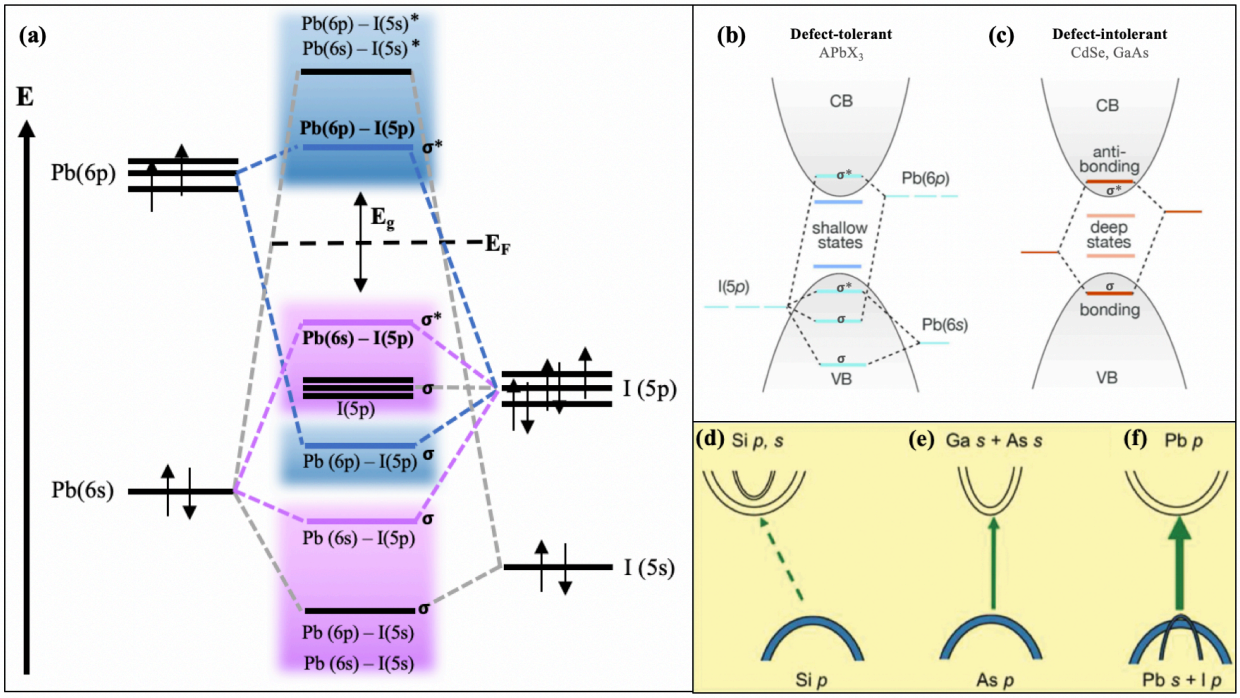

Figure 3-2: (a) Energy levels and band formation for $MAPbI_3$. (b-c) comparison of a the band structure formation for a (b) defect-tolerant material such as PVSK and (c) a defect-intolerant material such as common semiconductors as GaAs.[6] (d-f) A comparison of individual bands within CB and VB for (d) Si, (e) GaAs, and (f) PVSK.[7] The band transition (direct, indirect) and dispersion of the bands is an important consideration for DOS and corresponds to absorption coefficients of the material.

3.2.2 The origin of high absorption coefficients in hybrid perovskites

To understand the mechanisms behind the high optical absorption seen in hybrid perovskites, we can examine its band structure. The absorption coefficient is proportional to the transition matrix (as discussed in Section 2.2.2) and the joint density of states (JDOS), discussed in Section 2.1.2, which is directly related to the band dispersion. As we recall from Section 2.1.2, the dispersion is the relation of E and k on the E-k diagram, where a higher dispersion indicates a higher change in E for every change in k (i.e. higher curvature or band width). The JDOS, however, is inversely proportional to the slope of the E-k diagram, i.e. the flatter the band the greater the number of states at that energy level. However, a flatter band also means a higher effective mass, which is undesired (Section 2.1.2). Therefore, we can see that there is typically a tradeoff between DOS and effective mass.

Referring to Figure 3-2d-f, we can see that the Si p band is more dispersive than the Ga, As s bands, and would therefore be more preferred if not for the fact that Si transition is indirect. The dispersion of the band is directly related to orbital overlap, where more orbital overlap yields more dispersion. This becomes clear as k is related to atomic spacing, a, in reciprocal space, and is thus a measure of energy dispersion ('spreadness') as k varies. A higher dispersion is also known as band width because it implies a greater spread of energies within a given band (and thus a steeper slope). This means that the effective mass is lower, which is reasonable because the greater overlap of orbitals allows for the electron to more easily hop from one atomic site to another, and hence the electron has a smaller inertia (or mass). This must not be confused with the energy required to liberate an electron from a bond, where the stronger a bond the more energy required for the electron to become a free electron, which is related to the band gap energy. With effective mass, we are considering that the electron is already free and propagating

through the lattice, and the effective mass it the mass that it sees from interaction with the periodic potential as it propagates. Therefore, s bands will typically have greater dispersion than p bands owed to the greater bond overlap. The ideal case to increase absorption would be to have the p bands of Si (less dispersive) and the direct band gap nature of GaAs. As discussed previously, p-p transitions can only be possible for compound semiconductors with cations that have lone pair electrons in their s orbital, e.g. Ge^{2+}, Sn^{2+}, Pb^{2+}, Sb^{3+}, and Bi^{3+}.[7] However, most of these other compounds have indirect band gaps. This can explain the high absorption coefficients seen in hybrid perovskites, since they have both a direct band gap and p-p transitions due to the unique hybridization of its band structure. Yin et al. confirmed that the DOS of PVSK is higher than that of GaAs, corresponding to approximately an order of magnitude higher absorption coefficients for PVSK.[7] Other common PV absorber materials, such as CIGS, CZTS, CdTe have CB character similar to that of GaAs, and are therefore expected to have lower absorption coefficients than PVSK. For instance, the CBM of Copper Indium Gallium Selenide (CIGS) is formed via the antibonding between the In-5s band and Se-4p orbitals, which again is an s-p transition similar to GaAs. Figure 3-3 shows the absorption coefficients for MAPbI3 and common PV semiconductors such as Si, GaAs.

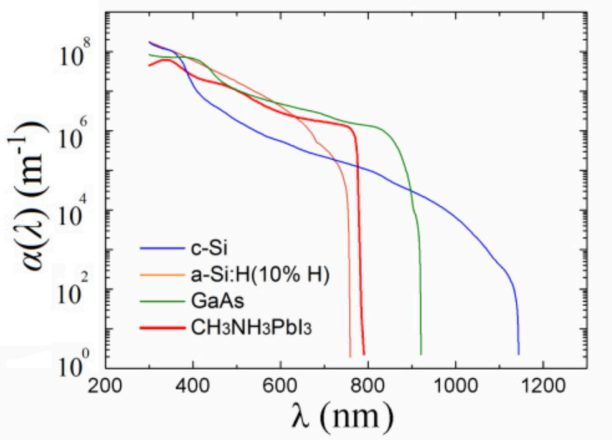

Figure 3-3: Absorption coefficient versus wavelength for $MAPbI_3$ and other common PV materials.[8]

Upon absorption of a photon, an electron-hole (e-h) pair is created, which is called an exciton. This exciton has an associated binding energy, called the exciton binding energy. In organic materials, this binding energy is large such that additional energy is needed to separate the electron and hole from one another. In hybrid perovskites, however, this energy is approximately between 20-50 meV, which is on the order of room temperature thermal energy (26 meV). Thus, essentially no extra energy is required to separate the e-h pair and the carriers can become a free charge and the exciton binding energy is not a large determining factor in efficiency.

3.2.3 The origin of long carrier diffusion lengths in hybrid perovskites

We have already seen that charge carrier diffusion length is a function of non-radiative recombination, scattering mechanisms, and effective mass. The effective mass is related to the curvature of the E-k diagram at the edges of the CBM and VBM, where those with larger dispersion and thus curvature indicate lower effective masses. We have seen that the CBMs of

GaAs and similar semiconductors are comprised of the cation-anion s-p orbitals and the VBMs of the p orbital of the anion. In PVSK, the lower region of the CB is composed of unoccupied Pb-6p orbitals, while the upper part of the VB is formed by the halogen p (I-5p) and Pb-6s states. This is inverted compared to the typical band structure of GaAs and related semiconductors (referred to as p-s semiconductors). Because the Pb-6s is very close in energy to the I-5p there is a strong antibonding coupling between the two bands, which leads to a large dispersion constituting the upper VB. This large dispersion results in small hole effective masses, which are comparable to the electron effective mass. Furthermore, Pb and I are heavy atoms, such that the 6p shells in Pb stabilize the Pb-6s orbital rendering it less likely to react or share its electrons (6s inert pair effect). As such, relativistic effects, that is, spin-orbit coupling (SOC), must be included in quantitative analysis of electronic band structure. Including SOC in calculations led to increased splitting of the Pb-6p CBM, and thus increased band dispersions and lower effective masses. Calculated values for effective masses of electrons and holes including SOC are in the range of $0.19-0.23m_0$ and for electrons and $0.25-0.29m_0$ for holes, where is the mass of an electron in vacuum.[3] This is comparable to inorganic semiconductors such as Si ($m_e{}^* = 0.019m_0, m_{h,light}{}^* = 0.16m_0,\ m_{h,heavy}{}^* = 0.53m_0$) and GaAs ($m_e{}^* = 0.066m_0, m_{h,light}{}^* = 0.05m_0,\ m_{h,heavy}{}^* = 0.08m_0$).[1]

3.2.4 Defects in hybrid perovskites

Defects, such as point, grain boundary, and surface defects, inevitably exist in solution-processed polycrystalline thin films. A solar absorber material must obtain sufficient shallow-level defects to generate free carriers within the device (dopants) but not deep-lying defects that

can lead to unwanted SRH recombination rates. Here I will first discuss defect formation in hybrid perovskites, followed by their implications on semiconductor properties and performance.

While optical absorption is certainly an important property of a solar absorber material, equally important are the charge carrier lifetime and mobility of the semiconductor, as has been established for conventional high performing PV materials such as Si, GaAs, CIGS, CdTe, etc. And while effective mass can provide some insight into the carrier mobility, we must also consider scattering and trapping, which is directly related to the defect nature of the material. These are the other two properties to consider in determining the mobility of carriers within the semiconductor, and are thus essential. In general, we can define a defect-tolerant semiconductor as one with the tendency to maintain its properties despite the presence of crystallographic defects.[9] Essentially, this is a material in which few defects form, and those that do form (either extrinsic or intrinsic) have very minimal impact on the carrier lifetime and mobility (i.e. are not detrimental). In this light, one of the reasons hybrid perovskites have achieved such high efficiencies is owed to their relatively high defect tolerance, in which they form shallow defect levels.

This shallow defect nature seen in $MAPbI_3$ leads to lower rates of SRH recombination because the energy barrier between the defect level and the adjacent band with the opposing charge carrier (e.g. the energy gap between a defect level near the CB and the VBM level) is only slightly lower than the band gap itself, thus preserving a similar recombination rate to the original material. In addition, de-trapping would be easier since the energy gap between the defect level and, for example, CBM is very small. This is in contradiction with the formation mechanism of conventional semiconductors (e.g. GaAs) where the bonding-antibonding orbital pair is formed *across* the band gap, and thus the VBM consists of bonding orbitals (Figure 3-

2b,c). Deep-lying defect levels lead to detrimentally high rates of SRH recombination. This comes at the expense of reduced open circuit voltage (V_{oc}), because the defects will act as recombination sites where electrons and holes recombine non-radiatively, thus preventing a higher voltage forming from the buildup of charge within the device because charge carriers are constantly being lost to recombination within these deep states. However, it is worth nothing here that extrinsic defects could still create deep-lying states within the gap depending on the relative positions of their atomic orbitals compared to the bands of the host material.

The formation of the shallow energy levels seen in hybrid perovskites is directly related to the presence of the filled Pb-6s orbitals that form a dispersive VB via antibonding hybridization of the Pb-6s and I-5p orbitals. This electronic structure permits the formation of intrinsic defects within the band or close to the band edge, rather than deep within the band gap. Any broken (dangling) bonds created by forming a vacancy will likely appear as resonances within the band, leaving the band gap free of defect states. For instance, when an iodine vacancy (an anion vacancy defect) formed in $MAPbI_3$, the defect state is comprised of Pb dangling bonds surrounding the iodine vacancy. The resulting defect state will thus lie between the CBM and Pb p orbital level, and because the difference between these two levels is small (as discussed earlier in this section), the iodine vacancy should be close to the CBM, i.e. a shallow donor state. Furthermore, SOC effects from the heavy Pb atom further reduce the energetic distance between defects and the band edge, by pulling the CBM down, resulting in an increased band dispersion. Similarly, for a missing Pb cation, iodine dangling bonds will surround the vacancy and the resulting energy level will lie between the higher-lying VBM and lower-lying I p atomic orbital levels, and is therefore a shallow acceptor.

Point Defects:

The prominent point defects that have been found to most readily form within perovskite materials, i.e. with the lowest formation energies, also lie shallow within the band gap. These point defect include (i) interstitials, such as iodine (I_i); (ii) vacancies, such as MA vacancies (V_{MA}), V_{Pb}; (iii) anti-sites from either cation-cation or anion-anion wrong bonding, such as MA-on-Pb anti-sites (MA_{Pb}), and MA_I, while those with deep transition levels, such as V_I, I_{MA}, I_{Pb}, Pb_i, Pb_I, and Pb_{MA}, have high formation energies (Figure 3-4).[3,1] Formation energies will be discussed in greater detail in Section 3.3.

Bonding type point defects can only be applied to the VB owed to the band structure of $MAPbI_3$ (bonding orbital lies within the VB), which would be cation vacancies (V_{Pb} , V_{MA}). Anion type vacancies (V_I) would form dangling bonds that fall within the CB only if the dispersion and band width allows the CB to lie lower than the Pb 6p atomic orbitals, where they would otherwise lie at a shallow level within the band gap.[10] Thus, vacancy-type defects resonate within the bands due to (i) the antibonding orbital that pushes the VBM energy upwards, and (ii) relativistic effects from Pb that pull the CB downwards in energy. This concept can also be extended for other defect types, such as grain boundary or schottky defects.

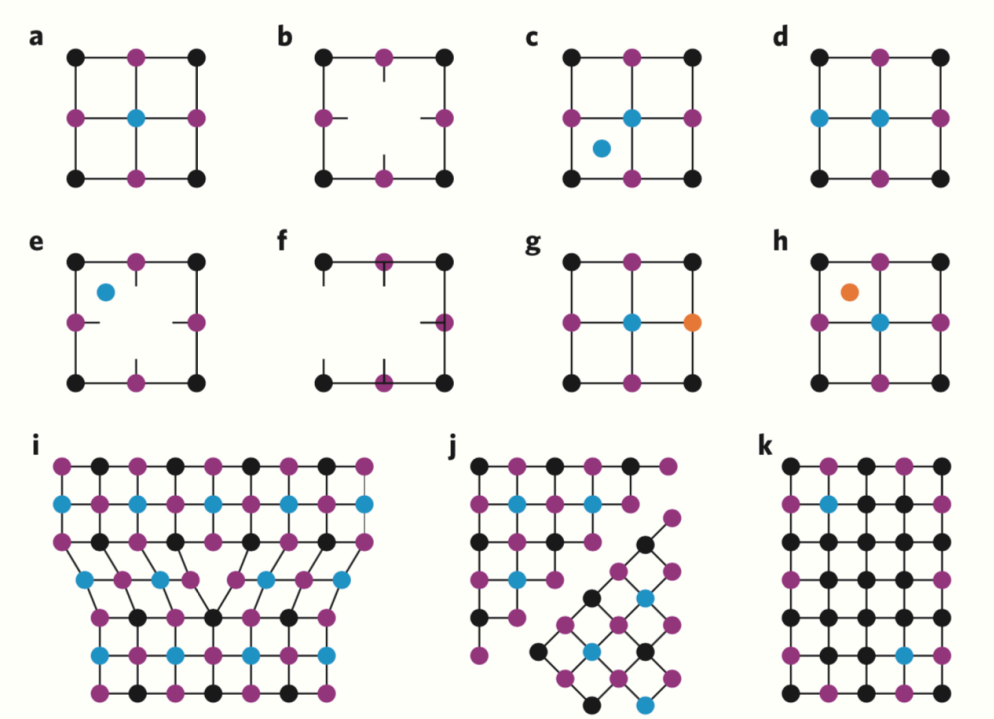

Figure 3-4: Defects in hybrid perovskites. (a) a perfect lattice; (b) a vacancy; (c) an interstitial; (d) an anti-site (wrong bond); (e) a Frenkel defect (interstitial-vacancy pair from same ion); (f) a Schottky defect (cation-anion vacancy pair); (g) a substitutional impurity; (h) an interstitial impurity; (i) an edge dislocation; (j) a grain boundary defect; (k) a precipitate.[11]

Schottky defects:

Schottky defects, that is, defect pairs in ionic materials, are also present in the ionic hybrid perovskite crystal (Figure 3-4f). Schottky defects in hybrid perovskites, such as MAI and PbI_2 vacancies, have been shown to not be deep lying states. However, an accompanying reduced carrier concentration was observed, and it was therefore postulated that schottky defects can self-regulate the carrier concentration via ionic compensation of charged point defects.

Surface defects:

Different defects can also arise depending on the nature of the surface termination. The PbI_x terminations on representative (110), (001), (100), and (101) surfaces were studied via computational methods, where it was found that either vacant or PbI_2-rich surface terminations do not create states within the band gap, thereby preserving the integrity of the $MAPbI_3$ bulk electronic structure.[3] The ability to maintain robust surface properties is another reason why hybrid perovskites exhibit long carrier lifetimes.

Grain boundaries:

Grain boundary defects (GBs) (Figure 3-4j) are a critical component in conventional semiconductor devices, such as CIGS, CZTS, GaAs, CdTe, Si where their associated defects can often form deep states within the band gap that can significantly affect PV properties. In hybrid perovskites, however, this is not the case. Considering the solution-processed nature and lack of stoichiometric composition at the surfaces of grains and at intra-grain regions, it is believed that most defects are located at GBs and surfaces of hybrid perovskites. Initially, GBs were shown to be electronically benign via computational studies, which showed that GB defects do not create deep-level states (via DOS analyses), but instead shallow levels similarly to point defects.[3] Since the atoms at GBs have similar chemical environments as bulk point defects, such as interstitials and vacancies, with dangling or wrong bonds, this is reasonable. However, many recent experimental studies have shown that GBs are not as benign as initially thought. GBs have been shown to be sources of high defect densities and loss of photovoltaic quality, as have been confirmed via experimental studies.[12] The defect densities of thin films and single crystal

perovskites were measured for comparison, showing a higher defect density of 10^{16}-10^{17} cm^{-3}, which is much higher than that of single crystals (10^{9}-10^{10} cm^{-3}). Coupled with visual micro-scale resolution evidence of photoluminescence (PL) quenching at grain boundaries, which implies a higher number of defects and faster non-radiative recombination, there is a strong consensus in the field that GBs and their associated defects are key to improving PV quality of perovskite films and devices. However, there is still some debate as to the exact role of GBs as there have been observed carrier lifetimes that are comparable even for vastly different grain sizes (reduced GB density). Moreover, band bending can result at GBs owed to charged ionic defects that cause depletion or accumulation and thus cause band bending upwards or downwards, which may either assist or impede the separation and movement of charge carriers. For instance, a small upward bending (potential barrier) has been seen at the electron-transporting layer (ETL)-PVSK interface due to the accumulation of positively charged defects, whereas for the hole-transporting layer (HTL)-PVSK interface a downward bending (potential barrier for holes) has been seen. Therefore, GB defects are highly sensitive to growth conditions, material composition, and substrate/surrounding material influences.

In addition to intrinsic defects, there can be extrinsic defects, i.e. via impurities, that can cause deep levels within the band gap. For instance, it has been shown that with time and higher temperature (>70C) the Au electrode can diffuse into the PVSK layer, where it has shown to cause severe loss of PV properties such as V_{oc}, FF, and J_{sc}. Impurities can also cause the formation of precipitates within the bulk or at grain boundaries (Figure 3-4k) that can affect optoelectronic properties. This can be due to dopants or alloying species, as well as diffusion from within other layers within the device (as in the example of Au).

Defect scattering and screening:

Scattering of carriers by defects is an important part of charge carrier mobility and SRH recombination. As we have discussed in Section 2.1.6, a high dielectric constant can reduce the capture cross-section of a defect state that can effectively screen the carriers from that defect site. A high dielectric constant reduces the potential barrier of a charged defect, thereby lowering its propensity to scatter electrons or holes. Since mobility is directly related to charge carrier scattering, this will cause an increase in the mobility of the material. In terms of scattering, it is thus ideal to have a high dielectric constant, alongside a low effective mass and trap density. The dielectric constants in hybrid perovskites are about 3 times larger than other thin film materials, such as CdTe, CZTS, etc. GB scattering can also be reduced for higher dielectric constants when the GB defect levels are shallow. Furthermore, the mobility may be influenced by phonon scattering. The phonon-limited mobility is related to the bulk modulus:

$$\mu_{phonon} = A \cdot B(m^*)^{-2.5} \tag{3.2}$$

where the phonon-limited mobility is related to the bulk modulus (B) and effective mass, and A is a constant. Since $MAPbI_3$ is a relatively soft material with a bulk modulus equal to approximately 22.6 GPa (for the cubic phase),[10] its phonon-limited mobility is lower than stiffer materials. This has been suggested to explain why the mobilities are not comparable to conventional high performance semiconductors (Si, GaAs), though still much greater than other third generation materials such as organics or dyes.

Doping in PVSK:

Doping in hybrid perovskites is generally thought to be unavoidable and small due to the nature of solution-based processing techniques employed. Self-doping has been reported, where the doping concentration can be varied based on the ratio of precursors methylammonium iodide (MAI) and lead iodide (PbI_2).[13] This is related to defect formation energies based on iodine-rich or Pb-rich conditions, which will be discussed in Section 3.3. Heavily n-doped perovskites can be Pb-rich or stoichiometric conditions, where a 1:1 ratio of PbI_2:MAI achieved a electron carrier concentration of $n_e = 2.8x10^{17} cm^{-3}$. Similarly, p-type perovskite can be achieved under iodine-rich conditions, where a ratio of 0.3 PbI_2:MAI achieved a hole carrier density of $n_h = 4.0x10^{16} cm^{-3}$. The acceptor defects are I_i, V_{MA}, V_{Pb}, $MA_{Pb,}$ I_{MA}, and I_{Pb}, while the donor defects are $V_{I,}$ MA_i, Pb_i, Pb_{MA}, MA_I, Pb_I.

Defect formation energies:

In accordance with the laws of thermodynamics, a defect will more readily form as its formation energy becomes more negative. The formation energy is dependent on the chemical potential, which is a function of concentration gradient, chemical activity, and the electronic activity (position of the Fermi level). As such, the thermodynamics of perovskite growth are critical in controlling the nature of crystallization and associated defect formation, which include concentration of precursor species, temperatures, solvents, doping, passivation and reaction rates, etc.

The most stable defect can vary based on the chemical potential (Fermi level), where even the most stable defect at one Fermi level value can transition to a deeper state for a different Fermi level, thus potentially becoming a significant source of SRH recombination. This is represented in Figure 3-4.

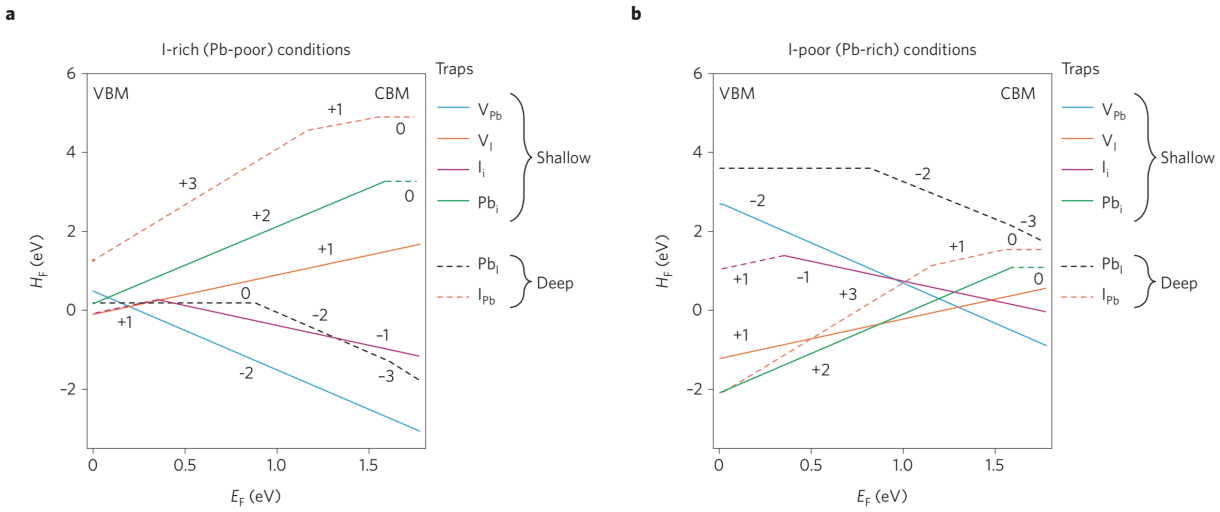

Figure 3-5: The change in formation energy versus Fermi level in (a) an iodine-rich (Pb-poor) conditions, and (b) I-poor (Pb-rich) conditions.[11]

The formation energy of a defect is given by:

$$\Delta H = (E_D - E_0) - \sum_i n_i(\mu_i + \mu_i{}^{bulk}) + q(E_{VBM} + E_F) \quad (3.3)$$

where E_D and E_0 are the total energies of defect and host, n_i is the difference in number of atoms between defect-containing and defect-free (bulk) regions, and μ_i is the relative chemical potential referenced to that of the bulk, $\mu_i{}^{bulk}$, and E_{VBM} and E_F are the energies of the VBM and Fermi level, respectively.[14] The second term signifies the change in energy respective to the

exchange of atoms from their relative positions. The last term represents the change in energy due to the exchange of electrons.

The defect concentration under thermal equilibrium is given by:

$$N_D = N_0 \exp\left(-{}^{\Delta H}/_{kT}\right) \quad (3.4)$$

where N_0 is the number of sites available for a vacancy to form, and ΔH is the formation energy of a defect (activation energy).

The defects with the lowest calculated formation energies include I_i, V_{MA}, V_{Pb}, MA_{Pb}, MA_I, which have been shown to lie shallow and not contribute significantly to SRH recombination, according to density functional theory (DFT) calculations. Meanwhile, deeper lying defects such as V_I, I_{MA}, I_{Pb}, Pb_i, Pb_I, and Pb_{MA} have shown to have higher formation energies (Figure 3-5).[3,1] However, DFT calculations have also shown that there exist some growth conditions in which the formation energies of these deep-lying defects can transition to can transition to become low enough to contribute significantly to SRH recombination. For instance, V_I was originally thought to be a shallow defect, but later shown to transition to a more detrimental state based on the Fermi level of the device. Likewise, it was postulated that the formation energy of Pb_i can make a transition to a lower value under iodine-rich conditions with a defect energy level that lies deep within the band gap. It is also predicted that the bonding of surrounding atoms with these defects can also form deep-lying energy levels. To prevent these defects from forming the equilibrium carrier concentrations should be controlled such that the Fermi level is only approximately 0.3 eV away from the band edges to prevent SRH recombination rates to become dominant. [7,11,15]

3.2.5 Effect of alloying on optoelectronic properties

The A-site cation has been shown to have its energy levels lie deep within the CBM and VBM, and thus its contribution towards the electronic properties of perovskites is negligible.[1] However, the size of the A-site cation can influence the optoelectronic properties of the crystal by causing distortion (tilting) of the BX_6 octahedral symmetry (Figure 3-1c),[1] thus affecting the B-X bonding interactions. As a result, the band gap can be changed by altering the size and structure of the A-site cation. While this variation of the band gap comes as an indirect effect, a more direct method is to substitute the X-site halide, where the bandgap can be tuned to absorb within the ultraviolet to infrared regions of the spectrum through simply variation of these components. For instance, by incrementally substituting the X halide from I^- to Br^-, a blue shift (shift to higher energy) is observed due to a lower ionization potential (binding energy) resulting from a VB transition from 5p → 4p.[16] In fact, this trend has a linear relationship following that of Vegard's Law. A-site cations of similar size (MA, FA) and corresponding crystal structure variations (cubic, tetragonal) can have similar effects in tilting the BX_6 octahedra which affects the Pb-I bond lengths and thus the wave function overlap, which alters the band gap. This unique feature allows for facile means of tuning the color and transparency of the film via simple component substitution. However, this feature also presents other implications in film optoelectronic quality and stability, which can lead to the major problems with hybrid perovskite films, as will be discussed in Section 3.6 and 3.7. Furthermore, the electronic band structure of hybrid perovskites has an associated pressure-dependence, for which a redshift in the energy gap occurs as a result of an increase in pressure. This is due to the antibonding and non-bonding natures of the VBM and CBM, respectively, which are pressure-sensitive. This is quite peculiar as it is in contradiction with most semiconductor materials.

3.3 Perovskite Solar Cells

3.3.1 A brief history of Perovskite PV

The hybrid perovskite made its debut in photovoltaics in 2006 when Miyasaka and colleagues employed $CH_3NH_3PbBr_3$ as a sensitizer on mesoporous TiO_2 in a liquid electrolyte-based DSSC, realizing an efficiency of 2.2%.[17] In 2009, a power conversion efficiency (PCE) of 3.8% was achieved by replacing Br with I.[18] In 2011, Park and co-workers achieved an efficiency of 6.5% by employing perovskite nanoparticles (~2.5nm in diameter) on TiO_2 to serve as sensitizers for improved absorption over conventional dyes.[19] However, these devices were highly susceptible to dissolution within the polar electrolyte solution. Consequentially, in 2012 a solid electrolyte 2,2′ ,7,7′ -tetrakis(N,N-di-p- methoxyphenylamine)-9,9′ -spirobifluorene (Spiro-MeOTAD) was employed as a hole transport material (HTM), achieving an initial efficiency of 9.7% and improved stability compared to the liquid-based design.[20] Later, Snaith et al. reported replacement of the n-type TiO_2 electron transport material (ETM) with an inert Al_2O_3 scaffold, demonstrating an efficiency of 10.9%.[21] These reports revealed the ambipolar nature of perovskites, which enlightened and encouraged the intensive employment of the planar heterojunction architecture in these devices. Later, bromine inclusion was reported to feature an adjustable band gap for perovskites. This sparked an enormous development in the hybrid lead halide perovskite $CH_3NH_3PbX_3$ (X = I, Cl, Br), obtaining a record PCE reaching up 23% in just five years using low cost production methods. This family of materials exhibits a myriad of properties ideal for PV such as high dual electron and hole mobility, large absorption coefficients resulting from s—p antibonding coupling, a favorable band gap, a strong defect tolerance and shallow point defects, benign grain boundary recombination effects and reduced surface

recombination. Consequently, hybrid perovskites have been implemented into various photonic devices and found great promise for applications beyond photovoltaics. The versatility of hybrid perovskites also presents a facile and affordable route, as 15% efficiencies can be obtained with relative ease through diverse architectures and processing techniques.

3.3.2 Device architecture and operating principles

The operation of hybrid perovskite PV cells is complex, but the consensus is that they operate as a p-i-n or n-i-p junction solar cell, where the perovskite absorber layer is the intrinsic layer (i) and the p-doped and n-doped layers are called selective contacts, as they are used to selectively transport one type of charge carrier. The electron transport layer (ETL) transports electrons (n-type) and the hole-transport layer (HTL) transports holes (p-type).

In addition to their unique optoelectronic properties and organic—inorganic hybrid nature, the versatility of perovskites in device architecture and processing techniques has been a main contributor to its extremely rapid development. $MAPbI_3$ was initially used in dye sensitized solar cells (DSSC) to replace conventional dyes. These device configurations feature semiconducting mesoporous TiO_2 scaffolds, which have been intensively studied for DSSCs. Further investigations have found perovskites absorbers to exhibit ambipolar transport properties, that is, the transport of both electrons and holes, which indicates that a mesoporous scaffold is not necessary. As such, planar heterojunction perovskite solar cells were constructed to achieve competitive efficiencies with a simpler architecture and processing requirements. The major device architectures for perovskite solar cells are shown in Figure 3-5a-c.

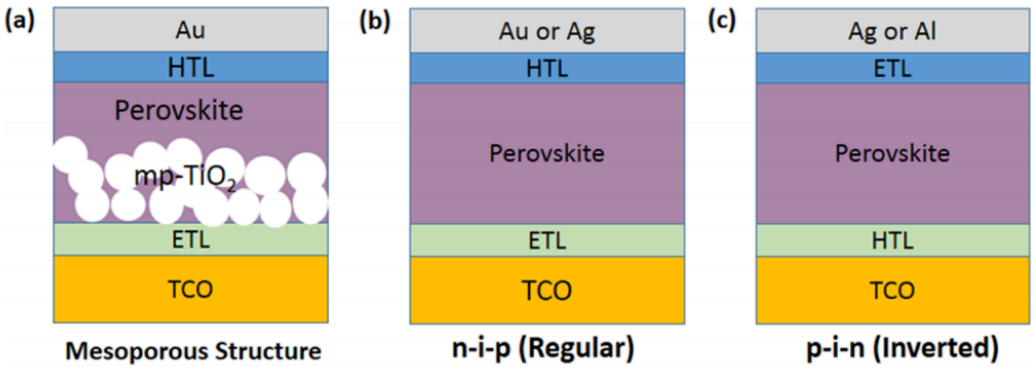

Figure 3-6: The device architectures for perovskite PV cells. (a) mesoporous, (b) n-i-p, (c) p-i-n.[22]

The transparent conductive oxide (TCO) is deposited onto a glass substrate, which is typically indium tin oxide (ITO) or fluorine-doped tin oxide (FTO). Adopted from the DSSCs, the mesoporous device architecture employs a slightly porous scaffold layer (mesoporous), typically titania (TiO_2), that the perovskite film is then fabricated onto. This allows for a greater surface area of contact between the perovskite film and titania layer that can aid in charge transport. Planar device architectures do not have this mesoporous layer, but rather planar (non-porous) layers either in an electron transporting (n-i-p) or hole-transporting (p-i-n) layer first, followed by subsequent layer deposition according to the figure. The selection of materials is different for these architectures due to processing constraints. n-i-p structures most commonly employ TiO_2 or SnO_2 as electron-selective contacts, and the small molecule Spiro-OMeTAD as the hole-selective contact. Conversely, for p-i-n structures, poly(3,4-ethylenedioxythiophene) polystyrene sulfonate (PEDOT:PSS) and [6,6]-phenyl-C_{61}-butyric acid methyl ester (PCBM) are typically employed as hole- and electron-selective contacts, respectively, however other materials have been used such as inorganic nickel oxide (NiO_x), and other various organic polymers and small molecules.

While conditions arising during continuous operation of perovskite PV cells can be quite complex, the operating principle is rather simple. Figure 3-7 depicts the energy band alignment of the perovskite and selective contact materials and associated band bending under (b) contact and (c) illumination. The band alignment is often used to as a guideline for material selection, where lining up the CBM/VBM for hole or electron extraction is selected such that the difference between these energy level is minimized. The Fermi level is another important consideration, but due to the solution-processed nature of these materials it is difficult to control precisely. TiO_2 is n-type doped, where the Fermi level has been shown to lie approximately ~0.1 eV below the CBM. The position of the Fermi level depends on concentration, annealing temperature, and atmosphere that can affect the formation of donor states, which are typically oxygen vacancies or Ti interstitials (self-doping. For Spiro-OMeTAD (p-type), the Fermi level has been shown to be approximately 0.8 eV from the VBM, which is typically accomplished by doping with a Li-TFSI salt. Perovskite, on the other hand, can be n-type or p-type depending on the stoichiometry of precursors during processing, as described in Section 3.2.4. In Figure 3-7 it is represented as intrinsic strictly for representing the band diagram.

Under equilibrium conditions, the Fermi levels align as shown in Figure 3-7b. Band bending occurs at the interfaces between perovskite and the selective contacts as small depletion regions are created. The nature of these interfaces, associated band bending characteristics, and effects on charge extraction are dependent on the respective carrier concentrations, the processing conditions, resulting quality of films, and associated interfacial defect states (as well as impurities). The nature of these interfaces is complex and only recently being understood in greater detail. Upon illumination (Figure 3-7c), the perovskite material absorbs a photon to generate an electron hole pair. Since the binding energy between this exciton pair is relatively

weak, a free electron and hole are created within the intrinsic perovskite layer, represented as an electron excitation from the VBM to CBM. Since the electron wants to move downwards in energy to a more stable state it moves downhill into the TiO_2 material and is blocked by the opposing energy barrier on the Spiro side. Likewise, the hole wants to move upwards in energy and therefore moves easily uphill to the Spiro side, and is blocked by the TiO_2 energy barrier on the other side. Thus, it is important to not only select materials with good alignment to extract the appropriate carrier, but that can also sufficiently block the other carrier (i.e. wider bandgap materials are preferred as selective contacts).

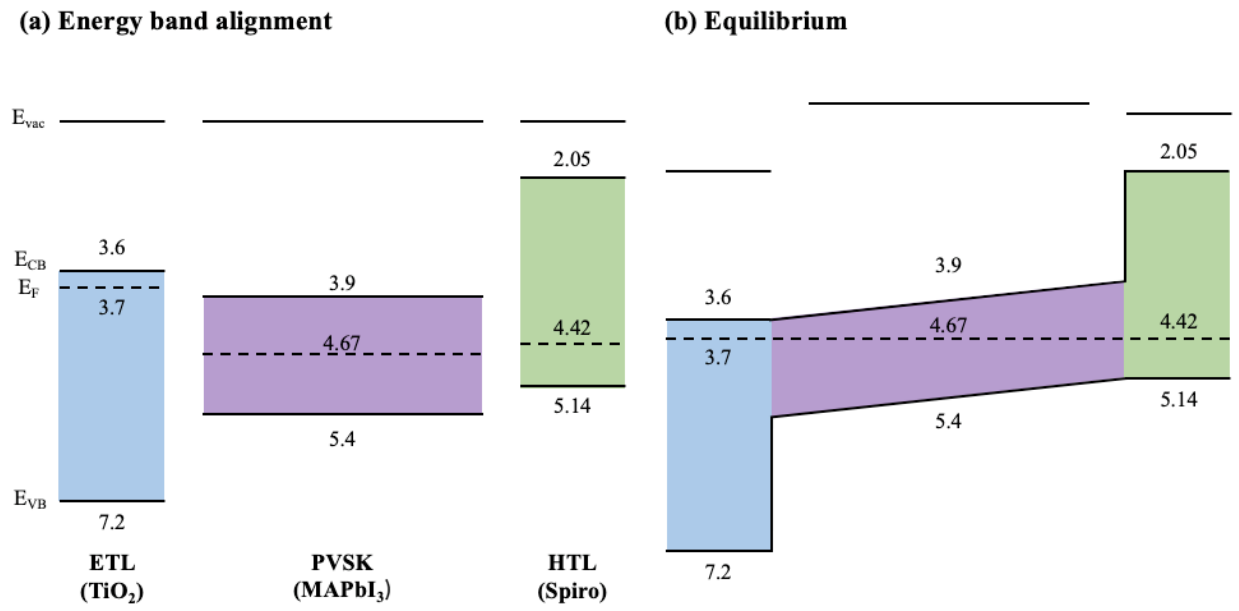

Figure 3-7: (a) Energy band alignment in a hybrid perovskite PV cell, (b) band bending occurring at junctions of interfaces due to unintentional doping of the PVSK layer, (c) quasi fermi level splitting under illumination.

Based on this understanding of perovskite PV cell operation, some criteria for high performance perovskite PV devices can be established:

a. Ideal band gap close to SQ limit
b. Minimized SRH recombination
c. Long diffusion length
d. High absorption coefficient
e. High mobility
f. High charge carrier lifetimes
g. Low trap density
h. Efficient charge carrier extraction
i. Smooth, continuous films (i.e. no pinholes)
j. High radiative recombination

3.3.3 Photoluminescence characteristics

The principle of detailed balance requires that photons must be continuously exchanged between a semiconductor and its surroundings for charge carrier generation and recombination processes. Therefore, radiative recombination is a necessary process in semiconductors. Photoluminescence (PL) is the light emission (or re-radiation) that occurs after absorbing a photon and is an important characteristic of solar absorbing semiconductor materials. It is related to the electronic structure and charge carrier dynamics within the semiconductor film and is typically used to identify and quantify the amounts of radiative and SRH recombination within

the material. As we will see in this section, is also directly connected to the open-circuit voltage (V_{oc}) and PL quantum efficiency (PLQE) of the material.

When a charge carrier approaches spatially localized defect state within the band gap, it is likely it will become trapped in that state. The carrier can then either remain trapped or de-trap (be emitted) back to the respective band (VB/CB) if the activation energy is small enough. On the other hand, if the activation energy is large, then it is more likely that the carrier will remain trapped and annihilate with an oppositely charged carrier before it can be de-trapped. This process can be non-radiative and also emit phonons. The recombination rate is determined by SRH statistics and given by the following time-dependent carrier population (or rate) equation:

$$\frac{dn}{dt} = -k_3 n^3 - k_2 n^2 - k_1 n \tag{3.5}$$

where n is the photogenerated carrier density, and k_1, k_2, and k_3 are the rate constants for monomolecular, bimolecular, and trimolecular recombination, respectively.[11] Monomolecular signifies recombination that involves one carrier at a time, such as indirectly via a recombination center (trapping). Bimolecular recombination is that which involves two free carriers simultaneously, such as band-to-band recombination (radiative). Trimolecular, or three-body, recombination involves three free-body carriers simultaneously, such as Auger type recombination where one electron in the CB recombines with a hole in the VB, giving off that relaxation energy to another electron in the CB. The excitation density can be used to probe these specific modes of recombination. At low excitation densities, monomolecular rates of recombination will dominate as the trap states begin to fill and carriers interact with the background carriers within the material. As the photogenerated carrier density increases, these monomolecular (trap) states fill which allows bimolecular recombination rates (radiative) to

begin to contribute more towards the overall recombination rate. At very high densities, the occurrence of Auger (trimolecular) recombination becomes more probable. These rate constants can be probed experimentally using time-resolved PL decay techniques, and thus, the PL yield and decay rates are important indicators for recombination mechanisms within perovskite films.

Under illumination in the steady-state, electrons are excited from the VB to CB, causing a splitting of the electron and hole quasi Fermi levels, the difference of which is determined by the charge density for which the generation rate is equivalent to the recombination rate, in accordance with the principle of detailed balance, and sets the value for the V_{oc} in the device. When SRH recombination is more dominant, the carriers will have a shorter lifetime than that of radiative recombination, and the steady-state carrier density will decrease. This inevitably reduces the splitting of the quasi Fermi levels, and hence V_{oc}. The V_{oc} is related to the external luminescence quantum efficiency (PLQE) by the following relationship:

$$qV_{OC} = qV_{OC,rad} - kT|\eta_{ext}| \tag{3.6}$$

where η_{ext} is the PLQE and $V_{OC,rad}$ is the ideal V_{oc} with pure band-to-band emission. The ideal voltage to expect is the quasi Fermi level separation, or chemical potential, related to the Boltzmann factor as:

$$exp\left(\frac{free\ energy}{kT}\right) = \left(\frac{excitation\ population\ in\ the\ light}{excitation\ population\ in\ the\ dark}\right) \tag{3.7}$$

Thus, in quasi-equilibrium we have:

$$qV_{OC} = kT\left(\frac{external\ luminescent\ emission}{band-to-band\ emission\ in\ the\ dark}\right) \tag{3.8}$$

Therefore, we can see that the external luminescence intensity (PL intensity) is essentially a 'volt-meter' into the PV cell, where a higher fraction of radiative recombination indicates a higher obtainable voltage and higher performing PV cell. This is because at open-circuit condition the carriers have nowhere to go and ideally all of the carriers would recombine radiatively. Thus, the ideal PV cell should also be a good LED. A lower η_{ext} indicates that there is more SRH recombination present, and thus a lower quasi Fermi level splitting and V_{oc}.

3.4 Thermodynamics of Film formation

The resulting optoelectronic properties of hybrid perovskite materials are highly tied to their growth mechanisms. The nucleation and growth of high quality polycrystalline films is of paramount importance and can make significant differences in resulting PV cell performance (i.e. 10-12% PCE to >20% PCE). In this section, we will discuss the mechanisms of nucleation and growth as well as well as the impacts from the solution chemistry. But first, an introduction to the processing techniques of perovskites will be provided.

From a processing standpoint, hybrid perovskites are unique in that they can be processed from solution. Spin-coating is the most commonly employed technique owed to its simplicity in creating reproducible thin films on small sized substrates. The overall chemical reaction between MAI and PbI_2 is spontaneous, forming $MAPbI_3$ according to:

$$PbI_2 + CH_3NH_3I \rightarrow CH_3NH_3PbI_3 \tag{3.9}$$

Typically, a one- or two-step spin casting method is employed (Figure 3-8). For conventional one-step techniques, common perovskite precursor salts (MAI, FAI, PbI_2) are dissolved into a

solvent (DMF, DMSO), cast and spun onto the substrate to create a thin film, and subsequently heated to crystallize the film.

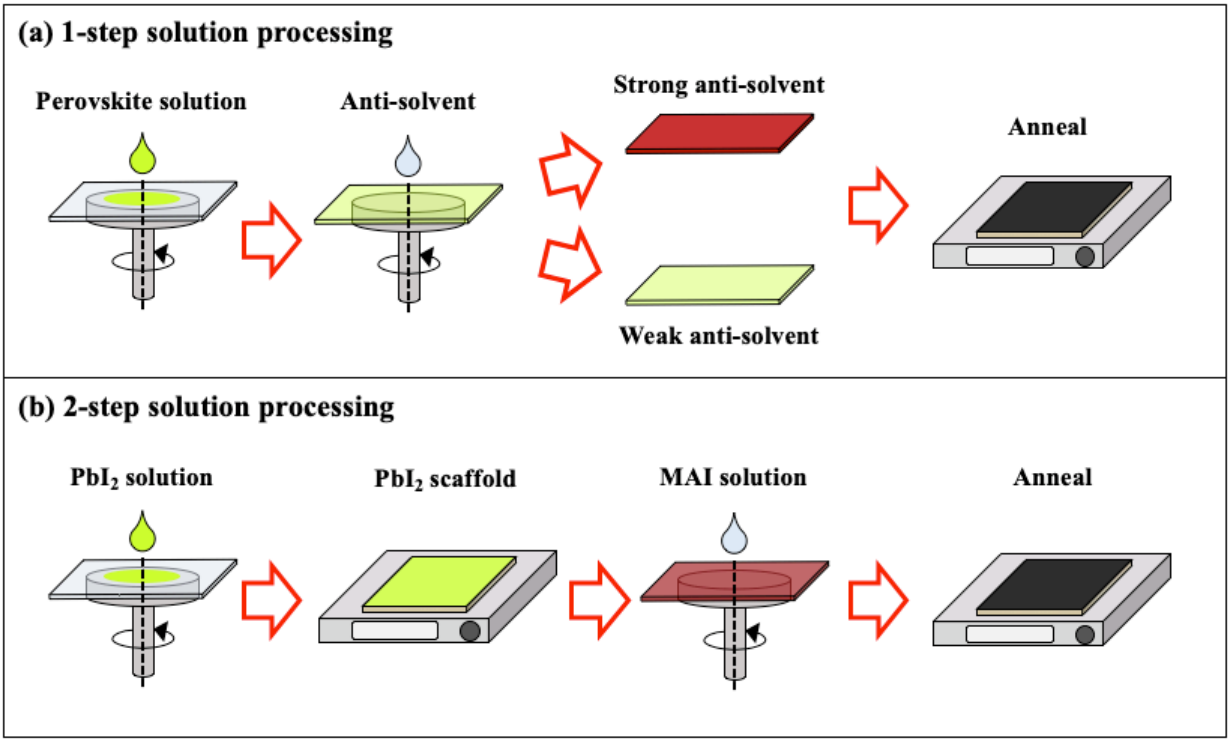

Figure 3-8: Perovskite film processing via (a) one-step and (b) two-step techniques.

Typically, an anti-solvent is applied during one-step techniques to improve quality and reproducibility of the resulting perovskite film morphology. The anti-solvent is applied at an optimized timing after the initial perovskite precursor solution begins spinning, but before it dries (Figure 3-8a). The optimal timing is different for each combination of precursor components and solvents. For perovskites, an anti-solvent is one that is non-polar. Depending on the anti-solvent used, this can induce different degrees and rates of crystallization. Strong anti-solvents, such as chlorobenzene, will induce rapid crystallization upon application to the

spinning perovskite film by helping to flush out the solvent. A rapid and distinct color change is to a darker translucent color observed upon application, indicating partial formation of the photo-active perovskite crystalline structure. Heating will complete the formation of the black perovskite phase. On the other hand, a more mild anti-solvent, such as diethyl ether, will less effectively flush out the solvent and can result in the formation of an intermediate complex of the perovskite precursor-solvent components, where there is still some solvent remaining that has not been removed or evaporated. This intermediate complex has a transluscent color similar to that of the precursor solution, but can vary based on the components within the solution and the conversion time of the intermediate phase to the perovskite crystal structure. Subsequent heating at an appropriate temperature will liberate these solvent molecules and induce rapid crystallization of the perovskite structure. Further details on the impacts of solution chemistry will be discussed in Section 3.4.2.

Owed to the fact that high performing perovskite films can be fabricated under different fabrication conditions and different precursor stoichiometries, a phase diagram has been recently constructed to provide insight into the ranges of compositions for which $MAPbI_3$ can form (Figure 3-9).[23] The figure presents two phase diagrams, where Figure 3-9a represents a phase diagram that is representative of phase formation during processing (and processing conditions), but is not necessarily a good representation of the material at equilibrium, whereas Figure 3-9b depicts the phase diagram under equilibrium conditions. The main difference comes from the regions greater than 140˚C for a MAI concentration of approximately 60% and higher. Figure 3-9a accounts for the fact that MAI readily liberates during processing at higher temperatures, and thus the α perovskite phase is not stable, whereas Figure 3-9b was constructed under equilibrium conditions (constant MAI partial pressure). Thus, the former is more useful from a fabrication

standpoint. The phase diagram shows that a α' phase can be formed that can still maintain the 3-D dimensionality with a higher degree of stacking faults, which has a wider range of tolerance for MAI incorporation than the pure α phase.

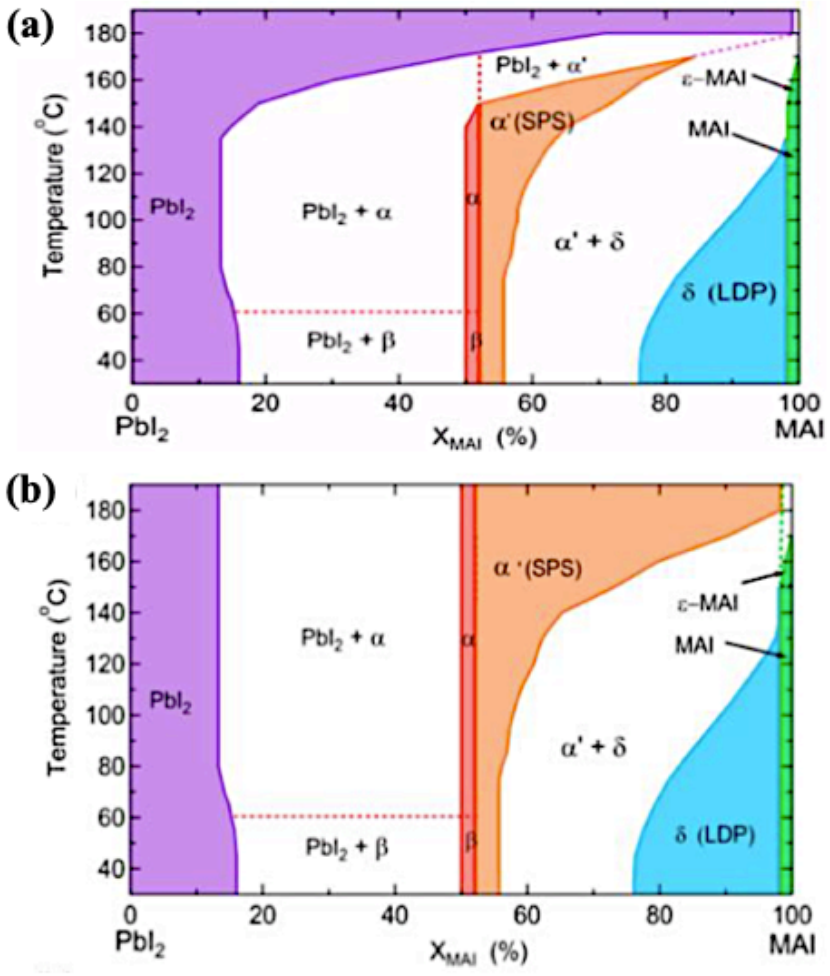

Figure 3-9: Phase diagrams for (a) non-equilibrium (processing) conditions, and (b) equilibrium conditions.[23]

Aside from controlling phase formation, the nucleation and growth kinetics are important in the resulting crystal quality. In the next section, we will discuss the factors that affect such processes.

3.4.1 Nucleation & Growth

According to classical nucleation theory, nucleation is a competing process between the reduction in free energy associated with formation of a bulk structure (bonding) and the increase in free energy associated with the formation of surfaces (broken, dangling bonds). As such, there exists a critical radius for which nucleation can occur such that the overall free energy is negative and the nucleus is stable (i.e. won't re-dissolve into its original components). Here, I will first discuss the case of homogeneous nucleation, meaning nucleation solely from the formation of clusters within a liquid (i.e. no surfaces for heterogeneous nucleation to occur). This is represented by the overall equation:

$$\Delta G = -\frac{4}{3}\pi r^3 \Delta G_v + 4\pi r^2 \gamma^{sl} \quad (3.10)$$

where ΔG is the total Gibbs free energy, r is the radius, ΔG_v is the volumetric Gibbs free energy term and γ^{sl} is the surface free energy term.[24] The first term represents the decrease in free energy associated with the formation of a stable bulk crystal structure (coordinated bonding), whereas the second term represents the opposing increase in free energy from surfaces being created (uncoordinated bonds). The volumetric Gibbs free energy term is given by:

$$\Delta G_v = \frac{kT}{v} ln(S) \quad or \quad \Delta G_v = \frac{kT}{v} ln\left(\frac{C}{C_0(T)}\right) \quad (3.11)$$

where S is the supersaturation and is equivalent to $C/C_0(T)$, C is the concentration of precursors and $C_0(T)$ is the concentration of precursors at equilibrium, and v is the molar volume.[25,26] In classical nucleation theory for metals, this bulk free energy term is dependent on the latent heat of formation and undercooling, which is similar to the thermal energy (kT/v) and supersaturation

ln[$C/C_0(T)$] terms here. The corresponding free energy diagram versus radius is shown in Figure 3-9.

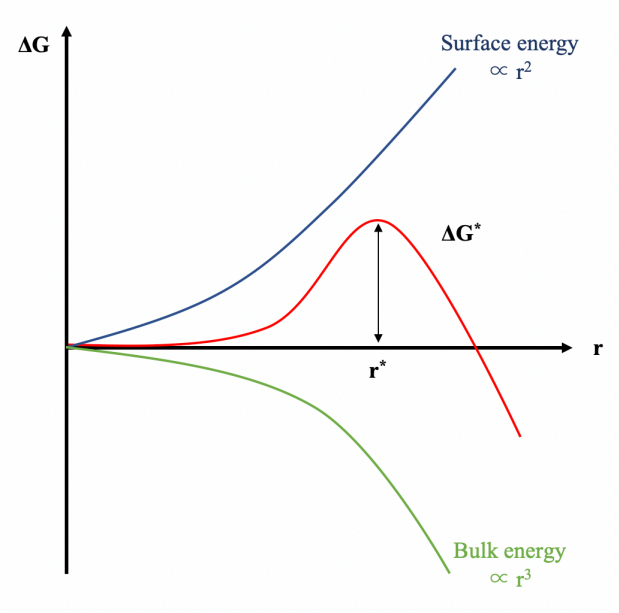

Figure 3-10: The Gibbs free energy curve for nucleation of a solid consisting of the volumetric and interfacial energy terms.

Initially the interfacial (surface) energy term with r^2 dependence will outweigh the volumetric term with r^3 dependence, but as the radius increases in this competing energetic process there will exist a critical radius value that is corresponds to a maximum on the free energy diagram. Once this critical radius is achieved, or this energy barrier is overcome, the free energy rapidly drops becoming more and more stable. This critical energy value, dependent on the radius of the nucleus (cluster of atoms), can be found by first taking the derivative of the total free energy equation with respect to the radius and setting equal to zero to find the radius corresponding to the maximum of the free energy curve in Figure 3-9. This critical radius value can then be

plugged back into the total free energy question to give the critical free energy (or activation energy, energy barrier) as:

$$r^* = \frac{2\gamma}{\Delta G_v} \tag{3.12}$$

$$\Delta G^* = \frac{16\pi\gamma^3}{3\Delta G_v{}^2} \tag{3.13}$$

where r^* is the critical radius and ΔG^* is the critical free energy. Thus, we can see that the activation energy depends on the critical radius size, which is a function of the surface and bulk free energy terms, where the bulk term is dependent on supersaturation. In classical diffusion of metals, this is related to undercooling, however our system is more complex as we are dealing with an ordered ionic crystal structure, and thus nucleation is not only dependent on undercooling, but ordering and diffusion as well as bonding strength and directionality.

The formation of nuclei is a dynamic process, where clusters of atoms/molecules constantly associate into clusters and disassociate back into solution until the critical cluster size (or critical radius) is achieved. An instantaneous picture would show many clusters of atoms that are temporarily in the same crystalline array as in the bulk solid. On average, the number of spherical clusters is given by:

$$n_r = n_0 \, exp\left(-\frac{\Delta G_r}{kT}\right) \tag{3.14}$$

where n_0 is the total number of atoms in the system, and ΔG_r is the free energy associated with the cluster. The nucleation rate is given by:

$$\frac{dN}{dt} = f_0 C_0 \, exp\left(-\frac{\Delta G^*}{kT}\right) \tag{3.15}$$

where k is Boltzmann constant, T is temperature and C_0 is the number of solute atoms per unit volume. f_0 is a complex function that depends on the activation energy for diffusion in the liquid, the surface area of the critical nuclei, and the vibrational frequency of the atoms. Hence, we can see that the kinetics of nucleation (nucleation rate) is also governed by the activation energy ΔG^*.

While this picture helps one understand the parameters dictating homogeneous nucleation, heterogeneous nucleation is the more likely the case for solution-processed perovskites where nucleation occurs at the substrate-liquid interface. The equation for heterogeneous is identical to that of homogeneous nucleation but with an additional term called the shape factor that accounts for the change in shape of the nucleus against a surface. The shape factor considers the interfacial surface tensions against the substrate surface. This effectively reduces the surface area of the nucleus needed, and can be qualified based on the wettability of the solvent/solute solution on the given substrate that dictates the contact angle between the nucleus and interface surface. Thus, the free energy for heterogeneous nucleation becomes:

$$\Delta G_{het} = \left\{-\frac{4}{3}\pi r^3 \Delta G_v + 4\pi r^2 \gamma^{sl}\right\} S(\theta) \tag{3.16}$$

where the shape factor is defined as:

$$S(\theta) = (2 + cos\theta)(1 - cos\theta)^2/4 \tag{3.17}$$

and θ is the 'wetting' angle on the substrate. The critical free energy and nucleation rate are thus:

$$\Delta G_{het}{}^* = \frac{16\pi\gamma^3}{3\Delta G_v{}^2} \cdot S(\theta) \tag{3.18}$$

and

$$\frac{dN}{dt} = f_1 C_1 \, exp\left(-\frac{\Delta G_{het}{}^*}{kT}\right) \tag{3.19}$$

where C_1 in this case is the number of atoms in contact with heterogeneous nucleation sites per unit volume of solution. Thus, we can see that the activation barrier against heterogeneous nucleation is smaller than that of homogeneous by a factor of $S(\theta)$, and the similarly the nucleation rate decreases exponentially by a factor of $S(\theta)$. Control over the nucleation energetics, kinetics, and density is critical in hybrid perovskites because it allows for the opportunity to control the resulting film properties. Next, we will look at how we can tune the solution chemistry in this regard.

3.4.2 Solution Chemistry

The obvious question upon obtaining an understanding of nucleation and growth processes is *'how can we control the bulk and surface free energy terms?'* Supersaturation is the key component in modulating the activation energy for nucleation and is related to the solubility of precursors within a given solvent, or the chemical interactions between precursors and solvents. The solvent choice, precursor composition, and anti-solvent choice will change the energetics within the solution such that certain interactions are more favorable than others, which dictate the mechanisms by which the nucleation and growth may proceed. This can be understood by considering the enthalpy (or heat) of mixing for a binary (two-atom) system:

$$\Delta H_{mix} = P_{AB}\left(\varepsilon_{AB} - \frac{\varepsilon_{AA}+\varepsilon_{BB}}{2}\right) \tag{3.20}$$

where P_{AB} is the number of A-B bonds, and ε_{AB}, ε_{AA}, and ε_{BB} are the bond energies of the A-B, A-A, and B-B bonds, respectively. Upon analyzing this equation, we can see that there exist three cases determined by the sign of the portion within brackets. If it is equal to zero, then the solution is considered an ideal solution, where there is no heat of formation as the A and B atoms do not prefer to interact with one species over the other, thereby not giving off or taking in any energy (heat). If it is positive, then there is a positive heat of mixing and atoms/molecules of one type will want to be around atoms/molecules of the same type. This is because a lower value of ε_{AA} and ε_{BB} means these bonds are more stable, and ε_{AB} is higher in energy and thus more unstable, thereby causing a preferred formation of A-A and B-B bonds (phase separation, exothermic). If it is negative, then the converse occurs where atoms/molecules will want to be surrounded by those of a different type (alloying). Generally speaking, this concept can be extended for a ternary system during crystallization from solution, which would include more mixing terms for the three-component interaction. However, the case becomes more complicated for hybrid perovskites as we must consider the relative sizes of the atomic/molecular constituents (geometrical mismatch), the bond strength between atoms/molecules, and the electronegativity of each constituent.[2]

Since hybrid perovskites are ionic solids, the coulombic forces between the ionic and highly polar molecular species are what bind the crystal together. Thus, like the solid form, the strength of the precursor-solvent interactions in solution is in principle related the electronegativity and/or polarity of the individual atoms or molecules. Upon forming the solution, the ion-dipole interactions of the ions of the crystal and solvent molecules must be stronger than the coulombic forces holding the lattice (crystal) together of the precursor solids. Thus, a stable liquid solution is formed full of the dissociated ionic species free flowing within

the solvent liquid. The solubility depends on the strength of this ion-dipole interaction. On the other hand, during subsequent nucleation and growth processes temperature is used to drive the crystallization reaction by selectively evaporating the lower boiling point solvent while the solid components remain on the substrate to subsequently crystallize into the perovskite structure. The activation energy for this will again depend on the ion-dipole interaction strength of the perovskite precursors and solvent molecules. This fundamental understanding can be used to intentionally manipulate the solute-solvent chemistry by introducing different perovskite precursor and solvent species to change the solubility (supersaturation levels) and hence control the nucleation and growth dynamics, which is the underlying principle for modifying growth of hybrid perovskites in this work.

3.6 Challenges with perovskite PV

While the hybrid perovskite material is full of appeal and impressing results, there are several important challenges to be resolved in order to realize a commercial PV technology, namely, the poor long-term stability of the material and devices, anomalous hysteresis effects, and the performances that still fall short of the industry-leading PV technologies. We will see in the following sections that these challenges are all related to the film quality, and namely, defects, which are connected to grain boundaries and surfaces, and film formation.

3.6.1 Intrinsic instability

The stability of hybrid perovskites can be broken down into two categories: intrinsic and extrinsic instability, where the former relates to the thermodynamics of intrinsic crystal phase stability under ambient and/or processing conditions, and the latter is due to extrinsic stimuli that induce degradation of the material.

The intrinsic instability of hybrid perovskites is related to the thermodynamics of the crystal structure and phase(s) present in the system. The most stable structure will be that with the lowest free energy, in accordance with the expression we know for Gibbs free energy, $\Delta G = \Delta H - T\Delta S$, where ΔH is the enthalpy term, and $T\Delta S$ the entropy term. A more negative ΔG indicates a more stable system. Thus, it is important to look at the enthalpy, or formation energy, to understand how intrinsically stable the structure is. Taking the conventional $MAPbX_3$ family as an example, the overall reaction for its decomposition is given by:

$$PbI_2(s) + CH_3NH_3X\ (s) \rightarrow CH_3NH_3PbX_3(s) \tag{3.21}$$

Experimental calorimetric measurements have shown the formation energies for $MAPbI_3$, $MAPbBr_3$, and $MAPbCl_3$, to be 34.5 ± 1.01 kJ/mol (strongly positive), 6.69 ± 1.41 kJ/mol (weakly positive), and -9.03 ± 0.68 kJ/mol (weakly negative), respectively.[2] There are three major factors that have been identified to influence these enthalpy (heat) of formation observations:

(i) tolerance factor (geometrical mismatch)

(ii) electronegativity

(iii) Pb-X bond strength

The tolerance factor is an important consideration because it is related to the strain within the lattice owed to bond length mismatch. The trend of tolerance factor to enthalpy of formation are inversely related, where the enthalpy of formation becomes more exothermic (more negative) with increasing tolerance factor. Similarly, both the electronegativity and Pb-X bond strength increase from I^- to Br^- to Cl^- alongside a decrease in the enthalpy of formation, which indicates that the stability increases in this sequence. These results show that $MAPbI_3$ is intrinsically metastable, and could dissociate into its separate binary components (the reverse of its formation equation) even in the absence of external stimuli. Here it is important to note that even if entropic effects are considered, it is unlikely that they would be high enough to render ΔG net negative for $MAPbI_3$ at room temperature. Thus, the decomposition of $MAPbI_3$ is inevitable from a thermodynamics perspective, and its rate of decomposition will therefore be governed by kinetic effects. These three factors, and particularly the tolerance factor, are important guidelines for improving the intrinsic stability of perovskite materials, where alloying with different components (A-site, X-site, and even B-site) cations show promise in terms these criteria as well as based on experimental results.

3.6.2 Extrinsic instability

Equally important as the intrinsic stability of perovskite materials are their robustness against external factors that can cause their degradation. The major external stimuli that cause degradation of hybrid perovskites can be classified as chemical: (i) moisture, (ii) oxygen, (iii) light (UV), (iv) electrical bias, (vi) chemical reactions from surrounding materials and

processing, and (vi) temperature. Here I will discuss these factors in greater detail, based on a thorough review by Niu et al.[27]

Moisture and oxygen:

Moisture is the most severe cause for degradation of hybrid perovskites, as they tend to hydrolyze in the presence of water. Taking $MAPbI_3$ as an example, the degradation process is:

$$CH_3NH_3PbI_3(s) \overset{H_2O}{\longleftrightarrow} PbI_2(s) + CH_3NH_3I\ (aq) \quad (3.22)$$

$$CH_3NH_3I\ (aq) \leftrightarrow CH_3NH_2\ (aq) + HI\ (aq) \quad (3.23)$$

$$4HI\ (aq) + O_2(g) \leftrightarrow 2I_2(g) + 2H_2O\ (l) \quad (3.24)$$

$$2HI\ (aq) \leftrightarrow H_2(g) + I_2(g) \quad (3.25)$$

First, water interacts with the $MAPbI_3$ solid to form lead iodide solid and aqueous methylammonium iodide. Subsequently, the methylammonium iodide forms aqueous methylamine and hydriodic acid. The hydriodic acid can then proceed via either of the last two reactions, reacting with oxygen to form iodine and water or evaporating to form hydrogen and iodine gases. Therefore, the net effect of $MAPbI_3$ decomposition in the presence of water is the liberation of the methylammonium A-site cation, leaving behind solid lead iodide (PbI_2) that is typically a yellow color. For this reason, it is common to observe degradation as the transformation from the black perovskite phase to yellow non-perovskite phase. This is typical for most types of hybrid perovskites, such as $FAPbI_3$, however each A-site cation will yield a different stability based on the criteria outlined in the intrinsic stability section as well as its

affinity towards water. We can also see that the combination of water and oxygen can accelerate degradation due to the reaction of oxygen with hydriodic acid. There have also been other proposed mechanisms for moisture-induced degradation that include a perovskite –moisture intermediate complex due to deprotonation of ammonium. Thus, it is believed that an aprotic cation would greatly alleviate moisture-related stability issues.

U-V light:

The chemical instability of perovskites under UV-light mainly comes from the common ETM TiO2, which is a photo-catalyst typically used for oxidizing water, thereby creating hydroxyl radicals, and other organic materials. In DSSCs TiO_2 is used to extract electrons from iodide within the electrolyte solution. In $MAPbI_3$, it has been shown to transform to PbI_2 under 12 hours of UV exposure, where it has been proposed that electrons are extracted from the iodine in perovskites to form I_2, where subsequently the methylammonium can form volatile methylamine gas and I_2 volatile HI. This effect has been remedied by inserting a thin UV-blocking layer between the perovskite and TiO_2 layers, thus confirming this hypothesis.

Processing and surrounding material reactions:

The influences of processing materials and conditions as well as reactions that can occur between perovskite and the adjacent layers within the material can cause its degradation. For instance, solvent compatibility is important when processing films on top of perovskites, where the solvent ideally should not be polar so as not to re-dissolve the perovskite components. The

components of the surrounding layer material can also degrade the perovskite film. For instance, the common additive for Spiro-OMeTAD to dope it p-type is a lithium salt (Li-TFSI), that has been shown to degrade the perovskite film over time as it can diffuse to the interface and react with the perovskite material. Unfortunately, Li-TFSI is a necessary doping component for Spiro-OMeTAD in the presence of oxygen and no better dopant has yet been identified that does not lead to such degradation while maintaining high performances. Moreover, components such as ammonium, acetonitrile, have shown to accelerate degradation. Therefore, processing conditions, solvent, and material selection should be optimized to prevent degradation from occurring.

Electrical bias and hysteresis:

Electrical bias can also induce degradation of $MAPbI_3$ related to anomalous hysteresis effects seen in hybrid perovskite materials. Hysteresis effects are present in I-V scans of perovskite materials, where the I-V characteristics and resulting efficiencies are dependent on the direction of voltage sweep (i.e. positive to negative or negative to positive).[28] It is believed that ion migration (predominantly iodine species) and defect charging/discharging or capacitance (interfacial) effects are responsible for this observed behavior. It has been shown through in-situ TEM measurements that the application of an external bias can induce degradation of $MAPbI_3$, where the electrical bias causes ion migration of iodine to the positively biased interface, followed by volatization of the iodine and organic species at the interface that leads to nucleation of PbI_2 and associated voids within the material.[28] This effect has been shown to occur under vacuum even in the absence of moisture and other atmospheric effects, but may be accelerated by the low pressure within the vacuum chamber.

Grain boundaries:

It has been shown that grain boundaries are locations of increased ion migration due to the termination of the lattice that allows for facile means of ionic movement,[29] and thus an increase in GB density can lead to increased ion migration and bias-induced degradation. Grain boundaries have also shown to be locations susceptible to moisture infiltration and attack, that lead to higher rates of degradation.[30] The GB layer is thought to consist of an amorphous region in which diffusion of moisture is much more rapid than within the crystalline region, mainly attributed to the hygroscopic methylammonium ions at the surfaces. Hence, these effects indicate that the processing techniques and resulting film morphology and quality are of the utmost importance in hybrid perovskite materials.

Dimensionality impacts on stability:

Now that we have discussed the compositional variations of perovskite within the 3-D tolerance range, we can also discuss dimensional effects on intrinsic stability. It has been shown that the stability of perovskites is linked to its dimensionality, where the lower formation energy (more negative) occurs for lower dimensionality (denoted *n*), and thus will form more spontaneously and be more stable. Figure 3-11 shows the relationship between n, formation energy, and stability, where a lower *n* corresponds to a more negative formation energy (enthalpy) and higher stability compared to higher *n* values, where $n=\infty$ is a purely 3-dimensional structure. The exact mechanism of the more negative formation energy is not exactly understood, but is related to the bonding nature of the head of the longer molecular chain with the exposed 3-D octahedral surface and the low surface energy created by the longer tail (no

dangling bonds, relatively unreactive and stable). However, this has implications in terms of performance that we will see in the following section.

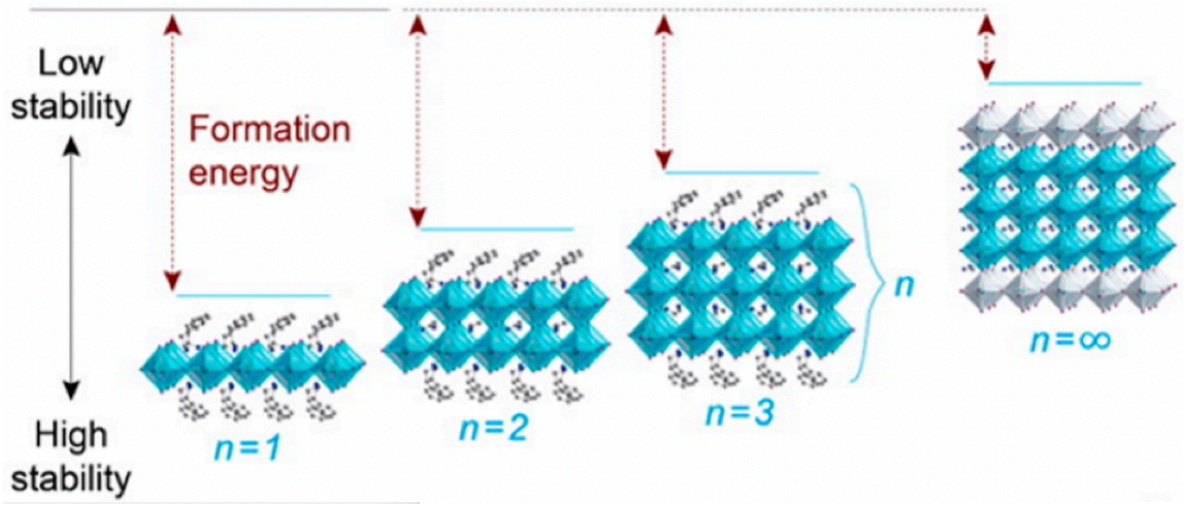

Figure 3-11: The relationship between dimensionality, formation energy, and stability for 2-D to 3-D perovskites. n represents the number of repeat crystalline units capped by longer organic molecules.[31]

In terms of nucleation, we often see that the rate decreases through use of larger molecules for 2-D perovskites. Referring to equation 3.13 for the critical free energy (or activation energy) of nucleation, we can observe its dependence on the molar volume, *v*. Since the molar volume is larger for 2-D perovskites, i.e. a higher volume per mole of substance due to longer length of the molecules, this would drive the volumetric free energy component (equation 3.11) down since the molar volume term is in the denominator. Thus, the total free energy (equation 3.10) and critical free energy/activation energy (equation 3.13) terms would be higher since the volumetric free energy term is lower, which can help explain why we see an increase in activation energy and decrease in nucleation rate (equation 3.15) through use of longer molecules that form 2-D perovskites. In addition, there are other factors that can influence this process, such as the

kinetics of diffusion processes for the larger organic molecules that could create a diffusion-limited case of nucleation, where the rate of nucleation is limited by the ability of the organic species to move and diffuse to the necessary location. Similarly, the surface energy term could change based on the nature of the organic molecule used and its interaction with the precursor components. The nature of the grain boundaries and their associated stability is also related to the defect nature at GBs, where different quantities and types of defects will affect the energetics and rates of degradation. Thus, we can see that the processes of nucleation and growth are intimately connected with the resulting GB defect nature and overall perovskite material stability.

3.6.3 Performance

Despite the appeal that high efficiencies can be reached for a solution-processed PV material, this solution-processed nature is also a bottleneck to reaching the performance levels of industry-dominating PV technologies, such as Si (~26%), GaAs (28.9%), CdTe (22.1%), etc (Figure 3-12).

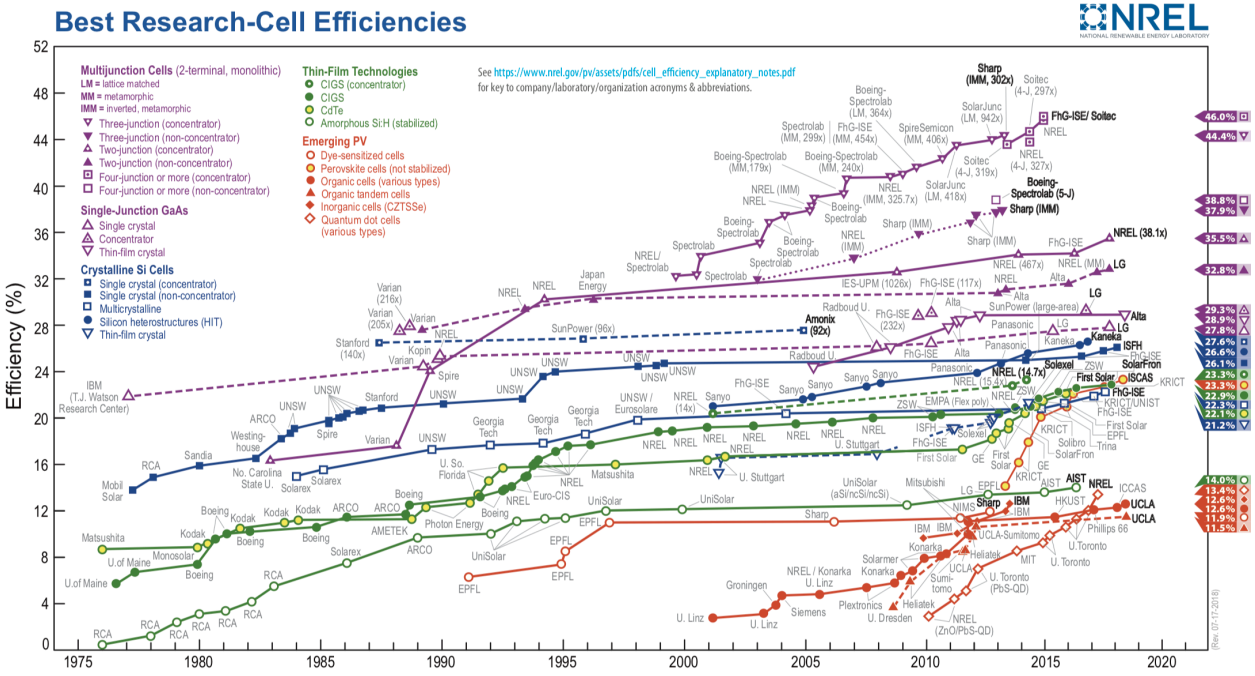

Figure 3-12: NREL best research-cell efficiencies chart. Perovskite has achieved an impressive 23.3% record PCE, yet, still falls short of industry standard technologies.[32]

This bottleneck is directly related to the issues mentioned for stability: GBs, defects, and ion migration. Like stability, these are all tied directly to the nucleation and growth processes, and thus performance and stability are connected and it becomes possible to solve them simultaneously. Performance has clearly been shown to be directly tied to the technique used to fabricate the films, the precursor materials and solvent used, as well as additives and other external factors such as temperature and environment. In terms of GBs and their influences, this is still under some debate. Many computational studies have shown GBs to be benign as their associated defects lie at shallow levels (if at all) within the band gap. Some have even claimed that GBs may be beneficial in extracting charge due to the potential difference across them, where charges are more readily swept across the GBs than within grains, thus leading to

enhanced mobility.[33] However, several studies have depicted that the variation in PL intensity at the micro-to-nano scale and at GB regions and for different grains, indicating that GBs are not as benign as originally thought and that the efficiency depends on the crystal facet and its associated defects (Figure 3-13).[34,35,36] In addition, charge carrier diffusion lengths have proven longer for single crystals (>150 µm) than in thin films (>1 µm), which further suggests that GBs contribute to non-radiative losses within perovskite PV cells.[37,38] Based on these experimental findings, it is believed that the nature of defects at GB regions and different crystal facets can negatively impact the local micro-to-nano scale performance as compared to single crystals. Thus, it becomes apparent that both stability, performance, and hysteresis issues are likely all attributed to GBs and their associated defect natures. The focus of my work presented in this thesis is dedicated to identifying and solving the issues of grain boundaries and defects through modifying film formation processes, composition, and dimensionality.

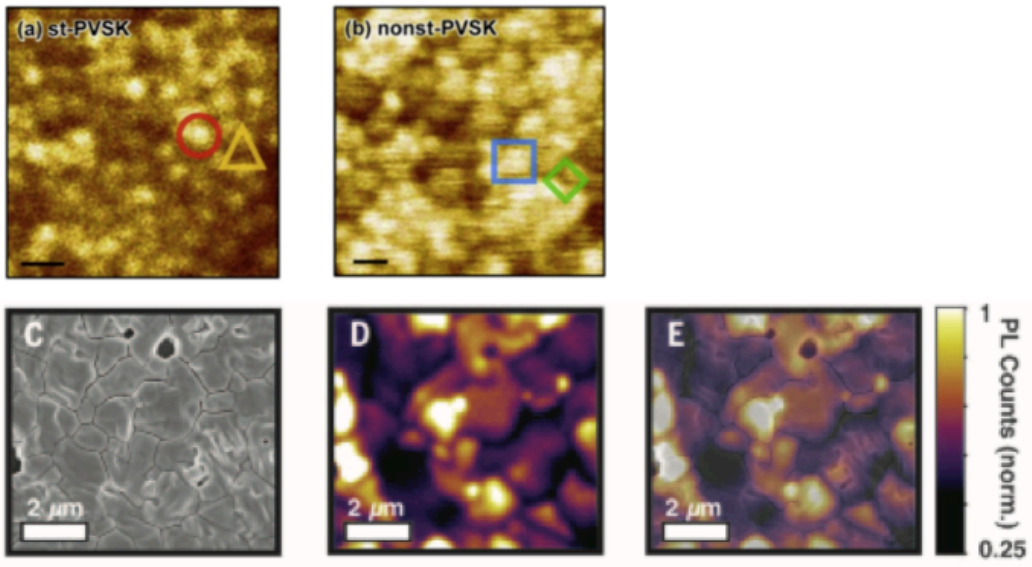

Figure 3-13: (a-b) Microscale PL mapping depicting grain and grain boundary differences in PL quenching for (a) a stoichiometric PVSK film and (b) a non-stoichiometric PVSK film. (c-d) SEM image

overlaid with PL emission. (c) SEM image of PVSK film, (d) PL image of same region of PVSK film, (e) overlay of PL on SEM image showing crystal facet and grain boundary dependencies on PL yield.[34,36]

References:

1. Chen, Q. *et al.* Under the spotlight: The organic–inorganic hybrid halide perovskite for optoelectronic applications. *Nano Today* **10**, 355–396 (6).
2. Nagabhushana, G. P., Shivaramaiah, R. & Navrotsky, A. Direct calorimetric verification of thermodynamic instability of lead halide hybrid perovskites. *Proc. Natl. Acad. Sci.* **113**, 7717–7721 (2016).
3. Xiao, Z. & Yan, Y. Progress in Theoretical Study of Metal Halide Perovskite Solar Cell Materials. *Adv. Energy Mater.* **7**, 1701136 (2017).
4. Umebayashi, T., Asai, K., Kondo, T. & Nakao, A. Electronic structures of lead iodide based low-dimensional crystals. *Phys. Rev. B* **67**, 155405 (2003).
5. Huang, H., Bodnarchuk, M. I., Kershaw, S. V., Kovalenko, M. V. & Rogach, A. L. Lead Halide Perovskite Nanocrystals in the Research Spotlight: Stability and Defect Tolerance. *ACS Energy Lett.* **2**, 2071–2083 (2017).
6. Kovalenko, M. V., Protesescu, L. & Bodnarchuk, M. I. Properties and potential optoelectronic applications of lead halide perovskite nanocrystals. *Science* **358**, 745–750 (2017).
7. Yin, W.-J., Shi, T. & Yan, Y. Superior Photovoltaic Properties of Lead Halide Perovskites: Insights from First-Principles Theory. *J. Phys. Chem. C* **119**, 5253–5264 (2015).
8. Ziang, X. *et al.* Refractive index and extinction coefficient of $CH_3NH_3PbI_3$ studied by spectroscopic ellipsometry. *Opt. Mater. Express* **5**, 29–43 (2015).

9. Zakutayev, A. *et al.* Defect Tolerant Semiconductors for Solar Energy Conversion. *J. Phys. Chem. Lett.* **5**, 1117–1125 (2014).
10. Brandt, R. E., Stevanović, V., Ginley, D. S. & Buonassisi, T. Identifying defect-tolerant semiconductors with high minority-carrier lifetimes: beyond hybrid lead halide perovskites. *MRS Commun.* **5**, 265–275 (2015).
11. Ball, J. M. & Petrozza, A. Defects in perovskite-halides and their effects in solar cells. *Nat. Energy* **1**, 16149 (2016).
12. Wang, F., Bai, S., Tress, W., Hagfeldt, A. & Gao, F. Defects engineering for high-performance perovskite solar cells. *Npj Flex. Electron.* **2**, 22 (2018).
13. Wang, Q. *et al.* Qualifying composition dependent p and n self-doping in CH3NH3PbI3. *Appl. Phys. Lett.* **105**, (2014).
14. Ming, W., Chen, S. & Du, M.-H. Chemical instability leads to unusual chemical-potential-independent defect formation and diffusion in perovskite solar cell material CH3NH3PbI3. *J. Mater. Chem. A* **4**, 16975–16981 (2016).
15. Agiorgousis, M. L., Sun, Y.-Y., Zeng, H. & Zhang, S. Strong Covalency-Induced Recombination Centers in Perovskite Solar Cell Material CH3NH3PbI3. *J. Am. Chem. Soc.* **136**, 14570–14575 (2014).
16. Eperon, G. E. *et al.* Formamidinium lead trihalide: a broadly tunable perovskite for efficient planar heterojunction solar cells. *Energy Environ. Sci.* **7**, 982–988 (2014).
17. Kojima, A., Teshima, K., Shirai, Y. & Miyasaka, T. Novel Photoelectrochemical Cell with Mesoscopic Electrodes Sensitized by Lead-halide Compounds (5). *Meet. Abstr.* **MA2007-02**, 352–352 (2007).

18. Kojima, A., Teshima, K., Shirai, Y. & Miyasaka, T. Organometal Halide Perovskites as Visible-Light Sensitizers for Photovoltaic Cells. *J. Am. Chem. Soc.* **131**, 6050–6051 (2009).
19. Im, J.-H., Lee, C.-R., Lee, J.-W., Park, S.-W. & Park, N.-G. 6.5% efficient perovskite quantum-dot-sensitized solar cell. *Nanoscale* **3**, 4088–4093 (2011).
20. Kim, H. S. *et al.* Lead Iodide Perovskite Sensitized All-Solid-State Submicron Thin Film Mesoscopic Solar Cell with Efficiency Exceeding 9%. *Sci. Rep.* **2**, 591 (2012).
21. Lee, M. M., Teuscher, J., Miyasaka, T., Murakami, T. N. & Snaith, H. J. Efficient Hybrid Solar Cells Based on Meso-Superstructured Organometal Halide Perovskites. *Science* **338**, 643–647 (2012).
22. Meng, L., You, J., Guo, T.-F. & Yang, Y. Recent Advances in the Inverted Planar Structure of Perovskite Solar Cells. *Acc. Chem. Res.* **49**, 155–165 (2016).
23. Song, Z. *et al.* Impact of Processing Temperature and Composition on the Formation of Methylammonium Lead Iodide Perovskites. *Chem. Mater.* **27**, 4612–4619 (2015).
24. Porter, D. *Phase Transformation in Metals and Alloys*. (Van Nostrand Reinhold, 1981).
25. Thanh, N. T. K., Maclean, N. & Mahiddine, S. Mechanisms of Nucleation and Growth of Nanoparticles in Solution. *Chem. Rev.* **114**, 7610–7630 (2014).
26. Ahn, N., Kang, S. M., Lee, J.-W., Choi, M. & Park, N.-G. Thermodynamic regulation of CH3NH3PbI3 crystal growth and its effect on photovoltaic performance of perovskite solar cells. *J. Mater. Chem. A* **3**, 19901–19906 (2015).
27. Niu, G., Guo, X. & Wang, L. Review of recent progress in chemical stability of perovskite solar cells. *J. Mater. Chem. A* (2015). doi:10.1039/C4TA04994B
28. Jeangros, Q. *et al.* In Situ TEM Analysis of Organic–Inorganic Metal-Halide Perovskite Solar Cells under Electrical Bias. *Nano Lett.* **16**, 7013–7018 (2016).

29. Shao, Y. *et al.* Grain boundary dominated ion migration in polycrystalline organic–inorganic halide perovskite films. *Energy Environ. Sci.* **9**, 1752–1759 (2016).
30. Wang, Q. *et al.* Scaling behavior of moisture-induced grain degradation in polycrystalline hybrid perovskite thin films. *Energy Environ. Sci.* **10**, 516–522 (2017).
31. Quan, L. N. *et al.* Ligand-Stabilized Reduced-Dimensionality Perovskites. *J. Am. Chem. Soc.* **138**, 2649–2655 (2016).
32. NREL 2019. *Res. Cell Effic. Rec. NREL Httpwwwnrelgovncpvimagesefficiencychartjpg* (2019).
33. Yang, M. *et al.* Do grain boundaries dominate non-radiative recombination in CH3NH3PbI3 perovskite thin films? *Phys. Chem. Chem. Phys.* **19**, 5043–5050 (2017).
34. Leblebici, S. Y. *et al.* Facet-dependent photovoltaic efficiency variations in single grains of hybrid halide perovskite. *Nat. Energy* **1**, 16093 (2016).
35. deQuilettes, D. W. *et al.* Impact of microstructure on local carrier lifetime in perovskite solar cells. *Science* **348**, 683–686 (2015).
36. Lee, J.-W. *et al.* The role of grain boundaries in perovskite solar cells. *Mater. Today Energy* **7**, 149–160 (2018).
37. Dong, Q. *et al.* Electron-hole diffusion lengths >175 μm in solution grown CH3NH3PbI3 single crystals. *Science* (2015).
38. Stranks, S. D. *et al.* Electron-Hole Diffusion Lengths Exceeding 1 Micrometer in an Organometal Trihalide Perovskite Absorber. *Science* **342**, 341–344 (2013).

Chapter 4. Guanidinium – the emergence of defect engineering

(This chapter is based on the published work: De Marco et. al. Nano Lett. 2016, 16, 1009−1016)

A major advantage of hybrid perovskite materials is the compositional flexibility within its crystal structure. So long as the charges of the ionic species are appropriate such that charge neutrality is conserved and the sizes of the components are appropriate to maintain 3D symmetry, in principle any ionic component may be used. The Goldschmidt Tolerance Factor is a valuable parameter that can predict deviation from cubic 3D symmetry in terms of size mismatch between constituents, which has important implications for the intrinsic stability of the crystal as well for defect formation energies. In this work, we pioneered the use of the guanidinium (GA) cation within the perovskite thin film to achieve extraordinarily enhanced charge carrier lifetimes by two orders of magnitude alongside increased open circuit voltages, which led to power conversion efficiency (PCE) improvements from 16% to over 17%. A reduction in defect emission energy over 30% was calculated via admittance spectroscopy, and confocal fluorescence intensity mapping provided further evidence of successful passivation of recombination/trap centers at grain boundaries. These improvements were attributed to a partial relaxation of lattice strain (octahedral tilting) that shifts the tolerance factor closer to unity, thereby increasing intrinsic crystal stability and reducing defect density. We speculate that GA lattice inclusion results in suppression of iodine defect formation, and GA not incorporated in the lattice likely lies at grain boundaries where it serves to passivate under-coordinated iodine species owed to its Lewis acid nature and 6-fold hydrogen bonding capability. Parts of this hypothesis were later confirmed separately by several groups.[1,2]

4.1 Motivation

The Goldschmidt Tolerance Factor (t) describes the relationship between crystal species necessary to achieve cubic symmetry and can be derived based on the geometrical relationship within the cubic structure. It is a very useful and important parameter that can be used to predict the degree of 3D cubic symmetry achieved through the combination of species used, where 3D hybrid perovskites form within the range of approximately $0.85 < t < 1.1$ (Figure 4-1a).[3] This degree of symmetry has been shown to have implications in terms of intrinsic crystal stability, where the enthalpy of formation (and Gibbs free energy) becomes lower (more stable) with increasing tolerance factor towards unity (Figure 4-1b), and also in terms of defect formation where the greater degree of strain within the lattice can increase point defect formation and thereby increase likelihood of reaction with external stimuli to degrade photovoltaic performance (Figure 4-1c).[4,5] Moreover, the A-site within the perovskite crystal lattice provides the greatest degree of flexibility in terms of selection because it does not contribute directly to the electronic structure of the material, but only indirectly by altering the strain within the lattice. Therefore, its selection criteria lie only in its size and valency to tune the tolerance factor without disturbing the Pb-I bonding nature that gives rise to the great optoelectronic properties of hybrid perovskites. Thus, tuning the tolerance factor by varying the A-site cation of hybrid perovskites demonstrates great potential to alleviate large bottlenecks on device performances and stability via defect mitigation.

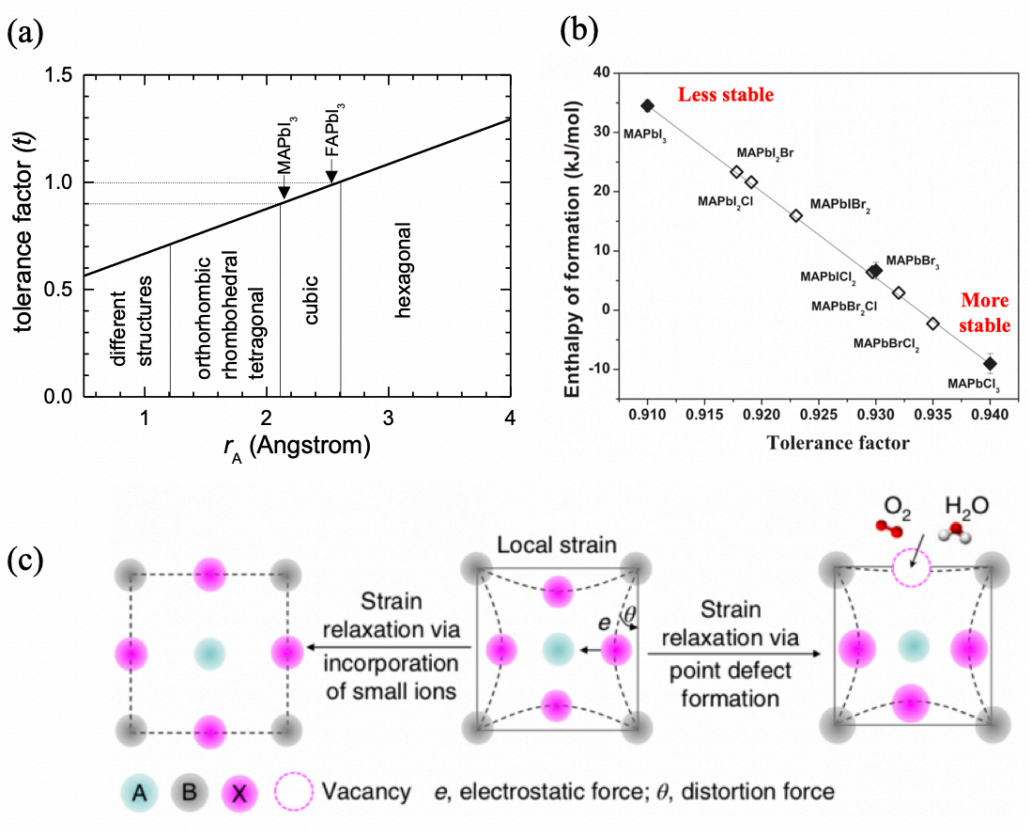

Figure 4-1: (a) tolerance factor versus A-site atomic radius and resulting crystal symmetry of perovskite structures. (b) relationship between enthalpy of formation and tolerance factor for hybrid perovskites. (c) lattice strain-defect formation relationship and implications.[4,5]

In addition, a high quality active layer of a solar cell device must efficiently generate and extract charge carriers to enable high performance solar devices. Initially it was thought that grain boundaries (GBs) did not contribute largely to recombination losses in hybrid perovskites, owed to the high defect tolerances observed and theoretical defect calculations that indicate relatively shallow and non-detrimental trap levels.[6,7,8,9] However, recent experimental evidence indicates that recombination centers exist at GBs and pose great limitations on reaching higher efficiencies

and long-term stability of perovskite materials.[10,11,12,13,14] To effectively mitigate non-radiative carrier losses requires suppression of recombination pathways within the perovskite active layer, namely, defects. Owed to their solution-processed nature, GBs inevitably exist for which under-coordinated ions may exist at their lattice terminations and surfaces of perovskites that can serve as charge carrier trap or recombination centers.[15,16] Therefore, one of the greatest knobs that can be used to fine-tune the optoelectronic quality of perovskite films lies within its compositional flexibility and the dynamic versatility of solution chemistry.

4.2 State-of-the-art and challenges

There have been several reports on attempts to vary the A-site cation of perovskites and observe changes in optoelectronic properties. MA and FA are the base A-site cations that make up the majority of the composition owed to their appropriate sizing and the high efficiencies seen through their use. At this time, the state-of-the-art efficiency was 20.1%, accomplished via use of DMSO solvent engineering in pure FA-based perovskite films.[17] However, other A-site cations have been employed as dopants to partially replace the MA or FA and induce strain within the lattice, thereby altering optoelectronic properties and stability of the perovskite films to achieve competitive performances. The most common is (partial) substitution with Cs, which has a relatively smaller size than MA and FA at 181 pm. Cs has shown to improve PCE and moisture-related stability for both MA and FA with an optimized amount of 10% Cs (mol %), which can be attributed to tuning of the tolerance factor.[18,19] Furthermore, ethylammonium (EA) has been another explored cation,[20] having only one extra -CH than MA with an effective radius of 274 pm and a tolerance factor of 1.030.[21] This is slightly over the 1.0 tolerance factor limit for 3-D

perovskite integration, and thus forms a 2-D dimensionality for pure EA use and is not expected to fit within the lattice to maintain 3-D symmetry. Incorporation of 0.5 vol% proved to improve performances, attributed these effects to suppressed crystallization of the perovskite film, as well as improved stability.[20] However, EA has been unable to achieve efficiencies competitive with the state-of-the-art compositions.

Similarly to EA, other species used in compositional engineering have shown to alter film formation mechanisms and thus the resulting quality of the perovskite films. For instance, chlorine (Cl) use has shown to modify grain growth processes and greatly enhance the surface coverage of perovskite films, leading to higher performances within the devices.[22,23] However, Cl has been shown to not directly substitute for I within the $MAPbI_3$ crystal structure. We have attributed its role to improving charge transport across the heterojunction interfaces, rather than between grains within the perovskite film.[24] In addition to geometrical and film formation effects, these cationic species can serve to suppress or passivate defects within the perovskite film. Passivation of under-coordinated species was demonstrated by several groups. For example, Abate and co-workers used an iodopentafluorobenzene (IPFB) post-treatment to successfully passivate under-coordinated iodine ions, while Noel et al. used the Lewis bases, thiophene and pyridine, to passivate under-coordinated Pb ions and achieve carrier lifetimes of perovskite films up to 2 μs.[15,16] Internal passivation methods have also been reported. For instance, Chen and collaborators demonstrated a self-induced passivation effect due to residual PbI_2 to serve as recombination barriers[25]. In addition, Br and Cl were suggested to preferentially locate at grain boundaries where they serve to assist in suppressing recombination and decoupling electron−hole pairs.[26,27] Thus, we can see that the selection of organic A-site cationic species are critical to achieving high performance perovskite solar cells in terms of tolerance,

film formation dynamics, and defect suppression and passivation effects. The challenge is to find a molecule that is able to carry out all these functionalities simultaneously.

4.3 Results and discussion

4.3.1 Investigation of A-site candidates

MA and FA are the major A-site cations utilized in hybrid perovskite materials, while other molecules have mostly been implemented in small quantities as dopants. At the time, various organic molecules with various atomic radii had been proposed as potential A-site candidates that had not yet been explored.[21] We surveyed several candidates based on their relative radius size compared to MA and revealed $CH_5N_3^+$, known as guanidinium (GA), as a promising candidate. GA had recently been revealed via computational studies to be promising for use in PVSK PV cells owed to its near zero dipole moment and was hypothesized to have a positive influence on bias-induced ionic motion and hysteresis effects seen in perovskite solar cells. However, the size of GA is much larger (278 pm) than the commonly employed MA (217 pm) or FA (253) cations, and ought to form a 2D PVSK structure as the sole A-cation.[28,28] Figure 4-2 shows a comparison of molecular structure, sizes, tolerance factors, and dipole moments of the MA and GA A-site organic cations.

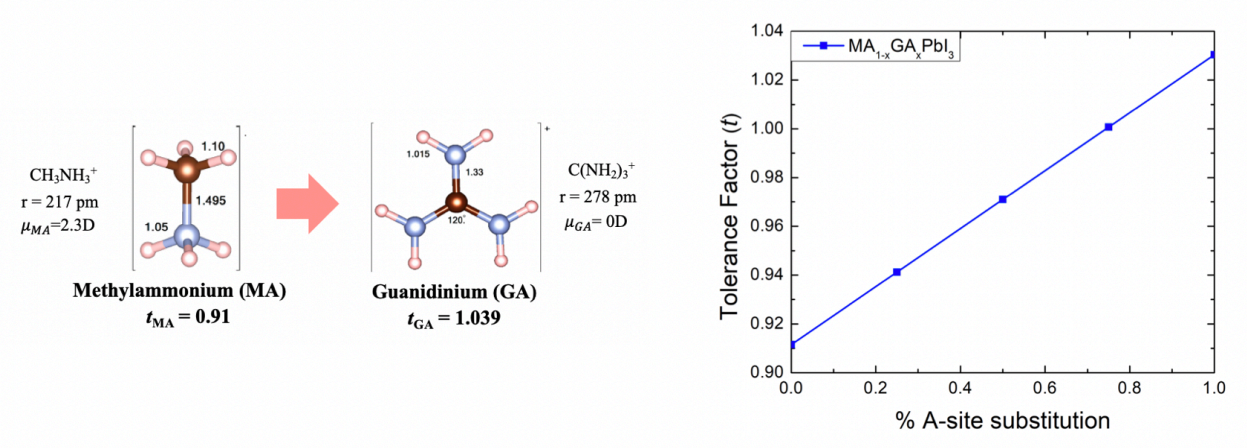

Figure 4-2: Strategy using guanidinium (GA) to partially replace methylammonium (MA) in the perovskite lattice, thereby tuning the tolerance factor towards unity.

Here we utilize $MAPbI_3$ due to its superior efficiencies at the time of this work. We can see that the tolerance factor for pure GA (100% A-site substitution) is slightly over unity, which means that it should not form 3-D $GAPbI_3$, but rather 2-D GA_2PbI_4, owed to the excessive strain exerted by the oversized molecule that breaks the 3-D symmetry. However, introducing GA in smaller quantities to partially substitute for MA is a plausible route to tune tolerance factor and create a more intrinsically stable structure and suppress defect formation.

4.3.2 Investigation of optical, structural, and morphological effects of GA incorporation

In order to test the effects of GA addition within the perovskite film, incremental amounts of GA were added to the perovskite solution processed via a two-step spin-casting approach, where the quantities of such addition are shown in the table of Figure 4-3a. A prominent reddish color change of the pre-annealed PVSK film and an increase in resulting film

transparency post-annealing was observed as shown in Figure 4-3a. A nominal stoichiometry (which is not precise due to the lack of stoichiometric control in the 2-step process) is given to quantify molar ratios of MA to GA in the precursor solution. It was found that around 33 mol% was the upper limit of GA incorporation for successful 3D PVSK formation indicated by a distinct yellow resultant film color. UV-Visible absorption spectroscopy was utilized to investigate the optical effects of GA inclusion. Figure 4-3b shows the absorption spectra for increasing GA content, from which an increase in GA content results in a decrease in light absorption. At the initial time of this study, our interpretation of the data indicated that GA did not directly substitute for MA. However, a subsequent deeper analyses of composition and finer XRD measurements shows that GA does partially substitute for MA within the crystal lattice. Due to the 2-step processing technique, it is hard to determine to what extent the incorporation was successful for each molar ratio. From the Tauc plots in the inset of Figure 4-3b, it is apparent that the band gap (E_g) shifts to higher energies in accordance with increased GA amounts, forming what appears to be mixed $MAPbI_3$ and either 1D or 2D GA phases in the intermediate ranges. However, with small GA incorporation approximately <15 mol%, the absorption characteristics and band gap can be preserved (Figure 4-3c,d). We found an optimal amount of GA incorporation to be 14 mol%, corresponding to $MA_{86}GA_{14}PbI_3$. Herein after I will refer to this optimized composition as 'GA' and compare it to the reference $MAPbI_3$ composition, labeled 'MA.' The extracted band gap for MA and GA were 1.56 eV and 1.55 eV, respectively. It was later confirmed by follow-up studies to this work that GA can successfully be incorporated into the PVSK crystal lattice and shows similar results.[29,30]

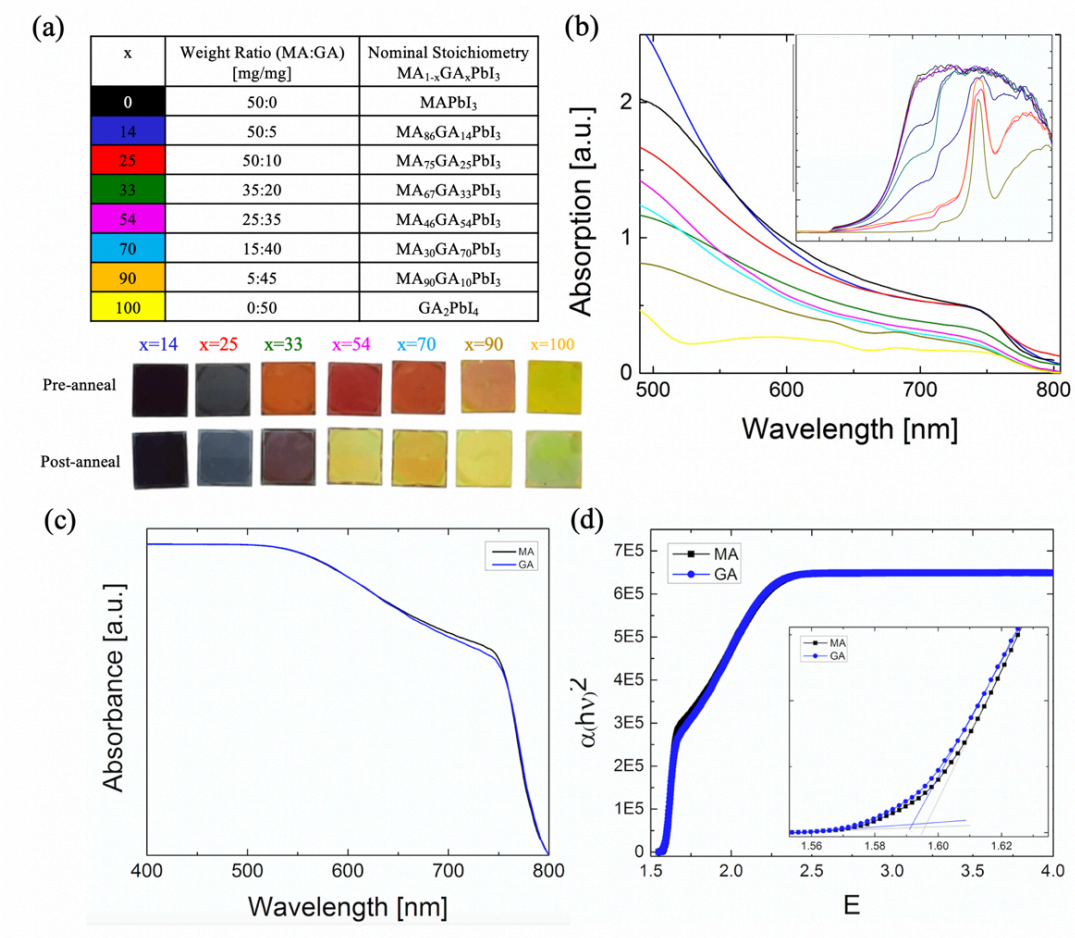

Figure 4-3: (a) Molar and weight ratios ranging from pure MA (Ref) to pure GA (Film 7) used in this study; (b) corresponding film colors for pre-annealed (top) and post-annealed (bottom) GA films; (c) absorption spectra for varying GA content with a log scale plot in the inset.

We further examined the XRD spectra for the MA and GA samples (Figure 4-4a). It appears at first observation that the spectra are unchanged in comparison to the reference MA film as there are no peak changes (with the exception of a small peak splitting around 43 degrees 2-theta that corresponds to formation of a cubic perovskite phase). We also see that the relative peak intensity is increased via GA incorporation, indicating that the crystallinity is enhanced through

use of GA. Upon closer inspection of the major tetragonal perovskite peaks, we can see that there is a peak shift to lower 2-theta values via GA inclusion (Figure 4-4b,c). This indicates a slight lattice expansion of the perovskite unit cell, which was confirmed after extracting the lattice parameters from the XRD spectra and calculating the volume of the tetragonal unit cell to be 901.45 $Å^3$ for GA and for 890.76 $Å^3$ for MA. To confirm the incorporation of GA into the film, fourier transform infrared spectroscopy (FTIR) was used to probe the molecular vibrations within the films (Figure 4-4d). Clear signature N-H and N=C stretching modes of the guanidinium molecule were observed between 3300-3500 cm^{-1} and at 1670 cm^{-1}, confirmed by several literature sources.[31,32] Thus, we can confirm that the guanidinium ion successfully incorporates into the tetragonal $MAPbI_3$ lattice for an optimized amount of 14 mol%. It is also to be noted that an increased amount of guanidinium results in disappearance of the characteristic (110) and (220) tetragonal perovskite peaks, and lower 2-theta peaks emerge that likely correspond to 1D or 2D guanidinim-based perovskites, which correlates with the absorption trends seen regarding band gap (see SI of publication for more information on XRD spectra).

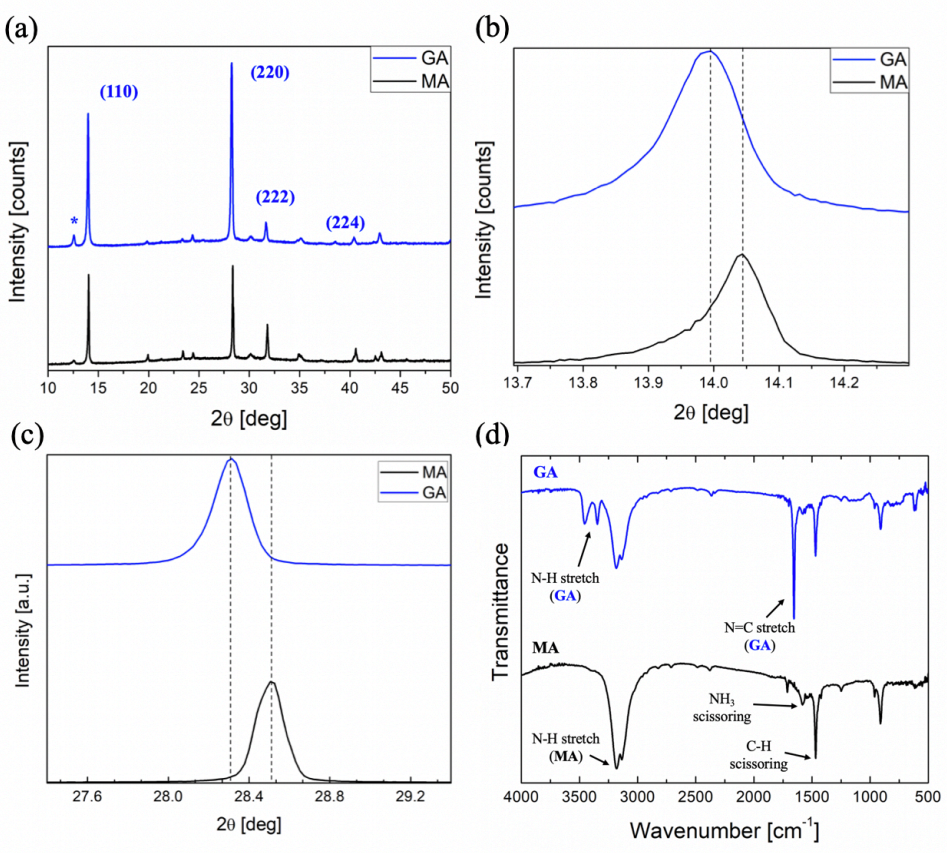

Figure 4-4: (a) XRD spectra for MA and GA films depicting preserved tetragonal structure of MA and enhanced crystallinity with GA incorporation. (b,c) peak shifts due to GA incorporation indicating lattice expansion. (d) FTIR spectra confirming GA inclusion within the film.

To correlate the observed XRD improvements in relative peak enhancement, Scanning Electron Microscopy was employed to observe the surface features of the MA and GA films. Here, not only the MA and GA films are shown, but a film also with more GA content (25 mol%). Figure 4-5 depicts these films with corresponding approximate stoichiometry, portraying a possible slight improvement in film continuity for the GA-based films as fewer grain protrusions and less prominent grain boundaries are apparent. The trend can be observed via both

magnifications to provide evidence that this feature is present on smaller and larger scales. However, these improvements (if any) are small and thus non-conclusive to correspond with XRD intensity increases. Moreover, FWHM values are similar for MA and GA films.

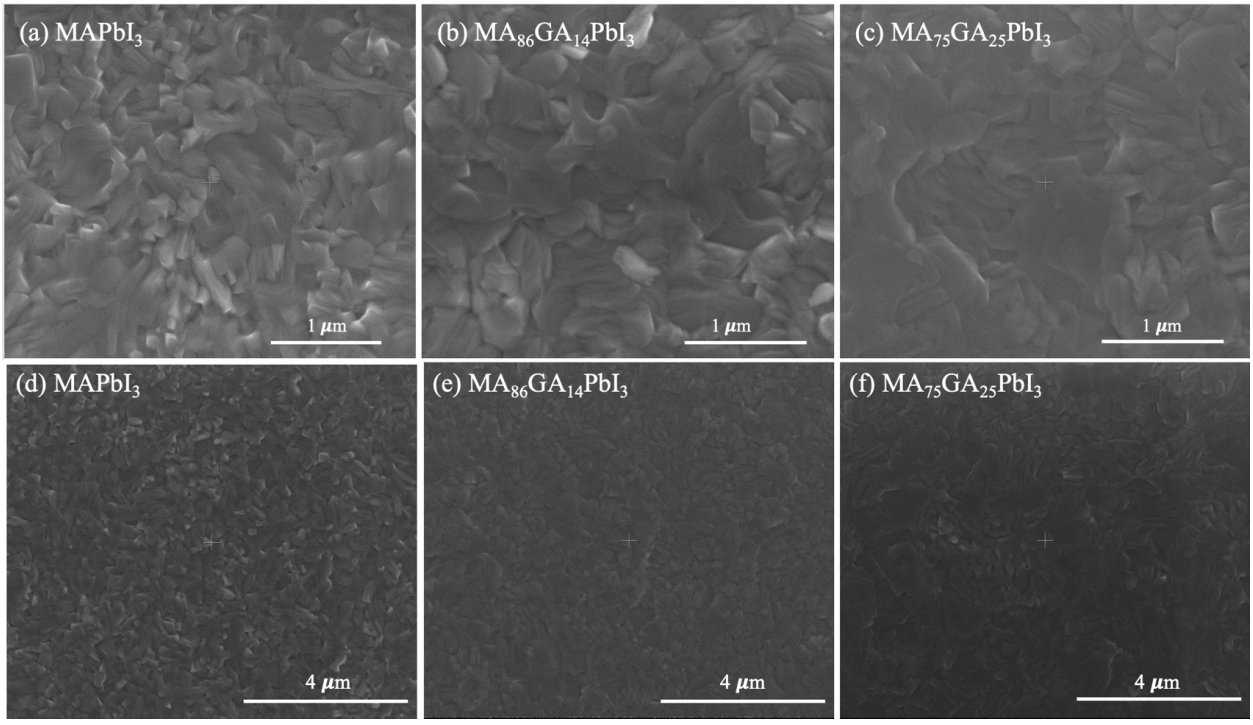

Figure 4-5: Scanning Electron Microscopy (SEM) of (a,d) $MAPbI_3$, (b,e) $MA_{86}GA_{14}PbI_3$, and (c,f) $MA_{75}GA_{25}PbI_3$ films, respectively. An improved morphology is observed yielding enhanced grain continuity via GA inclusion, correlating to enhanced crystallinity observed.

4.3.3 Photo-physical studies

PL spectroscopy was conducted to extract information regarding the charge carrier dynamics within the PVSK thin film. The carrier dynamics of $MAPbI_3$ films with and without GA were carefully examined through steady-state PL (SSPL) and time resolved PL (TRPL) measurements.

The results showed the best performance came from a small amount of GA addition (Film 1), as shown in Figure 4-6. The PVSK films for this measurement were prepared on glass substrates with an identical sequential two-step deposition technique as used for device fabrication. GA shows a large rise in SSPL intensity over four times that of the pure MA devices, as shown in Figure 4-6a. Even more intriguingly, the TRPL spectra shows a substantial enhancement in carrier lifetime (τ), superseding that of the reference by an order of magnitude. The curves display bi-exponential character and were fitted accordingly with both fast and long decay components, where the fast decay component represents charge carrier trapping and the long decay component (τ) can be described as free carrier recombination.[15] Figure 4-6b portrays an enhanced $\tau_{avg,GA}$ of 692 ns for the GA film compared to $\tau_{avg,MA}$=5.13 ns in the case of the MA reference. This substantial increase in τ_{GA} over two orders of magnitude (10^2) shows that charge carrier recombination is significantly suppressed, and suggests that trapping of carriers at defect states is greatly mitigated through use of GA. Interestingly, it was observed that additional GA amount reduces the PL intensity and carrier lifetime, indicating that exceeding the optimized 14 mol% ratio will begin to reverse the effects. This result is in accordance with the observed structural and morphological trends.

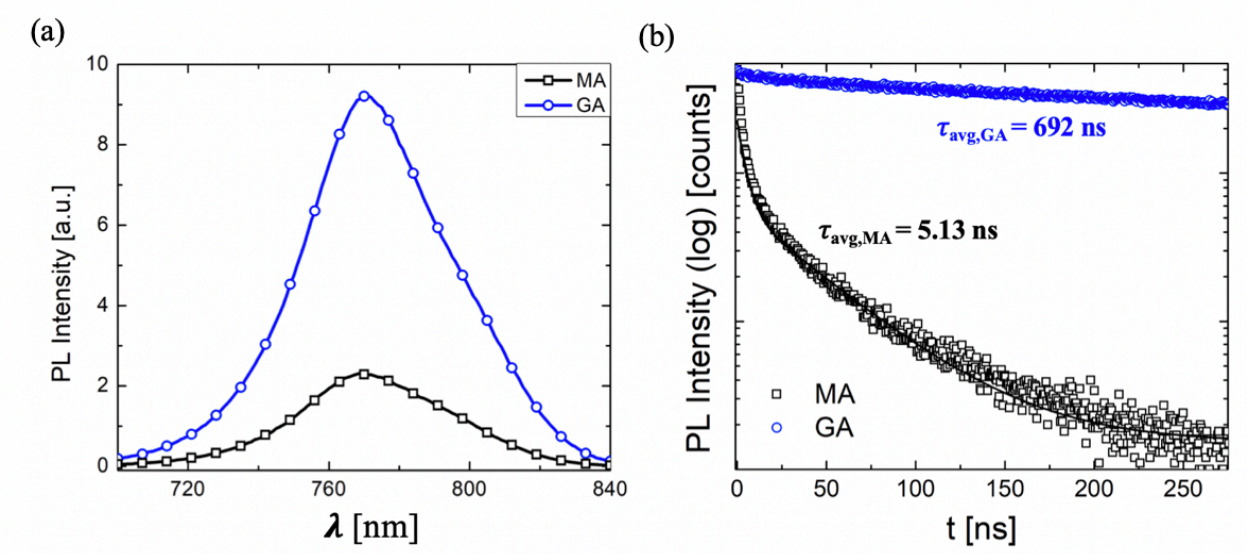

Figure 4-6: (a) Comparison of relative PL intensities and (b) TRPL spectra of pure MA and GA PVSK films deposited on glass substrates. GA shows an increased PL intensity over 4 times MA and an enhanced carrier lifetime two orders of magnitude over that of MA.

To gain insight into the enhancement of PL observed via use of GA, ultraviolet photoelectron spectroscopy (UPS) was used to identify the Fermi level (E_F) and VB edge positions of MA and GA thin films (Figure 4-7). In comparing the two spectra, there appears to a slight shift in E_F, with values located at approximately 4.59 eV and 4.54 eV for MA and GA, respectively, indicating an n-type nature of the PVSK film. A slight change in the VB energy level (E_{VB}) is observed, where the pure-MA reference device yielded an E_{VB} value of 5.95 eV in comparison to a slight shift to 5.75 eV for GA. However, UPS is a very sample-sensitive

technique, and thus these values are within the small ranges of error between samples. Thus, this Fermi level shift cannot be conclusive as a major factor for the improved performances.

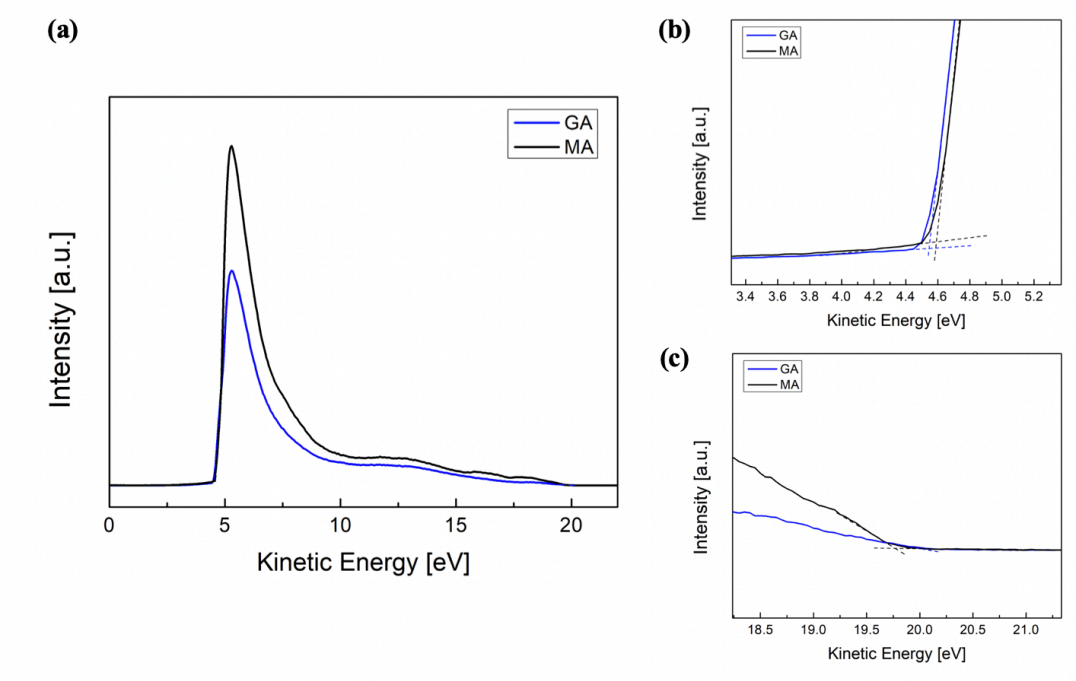

Figure 4-7: Ultraviolet photoelectron spectroscopy of MA and GA films. (a) full spectrum, (b) work function extraction from secondary electron cutoff, (c) VBM extraction.

4.3.4 Electronic measurements

To observe the effects of GA on device performance, current-voltage (J-V) measurements were employed for varying GA content with a planar device architecture of ITO/TiO_2/PVSK/Spiro-OMeTAD/Au. A prominent enhancement of V_{oc} through GA incorporation was observed, which is well correlated with the PL results. Figure 4-8a shows the J-V curve of the champion GA device in comparison to the reference (MA) sample,

demonstrating an enhancement of V_{oc} from 1.025 V in the standard MA-based device to 1.071 V for GA. Furthermore, a slight increase in fill factor (FF) from 75.00 to 75.31 for MA and GA was observed, respectively. The J_{sc} remained relatively unaffected with GA inclusion, achieving 21.24 mA/cm^2 compared to 21.27 mA/cm^2 for the pure MA device. The much improved V_{oc} and slightly increased FF led to an overall power conversion efficiency (PCE) gain of 17.13% compared to 16.35% for the MA reference device. The average device characteristics (Figure 4-8b) show the reproducibility of the observed performance enhancement for GA addition. We can see that GA provides an average increase in V_{oc} of approximately 50 mV, while preserving the J_{sc} and improving the FF from 74.87% to 76.04%. These improvements lead to a device performance average of 16.27% over the 15.75% PCE of its MA-based counterpart. As the GA content was increased over 25 mol% GA, a steady decrease in J_{sc} was observed. For higher molar ratios, a V_{oc} between 1.07-1.09 V was consistently achievable, where the maximum reached an impressive 1.112 V. However, the overall efficiencies of the higher V_{oc} devices were inferior to that of the champion device due a large sacrifice in the J_{sc} and FF. This decrease in J_{sc} is attributed to the decrease in absorption intensity resulting from further breaking of the 3-D symmetry and secondary phase formation due to increased GA content within the film.

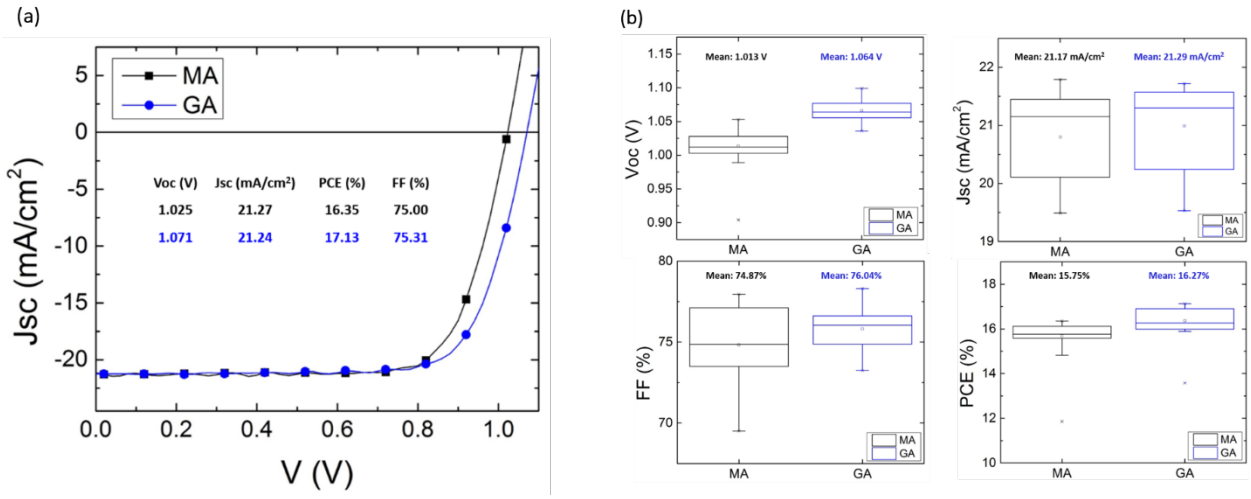

Figure 4-8: (a) Current-voltage characteristics of the champion GA and MA reference devices. The optimized GA device shows an improved V_{oc} and preserved FF and J_{sc} yielding an overall efficiency improvement, as depicted in the inset. (b) Device averages demonstrating the consistency of enhanced performance characteristics for GA addition.

To further probe the defect characteristics of GA-incorporated $MAPbI_3$ films, admittance spectroscopy was employed. Carrier recombination dynamics in solar devices are largely influenced by defects within the absorber material, and the TRPL results indicate that defects are the culprit here. Admittance spectroscopy provides a useful route to extract the energy levels of defects residing within semiconductor materials. In this technique, the capacitance is directly associated with the charging and discharging of trapped charge carriers within the material, as has been described in further detail in our previous report.[25] Occupancy of these trap sites depends on the location of the Fermi level, where traps below the Fermi level are assumed filled. Accordingly, by varying the AC voltage frequency and the temperature of the system we can probe these trap levels per Fermi level shift and extract information regarding the energy

required to de-trap the carrier from that trap state. A comparison of defect activation energies and densities determined from admittance spectroscopy measurements are provided in Figure 4-9. The activation energy of the MA-based device was calculated as 44.89 meV, which is in accordance with our previous report.[26] We can observe that the defect activation energy of the GA-based device is significantly lower (24.42 meV), indicating that recombination within the bulk of the film has been successfully suppressed. Furthermore, the trap densities are reduced for the GA device versus MA. Among the native point defects within PVSK, iodine vacancies have shown to be most detrimental for charge trapping and non-radiative recombination due to their deep lying energy levels.[34] It was suggested that chlorine inclusion can alter the lattice constant of PVSK and prevent formation of iodide vacancies, while chlorine has also proven to not remain in within the lattice upon solidification. GA may similarly affect the lattice constant during the solidification process thereby suppressing formation of deep iodide vacancies, as evidenced by the reduced defect activation energy.

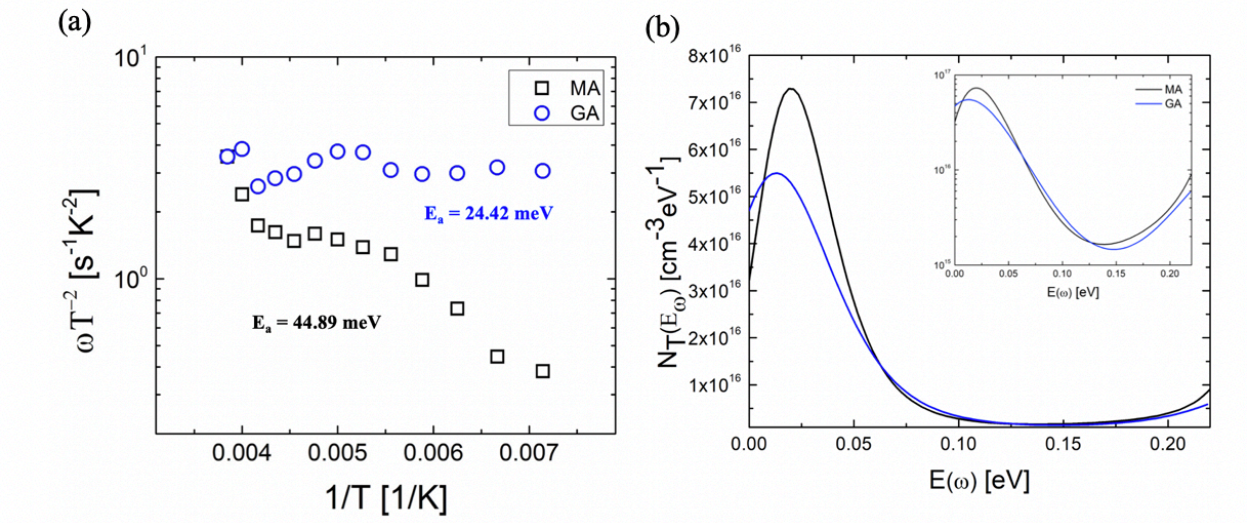

Figure 4-9: (a) Defect emission (activation) energies and (b) trap densities for the MA and GA devices extracted from thermal admittance spectroscopy. The lower de-trapping activation

energy and densities in the GA-based devices suggests successful suppression of trap-mediated recombination.

Suppressing the formation of defects evidenced by the data presented in this study results in reduced trap-mediated recombination within the films and devices, leading to the enhanced optoelectronic quality and photovoltaic performance seen. Strain relaxation via tolerance factor tuning is likely the major factor for these observed results based on the evidence here. However, such a drastic improvement is relatively unprecedented via solely tolerance factor tuning, and thus there is likely more at play here. As such, we also turn our attention to defect passivation. Passivation effects have also been seen with perovskite films that show similar enhancements in PL, V_{oc}, and PCE. For instance, passivation of under-coordinated iodine species has been demonstrated via post-film formation treatments using the IPFB Lewis acid.[15] As a free cation, GA is a Lewis acid owed to the difference in covalent character between the central C atom and surrounding nitrogen. The C-N partial charge difference for GA within the solid state PVSK film has shown greater than for the free GA cation according to recent theoretical studies.[28] In fact, the unique hydrogen bonding capability of GA has been previously demonstrated in metal-organic frameworks (MOFs).[35] The symmetry of the amine groups allows the GA molecule to form six hydrogen bonds with neighboring octahedra of the MOF, which enhanced its mechanical stability. Hence, we expect an increased quantity of hydrogen bonding capability between the partial negative (δ^-) iodine ions of exposed PbI_6^{4-} of neighboring PVSK crystals and the partial positive (δ^+) ammonium ions of the organic GA species. In a similar manner, Li *et al.* utilized a phosphonic acid ammonium additive to induce a strong crosslinking hydrogen bonding between halide anions of neighboring grains within the PVSK crystal.[36] Here, both the

ammonium and phosphonic terminal groups can effectively bind to the surface of PVSK, creating a strong crosslinking between adjacent grains that provides a smother morphology and better cohesion that led to enhanced performance and stability. Along these lines, we propose that any remaining GA that does not incorporate within the crystal structure (which is probable given the 2-step nature of deposition) preferentially resides at grain boundaries and can form hydrogen bonds with under-coordinated iodine species to effectively suppress associated defect states and non-radiative recombination pathways. However, a crosslinking effect from GA is unlikely as for the phosphonic acid ammonium crosslinking agents, since the GA molecule is significantly smaller and could only provide such crosslinking effects if the grains are very close to one another. We thus conclude the major role of GA is to tune the tolerance factor to increase intrinsic structural stability and suppress defect formation, accompanied by a minor role in passivation of under-coordinated iodide species at grain boundaries and surfaces and that incorporation of the passivant GA molecule directly into the precursor solution, as opposed to merely a surface treatment, may allow for suppression of defect formation throughout the film growth process, which would otherwise be inaccessible through post-film formation surface treatments. This may explain the exceptional carrier lifetime characteristics observed.

4.3.5 Impacts of GA on stability

The stability for the GA-based device was compared to the standard MA-based reference device (Figure 4-10). The devices were stored under a dry oxygen environment for and only exposed to ambient environment during measurement. We can see that initially both devices are relatively stable, whereas both devices later undergo a rapid decrease of the initial PCE.

Interestingly, the rate of PCE drop for the pure MA-based device is much higher than that of the device with GA inclusion, where the GA device maintains over 80% of its initial PCE compared to approximately 60% for the pure MA device over the time period. We can define the T80 lifetime (which is the current standard for measuring stability in the field) as the time at which the PCE decays to 80% of its initial PCE. In comparing GA to MA, we see that the GA film has a T80 lifetime of 286 hours compared to 198 hours for the MA device. The enhanced stability could be explained by the following: the strain-relaxed crystal structure of the GA composition reduces the defect density within the material and can possibly enhance the crystallinity of the GA film that can allow for enhanced cohesion of neighboring PVSK grains, thereby providing a smoother and more continuous grains, as evidenced by XRD spectra and SEM images. As grain boundaries are highly susceptible to invasion by water molecules, the less vulnerable grain boundaries would mitigate the effects of attacking water molecules. Since the water molecules will primarily attack the more susceptible grain boundary regions, the GA ions located in these regions can passivate defect locations and prevent these defects from reacting with the incoming water molecules, since dangling bonds or under-coordinated species located at defect sites are more reactive sites. This would preserve the crystalline PVSK domains for longer than films without GA present, showing a similar decay trend to that of MA but at a different rate.

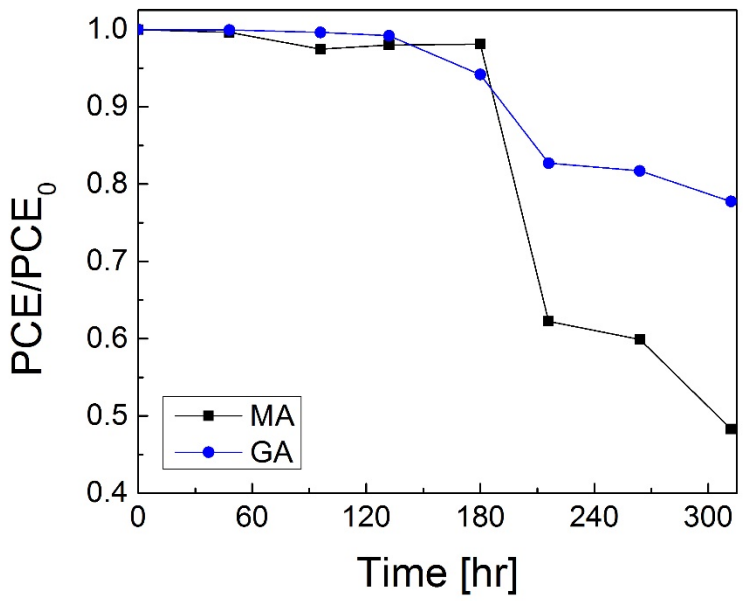

Figure 4-10: Normalized device PCE versus time for MA and GA devices. After approximately 180 hours both devices begin to rapidly decay in performance, however GA shows a slightly improved PCE retention compared to MA.

4.4 Summary

In this work the have pioneered the guanidinium ion as a route to suppress defects in $MAPbI_3$ thin films, leading to extraordinarily enhanced carrier lifetimes and open circuit voltages. Charge carrier dynamics were explored using time-resolved photoluminescence and photovoltage decay techniques, demonstrating an unprecedented improvement in carrier lifetime for GA-based films one two orders of magnitude larger than the pure MA films that led to an average open circuit voltage increase of 50 mV. A reduced defect activation energy measured by admittance spectroscopy indicates successful suppression and/or passivation of non-radiative recombination/trap centers within the $MAPbI_3$ film. We initially proposed that the large

hydrogen bonding capability of the GA molecule allowed for effective passivation of under-coordinated iodine species located at grain boundaries and surfaces and improved film quality by modifying the growth dynamics and associated defect formation energies and levels. We later re-analyzed the role of GA and found its effects to be attributed to a strain relaxation effect, using the tolerance factor as a guideline to predict crystal stability. Due to the degree of carrier lifetime increase observed through TRPL, we further speculate that GA could serve to passivate defect sites at grain boundaries for those species that are inevitably unincorporated in the bulk lattice. After this work it was discovered that the organic A-site cation plays a critical role in carrier lifetimes observed owed to its polar nature and ability to reorient it in response to a photo-generated carriers on the picosecond timescale, forming a large polaron that can enable charge carrier screening effects.[37,38,39] For GA in particular, it was shown through NMR spectroscopy that GA reorients an order of magnitude faster than MA and achieves 10^2 increase in carrier lifetime, which correlates to the results of our work.[29] Thus, there may be multiple factors that give rise to the extraordinary carrier lifetimes observed via use of guanidinium in hybrid perovskites. Further work should be done to decouple these mechanisms and truly understand how guanidinium can be utilized to construct high optoelectronic quality and stable perovskite materials and devices. This study represented the beginning of future studies relating to control of film formation, grain boundaries and associated defects, and passivation.

4.5 Experimental

4.5.1 Perovskite Solar Cell Fabrication:

Methylammonium iodide (CH_3NH_3I, MAI) and methylammonium chloride (CH_3NH_3Cl, MACl) were synthesized according to methods described elsewhere. Guanidinium iodide (CH_6N_3I, GAI) and guanidine hydrochloride (CH_6N_3Cl, GACl) were purchased from Dyesol and Sigma Aldrich, respectively. Titanium dioxide (TiO_2) was synthesized via a non-hydrolytic sol-gel approach. Glass and ITO substrates were prepared by sequential washing with acetone, detergent, deionized water, and 2-propanol. A solution containing TiO_2 nanoparticles and a titanium diisopropoxide bis(acetylacetonate) (Ti-AcAc) stabilizing agent was spin-coated onto the substrate at 3000 RPM for 30 seconds and annealed in ambient environment at 150 ºC for 30 minutes. After cooling, a solution of PbI_2 (Sigma) in dimethylformamide (DMF) at a concentration of 450 mg-mL^{-1} was spin-coated onto the ITO/TiO_2 substrate at 3000 RPM for 30 seconds and annealed at 70 ºC for 15 minutes. A solution consisting a mixture of 50 mg/mL MAI and appropriate quantities of the additive (e.g. MACl, GAI, GACl, etc) dissolved in 2-propanol was spin-coated onto the PbI_2 layer and subsequently annealed at 135 ºC for 15 min in ambient air. After allowing the films to cool, a 90 mg-mL^{-1} solution of spiro-OMeTAD in chlorobenzene with the addition of 45 μL Li-TFSI/acetonitrile (170 mg-mL^{-1}) and 10uL tBP was spin-coated on top of the perovskite film at 3000 rpm RPM for 30 seconds. Lastly, a 100 nm layer of gold was thermally evaporated as the counter electrode with an active area of 0.108 cm^2.

4.5.2 Solar Cell and Thin Film Characterization

Current-Density (J-V) Measurements:

J-V curves were measured using a Keithley 2401 source unit measured under standard AM1.5G illumination (100 mW/cm^2) provided by an Oriel Sol3A solar simulator. The light intensity was calibrated using a KG-5 filter diode as a reference cell. Reverse (1.2 V→-0.1 V) or forward (-0.1 V→1.2 V) scans with a step size of 20 mV and delay time of 0.2s were used to obtain the J-V curves for an active area of 0.10 cm^2. Differential light intensity response measurements utilized neutral density filters and aperture sizes to tune the light intensity, and a Si-diode was used to calibrate the light intensity.

X-Ray Diffraction Analysis:

θ-2θ scans were obtained using a Bruker D8 Discover Powder X-Ray Diffractometer equipped with a push plug gobel mirror and a monochromatic CuKα (λ = 1.5405 Å) radiation source.

Photoluminescence (PL) and Time Resolved Photoluminescence (TRPL) Measurements:

A Horiba Jobin Yvon system with a red light source with an excitation at 640 nm was used to conduct PL measurements. TRPL spectra was obtained using a Picoharp 300 with time-correlated single-photon counting capabilities. A picosecond diode laser provided excitation at a wavelength of 640 nm with a repetition frequency of 1 MHz (PDL 800B).

Scanning Electron Microscopy (SEM):

An emission Nova 230 NanoSEM was used to obtain SEM images with an electron beam acceleration in the range of 500V to 30 kV.

Admittance Spectroscopy:

A Hewlett-Packard 4284A LCR Meter was used to conduct capacitance-voltage and capacitance-frequency measurements. A Janis cryogenic probe station with an attached Lakeshore 331 temperature controller with a thermocouple placed in contact with the sample were used as the electrical contacts and temperature control for this measurement.

4.6 References

1. Kanno, S., Imamura, Y. & Hada, M. First-Principles Calculations of the Rotational Motion and Hydrogen Bond Capability of Large Organic Cations in Hybrid Perovskites. *J. Phys. Chem. C* **122**, 15966–15972 (2018).
2. Deng, Z., Kieslich, G., Bristowe, P. D., Cheetham, A. K. & Sun, S. Octahedral connectivity and its role in determining the phase stabilities and electronic structures of low-dimensional, perovskite-related iodoplumbates. *APL Mater.* **6**, 114202 (2018).
3. Chen, Q. *et al.* Under the spotlight: The organic–inorganic hybrid halide perovskite for optoelectronic applications. *Nano Today* **10**, 355–396 (6).

4. Nagabhushana, G. P., Shivaramaiah, R. & Navrotsky, A. Direct calorimetric verification of thermodynamic instability of lead halide hybrid perovskites. *Proc. Natl. Acad. Sci.* **113**, 7717–7721 (2016).
5. Saidaminov, M. I. *et al.* Suppression of atomic vacancies via incorporation of isovalent small ions to increase the stability of halide perovskite solar cells in ambient air. *Nat. Energy* **3**, 648 (2018).
6. Kojima, A., Teshima, K., Shirai, Y. & Miyasaka, T. Organometal Halide Perovskites as Visible-Light Sensitizers for Photovoltaic Cells. *J. Am. Chem. Soc.* **131**, 6050–6051 (2009).
7. Burschka, J. *et al.* Sequential deposition as a route to high-performance perovskite-sensitized solar cells. *Nature* **499**, 316–319 (2013).
8. Etgar, L. *et al.* Mesoscopic CH3NH3PbI3/TiO2 Heterojunction Solar Cells. *J. Am. Chem. Soc.* **134**, 17396–17399 (2012).
9. Lotsch, B. V. New Light on an Old Story: Perovskites Go Solar. *Angew. Chem. Int. Ed.* **53**, 635–637 (2014).
10. Yin, W.-J., Shi, T. & Yan, Y. Unusual defect physics in CH3NH3PbI3 perovskite solar cell absorber. *Appl. Phys. Lett.* **104**, 063903 (2014).
11. Kim, J., Lee, S.-H., Lee, J. H. & Hong, K.-H. The Role of Intrinsic Defects in Methylammonium Lead Iodide Perovskite. *J. Phys. Chem. Lett.* **5**, 1312–1317 (2014).
12. deQuilettes, D. W. *et al.* Impact of microstructure on local carrier lifetime in perovskite solar cells. *Science* **348**, 683–686 (2015).
13. Agiorgousis, M. L., Sun, Y.-Y., Zeng, H. & Zhang, S. Strong Covalency-Induced Recombination Centers in Perovskite Solar Cell Material CH3NH3PbI3. *J. Am. Chem. Soc.* **136**, 14570–14575 (2014).

14. Kutes, Y. *et al.* Mapping the Photoresponse of CH3NH3PbI3 Hybrid Perovskite Thin Films at the Nanoscale. *Nano Lett.* **16**, 3434–3441 (2016).
15. Abate, A. *et al.* Supramolecular halogen bond passivation of organic-inorganic halide perovskite solar cells. *Nano Lett* **14**, 3247–54 (2014).
16. Noel, N. K. *et al.* Enhanced Photoluminescence and Solar Cell Performance via Lewis Base Passivation of Organic–Inorganic Lead Halide Perovskites. *ACS Nano* **8**, 9815–9821 (2014).
17. Yang, W. S. *et al.* High-performance photovoltaic perovskite layers fabricated through intramolecular exchange. *Science* (2015).
18. Lee, J.-W. *et al.* Formamidinium and Cesium Hybridization for Photo- and Moisture-Stable Perovskite Solar Cell. *Adv. Energy Mater.* **5**, n/a-n/a (2015).
19. Choi, H. *et al.* Cesium-doped methylammonium lead iodide perovskite light absorber for hybrid solar cells. *Nano Energy* doi:10.1016/j.nanoen.2014.04.017
20. Hsu, H.-L. *et al.* High-performance and high-durability perovskite photovoltaic devices prepared using ethylammonium iodide as an additive. *J. Mater. Chem. A* **3**, 9271–9277 (2015).
21. Kieslich, G., Sun, S. & Cheetham, A. K. Solid-state principles applied to organic-inorganic perovskites: new tricks for an old dog. *Chem. Sci.* **5**, 4712–4715 (2014).
22. You, J. *et al.* Low-Temperature Solution-Processed Perovskite Solar Cells with High Efficiency and Flexibility. *ACS Nano* **8**, 1674–1680 (2014).
23. Zhou, H. *et al.* Interface engineering of highly efficient perovskite solar cells. *Science* **345**, 542–546 (2014).
24. Chen, Q. *et al.* The optoelectronic role of chlorine in CH3NH3PbI3(Cl)-based perovskite solar cells. *Nat Commun* **6**, (2015).

25. Chen, Q. *et al.* Controllable Self-Induced Passivation of Hybrid Lead Iodide Perovskites toward High Performance Solar Cells. *Nano Lett.* **14**, 4158–4163 (2014).
26. Yin, W.-J., Chen, H., Shi, T., Wei, S.-H. & Yan, Y. Origin of High Electronic Quality in Structurally Disordered CH3NH3PbI3 and the Passivation Effect of Cl and O at Grain Boundaries. *Adv. Electron. Mater.* **1**, n/a-n/a (2015).
27. Kim, G. Y. *et al.* Efficient Carrier Separation and Intriguing Switching of Bound Charges in Inorganic–Organic Lead Halide Solar Cells. *J. Phys. Chem. Lett.* **6**, 2355–2362 (2015).
28. Giacomo, G. & Koichi, Y. Zero-dipole molecular organic cations in mixed organic–inorganic halide perovskites: possible chemical solution for the reported anomalous hysteresis in the current–voltage curve measurements. *Nanotechnology* **26**, 442001 (2015).
29. Kubicki, D. J. *et al.* Formation of Stable Mixed Guanidinium–Methylammonium Phases with Exceptionally Long Carrier Lifetimes for High-Efficiency Lead Iodide-Based Perovskite Photovoltaics. *J. Am. Chem. Soc.* **140**, 3345–3351 (2018).
30. He, J., Fang, W.-H., Long, R. & Prezhdo, O. V. Increased Lattice Stiffness Suppresses Nonradiative Charge Recombination in MAPbI3 Doped with Larger Cations: Time-Domain Ab Initio Analysis. *ACS Energy Lett.* **3**, 2070–2076 (2018).
31. Drozd, M. Molecular structure and infrared spectra of guanidinium cation: A combined theoretical and spectroscopic study. *Mater. Sci. Eng. B* **136**, 20–28 (2007).
32. Xue, B. *et al.* Retardation of Trap-Assisted Recombination in Lead Halide Perovskite Solar Cells by a Dimethylbiguanide Anchor Layer. *Chem. – Eur. J.* **25**, 1076–1082 (2019).
33. Stranks, S. D. *et al.* Electron-Hole Diffusion Lengths Exceeding 1 Micrometer in an Organometal Trihalide Perovskite Absorber. *Science* **342**, 341–344 (2013).

34. Du, M. H. Efficient carrier transport in halide perovskites: theoretical perspectives. *J. Mater. Chem. A* **2**, 9091–9098 (2014).
35. Li, W. *et al.* Mechanical Tunability via Hydrogen Bonding in Metal–Organic Frameworks with the Perovskite Architecture. *J. Am. Chem. Soc.* **136**, 7801–7804 (2014).
36. Li, X. *et al.* Improved performance and stability of perovskite solar cells by crystal crosslinking with alkylphosphonic acid ω-ammonium chlorides. *Nat Chem* **7**, 703–711 (2015).
37. Zhu, X.-Y. & Podzorov, V. Charge Carriers in Hybrid Organic–Inorganic Lead Halide Perovskites Might Be Protected as Large Polarons. *J. Phys. Chem. Lett.* **6**, 4758–4761 (2015).
38. Miyata, K., Atallah, T. L. & Zhu, X.-Y. Lead halide perovskites: Crystal-liquid duality, phonon glass electron crystals, and large polaron formation. *Sci. Adv.* **3**, e1701469 (2017).
39. Gong, J. *et al.* Electron–Rotor Interaction in Organic–Inorganic Lead Iodide Perovskites Discovered by Isotope Effects. *J. Phys. Chem. Lett.* **7**, 2879–2887 (2016).

Chapter 5. Lewis acid-base adduct method to control crystal growth

(This chapter is based on the published work: *Chem*. 3, 2017, 290-302)

Results seen through use of guanidinium-based precursors opened the door to numerous scientific questions to be answered and the possibility of further enhancement of perovskite thin film optoelectronic quality. In this light, we sought to explore the underlying solution and solid-state chemistry during casting and crystallization processes to better understand the mechanisms by which thin film growth occurs and how enable further control. This work systematically explored the properties of Lewis-bases by substituting single functional groups compared to conventional precursor solvents to further understand the connection between Lewis-base adduct formation and resulting perovskite thin film optoelectronic quality. Our results revealed the Lewis-base additive urea to most effectively improve optoelectronic quality of perovskite thin films, achieving a significant enhancement of macroscopic photoluminescence charge carrier lifetime from 200 ns of the base perovskite film to 752 ns with 4 mol % urea addition and an improvement in device performance from 17.34% to 18.55%.[1] These effects were attributed to an effective mitigation of trap-mediated non-radiative recombination resulting from an observed retardation of crystal growth kinetics, attributed to the strong Lewis acid-base adduct formed between urea and perovskite precursors. A stronger interaction delays the crystallization process, thereby increasing the quality and sizes of individual crystal grains, evidenced by a reduced bulk defect density and increased photoluminescence properties. The non-volatile urea Lewis base was found to precipitate at grain boundaries and serve as a passivating agent for grain boundary defects, in a similar manner to guanidinium.

5.1 Motivation

Although macroscopic properties of perovskite thin films have proven superior to many other photovoltaic materials, it was shown that heterogeneity at the microscale indeed exists and contributes to loss in optoelectronic quality.[2,3] Initially, it was thought that grain boundaries were relatively benign, owed to the high performances achieved for hybrid perovskites, where the origin of such was said to be due to defects (structural disorders) at both grain boundaries and interiors that induce shallow trap states where charge carriers can localize and undergo non-radiative recombination processes.[1,2,4,5] Moreover, the defect density of grain interiors has been shown to be dependent on crystal facet orientation, resulting in facet-dependent photovoltaic performance within a single grain.[3] Therefore, the ability to control solution-based crystallization is crucial in addressing the performance and stability implications imposed by grain boundaries, facets, and associated defects during growth processes. In addressing these challenges of microscopic heterogeneity in perovskite thin films, improved optoelectronic quality and film stability can be realized.

5.2 State-of-the-art and challenges

There have been several methods to control solution chemistry and crystal growth processes of hybrid perovskite thin films, where the majority of this control comes from the use of precursor composition, solvent, and additive choice. Early on, it was shown by Liang *et al.* that the crystallization rate can be controlled through introduction of a 1,8-diiodooctane additive.[6] This Lewis base was said to temporarily chelate with Pb^{2+} (a Lewis acid), thereby

increasing the internal energy and entropy of the system to promote homogeneous nucleation and modify crystallization kinetics. Similarly, Wei and company utilized the precursor additive 1-chloronphthalene to regulate the crystallization kinetics.[7] More recently, Li and company have shown that use of acetonitrile as a solvent additive instead of DMSO can achieve similar effects using a two-step deposition technique, where the PbI_2 scaffold layer grown using acetonitrile as a solvent additive achieved higher crystallinity and resulted in higher quality perovskite thin films upon conversion (with MAI) due to slower reaction kinetics.[8] These results highlight that the choice of solvent and additive for each specific perovskite composition is critical in order to improve film formation and crystallization processes. In fact, even using a slightly off-stoichiometry between the perovskite precursors, such as excess methylammonium iodide/chloride (MAI/MACl), or excess lead iodide (PbI_2), have been reported to show improvements in film quality and resulting optoelectronic performance of perovskite films.[9,10] However, the underlying mechanisms remain elusive must be better understood in order to provide guidelines to pursue growth of higher quality perovskite thin films.

More recently, Choi group has shed light onto a simple selection process of chemical additives based on the Mayer Bond Order (MBO), which is related to the strongest bond unsaturation. Their computational studies revealed that the chemical tetrahydrothiophene 1-oxide (THTO) was a strong candidate to control crystallization kinetics.[11] The simulation results showed THTO to have a strong interaction with Pb^{2+}, which they claimed to significantly delay crystallization and suppress formation of intermediate structures and homogeneous nucleation. As a result, heterogeneous nucleation at the interface was promoted and a slow growth rate along a preferred (100) plane occurred. Moreover, they claimed (via DFT studies) that this could be achieved because THTO could alter the surface energy of specific perovskite crystal orientations.

However, no concrete mechanism was unveiled nor guidelines for future work to build upon with chemical additives towards improving device performance.

The solubility of perovskites is also an important factor to consider in terms of precursor chemistry. Hybrid perovskites demonstrate the unique property of retrograde (or inverse temperature) solubility, where the solubility typically decreases with increasing temperature as opposed to most salts where solubility increases with increases temperature, thus requiring undercooling to reach supersaturation. The solubility of each different perovskite precursor species is dependent on the particular solvent used. Interestingly, this only occurs when the precursor species are all mixed into one solution, whereas the individual perovskite precursors (e.g. MAX and PbX_2) do not display this phenomenon (precipitation upon heating) and appear to follow the conventional solubility trend. This implies that the phenomenon is linked to the perovskite structure, and hints to the likelihood that intermediate complexes exist within the precursor solution. A proposed mechanism for this phenomenon has been provided by Saidaminov et al.[12]

Along these lines, further insight into the precursor chemistry leading up to nucleation has recently been shown by Nayak et al. through single crystal studies.[13] It was shown that perovskite precursors solutions contain colloidal Pb-based species and are thus not real solutions. These colloids are believed to be the seeds that initiate nucleation and subsequent growth of the perovskite film from solution, which can be influenced by acidic species that can arise from decomposed solvents. DMF can decompose into dimethylamine and formic acid, which they prove to be an important component to nucleation with the colloidal Pb species by adding excess MAI precursor and formic acid. The important take away from this study is that the choice of

solvent or chemical additive and its potential acidity influences on the solution are important considerations in the selection process that require further study.

Furthermore, Niu et al. have demonstrated that nucleation is dependent on perovskite composition for thin films by showing that cesium-based perovskites precipitate and serve as heterogeneous nucleation sites that affect the overall growth dynamics and orientation.[14] This highlights the importance in considering the specific solubility of the precursor components in a given solvent. This is also the case for use of chloride-based perovskite precursors, which have shown improved film formation and resulting optoelectronic properties. Tidhar and company showed that poor solubility of $PbCl_2$ results in facile formation of precipitates that serve as nucleation sites, or "seeds," that control the growth orientation and rate. Huang group showed that depositing multiple layers of methylammonium chloride onto the as-fabricated methylammonium iodide perovskite film (cycling) promotes a (220) preferential growth. Their studies reveal that Cl causes intermediate phase formation that slows crystallization kinetics of $MAPbI_3$. Quick formation of $MAPbI_3$ is expected to form randomly oriented grains because of the fast kinetics and thus random nature of the nucleation process. Slowed crystallization, on the other hand, allows for the nuclei to adjust orientation for more controlled growth along orientations that minimize the total Gibbs free energy.[15]

Single crystal and shape evolution studies are important for observing and understanding growth mechanisms of materials under controlled environments. Hou et al. have demonstrated controlled growth orientations in oxide-based perovskites using additives in hydrothermal methods. In one study, urea was used as the additive, which decomposed to ammonium within the hydrothermal environment. The concentration of ammonium was found to control the shape evolution of the single crystals by preferentially binding to the (110) facets, thus slowing the

growth rate. While this is for oxide-based perovskites and using hydrothermal methods, the principles are relevant for this work.[16,17] In terms of growth along preferred orientations in hybrid perovskites, Zhu and co-workers showed preferential growth of $MAPbI_3$ by mixing the perovskite precursors in a polar solvent (acetonitrile) and "crashing" with a much less polar solvent (toluene). This technique effectively induced growth along a preferred orientation (acetonitrile), followed by subsequent precipitation (toluene).[18] Similar effects were seen using large organic cations such as n-octylammonium and 1,3,-pentanediammonium. With optimal additive/precursor concentrations and rate of addition allowed for control of aspect ratios from bulk nanowires to nanosheets or nanoplates. This work highlights that both the rate of dissolution, concentration of precursors, and use of additives can be used to control the growth kinetics and resulting structure/orientation of perovskite crystals.

Passivation is also a critical component to achieving high performance photovoltaic devices. In fact, it was not until the introduction of the amorphous hydrogenated silicon layer to passivate the crystalline silicon layer that silicon-based photovoltaic cells were able to achieve the higher efficiencies seen today. We have seen that as a result of the solution-processed nature of perovskite, under-coordinated ions may exist at grain boundaries and surfaces, as well as within the bulk, that can alter the defect properties within the thin film and thus trapping/non-radiative recombination rates within the material. Thus, it is clear from these works that the solution chemistry is important for controlling nucleation and growth processes, suppressing formation of defects and grain boundaries, and enabling passivation effects within perovskite thin films to improve optoelectronic film quality. The key challenge is to find the right balance of precursors, solvents, and processing considerations that minimize trap density and provide the most control over film formation processes.

5.3 Methodology

There are three important steps that ought to be considered during the film formation process in terms of identifying the best Lewis base candidates: precursor chemistry, nucleation, and growth. In addition, a fourth consideration for the solid-state film is *passivation* effects. In this section I will discuss the important factors in these steps as they pertain to selection criteria.

5.3.1 Precursor chemistry

These parameters are both related to the electron donating/withdrawing strengths of our atoms and/or molecules in solution. Those molecules with a high degree of polarity will have a stronger solvation with other polar molecules and atoms surrounding it. This will change the chemistry within the solution and inevitably affect the assembly, kinetics, and thermodynamics of nucleation. The Pb^{2+} precursor species of perovskites acts as a Lewis acid and interact with the partial negative side (with the lone pair of electrons) of the Lewis base solvent or additive, such as the S=O on the common solvents dimethyl formamide (DMF) and dimethyl sulfoxide (DMSO). The strength of this interaction can be changed with variations to the chemical properties of the solvent/additive molecule that interacts with the Pb^{2+}, thus changing the solvation energy and solubility of the components, which will ultimately affect the precursor chemistries that dictate the subsequent nucleation process.

5.3.2 Nucleation

It is well known that Pb(II) halides are Lewis acids because they accept iodide anions to form iodoplumbate anions such as $[Pb_3I_{10}]_4^-$ and $[Pb_5I_{16}]_6^-$. For this reason, the chemical additives chosen are Lewis bases (electron donators) that can coordinate with Pb^{2+} halides in solution (Lewis acids) to form Lewis acid-base adducts (intermediate phases) through dative bonding, such as the comment solvent and additive used DMF and DMSO. DMSO forms a stronger adduct than DMF with Pb species, and as a result changes the activation energy barrier for nucleation. In this way, the growth rate can be slowed down. This is why DMSO has been largely used to achieve higher film coverage and reproducibility as it slows the growth process. The adduct is isolated from the main solvent (DMF) through dripping of an anti-solvent, such as ether, chlorobenzene, toluene, and other non-polar solvents. Since DMF forms a weaker adduct with Pb complexes than DMSO, the DMF is more readily forced out of the film and volatize due to the anti-solvent dripping, leaving behind the DMSO-Pb-halide adducts. Hence, by introducing species that form even stronger adducts than DMSO with Pb-halides, we can further control and optimize nucleation and growth dynamics by suppressing homogeneous nucleation and promoting heterogeneous nucleation. This can be understood by considering the activation energy barrier for nucleation, as provided below in Section 3.4.1. As we have seen, there are two contributions from (i) a reduction in total free energy due to bulk formation (bond formation) and (ii) a rise in total free energy due to the creation of a surface (broken bonds). The surface free energy increases with r^2, while the volume (bulk) free energy decreases with r^3. Thus, these two competing thermodynamic factors dictate the barrier for nucleation (activation energy) based on the critical point (radius or energy) in which the reduction in bulk free energy can overcome the interfacial (surface) free energy addition. This effect can be modulated through the adduct

method. By forming an adduct, the energy barrier for nucleation can be increased because the Lewis base additive forms a stronger adduct with the Pb-based Lewis acid than the solvent (DMF) typically does. This means that there is an energy barrier associated with dissociating the Lewis base additive from the Pb^{2+} before a perovskite nucleus can initiate. In addition, the supersaturation component of the bulk free energy term may change based on the interaction of the Lewis base and perovskite precursors, where Thus, we can provide a degree of control over the nucleation kinetics and thermodynamics.

5.3.3 Growth:

Chemical additives are an effective means of controlling growth rates and orientations during crystal growth. In the tetragonal perovskite system, there are many different crystallographic orientations as compared to cubic structures, however, the (110) and (001) planes are expected to be the most stable for the tetragonal perovskite structure. The surface energy is an important parameter in crystal growth that can be understood by examining the change in Gibbs free energy, defined as:

$$dG = -SdT + VdP + \gamma dA$$

$$\gamma = \left(\frac{\partial G}{\partial A}\right)_{T,P}$$

where γ is the surface energy, defined as the change in Gibbs free energy per change in surface area (A) under constant temperature and pressure conditions. The driving force for equilibrium is to reduce the Gibbs free energy, and thus if we assume constant pressure and temperature

conditions, this is directly related to surface energy, which in turn is related to the number of "broken bonds" at the free surface. Of course, the relative free energies must be associated with the individual free energy associated with the bond broken of a specific atom. Those surfaces with the largest free energy associated with them will be the most unstable. As a result, the Lewis base additives will be more prone to interact more with a specific surface orientation depending on the exposed species at that orientation, for instance, those with more exposed Pb^{2+} species, thereby effectively lowering the surface energy of that orientation. These "capping" molecules can ultimately stunt growth along those unstable surfaces due to its adsorption to those surfaces. This potentially creates a situation in which growth must occur on a flat surface either by a ledge, spiral, or surface nucleation growth mechanism along the more stable orientations. Ledge growth mechanisms are much slower in growth rate as they are interface-controlled rather than diffusion controlled as in the case of higher energy surfaces. If a single atom/molecule leaves the liquid and attaches itself to the flat solid surface, the number of broken bonds associated with the interface will increase, thus increasing the surface energy. This increase in surface energy will be highly unstable and the atom/molecule will be more prone to de-attach back into the liquid solution. This means that the rate-limiting step occurs at the interface rather than being limited by diffusion of the proper atoms/molecules to the interface. Thus, we can effectively control both the growth kinetics and orientation through use of Lewis base additives in this way.

5.4.4 Passivation (solid-state effects)

Lewis bases have the capability to act as passivating agents within the solid-state perovskite thin film after film formation. It has been shown that under-coordinated species and anti-site defects such as PbI_3^- (iodine occupies Pb site and forms a trimer with neighboring iodine atoms) commonly exist at free surfaces and grain boundaries, that can act as trap/recombination centers for charge carriers. An under-coordinated Pb at the free surface will mimic a Lewis acid, whereas under-coordinated I species a Lewis base at these surfaces. If the Lewis base additives do not incorporate into the perovskite crystal structure, they can interact with these under-coordinated Lewis acid species, thus passivating the trap center. It is believed that these Lewis base additives may preferentially reside and grain boundaries, assuming they will not readily incorporate into the perovskite crystal structure, which is likely the case for larger passivating agents but may not be for smaller ones. However, this mechanism is not clearly defined.

With a better understanding of the underlying interactions of perovskite precursors, solvents, and chemical additives for the different perovskite systems, processing techniques must be carefully tuned to construct perovskite films with high optoelectronic quality and stability. An important parameter for passivation considerations that must be taken into account is the Lewis base additive volatility. Those with higher volatility will be less likely to remain within the solid state film after film formation, and thus may be less effective as passivating agents. Thus, the volatility, which is related to the vapor pressure of the chemical, is an important component to this study that has not been largely identified nor systematically studied. An optimal balance must be established between interaction strength of the chemical additives with perovskite precursors and solvents, the solubility of precursors in the solution, and the processing dynamics

(volatility) of the selected additives in order to control crystallization processes to enhance film optoelectronic quality and stability.

5.3.5 Selection Criteria

Based on these considerations outlined in the prior section, the selection criteria for Lewis base candidates will be based on two properties: dipole moment, and volatility. Both of these factors will dictate the strength of the interactions between the perovskite precursors and Lewis base additives, which will in turn affect nucleation, growth, and passivation effects.

The selection process for Lewis base additives will consist of systematic changes to the molecular structure of the reference DMSO additive. These molecules, shown in Figure 5-1 have incremental changes to the unsaturated bonds and functional groups. The unsaturated bonds change from C=O to C=S, while the functional groups change from methyl (CH_3) to amine (NH_2) one at a time. Each of these parameters will affect the overall dipole moment of the molecule and its corresponding interaction strength with Pb^{2+}, which is directly correlated to the electronegativity of the elements involved. Amine groups are more electron withdrawing due to the nitrogen atom, and similarly it is expected that C=O will be more partial negative due to the strong electron withdrawing nature of the more electronegative oxygen atom compared to sulfur. Thus, molecules with C=O ought to have a stronger interaction with the Pb^{2+}, and it is expected that the top row will have a higher interaction strength with the precursors than the bottom row (thio-sulfur-based). Since these molecules are added in small quantities and meant to interact directly with the Pb^{2+} (and MA^{+}) precursors, the solubility is not the major factor explored, though it has an important effect in nucleation dynamics. Thus, the dielectric constant of the

additive is not strongly considered as the additive amounts introduced into the system are relatively small compared to the solvent and solute amounts.

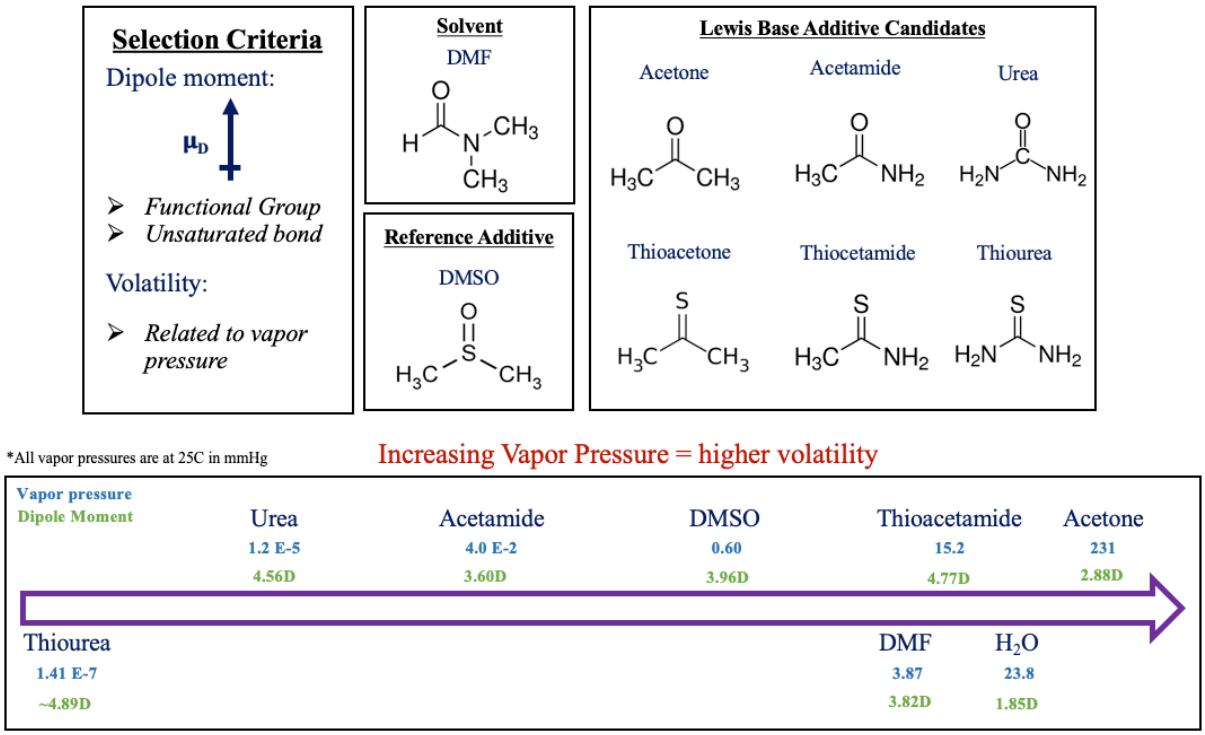

Figure 5-1: Selection criteria and candidates for Lewis base additives.

5.4 Results and discussion

5.4.1 Lewis base candidate selection

Acetamide, urea, and thiourea were first analyzed to elucidate the best Lewis base candidate. Thin films were fabricated using the adduct approach where different molar ratios of each additive respective to the amount of Pb^{2+} in the system were used to form MAI•PbI_2•Lewis base adduct species. The films were subsequently analyzed using SEM and XRD to observe

effects on crystal growth modulation. A molar ratio of 10 mol% of the additive was used to observe impacts via SEM and XRD (Figure 5-2). Acetone (and also thioacetone) is excluded from this data set as its highly volatile nature results in near identical results to the reference (DMF), and it thus has very minimal impact on modulating crystal growth since it evaporates very quickly before the major solvent begins to dry. From the SEM images in Figure 5-2a, there is a clear trend following our hypothesis (scale bar for all images is 1μm). The grain size is greatly enhanced in the order of DMF→ acetamide → urea → thiourea. This is accompanied by an increase in intensity of the XRD spectra that represents the number of planes of atoms contributing to a particular orientation within the crystal, which correlates to the larger grains oriented along the (110) and (220) directions (Figure 5-2b). Here we can also note the change in intensity scale (y-axis) for thiourea, where the maximum of the scale increases from 25k to 1M counts. This clearly corresponds to the greatly increased grain size seen for thiourea. However, we also note that there seem to be some secondary phase formation for the thiourea films seen as white inclusions. The thioacetamide XRD spectra is provided in Figure 5-2d, which shows a slight enhancement of XRD intensity compared to the reference, but not nearly as significantly as thiourea. This suggests that it is not only the thio- group that leads to stronger precursor-additive interactions, but perhaps equally important are the amine functional groups in determining adduct strength.

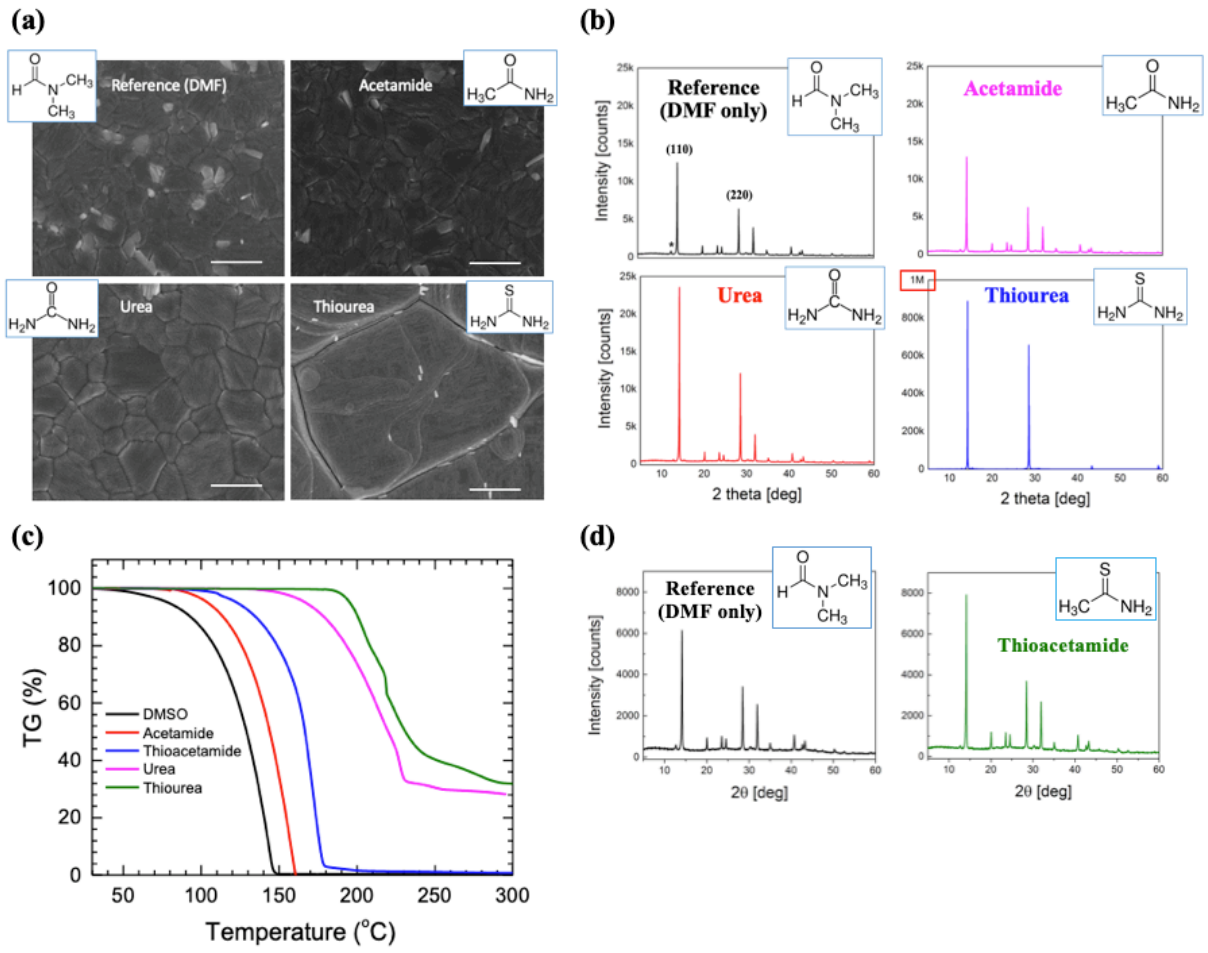

Figure 5-2: (a) Top view SEM images of $MAPbI_3$ with Lewis base additives, (b) XRD spectra of films with additives, (c) TGA of additive candidates, (d) XRD spectra of thiourea (with separate reference than those of (b).

Figure 5-2c depicts the TGA analysis for the additives of interest. We observe the same trend, where DMSO is the first to evaporate around 50˚C, acetamide next around 90˚C, thioacetamide around 110˚C, urea <150˚C, and thiourea <180˚C. This follows the observed trend of XRD

spectra and grain sizes, and also the volatility and dipole moment trends shown in Figure 5-1, with the exception of thioacetamide, which may be a result of its higher volatility.

5.4.2 Device Performance

To directly observe the effects of these Lewis base candidates on optoelectronic quality and PV device performance, perovskite films were formed using the 1-step adduct method to measure PL characteristics and in a p-i-n device configuration of ITO/SnO_x/$MAPbI_3$/Spiro/Ag to measure device characteristics. Urea was first elucidated as the best Lewis base candidate to improve performances reproducibly. The photovoltaic performance of $MAPbI_3$ perovskite solar cells was evaluated with different amounts of added urea, as detailed in Figure 5-3. The amount of urea varied from 0 mol % (without urea) to 6 mol % (0.06 mmol) with respect to MAI and PbI_2 (1 mmol). As the urea amount increased from 0 (reference) to 4 mol %, the open-circuit voltage (V_{OC}) and fill factor (FF) were systematically enhanced. With the addition of 4 mol % urea, the average V_{OC} and FF were enhanced from 1.049 ± 0.016 to 1.089 ± 0.028 V (3.81% enhancement) and 0.72 ± 0.03 to 0.75 ± 0.03 (4.1% enhancement), respectively. This resulted in an improvement in the average PCE from 16.10% ± 0.70% to 17.75% ± 0.71% (10% enhancement). The current density and voltage (J-V) curves of the best-performing devices are shown in Figure 5-3b. A PCE of 18.55% was achieved with the addition of 4 mol % urea and 17.34% was achievable without urea. The steady-state PCEs of the best-performing devices were 16.80% and 18.25% without and with urea, respectively. The enhanced PCE was partially ascribed to a slight enhancement in J_{SC}, which was confirmed from the external quantum efficiency (EQE) spectra in Figure 5-3c. The integrated J_{SC} was calculated to be 20.91 mA/cm^2

for the reference and 21.26 mA/cm2 with 4 mol % urea, which is well matched with the J_{SC} measured from the J-V curve.

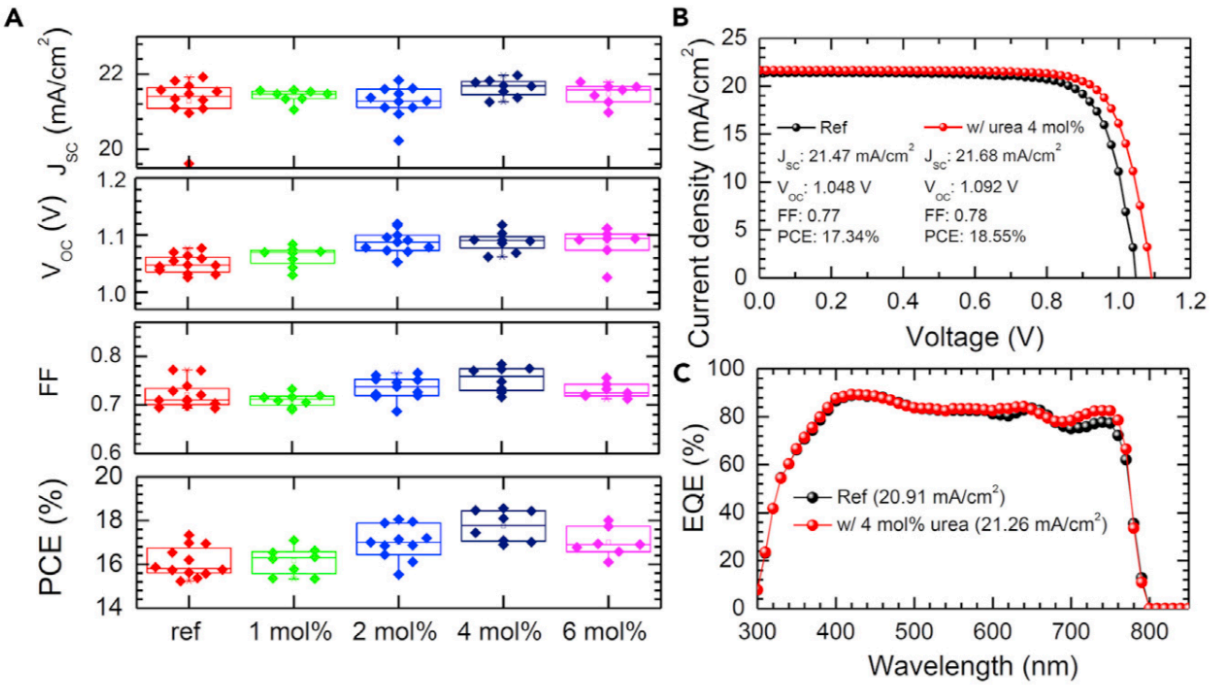

Figure 5-3: (A) Photovoltaic parameters of $MAPbI_3$ perovskite solar cells as a function of the amount of urea: short-circuit current density (JSC), open-circuit voltage (VOC), fill factor (FF), and power conversion efficiency (PCE). (B and C) Current density-voltage (J-V) curves (B) and external quantum efficiency (EQE) spectra (C) of the best-performing device with and without 4 mol % urea.

5.4.3 Crystallization and Morphology

Next, we sought to investigate the crystallization dynamics of urea responsible for this increase in performance. The adduct film formed without urea ($MAI•PbI_2•DMSO$) was

immediately converted to $MAPbI_3$ upon heating at 65˚C, whereas a much slower conversion with an increased temperature of 100˚C was observed with addition of urea (Figure 5-4a,b). This effect is most likely a result of the change in intermolecular interactions upon addition of urea. We confirmed the interaction of urea with MAI, PbI_2, and DMSO by measuring the FTIR spectra of the synthesized adduct powders in Figures 5-4c,d. The characteristic S=O stretch peak of DMSO in the MAI•PbI_2•DMSO adduct was shifted from 1,018 to 1,010 cm^{-1} upon addition of urea. Also, the C=O stretch peak in urea was shifted from 1,676 to 1,651 cm^{-1}, which is most likely caused by the interaction between urea and the MAI•PbI_2•DMSO adduct to form a MAI•PbI_2•DMSO•urea adduct. Considering the negligible shift of the C=O stretch peak of urea in MAI•PbI_2•urea, the interaction of urea with MAI•PbI_2 seems to be weak in the absence of DMSO, which probably allows the formation of $MAPbI_3$ at a lower temperature than the sublimation temperature of urea.

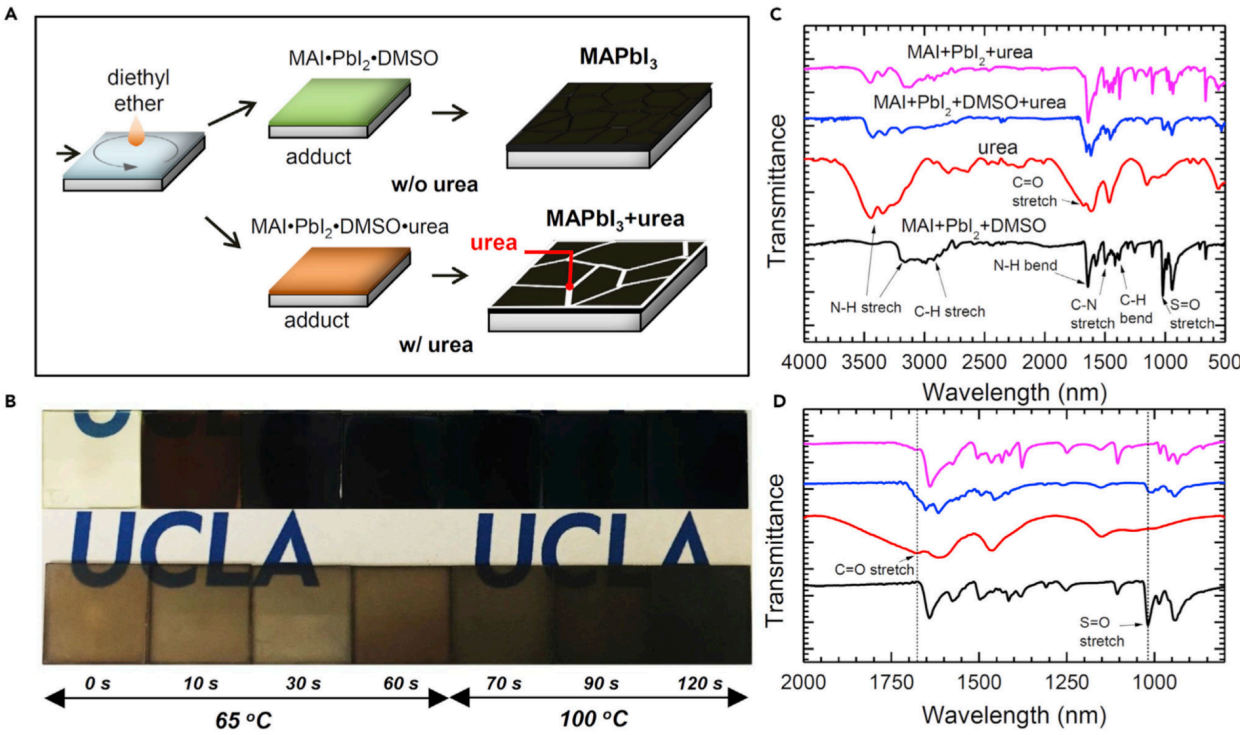

Figure 5-4: (A) Schematics showing the formation of the perovskite layer with and without urea. (B) The films without (upper) and with 1 mmol of urea (lower) as a function of heat-treatment temperature and time. (C) Fourier transform infrared (FTIR) spectra of MAI,PbI_2,DMSO adduct, urea, MAI,PbI_2,DMSO,urea, and MAI,PbI_2,urea adduct powder. (D) The magnified FTIR spectra showing the fingerprint region for C=O and S=O stretch.

Per the Arrhenius equation, the nucleation rate is inversely exponentially proportional to the activation energy (E_a) at constant temperature. Slower crystallization with the addition of urea is thus thought to originate from the strengthened interaction between perovskite precursors and Lewis bases (DMSO and urea), which increases the E_a. The stronger interaction is probably due to higher dipole moment of urea (4.56 D) than of DMSO (3.96 D) (Figure 5-1) and the

resulting enhanced Lewis acid-base interaction. The slower crystallization rate implies a higher critical Gibbs free energy for nucleation (ΔG_c), which decreases the number of nuclei formed and growth proceeds from a fewer number of nuclei. Therefore, the growth of larger grains is expected from the addition of urea. Furthermore, it has been reported that Lewis bases can interact with grain boundaries of perovskite films to passivate the defect sites. We presume that urea likely precipitates at grain boundaries and can interact with these defects after completion of crystal growth. However, too much residual photo-inactive urea can degrade photovoltaic performance. Thus, our motivation was to investigate the effects of the amount of urea added on photovoltaic performance.

The FTIR spectra were also measured (Figure 5-5A) to investigate whether urea remained in the film after film formation. A magnified region containing the finger print region for the C=O stretch, N–H bend, and C–N stretch is shown in Figure 5-5B. Asymmetric peaks around 1,647 and 1,577 cm^{-1} (red arrows in Figure 5-5B) in the bare $MAPbI_3$ film are reported to originate from N–H bending. With the addition of 4 mol % urea to the perovskite precursor solution, the peak at 1,647 cm^{-1} shifted to 1,665 cm^{-1} (black arrow), which can be attributed to overlap with the C=O stretching peak of urea at 1,676 cm^{-1}, confirming the presence of urea. Furthermore, the XRD patterns in Figure 5-5C show no additional peaks or peak shifts upon addition of 4 mol % urea in comparison with the bare $MAPbI_3$ film, implying that the added urea does not react with precursors to produce byproducts and exists in an amorphous form. The (110) oriented peaks of $MAPbI_3$ were enhanced with addition of urea, whereas the intensities of the other peaks were essentially unchanged ($intensity_{(110)}/intensity_{(222)}$ increased from 1.25 to 1.34). The preferred orientation induced by urea was further confirmed by XRD patterns with a higher amount of urea, in which the (110) orientation peaks were further enhanced. Furthermore, the

full-width half-maximum (FWHM) values of the peaks originating from perovskite were reduced (e.g., from 0.133 to 0.109 for the (110) peak), confirming that added urea interacts with perovskite precursors during crystal growth to enhance crystallinity and induce the preferred orientation.

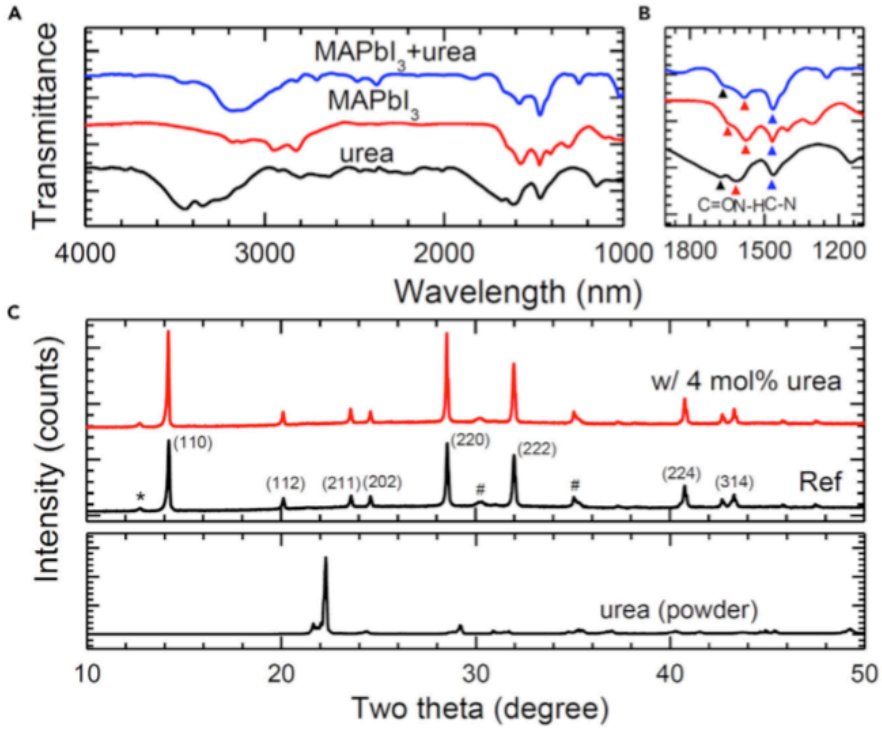

Figure 5-5: (A) Fourier transform infrared (FTIR) spectra of urea (powder), $MAPbI_3$ (film), and $MAPbI_3$ with 4 mol% urea (film). (B) The fingerprint region for C=O stretch (black arrows), N–H bend (red arrows), and C–N stretch (blue arrows). (C) X-ray diffraction patterns of urea (powder) and perovskite film without and with 4 mol % urea. Peaks indexed with * and # originate from PbI_2 and ITO, respectively.

The effect of added urea on the surface and cross-sectional morphology of the $MAPbI_3$ layer is investigated in Figure 5-6. As seen in the AFM images in Figures 5-6A,B, the constitutive grains were significantly enlarged from about 200 nm to larger than 1 mm, which correlates with enhanced FWHM in the XRD measurements in Figure 5-5C. The cross-sectional scanning electron microscopic (SEM) images of the perovskite solar cell based on $MAPbI_3$ with and without 4 mol % urea are shown in Figures 5-6C,D, respectively. The thickness of the $MAPbI_3$ layer was around 580 nm regardless of the addition of urea; the perovskite film with added urea displayed single interfaces of large grains along the direction perpendicular to the substrate, whereas the bare $MAPbI_3$ film showed multiple interfaces between several smaller grains. The enlarged grains are also confirmed in the top-view SEM images in Figure 5-6E,F, in which nano-sized bumps can be observed on the surface of $MAPbI_3$ grains with the addition of 4 mol % urea. We speculate that the nano-sized bumps are related to the added urea. Because urea does not integrate as part of the perovskite lattice, it is possible that it can precipitate at the grain boundary of $MAPbI_3$ and the surface of the film after completion of crystal growth, as has been previously observed for excess CH_3NH_3I and CH_3NH_3Br. It is expected that the precipitated urea interacts with the grain boundaries of perovskite to change the optoelectronic properties of perovskite film.

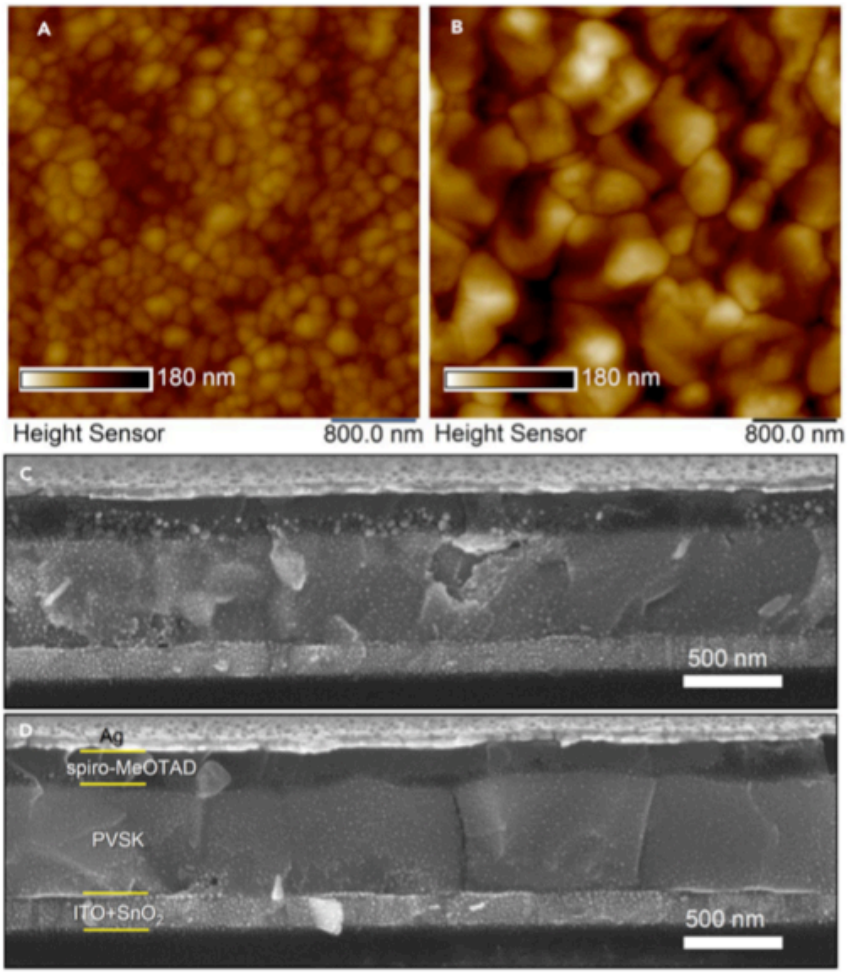

Figure 5-6: Atomic force microscopy (AFM) images of (A) bare $MAPbI_3$ and (B) $MAPbI_3$ with 4 mol % urea on SnO_2-coated ITO substrates. Cross-sectional scanning electron microscopy (SEM) images of perovskite solar cells based on (C) bare $MAPbI_3$ and (D) $MAPbI_3$ with 4 mol % urea.

5.4.4 Macroscopic Photoluminescence and the Role of Remnant Urea

In Figure 5-7, UV-visible and PL of the $MAPbI_3$ perovskite films were measured to evaluate the effect of added urea on the absorption and charge-carrier properties of the film. The

absorption of the $MAPbI_3$ film in the wavelength region from 600 to 780 nm was slightly enhanced with the addition of urea, which can be correlated with the enhanced EQE in the same wavelength region. The enhancement of the absorption might result from the larger crystal size, which was found to enhance light-harvesting efficiency caused by enhanced light scattering, as reported previously. From closer inspection of the (1 – transmittance) spectra in Figure 5-7E, a steeper onset of absorption was observed with 4 mol % urea (slope of linear fit = 6.83) than with that of bare $MAPbI_3$ film (slope of linear fit = 6.64). Thus, smaller Urbach (E_u) energy is expected with 4 mol % urea, which indicates a higher level of electronic order with 4 mol % urea. The steady-state PL is shown in Figure 5-7B. Notably, the PL peak intensity was increased more than three times from 0.9114×10^5 to 3.1839×10^5 upon addition of urea. The time-resolved PL decay profiles of the $MAPbI_3$ films were monitored at the peak emission (770 nm) in Figure 5-7C to find the origin of the enhanced PL intensity. The bare $MAPbI_3$ film shows bi-exponential decay with fast (t_1 = 5.8 ns) and slow (t_2 = 200.5 ns) components, whereas single exponential decay was observed (t_2 = 738.3 ns) with 4 mol % urea without the fast component. The fast component (t_1) might be related to trap-mediated monomolecular non-radiative recombination derived by defects at the grain boundaries. It has been reported that trap-mediated non-radiative recombination becomes dominant with a low intensity of excitation because of slow depopulation of charge carriers from the trap states. Time-resolved PL spectra of bare $MAPbI_3$ films under different intensities of excitation was measured. As the excitation intensity decreased, t_1 was highly increased from 17.15% to 92.51%, indicating that monomolecular trap-mediated recombination becomes dominant, which supports the correlation between the fast-decaying component and trap-mediated non-radiative recombination. In contrast, the PL decay profile of $MAPbI_3$ film with 4 mol % urea shows a single exponential decay with t_2~700 ns

regardless of the excitation intensity, which suggests a significantly decreased defect density after the addition of urea. Furthermore, t_2, which is associated with bi-molecular radiative recombination of the perovskite film in bulk, was greatly increased from 200.5 to 752.4 ns with the addition of urea. This indicates that the charge-carrier lifetime is highly prolonged, which likely contributes to the enhanced V_{OC} and FF observed. The measured PL lifetime of $MAPbI_3$ film with 4 mol % urea is superior to that of $MAPbI_3$ film prepared with a variety of techniques to enlarge the grain size. The decrease in defect density with the addition of urea can be attributed to increased grain size as a result of slower crystallization with higher activation energy during the crystallization (Figure 5-7D), resulting in decreased grain boundaries and their associated defects. Moreover, the Lewis base urea is most likely precipitated at grain boundaries

in the final film, which serves to passivate the grain boundary defect sites and remove trap states, which will facilitate charge transport and enhance the quasi-Fermi level and thereby V_{OC}.

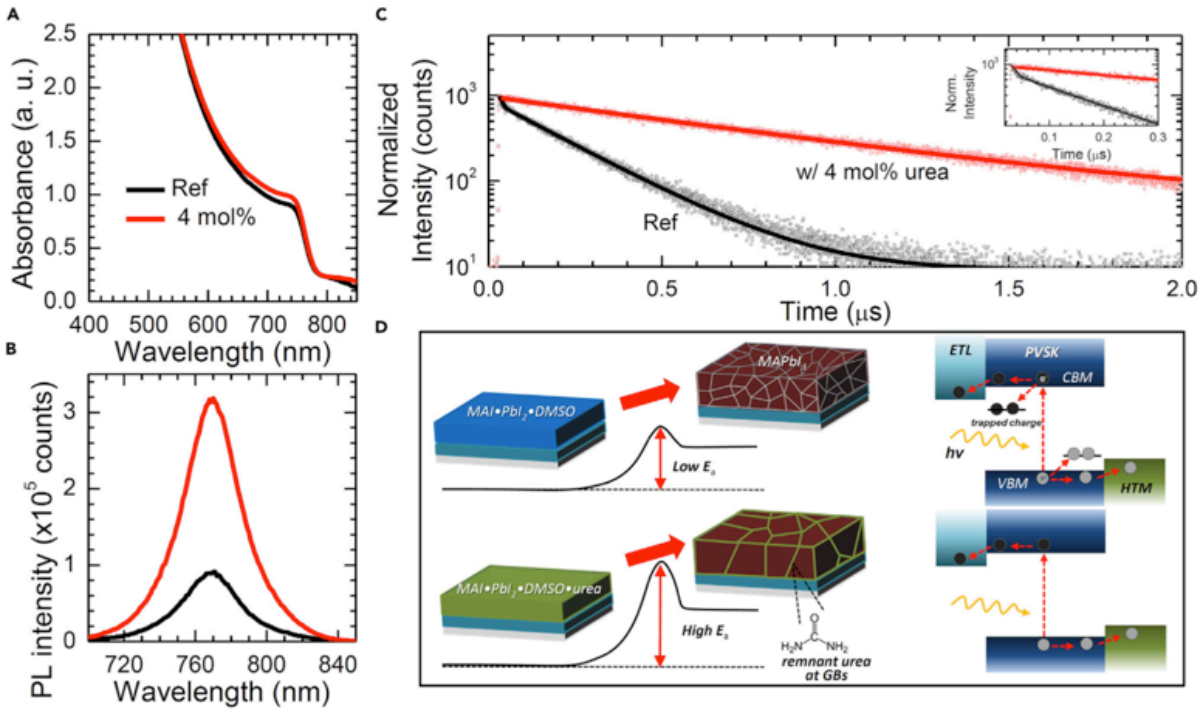

Figure 5-7: (A–C) UV-visible absorption (A), steady-state photoluminescence (PL) (B), and time-resolved PL decay profiles (C) of $MAPbI_3$ film without and with 4 mol % urea. The films were deposited on a glass substrate. Inset in (C): magnified spectra showing the initial decay profile. Empty circles and solid lines indicate measured data and fitted curves, respectively. (D) Schematics showing film crystallization and corresponding charge transporting characteristics.

To further confirm the nature of the decreased defects, we first investigated the presence of coordination species defects by using absorption spectra (Figure 5-8). To avoid saturation of

absorption, we diluted the precursor solutions five times to decrease the thickness of $MAPbI_3$ films. As seen in Figure 5-8, an increase in absorption from 420 to 500 nm was reproducibly observed after the addition of urea. The absorption at these wavelength regions was reported to originate from coordination species such as $PbI_4S_2^{2-}$ (S is undesired coordinating species such as solvent molecules), thus the increase in the absorption indicates an increase in the coordination species, which seems to be reasonable because remnant urea with higher dipole moment than DMSO is expected to form more coordinating species in the resulting $MAPbI_3$ film. Therefore, in this study, the reduced defect density does not originate from coordination species defects.

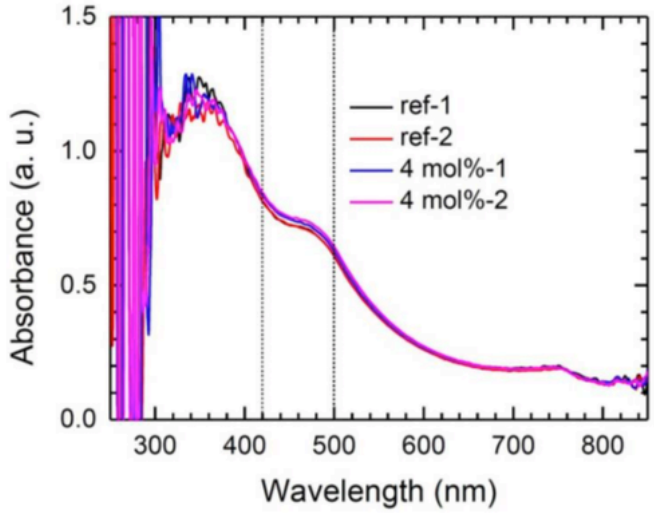

Figure 5-8: Absorption spectra of $MAPbI_3$ film without and with 4 mol% urea. The precursor solution was diluted by 5 times (10.4 wt%) compared to one used for device fabrication (51.8 wt%).

Next, admittance spectroscopy was carried out to measure the density of the trap (Figures 5-9A and 5-9B). The structural disorders at the grain boundaries were reported to form a shallow trap

state close to the valance band maximum (VBM), which can be monitored by admittance spectroscopy. The density of the trap (N_T) was estimated from the angular-frequency-dependent capacitance according to the following equation:

$$N_T(E_\omega) = -\frac{V_{bi}}{qW}\frac{dC}{d\omega}\frac{\omega}{kT}$$

where V_{bi} represents the built-in potential, W denotes the depletion width, C is the capacitance, ω is the angular frequency, k is the Boltzmann constant, and T is the temperature. $E_u = E_T - E_V$, where E_T and E_V are the trap energy and valance band maximum, respectively. V_{bi} and W were measured with a Mott-Schottky plot (inset in Figure 5-9A), in which the measured V_{bi} values were 1.05 and 1.17 V for the devices without and with urea, respectively, correlating with enhanced V_{OC} with urea. The calculated N_T from frequency-dependent capacitance spectra (Figure 5-9A) is demonstrated in Figure 5-9B. With the addition of 4 mol % urea, the trap density is more than one order of magnitude decreased at around E_ω= 0.25 eV, corresponding to a shallow trap state, which possibly originates from structural disorder at the grain boundaries. Thus, we concluded that the addition of urea effectively reduces the trap state originating from grain boundaries.

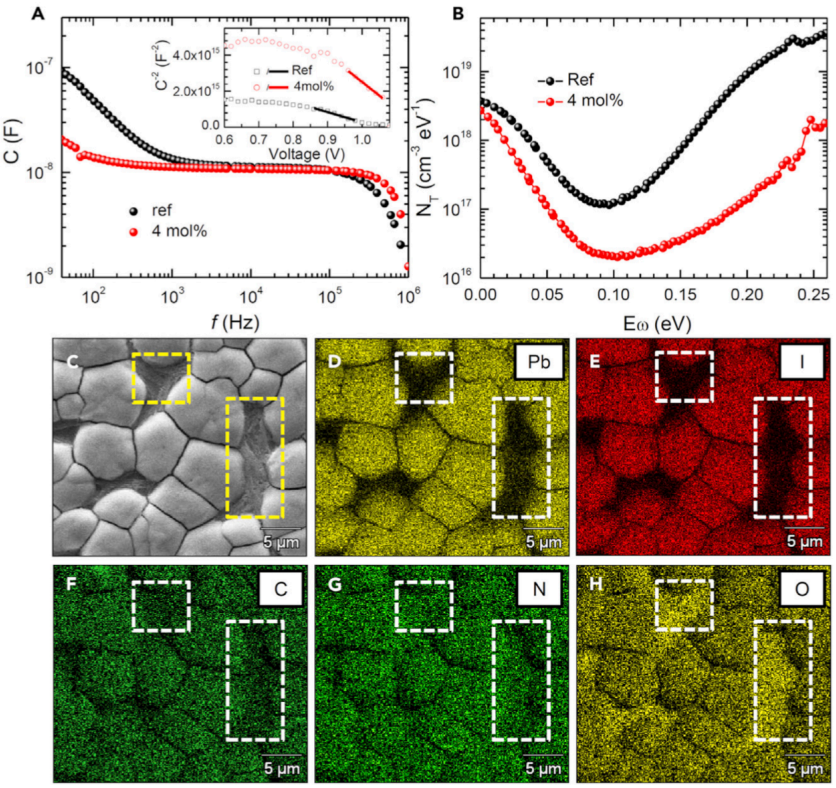

Figure 5-9: (A and B) Frequency-capacitance (f-C) (A) and trap density curves (B) measured from perovskite solar cells without and with 4 mol % urea. Inset in (A) shows the Mott-Schottky plot of the devices; empty circles and squares represent measured data and solid lines indicate the linear fit of the data. (C) Scanning electron microscopic (SEM) images of $MAPbI_3$ film with 50 mol % urea. (D–H) Elemental distribution mapping images of the film. Dashed rectangular boxes in the images indicate the secondary phase formed at grain boundaries.

Although the effect of urea on crystal growth is obvious, it was difficult to confirm the presence of urea at the grain boundaries and its passivation effect. We carried out supplemental experiments to investigate the passivation effect of urea. Urea was dissolved in 2-propanol at different concentrations (13.5, 27, and 54 mM) and was spin-coated on $MAPbI_3$ film followed by

drying at 100˚C for 5 min. With 27 mM of urea, the average PCE of the devices was enhanced from 16.19% ± 0.65% to 16.86% ± 0.98%, and the steady-state PCE of the best-performing devices was enhanced from 17.11% to 17.94%. The enhanced PCE mainly resulted from enhanced V_{OC} (1.089 ± 0.017 to 1.103 ± 0.027 V) and FF (0.693 ± 0.018 to 0.707 ± 0.024); no significant change in J_{SC} was found as confirmed from the EQE spectrum. Steady-state and time-resolved PL decay profiles of the film with and without urea post-treatment were also measured to investigate the origin of the improved photovoltaic performance. The steady-state PL intensity was increased more than 2 times after treatment with urea solution. In the time-resolved PL decay profiles, the fast-decay component (t_1 = 5.4 ns), associated with trap-mediated non-radiative recombination, observed from the reference film was significantly retarded to 30.7 ns. This is likely related to a radiative component resulting from passivation of the traps by urea considering the enhanced steady-state PL intensity. t_2, which can be related to the bulk carrier lifetime, was hardly changed probably because the morphology (grain size) of the $MAPbI_3$ film was pre- served. Finally, the photovoltaic performance of perovskite solar cells based on bare $MAPbI_3$ with post-treatment urea and with 4 mol % urea was compared, and the devices with 4 mol % urea showed the highest performance. Further details on these results can be found within the supplementary information portion of the manuscript.

With a small amount of urea (4 mol %), however, it was difficult to identify the remnant urea at the grain boundaries of $MAPbI_3$ film. We increased the amount of urea by 50 mol % to see whether the excessive urea crystallized at the grain boundaries. In SEM images of the $MAPbI_3$ perovskite film with 50 mol % urea (Figure 5-10), we identified the formation of the secondary phase at the grain boundaries (yellow arrows in Figure 5-10).

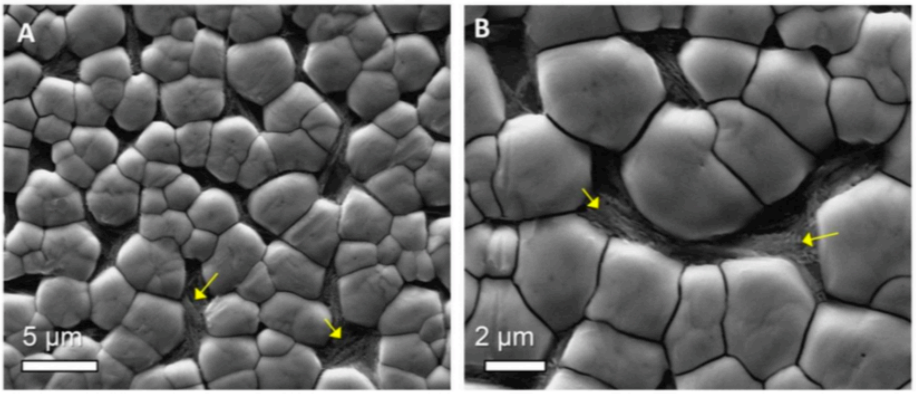

Figure 5-10: Scanning electron microscopic (SEM) images of $MAPbI_3$ film with 50 mol% urea. Yellow arrows in the image indicate secondary phase formed at grain boundaries

To investigate the chemical composition, elemental distribution mapping was carried (Figures 5-9C–H). The mapping images clearly indicate the absence of Pb and I and the presence of C and N in the secondary phase as indicated in the dashed rectangular boxes, probably detected from urea (oxygen possibly comes from indium tin oxide [ITO] substrate). Therefore, we concluded that the added urea is precipitated at the grain boundaries of perovskite films. The urea was reported to behave like a semiconductor as a result of electron delocalization via p-bond formation (C=NH, $C=NH_2^+$) and generation of a highly polar resonance hybrid structure. However, its conductivity is still low (3–6 x 10^{-8} S/cm). As a result, the thick layer of urea impedes extraction of the photo-generated hole from the perovskite layer.

5.4.5 Microscopic c-AFM

c-AFM measurements were carried out (Figure 5-11) to investigate the spatially resolved electrical properties of the $MAPbI_3$ films. Figures 5-11A,B show the distribution of the current signal measured between the tip and the perovskite film, which is over- laid on the topological images (grayscale). The current was measured under a DC bias voltage of 1.0 V in an ambient atmosphere and room-light conditions. For the bare $MAPbI_3$ film (Figure 5-11A), the measured current was highly heterogeneous over the whole film. The heterogeneity existed between grains and different regions of the grain interior, which is in accordance with previous studies. Some of the grains showed a very low current signal (red region), indicating poor mobility and/or depleted charge carriers in this region, which degrades the overall photovoltaic performance of the perovskite solar cell. Figure 5-11C shows the trajectory of the scan of the height and current signal, in which the measured current varied significantly along the trajectory. The current signal was measured to be relatively higher at grain boundaries than in the grain interior, which was found to be caused by down- ward bend-bending at the grain boundary causing electron trapping. With the addition of urea (Figure 5-11B), the current signal was enhanced overall with much better homogeneity than bare $MAPbI_3$ film. The homogeneous current can be confirmed from the scan trajectory in Figure 5-11D. The measured current was relatively constant across the two different grains regardless of the grain boundary present between grains, indicating that urea successfully passivates the grain boundaries to reduce carrier trapping at grain boundaries. Moreover, we attribute the homogeneous current signal across the grain interior to higher crystallinity with preferred orientation, which decreases the bulk defects and their dependency on facet. The probability distribution of the measured current from the $MAPbI_3$ films with and without urea is shown in Figure 5-11E. Upon addition of urea, the overall current signal was

greatly increased with a narrower distribution, implying improved mobility and/or carrier density, which correlates with decreased trap density and improved carrier lifetime in the PL measurements.

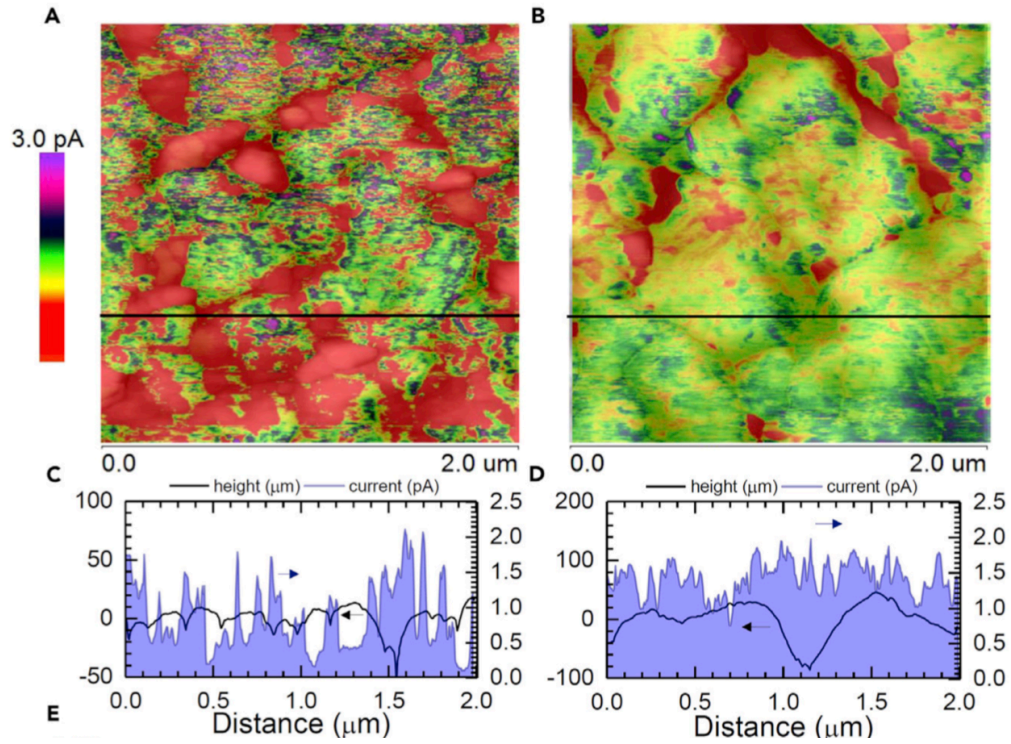

Figure 5-11: (A and B) Conducting AFM images of (A) bare $MAPbI_3$ and (B) $MAPbI_3$ film with 4 mol % urea formed on SnO_2-coated ITO substrates. Current images were overlaid on grayscale topology images. (C and D) Line-scan profiles of height and current along the black lines in (A) and (B), respectively.

5.4.6 Impact of Urea on Stability

Finally, the effect of the addition of urea on ex-situ and in-situ stability of the device was evaluated in Figure 5-12. For ex situ measurements (Figure 5-12A), the devices were stored

under dark conditions and measured over time; the devices were kept under light at maximum power for the in-situ measurements (Figure 5-12B). The reference device showed 43% degradation (from 17.1% to 9.8%) over 27 days; the device with urea showed 35% degradation (from 18.27% to 11.82%). During in situ measurement for 1 hr, the reference device showed 5% degradation but almost no degradation was observed with urea. The improved stability is probably a result of decreased grain boundaries, which can act as a pathway for ingression of moisture.55 However, accelerated degradation of $MAPbI_3$ film under prolonged light exposure was observed. The initial degradation was slower with urea but was accelerated after 90 min of light exposure. Further study will be required to fully understand the effect of added urea on the stability of the perovskite film and device.

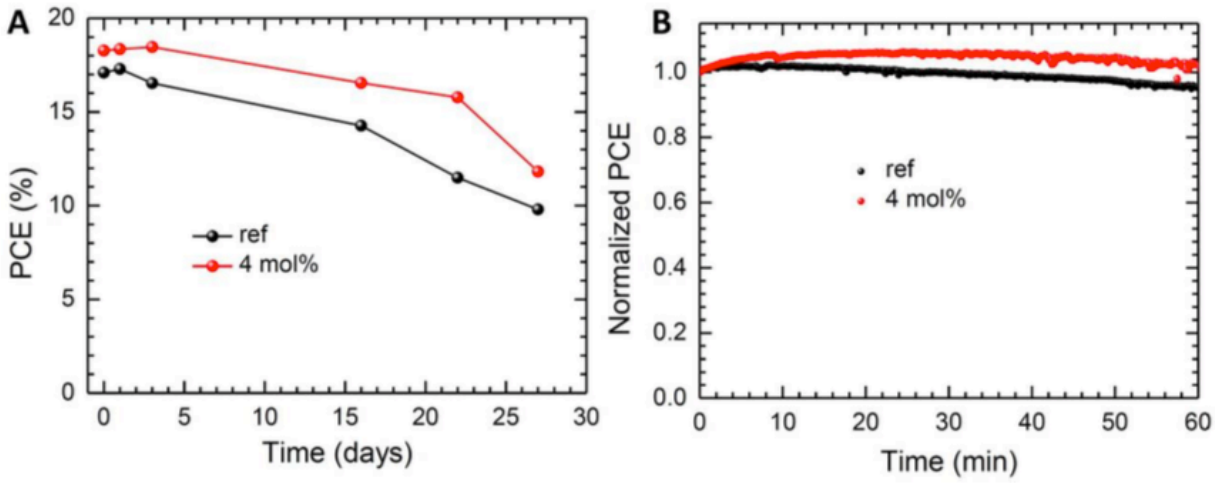

Figure 5-12: (A) Ex-situ and (B) in-situ stability test of $MAPbI_3$ perovskite solar cell without and with 4 mol% urea. The devices were stored under dark in ambient condition for ex-situ measurement while they were maintained at maximum power point under continuous one sun illumination for in-situ measurement.

5.5 Summary

In conclusion, we have successfully demonstrated a bifunctional Lewis base additive for enhanced grain growth and grain boundary passivation. Addition of the Lewis base urea was found to retard crystal growth to enhance crystallinity and induce a preferred orientation. Because of the non-volatile nature of urea, we propose that it precipitates at the grain boundary after completion of film formation to passivate the defects at the grain boundaries. As a result of the enhanced crystallinity and grain boundary passivation, the trap density in both the grain interior and at the boundaries was significantly reduced, resulting in an enhanced carrier lifetime and a more homogeneous conductivity across the film. Finally, the steady-state PCE of the $MAPbI_3$-based solar cell was enhanced from 16.80% to 18.25% upon an optimized addition of urea. We believe this work presents an effective strategy for decreasing microscopic heterogeneity in optoelectronic properties of perovskite films and will open new approaches to further enhancing the photovoltaic performance of perovskite solar cells toward their great potential.

5.6 Experimental

Device fabrication

Indium doped tin oxide (ITO) glass was cleaned by sonication in detergent, acetone and 2-propanol for 15 min respectively. UV-ozone treatment was performed for 15 min to enhance the wettability before spin-coating of SnO2 precursor solution. 30 mM SnCl2·2H2O (98%, Sigma-Adrich) in ethanol (anhydrous, Decon Laboratories Inc.) solution was stirred for an hour, which

was filtered by 0.2 μm syringe filter before use. SnO2 layer was formed by spin- coating the precursor solution at 3000 rpm for 30 s two times. After first spin-coating, the film was dried at 150 oC for 30 min while it was heated to 150 oC 5 min followed by 180 oC for 1 h after second cycle. Perovskite layer was formed from adduct solution. 1 mmol of CH3NH3I (MAI, Dyesol, 159 mg), PbI_2 (99.999%, Alfar Aesar, 461 mg) and dimethylsulfoxide (DMSO, anhydrous, >99.9%, Sigma-Aldrich, 78 mg) were dissolved in 500 mg of N,N-dimethylformamide (DMF, anhydrous, 99.8%, Sigma-Aldrich), to which x mmol (x=0.1, 0.2, 0.4, 0.6) of urea (99.0-100.5%, Sigma-Aldrich) was added. The solution was filtered by 0.2 μm syringe filter before use. SnO2 coated substrate was treated with UV- ozone for 15 min before spin-coating the perovskite solution. The pervoskite solution was spin-coated at 4000 rpm for 25 s, to which 0.3 mL of diethyl ether (anhydrous, >99.0%, contains BHT as stabilizer, Sigma-Aldrich) was dropped. The resulting transparent adduct film was converted to perovskite by heat-treatment at 65 oC for 1 min followed by 100 oC for 30 min. The spiro-MeOTAD solution was prepared by dissolving 85.8 mg of spiro-MeOTAD (Lumtech) in 1 mL of chlorobenzene (anhydrous, 99.8%, Sigma-Aldrich) in which 33.8 μl of 4-tert-butylpyridine (96%, Aldrich) and 19.3 μl of Li-TFSI (99.95%, Adrich, 520 mg/mL in acetonitrile) solution were added. The spiro-MeOTAD solution was spin-coated at 3000 rpm for 20 s by dropping 17 μl of the solution on spinning substrate. On top of the spiro- MeOTAD layer, 80 nm-thick silver was thermally evaporated at 0.5 Å /s to be used as an electrode.

Synthesis of adduct powder

To synthesize the MAI·PbI_2·DMSO adduct powder, 1 mmol of MAI, PbI_2 and DMSO was dissolved in 500 mg of DMF. The solution was added dropwise to 10 mL of diethyl ether, in

which light yellow precipitate was formed after stirring for 5 min. The precipitate was collected and dried for 12 h under vacuum. For MAI·PbI_2·DMSO·urea and MAI·PbI_2·urea adduct, same procedure was repeated while corresponding amount of urea (1 mmol) was added to the solution.

Material Characterization

Fourier transform infrared spectroscopy (FT-IR) measurement was carried out by FT/IR-6100 (Jasco) with nitrogen gas purged. The films were prepared on sodium chloride substrate by dropping the precursor solution, which was followed by drying at 100 oC for 30 min. Surface and cross sectional morphology was investigated by scanning electron microscopy (SEM, Nova Nano 230) and atomic force microscopy (AFM, Bruker dimension Fast Scan) using peakforce tapping mode. 1ohm silicon tip (OTESPA, Bruker) was used to probe the morphology. X-ray diffraction patterns were recorded by X-ray diffractometer (PANalytical) with Cu kα radiation at a scan rate of 4 o/min. UV-vis spectra was acquired by U- 4100 spectrophotometer (Hitachi).

Conducting atomic force microscopy

Conducting atomic force microscopy (c-AFM) was measured by Bruker Dimension Icon Scanning Probe Microscope equipped with TUNA module using contact mode. The perovskite layers were prepared on SnO2 coated ITO substrate in which the ITO electrode was connected to the stage by silver paste. 0.01-0.025 ohm-cm Antimony (n) doped Si tip (SCM-PIC, Bruker) was used to probe the morphology and current with scan rate of 1.98 Hz.

Photoluminescence spectroscopy

Steady-state photoluminescence (PL) was measure by a Horiba Jobin Yvon system. A 640 nm monochromatic laser was used as an excitation fluorescence source. Time resolved PL decay

profile was obtained using a Picoharp 300 with time-correlated single-photon counting capabilities. A picosecond laser diode head (PLD 800B, PicoQuant) provided excitation at a wavelength of 640 nm with a repetition frequency of 100 kHz.

Admittance spectroscopy

Admittance spectroscopy measurement was carried out under dark without DC bias voltage to avoid the degradation of the device during the measurement. To measure the capacitance, 20 mV AC sinusoidal pulses with frequency from 20 Hz to 1MHz were applied to the devices. The x-axis was converted from angular frequency (ω) to $E\omega$ by measuring the attempt-to- escape frequency, which was obtained from frequency-dependent capacitance plot via relaxation process instead of Arrhenius plot of characteristic frequency.

Device characterization

Current density-voltage (J-V) curves were recorded using Keithley 2401 source meter under simulated one sun illumination (AM 1.5G, 100 mW/cm2) in ambient atmosphere. The one sun illumination was provided by Oriel Sol3A with class AAA solar simulator (Newport), in which light intensity was calibrated by NREL-certified Si photodiode equipped with KG-5 filter. The J-V curves were measured at 0.1 V/s. During the measurement, the device was covered with metal aperture (0.103 cm2) to define the active area. All the devices were measured without pre-conditioning such as light-soaking and applied bias voltage. Steady-state power output was recorded by measuring time-dependent photocurrent density under constant bias voltage. The external quantum efficiency (EQE) was measured using specially designed system (Enli tech) under AC mode without bias light.

5.7 References

1. Lee, J.-W. *et al.* A Bifunctional Lewis Base Additive for Microscopic Homogeneity in Perovskite Solar Cells. *Chem* **3**, 290–302 (2017).

2. deQuilettes, D. W. *et al.* Impact of microstructure on local carrier lifetime in perovskite solar cells. *Science* **348**, 683–686 (2015).

3. Leblebici, S. Y. *et al.* Facet-dependent photovoltaic efficiency variations in single grains of hybrid halide perovskite. *Nat. Energy* **1**, 16093 (2016).

4. Kutes, Y. *et al.* Mapping the Photoresponse of CH3NH3PbI3 Hybrid Perovskite Thin Films at the Nanoscale. *Nano Lett.* **16**, 3434–3441 (2016).

5. Yin, W.-J., Shi, T. & Yan, Y. Unique Properties of Halide Perovskites as Possible Origins of the Superior Solar Cell Performance. *Adv. Mater.* **26**, 4653–4658 (2014).

6. Liang, P.-W. *et al.* Additive Enhanced Crystallization of Solution-Processed Perovskite for Highly Efficient Planar-Heterojunction Solar Cells. *Adv. Mater.* **26**, 3748–3754 (2014).

7. Wei, Q. *et al.* Effective solvent-additive enhanced crystallization and coverage of absorber layers for high efficiency formamidinium perovskite solar cells. *RSC Adv.* **6**, 56807–56811 (2016).

8. Li, L. *et al.* The Additive Coordination Effect on Hybrids Perovskite Crystallization and High-Performance Solar Cell. *Adv. Mater.* **28**, 9862–9868 (2016).

9. Bae, S., Park, J.-S., Han, I. K., Shin, T. J. & Jo, W. H. CH3NH3PbI3 crystal orientation and photovoltaic performance of planar heterojunction perovskite solar cells. *Sol. Energy Mater. Sol. Cells* **160**, 77–84 (2017).

10. Xie, Y. *et al.* Enhanced Performance of Perovskite CH3NH3PbI3 Solar Cell by Using CH3NH3I as Additive in Sequential Deposition. *ACS Appl. Mater. Interfaces* **7**, 12937–12942 (2015).

11. Foley, B. J. *et al.* Controlling nucleation, growth, and orientation of metal halide perovskite thin films with rationally selected additives. *J. Mater. Chem. A* (2016). doi:10.1039/C6TA07671H

12. Saidaminov, M. I. *et al.* High-quality bulk hybrid perovskite single crystals within minutes by inverse temperature crystallization. *Nat. Commun.* **6**, 7586 (2015).

13. Nayak, P. K. *et al.* Mechanism for rapid growth of organic–inorganic halide perovskite crystals. *Nat. Commun.* **7**, 13303 (2016).

14. Niu, G., Yu, H., Li, J., Wang, D. & Wang, L. Controlled orientation of perovskite films through mixed cations toward high performance perovskite solar cells. *Nano Energy* **27**, 87–94 (2016).

15. Dong, Q. *et al.* Abnormal crystal growth in CH3NH3PbI3−xClx using a multi-cycle solution coating process. *Energy Environ. Sci.* **8**, 2464–2470 (2015).

16. Hou, C., Feng, W., Yuan, L., Huang, K. & Feng, S. Crystal facet control of LaFeO3, LaCrO3, and La0.75Sr0.25MnO3. *CrystEngComm* **16**, 2874–2877 (2014).

17. Huang, K., Yuan, L. & Feng, S. Crystal facet tailoring arts in perovskite oxides. *Inorg. Chem. Front.* **2**, 965–981 (2015).

18. Zhu, F. *et al.* Shape Evolution and Single Particle Luminescence of Organometal Halide Perovskite Nanocrystals. *ACS Nano* **9**, 2948–2959 (2015).

Chapter 6. 2-D perovskite phase stabilization

(This chapter is based on the publication *Nat. Comm*., *9*, 3021, 2018)

So far we have demonstrated the important roles that compositional and additive engineering play in modulating crystallization processes and defect natures of perovskite thin films. However, our approach thus far has been focused on passivation of GBs via small molecules, which can be easily dissociated from their GB locations by external stimuli owed to their relatively weak bonding nature. Here we focus on $FAPbI_3$, which is a more ideal material than $MAPbI_3$ owed to its higher theoretical efficiency potential (its E_g is closer to that of the ideal SQ limit absorber material) and its higher intrinsic thermal stability, which is a major shortcoming of $MAPbI_3$. $FAPbI_3$, however, is plagued by a poor intrinsic phase stability as it readily forms a notorious 'yellow-' or 'δ-' non-perovskite phase, which can greatly affect its efficiency and long-term stability. While compositional engineering has shown to be an effective means to overcome the phase purity issues of $FAPbI_3$, this comes alongside an undesirable increase in bandgap that sacrifices the device photo-current. Here we report the fabrication of phase-pure formamidinium-lead tri-iodide perovskite films with excellent optoelectronic quality and stability via incorporation of long chain phenylethylammonium (PEA) into the precursor solution.[1] The PEA inclusion resulted in an order of magnitude enhanced photoluminescence lifetime and a stabilized power conversion efficiency (PCE) of 20.64% (certified stabilized PCE of 19.77%) with a short-circuit current density exceeding 24 mA-cm^{-2} and an open-circuit voltage of 1.130 V, corresponding to a loss-in-potential of 0.35V, and significantly enhanced operational stability. PEA incorporation was found to not only modulate crystallization kinetics,

but spontaneously form a 2-D perovskite phase at the $FAPbI_3$ grain boundaries to protect the perovskite grains from moisture-induced degradation and to suppress ion migration.

6.1 Motivation

Compositional engineering has been considered an important approach to enhance the stability and performance of PVSK solar cells. Important milestones have been achieved through compositional engineering. For example, incorporation of the formamidinium (FA) cation into the A-site has enabled the formation of a cubic $FAPbI_3$ phase with a lower bandgap (E_g) of 1.48 eV, higher absorption coefficient and longer carrier diffusion lengths than methylammonium (MA)-based tetragonal $MAPbI_3$ (E_g = 1.57 eV). However, $FAPbI_3$ has poor ambient stability because its non-PVSK hexagonal phase is more thermodynamically favorable than the cubic phase at room temperature. Partial substitution of FA and I with MA and/or Br has enabled fabrication of phase-pure $FAPbI_3$ with improved performance and stability. Recently, incorporation of smaller inorganic A-site cations, such as Cs and Rb, have further improved the stability and PCE of $FAPbI_3$ solar cells with the lowest open-circuit voltage (V_{OC}) deficit of 0.39V. As a result, high efficiency devices now typically utilize FA, MA, Cs, Rb, and Br in the perovskite structure, having a relative E_g larger than 1.60 eV. However, such compositional engineering has enhanced the V_{OC} and stability at the expense of short-circuit current density (J_{SC}) due to the increased E_g. Utilization of pure $FAPbI_3$ is desired in regards to its lower E_g, which is close to the optimum value for a single junction solar cell suggested by the detailed balance limit. However, no efficient method has been developed so far to fabricate high-quality phase-pure $FAPbI_3$ films and devices.

6.2 State of the art and challenges

Recently, the manipulation of surface energy has been proposed as a means to stabilize metastable PVSK phases such as $CsPbI_3$ and $FAPbI_3$. Swarnkar et al. reported ambient stable α-$CsPbI_3$ in the form of a colloidal quantum dot, in which the contribution of surface energy significantly increases due to the high surface-to-volume ratio. Very recently, Fu et al. reported that the cubic $FAPbI_3$ phase can be stabilized by functionalizing the surface with large-sized organic molecules. They demonstrated that the functionalized surface constitutes a lower formation energy that stabilizes the cubic $FAPbI_3$ phase at room temperature. However, the steady-state PCE was as low as 14.5%. Several attempts have been made to utilize this approach, where impressive improvements in performance and stability have been demonstrated. Li et al. reported compositional engineering of $FAPbI_3$ with PEA as a partial substitution of the FA A-site, as $FA_{1-x}PEA_xPbI_3$, where quasi-3D structure can be formed that consists of PEA within the lattice (to a small extent) and also at grain boundaries to serve as passivating agents.[2] They reported that the long hydrophobic chain of the PEA molecule can increase the transition energy from the black to yellow phase and help to improve moisture-related stability of the perovskite film. This work resulted in a device efficiency of 17.7%. Similarly, Zhou et al. demonstrated use of benzylamine (BA) in a FA, Cs, I, and Br based perovskite as a means to prevent phase segregation of the mixed perovskite and provide similar passivating and hydrophobic effects, achieving an efficiency of 18.1%.[3] BA was also shown to create a 3D-2D heterostructure where secondary platelet-like 2D BA perovskite phases formed between 3D perovskite grains at GBs, resulting in greatly enhanced crystallinity and passivation of defects.[4] The FA, Cs, I, Br based perovskite device achieved an efficiency of 17.6 with a 1.61 eV band gap, and 15.8% with a 1.72 band gap alongside 80% PCE retention over 1,000 hours in ambient air. While these works have

shown that incorporation of large organic A-site molecules can be beneficial, their performance and stability are still relatively poor comparing with those of $MAPbI_3$ or mixed-cation-halide PVSK solar cells. Here we report a method to fabricate high-quality stable $FAPbI_3$ PVSK films via addition of 2D phenylethylammonium lead iodide (PEA_2PbI_4) in the precursor solution. The 2D PEA_2PbI_4 is spontaneously formed at the grain boundaries of $FAPbI_3$ to protects the $FAPbI_3$ from moisture and assists in charge separation/collection. Owed to its superior optoelectronic quality, solar cells with a stabilized efficiency of 20.64% (certified stabilized efficiency of 19.77%) were fabricated. Notably, the PVSK solar cell shows a peak V_{OC} of 1.130 V, corresponding to a loss-in-potential of 0.35 V considering the E_g of 1.48 eV versus 0.39 V for mixed-cation-halide perovskite solar cells. Furthermore, the device demonstrates significantly enhanced ambient and operational stability.

6.3 Results and discussion

6.3.1 Effects of 2D perovskite on phase purity of $FAPbI_3$

$FAPbI_3$ films were prepared by the modified adduct method, in which N-methyl-2-pyrrolidone (NMP) was used as the Lewis base to form an intermediate adduct phase prior to crystallization. 2-dimensional (2D) PEA_2PbI_4 precursors with different molar ratios ranging from 1.25 to 10 mol% were added to the $FAPbI_3$ perovskite solution. The steady-state PL spectra of the films were measured and are shown in Figure 6-1. A PL intensity enhancement is seen for 2D PEA_2PbI_4 addition up to 5 mol%, after which the intensity decreased again towards that of the bare $FAPbI_3$ film Figure 6-1a.

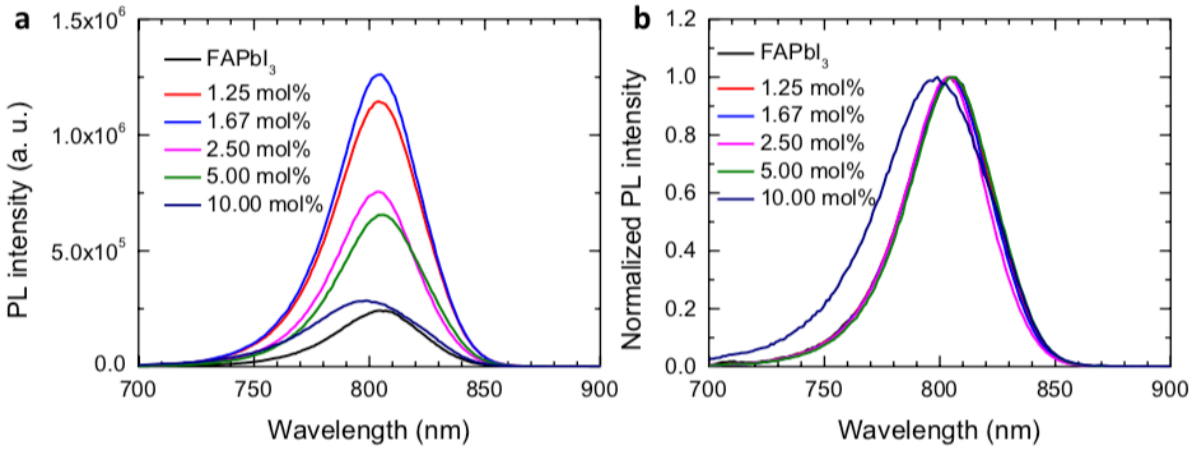

Figure 6-1: Steady-state photoluminescence spectra of $FAPbI_3$ perovskite film with different amount of added 2D PEA_2PbI_4 perovskite. (a) Original and (b) normalized spectra.

As seen in Figure 6-1b, we observed no obvious changes in PL peak position until the amount of PEA_2PbI_4 reached 10 mol%, for which the PL peak blue-shifted by 6 nm. This blue-shift may be due to the formation of quasi-3D PVSK, where charge carriers are confined by a large potential barrier originating from the PEA_2PbI_4. Based on this observation, we presume the added PEA_2PbI_4 does not result in the formation of the quasi-3D PVSK if it remains below a certain threshold (Figure 6-2a). This quantity was then optimized based on photovoltaic performance. A planar heterojunction architecture consisting of Indium doped SnO_2 (ITO) glass/compact-SnO_2/PVSK/spiro-MeOTAD/Ag or Au was utilized for construction of PVSK solar cells in this study. The addition of 1.67 mol% PEA_2PbI_4 was found to be optimal for photovoltaic performance, with an improvement in PCE of 11%. Notably, addition of 10 mol% PEA_2PbI_4 significantly degraded the PCE to lower than 1%, which might result from the formation of

quasi-3D PVSK as the large potential barrier originating from PEA_2PbI_4 could hinder charge transport. Hence, an optimized 1.67 mol% PEA_2PbI_4 was used for further analysis.

X-ray diffraction patterns (XRD) of pure $FAPbI_3$ and $FAPbI_3$ with 1.67 mol% PEA_2PbI_4 are shown in Figure 6-2b. As can be seen, the bare $FAPbI_3$ film contains a hexagonal non-PVSK phase (δ- phase) while the PVSK film prepared with 1.67 mol% PEA_2PbI_4 shows a pure PVSK phase. Furthermore, the overall signal intensity and full-width-half-maximum (FWHM) were enhanced with the addition of PEA_2PbI_4, indicating improved crystallinity. We speculate that the added large PEA molecules from PEA_2PbI_4 precursors interact with $FAPbI_3$ crystals to facilitate formation of the cubic PVSK phase during crystallization. Such a speculation is correlated with the XRD analysis, in which the signal intensity and FWHM of the XRD peaks are enhanced in accordance with the increased amounts of PEA_2PbI_4 added. The enhancement of preferred orientation along the (001) plane with increased PEA_2PbI_4 also indicates that the added precursors of PEA_2PbI_4 functionalize a specific crystal facet to change its surface energy during crystal growth, thereby promoting the growth of the (001) orientation. A closer inspection of the normalized XRD patterns of the PVSK films with different amounts of added PEA_2PbI_4 found that a systematic change in peak position was observed with different amounts of PEA_2PbI_4 for which the XRD peaks were slightly shifted toward higher angles with the addition of relatively smaller amounts of PEA_2PbI_4 (1.25, 1.67, 2.50, and 5.0 mol%). This indicates that the lattice constant of $FAPbI_3$ is reduced, likely due to compressive strain associated with the added PEA_2PbI_4. We speculate that the reduction in lattice constant can be also related to the enhanced phase purity of cubic $FAPbI_3$ as it will have equivalent effects with incorporation of smaller A-site cations on the tolerance factor and thus enthalpy of formation. Lower angle peaks around 12° appear upon addition of 10 mol% PEA_2PbI_4 corresponding to the formation of quasi-3D PVSK.

The pure phase PVSK film with 1.67 mol% PEA_2PbI_4 shows enhanced absorption over all wavelengths (Figure 6-2c) compared to the bare $FAPbI_3$ film where the absorption onset is hardly changed (inset of Figure 6-2c). The absorption onset is complemented by an almost identical normalized PL spectra, which indicates that the E_g was maintained. The enhanced absorption as seen when the PEA_2PbI_4 was added is probably due to an enhanced phase purity of the $FAPbI_3$, with partial contribution from an enhanced light scattering owing to the improved crystallinity.

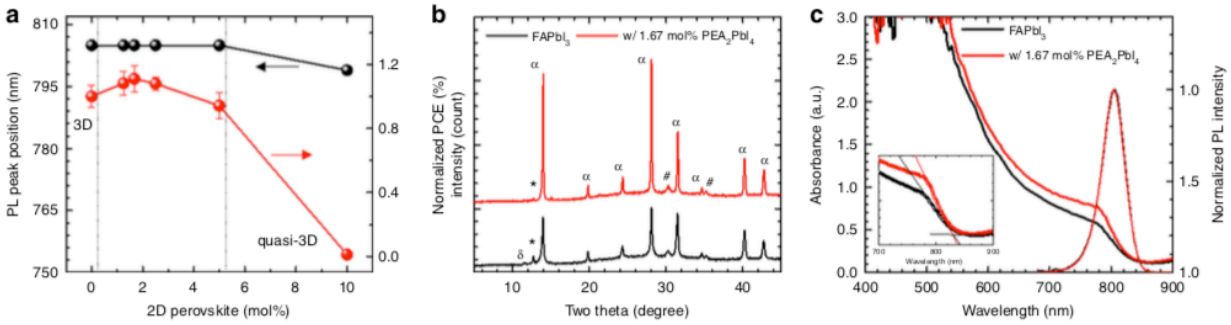

Figure 6-2: Crystallographic and absorption properties. a Peak position for steady-state photolumimescence (PL) spectrum and normalized power conversion efficiency (PCE) of the devices for $FAPbI_3$ perovskite with different amount of added 2D PEA_2PbI_4 perovskite. The error bar of the normalized PCE indicates standard deviation of the PCEs. At least 10 devices were fabricated for each condition. b X-ray diffraction patterns, c absorption and normalized PL spectra of bare $FAPbI_3$ and $FAPbI_3$ with 1.67 mol% PEA_2PbI_4. Inset of c shows onset region of the absorption spectra with linear approximation (solid lines).

6.3.2 Optoelectronic properties: PL and device efficiency

Steady-state (SS) and time-resolved PL (TRPL) characteristics were investigated (Figure 6-3). The steady-state PL intensity was largely enhanced more than five times from 4.3×10^5 to 2.3×10^6 with addition of 1.67 mol% PEA_2PbI_4 into $FAPbI_3$ film (Figure 6-3a). The large enhancement of PL intensity was attributed to a significantly elongated PL lifetime as seen in Figure 6-3b. The TRPL profiles were fitted with an exponential decay, in which bi- and tri-exponential decay models were used for the pure $FAPbI_3$ and PEA_2PbI_4 incorporated $FAPbI_3$ films, respectively. The relatively fast decay component (τ_1 around 3 ns) represents charge carrier trapping induced by trap states formed due to structural disorders, such as vacancy or interstitial defects, while the much slower components (τ_2, τ_3) represent free carrier radiative recombination. With addition of 1.67 mol% PEA_2PbI_4, the proportion of the fast decay component (τ_1) was decreased (from 51.8% to 46.5%) while τ_2 significantly elongated from 78.5 ns to 148.7 ns. This indicates a reduced defect density and enhanced charge carrier lifetime. We attributed such improvements to enhanced phase purity and crystallinity of $FAPbI_3$ as observed from the XRD measurements (Figure 6-2b), which decreases the structural disorders at grain interiors and/or boundaries. Moreover, a new decay component (τ_3) with a significantly long lifetime (>1 μs) appeared after addition of the PEA_2PbI_4, which is likely related to the added 2D PVSK. As a result, the average PL lifetime was enhanced by nearly an order of magnitude from 39.4 to 376.9 ns with addition of PEA_2PbI_4. During the optimization of the device, incorporation of 2 mol% Cs was found to further enhance the performance and reproducibility of the devices without a noticeable change in E_g. With additional 2 mol% Cs, the fraction of τ_1 was further decreased, indicating a further decreased defect density, which has also been observed in

previous studies. Consequently, the steady-state PL intensity and average PL lifetime were further enhanced, rationalizing the improved PCE with 2 mol% Cs.

The PCE distribution of the devices with different amounts of PEA_2PbI_4 and Cs are compared in Figure 6-3c. The average PCE of the bare $FAPbI_3$ PVSK solar cells was significantly enhanced by 13% from 15.95 ± 0.36% to 18.08 ± 0.52% with addition of 1.67 mol% PEA_2PbI_4. The average PCE was further enhanced to 19.16 ± 0.37% with 2 mol% of Cs Current density and voltage (J–V) curves of the optimized control and target devices are demonstrated in Figure 6-3d, in which the highest PCE of the target device reached 21.06% (J_{SC}: 24.44 mA-cm^{-2}, V_{OC}: 1.126V, FF: 0.765) while a PCE of 16.41% was achieved with the control device (J_{SC}: 24.23 mA-cm^{-2}, V_{OC}: 1.048V, FF: 0.646). A stabilized PCE of 20.64% was achieved with the target device while that of control device was 15.80% (Figure 6-3e). External quantum efficiency (EQE) spectra of the devices were compared in Figure 6-3f. An integrated J_{SC} of 23.9 mA-cm^{-2} from the target device was well-matched with the value measured from the J–V scan (<5% discrepancy), while control device shows that of 21.2 mA-cm^{-2} with a relatively large discrepancy of 14%. The relatively large discrepancy from the control $FAPbI_3$ device is probably due to a more pronounced hysteresis, as seen in Figure 6-3d, which also results in a large discrepancy between the stabilized PCE and the PCE measured from the J–V scan. The performance of control device was highly reproducible.

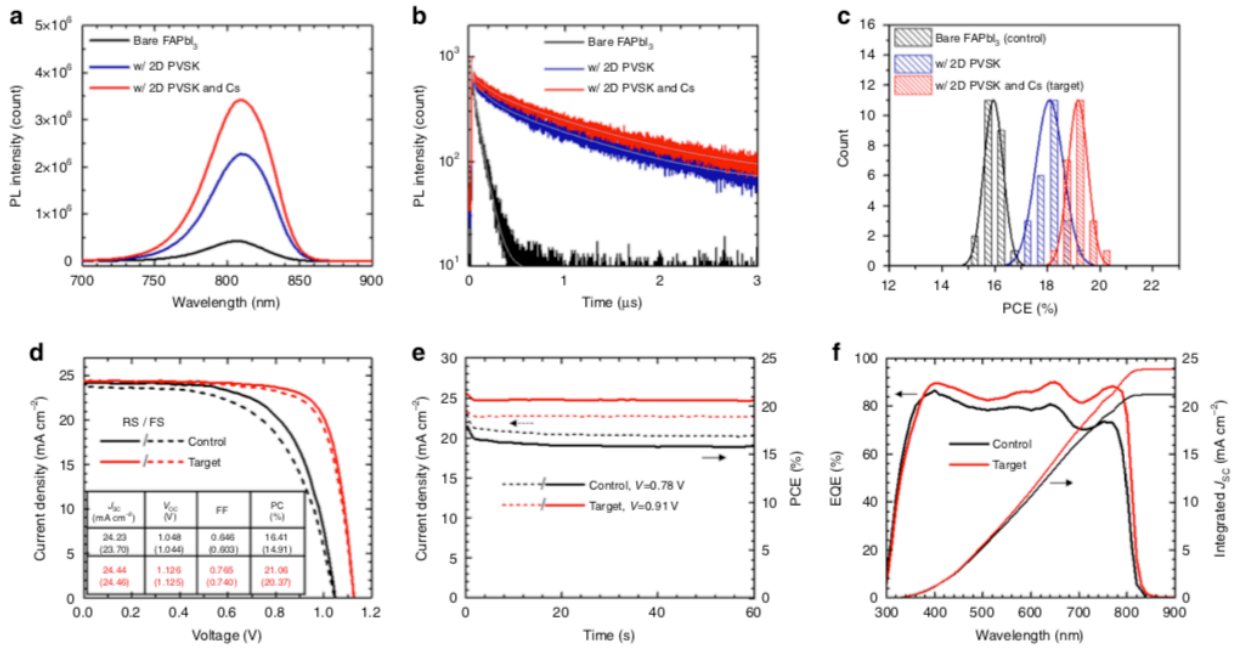

Figure 6-3: Photoluminescence properties and photovoltaic performance. a) Steady-state and b time resolved PL spectra of the perovskite films incorporating bare $FAPbI_3$, $FAPbI_3$ with 2D perovskite and $FA_{0.98}Cs_{0.02}PbI_3$ with 2D perovskite. Gray solid lines in b) are fitted lines for each curve. c) Power conversion efficiency (PCE) distribution of the devices incorporating the perovskites. All the devices were fabricated in same batch. d) Current density–voltage (J–V) curves, e steady-state PCE measurement and f external quantum efficiency (EQE) spectra of perovskite solar cells incorporating bare $FAPbI_3$ (control) and $FA_{0.98}Cs_{0.02}PbI_3$ with 2D perovskite (target). Photovoltaic parameters of the highest performing devices are summarized in the table in d), in which the values with and without parenthesis are from reverse (from VOC to J_{SC}) and forward scan (from J_{SC} to V_{OC}), respectively.

With optimized process parameters, an average PCE of 20.05 ± 0.45% was demonstrated, with a peak V_{OC} of 1.130V corresponding to a loss-in-potential of 0.35 V considering a E_g of 1.48 eV,

which is the lowest V_{OC} deficit reported to date for PVSK solar cells. One of the target devices was sent out for measurement in an independent laboratory and achieved a certified stabilized PCE of 19.77%. The enhanced device performance with PEA_2PbI_4 is mainly due to improved FF and V_{OC}, which can be attributed to improved phase purity and elongated carrier lifetime with reduced defect density, facilitating carrier transport and reducing the charge recombination.

6.3.3 The role of PEA_2PbI_4

Under ambient conditions, cubic $FAPbI_3$ can readily undergo conversion to a hexagonal non-PVSK phase, resulting in serious degradation in photovoltaic performance. The phase transformation is even accelerated under high-relative humidity conditions. To evaluate the effects of PEA_2PbI_4 incorporation on phase stability, we investigated changes in absorbance of the film under relative humidity (RH) of 80 ± 5%. Figure 6-4a shows photos of the PVSK film stored for different time periods. The bare $FAPbI_3$ film was almost completely bleached within 24 hours whereas no obvious change in color was observed for the films containing PEA_2PbI_4 both with and without Cs. Figure 6-4b demonstrates the absorbance (at 600 nm) of the $FAPbI_3$ films with and without PEA_2PbI_4 as a function of exposure time. The absorbance of the bare $FAPbI_3$ rapidly degraded within 24 hours, while $FAPbI_3$ films with PEA_2PbI_4 did not show noticeable degradation within 24 hours. Similarly, films with 2 mol% Cs also remained stable after 24 hours. The color change of the bare $FAPbI_3$ film under high RH is was shown to be due to its transformation to the δ-phase based on XRD spectra (Supplementary Figure 21 of the manuscript), whereas no detectable change in color for the films with PEA_2PbI_4 is correlated with their neat XRD spectra without the δ- phase. The enhanced phase stability under high RH

implies that the possible ingression pathway of moisture in the PVSK film is passivated. The concept from our previous works demonstrating grain boundary engineering techniques using the adduct approach, in which the additives precipitate at grain boundaries if not incorporated into the lattice of PVSK, can be extended to this work as well. Here, we postulate that grain boundaries within the film, which have been reported to be ingression pathways for moisture, might be passivated by the added PEA_2PbI_4.

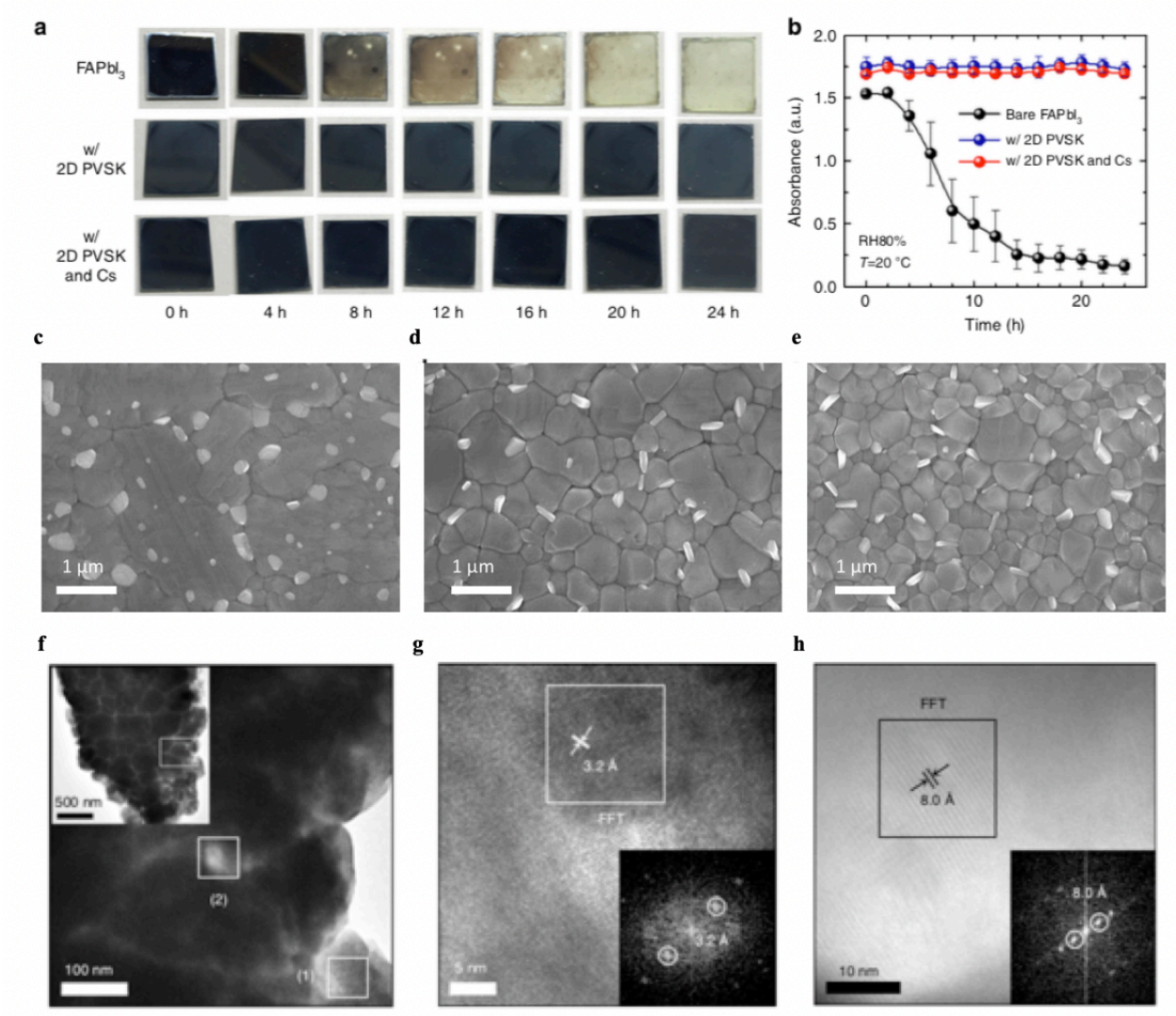

Figure 6-4: Improved moisture stability with 2D perovskite at grain boundaries. a) Photos of the perovskite films incorporating bare $FAPbI_3$, $FAPbI_3$ with PEA_2PbI_4 and $FA_{0.98}Cs_{0.02}PbI_3$ with PEA_2PbI_4 exposed to relative humidity (RH) of 80 ± 5% at 20 ± 2 °C for different time. b) Evolution of absorption of the films at 600 nm under RH 80 ± 5% at 20 ± 2 °C. The error bar indicates standard deviation of the absorbance measured from three films for each condition. c-e) top down SEM images of bare $FAPbI_3$, $FAPbI_3$ with PEA_2PbI_4 and $FA_{0.98}Cs_{0.02}PbI_3$ with PEA_2PbI_4. f-h) Transmission electron microscopic (TEM) images of the $FA_{0.98}Cs_{0.02}PbI_3$ film with 1.67 mol% PEA_2PbI_4. The inset of f demonstrates the lower magnification image showing

the polycrystalline nature with grain boundaries. The highlighted area (1) and (2) were investigated in d and e, respectively. Inset of h and h show Fast Fourier transform (FFT) analysis of the area within boxes, respectively.

The vertically aligned PEA_2PbI_4 was sparsely observed in SEM images (Figure 6-4c-e) with addition of PEA_2PbI_4. However, the enhanced moisture stability throughout the whole-film implies that PEA_2PbI_4 most likely exists along the grain boundaries. To confirm our assumption, transmission electron microscopic (TEM) images of the $FAPbI_3$ film with PEA_2PbI_4 was analyzed in Figure 6-4f–h. The inset of Figure 6-4c shows a piece of the polycrystalline film scratched off from the substrate. Several hundreds of nanometer sized grains and associated GBs are clearly visible from the image, and from which one of the grains is magnified in Figure 6-4c. The grain interior region, region (1), in Figure 6-4c was magnified and analyzed using Fast Fourier transform (FFT) in Figure 6-4d, in which an inter-planar spacing of 3.2 Å is well-matched with the (002) reflection of cubic $FAPbI_3$. The GB region, which is labeled region (2), reveals an inter-planar distance of 8.0Å (Figure 6-4e), which is well matched with the characteristic (002) reflection of 2D PEA_2PbI_4. This confirms the presence of 2D PEA_2PbI_4 at grain boundaries.

A schematic in Figure 6-5a shows PEA_2PbI_4 formation at the grain boundaries of the 3D PVSK film. Due to the aromatic rings and longer alkyl chains of PEA, PEA_2PbI_4 is expected to be more resistant to moisture-induced degradation and will protect the defective grain boundaries of 3D $FAPbI_3$ to provide significantly enhanced moisture stability of the film. Regardless of the improved stability, however, one can expect degraded electronic properties of the film due to the poor charge carrier mobility of PEA_2PbI_4. We investigated the band structure of $FA_{0.98}Cs_{0.02}PbI_3$ (with 1.67mol% PEA_2PbI_4) and PEA_2PbI_4, which is illustrated in Figure 6-5b. The VBM was

measured using ultraviolet photoelectron spectroscopy (UPS, Supplementary Fig. 25), while the E_g was determined from Tauc plots of absorption measurements (Supplementary Fig. 26). As seen in Figure 6-5b, $FA_{0.98}Cs_{0.02}PbI_3$ and PEA_2PbI_4 show a type I band alignment, which resembles the alignment between PVSK and PbI_2 formed at grain boundaries that has been found to reduce charge carrier recombination and assist in charge separation/collection. Thus, an analogous advantage of PEA_2PbI_4 at GBs can be expected. c-AFM was performed in Figure 6-5c-f to observe the spatially-resolved electrical properties of the films on the nano-to-micro scale. Under ambient light conditions (Figure 6-5c,d), current flow in the PVSK film with PEA_2PbI_4 was higher at/near the grain boundaries while relatively uniform current flow was observed in the bare $FAPbI_3$ film. With light illumination (Figure 6-5e,f), the current flow was further enhanced at/near the grain boundaries with PEA_2PbI_4 whereas current flow in the bare $FAPbI_3$ film was uniformly increased. This suggests that the charge separation and collection of photo-generated electrons is facilitated more effectively at grain boundaries with PEA_2PbI_4. As suggested for PbI_2, thin PEA_2PbI_4 regions at grain boundaries might suffer a downwards band-bending under illumination (dashed line in Figure 6-5b), where photo-generated electrons are transferred from grain interiors to GBs. Due to the high-potential barrier to the holes, charge recombination will be reduced, which might be the origin of the superior PL lifetime and photovoltaic performance seen through use of PEA_2PbI_4.

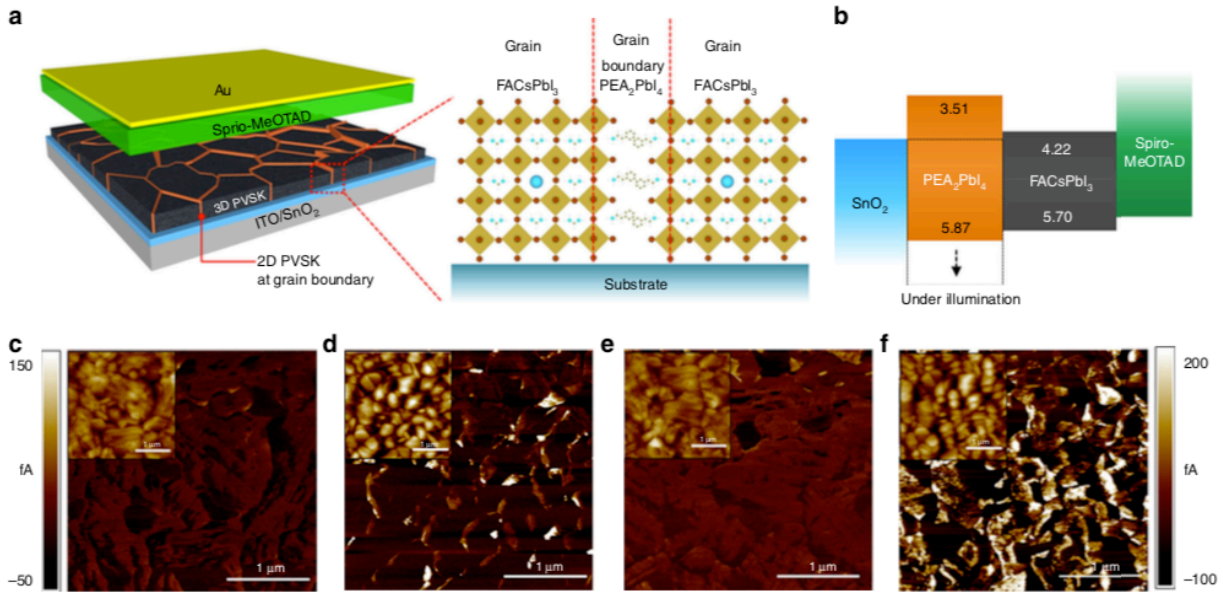

Figure 6-5: Band alignment and local conductivity with 2D perovskite. a Schematics of the device incorporating polycrystalline 3D perovskite film with 2D perovskite at grain boundaries and b band structure of each layer in device analyzed by ultraviolet photoelectron spectroscopy (UPS) and Tauc plots. Conductive atomic force microscopic (c-AFM) images of (c, e) bare $FAPbI_3$ and (b, d) with 2D perovskite films on SnO_2 coated ITO glass. The measurement was carried out with bias voltage of 100 mV under (c, d) room light or (d, f) low intensity light illumination provided by the AFM setup. Inset of each image shows corresponding topology of the films. Scale bar at left side is for (c) and (d) while at right side is for e and f.

6.3.4 Stability of PEA_2PbI_4-$FAPbI_3$

The stability of the control and target devices was compared. Figure 6-6a demonstrates the changes in PCE of the un-encapsulated devices stored in a desiccator with a relative humidity lower than 30%. While the control device degraded by 29% over 1392 hours, the PEA_2PbI_4–

based device maintained 98% of its initial efficiency during this time. The operational stability of the devices was also compared by maximum power point (MPP) tracking under 1 sun illumination in Figure 6-6b. Without encapsulation, the PCE of the control device rapidly degraded by 68% over 450 min whereas that of target device was relatively less (20%) during the time period. We performed 500 hours of light exposure test with the encapsulated control (bare $FAPbI_3$ device) and target devices (w/ 1.67 mol% PEA_2PbI_4). The encapsulated devices were exposed to ca. 0.9 sun (90 ± 5 mW cm^{-2}) under open-circuit condition, of which the steady-state PCE was periodically measured for different exposure times. As seen in Figure 6-6c, both of the devices showed a rapid initial decay in PCE followed by slower decay with an almost linear profile, which is in agreement with previous reports.

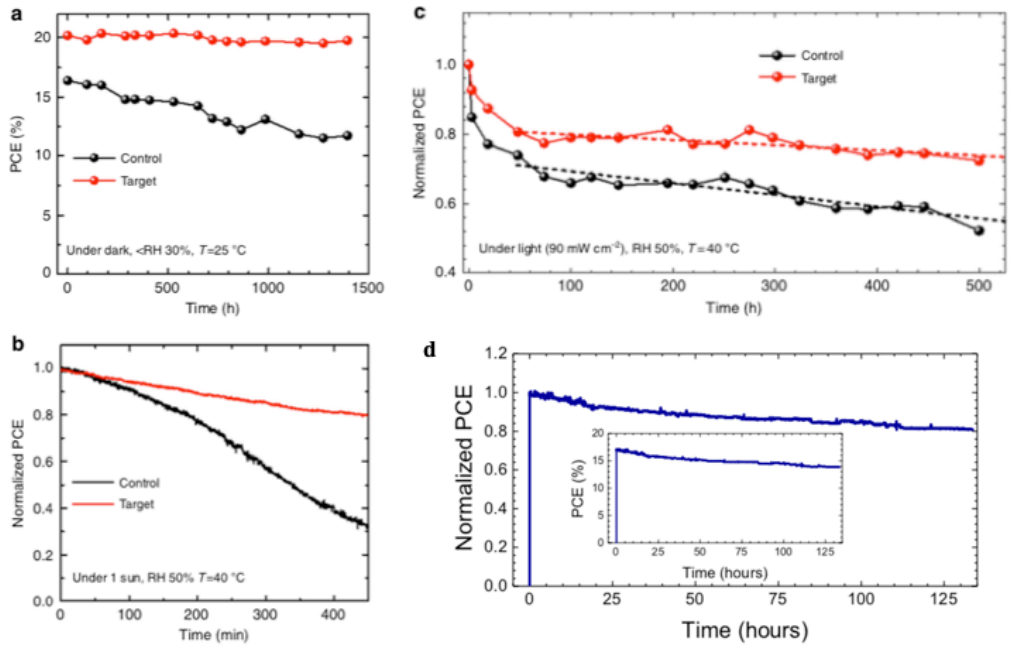

Figure 6-6: Improved stability with 2D perovskite. a) Evolution of power conversion efficiency (PCE) of control and target devices. The devices were stored under dark with controlled humidity. b) Maximum power point tracking of the devices under 1 sun illumination in ambient

condition without encapsulation. c) Evolution of the PCEs measured from the encapsulated control and target devices exposed to continuous light (90 ± 5 mW cm−2) under open-circuit condition. The stabilized PCEs were measured at each time. Initial stabilized PCEs for control and target devices were 14.5% and 17.5%, respectively. The broken lines are linear fit of the post-burn-in region (after 48 h). Relative humidity (RH) and temperature (T) are indicated in the graphs for each measurement. d) Maximum power point tracking of the target device. The measurement was performed under 1 sun illumination in ambient condition with encapsulation. Inset of the figure shows the PCE without normalization.

After 500 hours of exposure, the control device degraded to approximately 52.3% of its initial PCE whereas the target device maintained 72.3% of the initial PCE, indicating enhanced stability with addition of PEA_2PbI_4. We can extract the tentative time at which the PCE of the device decays to 80% of its initial PCE, denoted as T_{80}, for the devices via fitting of the post-burn-in region in which the PCE of the device shows a near linear decay profile (after 48 h). The T_{80} for control and target devices were calculated to be 592 hours and 1362 hours, respectively. This indicates the stability of the device was significantly improved with addition of PEA_2PbI_4. We also performed maximum power-point (MPP) tracking of the encapsulated target device under 1 sun (100 mW-cm^{-2}) illumination in Figure 6-6d. A total of 18.7% of initial PCE was degraded for 130 hours of operation, which is relatively slower compared to the device maintained at open-circuit condition. This is correlated with previous studies that attributed the faster degradation under open-circuit condition to larger number of photo-generated charge carriers recombining within the device. Under operational condition with abundant photo-generated charges and a built-in electric field, the major factors causing degradation might be the highly mobile and reactive charged defects (ions) and/or associated trapped charge carriers. We

suppose that the migration of charged (ionic) defects is possibly suppressed by PEA_2PbI_4 at grain boundaries. Temperature-dependent conductivity (σ) measurement of the lateral devices was performed to evaluate the activation energy for the ion migration (Fig. 6). The activation energy (E_a) for the migration can be determined according to the Nernst-Einstein relation,

$$\sigma(T) = \frac{\sigma_0}{T} exp\left(\frac{-E_A}{kT}\right)$$

where *k* is the Boltzmann constant and σ_0 is a constant. The inset of Figure 6-7a describes the structure of the lateral devices. With bare $FAPbI_3$, exponential enhancement in conductivity was clearly identified at around 130 K (Figure 6-7a), which is attributed to the contribution of ions. The E_a for the bare $FAPbI_3$ film was calculated to be 0.16 eV, indicating a significant contribution coming from activated ions at RT, which might cause degradation of the material and device under operational condition with built-in electric field. The pronounced current–voltage hysteresis behavior was observed even at very low temperature (180 K, Figure 6-7c). In the case of the $FAPbI_3$ film with PEA_2PbI_4, the film did not show noticeable enhancement in conductivity with increased temperature. However, the overall conductivity was relativity lower than the bare $FAPbI_3$ film (Figure 6-7c). Even with moderate light illumination the device does not show any indication of activated ions. As a result, the I-V curve does not display any hysteresis behavior (Figure 6-7d). Since GBs of 3D perovskites have been reported to be a major pathway for the migration of ions, passivation of GBs via incorporation of PEA_2PbI_4 likely suppresses the overall ion migration in the device. In addition, the improved phase purity of the film might also partially contribute to the suppressed ion migration since the secondary phase can generate defect sites that can act as an additional pathways for ion migration. We believe the suppressed ion migration contributes to enhanced operational stability of the target device.

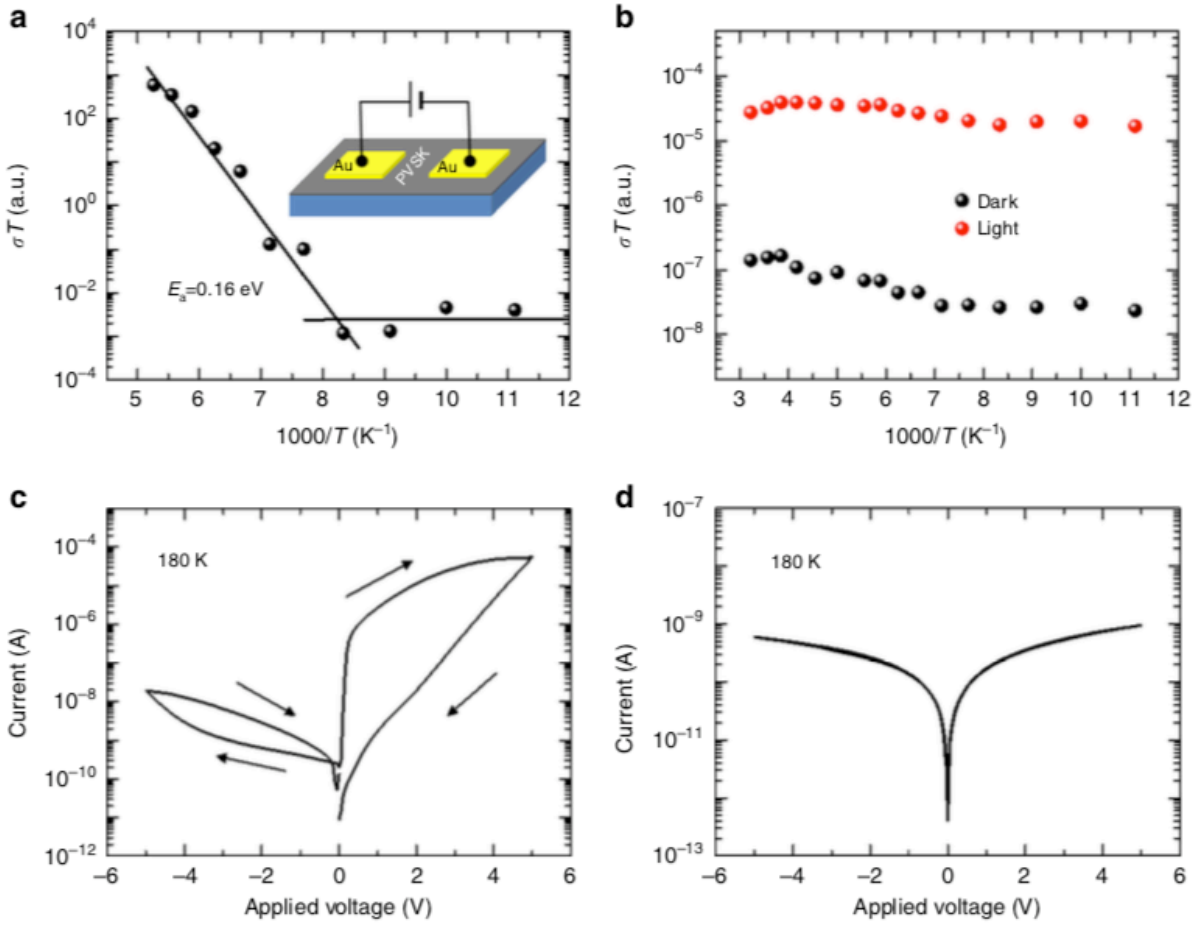

Figure 6-7: Suppressed ion migration with 2D perovskite. Temperature-dependent conductivity of a bare $FAPbI_3$ film and b with 1.67 mol% PEA_2PbI_4. Red circles in b indicate the data measured under moderate light illumination (intensity lower than 10 mW cm−2). Current–voltage curves measured from the devices at 180 K. c Bare $FAPbI_3$ film and d with 1.67 mol% PEA_2PbI_4.

6.4 Summary

In this work, we have demonstrated a reproducible method to fabricate phase-pure formamidinium tri-iodide PVSK with high-optoelectronic quality and stability by incorporating a small amount of 2-dimensional PEA_2PbI_4 perovskite phase. The large phenylethylammonium molecules of PEA_2PbI_4 precursors interact with $FAPbI_3$ crystals to facilitate formation of the cubic $FAPbI_3$ phase during crystallization, which subsequently functionalize grain boundaries after crystallization is complete. The resulting phase-pure PVSK film has an identical E_g to that of pure $FAPbI_3$ (1.48 eV) with an order of magnitude enhanced PL lifetime. An average PCE of 20.05 ± 0.45% with a highest stabilized PCE of 20.64% (certified stabilized PCE of 19.77%) was achieved. Regardless of its low E_g, the solar cell showed a peak V_{OC} of 1.130 V, corresponding to the lowest loss-in-potential of 0.35 V among all the reported PVSK solar cells. Owed to the functionalized grain boundaries by the 2D PEA_2PbI_4, the phase stability of the film under high relative humidity significantly improved and migration of ions (or charged defects) was suppressed, resulting in significantly improved ambient and operational stability of the device. Utilizing 2D perovskites, such as PEA_2PbI_4, at GBs will provide important insights for the research community to design PVSK materials to truly create highly efficient and durable solar cells for long-term field use.

6.5 Experimental

Synthesis of phenylethylammonium iodide

In a typical synthesis, 4.8 g of phenethylamine (39.6 mmol, Aldrich, >99%) was dissolved in 15 mL of ethanol and placed in iced bath. Under vigorous stirring, 10.8 g of hydroiodic acid (57 wt% in H_2O, 48.1 mmol, Sigma-Aldrich, 99.99%, contains no stabilizer) was slowly added to the solution. The solution was stirred overnight to ensure complete reaction, which was followed by removal of the solvent by a rotary evaporator. The resulting solid was washed with diethyl ether several times until the color is changed to white. The white solid was further purified by recrystallization in mixed solvent of methanol and diethyl ether. Finally, white plate-like solid was filtered and dried under vacuum (yield around 90%).

Device fabrication

Indium doped tin oxide (ITO) glass was cleaned with successive sonication in detergent, deionized (DI) water, acetone and 2-propanol for 15 min, respectively. The cleaned substrates were further treated with UV-ozone to remove the organic residual and enhance the wettability. A total of 30 mM $SnCl_2{\cdot}2H_2O$ (Aldrich, >99.995%) solution was prepared in ethanol (anhydrous, Decon Laboratories Inc.), which was filtered by 0.2 μm syringe filter before use. To form a SnO_2 layer, the solution was spin-coated on the cleaned substrate at 3000 rpm for 30 s, which was heat-treated at 150 °C for 30 min. After cooling down to room temperature, the spin-coating process was repeated one more time, which was followed by annealing at 150 °C for 5 min and 180 °C for 1 h. The SnO_2 coated ITO glass was further treated with UV-ozone before spin-coating of PVSK solution. The PVSK layer was prepared by the modified adduct method. The bare $FAPbI_3$ layer was formed from the PVSK solution containing equimolar amount of $HC(NH_2)_2I$ (FAI, Dyesol), PbI_2 (TCI, 99.99%) and N-Methyl-2-pyrrolidone (NMP, Sigma-

Aldrich, anhydrous, 99.5%) in N,N-Dimethylformamide (DMF, Sigma- Aldrich, anhydrous, 99.8%). Typically, 172 mg of FAI, 461 mg of PbI_2 and 99 mg of NMP were added to 600 mg of DMF. For the 2D PVSK (PEA_2PbI_4) and Cs incorporated PVSK, corresponding amount of FAI was replaced with PEAI and CsI. For example, $FAPbI_3$ with 1.67 mol% PEA_2PbI_4 was formed from a precursor solution containing 166.4 mg of FAI, 8.2 mg of phenylethylammonium iodide (PEAI), 453.4 mg of PbI_2 and 97.4 mg of NMP in 600 mg of DMF. With 2 mol% of Cs, the precursor solution was prepared by mixing 163.0 mg of FAI, 8.2 mg of PEAI, 5.0 mg of CsI (Alfa Aesar, 99.999%), 453.4 mg of PbI_2 and 97.4 mg of NMP in 600 mg. For the best performing devices, the amount of DMF was adjusted to 550 mg. Spin-coating of PVSK and hole transporting layer was performed in a glove box filled with dry air. The PVSK solution was spin-coated at 4000 rpm for 20 s where 0.15 mL of diethyl ether (anhydrous, >99.0%, contains BHT as stabilizer, Sigma-Aldrich) was dropped after 10 s on the spinning substrate. The resulting transparent adduct film was heat-treated at 100 °C for 1 min followed by 150 °C for 10 min. (for the best performing target device, the annealing condition was adjusted to 80 °C 1 min followed by 150 °C for 20 min) The spiro-MeOTAD solution was prepared by dissolving 85.8 mg of spiro-MeOTAD (Lumtec) in 1 mL of chlorobenzene (anhydrous, 99.8%, Sigma-Aldrich) which was doped by 33.8 µl of 4-tert-butylpyridine (96%, Aldrich) and 19.3 µl of Li-TFSI (99.95%, Aldrich, 520 mg mL^{-1} in acetonitrile) solution. The spiro-MeOTAD solution was spin-coated on the PVSK layer at 3000 rpm for 20 s by dropping 17 µl of the solution on the spinning substrate. On top of the spiro-MeOTAD layer, ca. 100 nm-thick silver or gold layer was thermally evaporated at 0.5 Ås−1 to be used as an electrode.

Material characterization

The PVSK layer was coated on a SnO_2 coated ITO substrate for the measurements. UV-vis absorption spectra were recorded by U- 4100 spectrophotometer (Hitachi) equipped with integrating sphere. The mono-chromatic light was incident to the substrate side. XRD patterns were obtained by X-ray diffractometer (PANalytical) with Cu kα radiation at a scan rate of 4° min^{-1}. Surface and cross-sectional morphology of the films and devices were investigated by scanning electron microscopy (SEM, Nova Nano 230). For the cross-sectional image, cross-sectional surface of the sample was coated with ca. 1 nm-thick gold using sputter to enhance the conductivity. Transmission electron microscopic (TEM) analysis was performed by Titan Krios (FEI). The PVSK film was scratched off from the substrate and dispersed in toluene by sonication for 10 min, which was dropped on an aluminum grid. An accelerating voltage of 300 kV was used for the measurement. Steady-state photoluminescence (PL) signal was analyzed by a Horiba Jobin Yvon system. A 640 nm monochromatic laser was used as a fluorescent excitation source. Time resolved PL decay profiles were obtained using a Picoharp 300 with time-correlated single-photon counting capabilities. The films were excited by a 640 nm pulse laser with a repetition frequency of 100 kHz provided by a picosecond laser diode head (PLD 800B, PicoQuant). The energy density of the excitation light was ca. 1.4 nJ cm^{-2}, in which carrier annihilation and non-geminate recombination are negligible. Ultraviolet photoelectron spectroscopic (UPS) analysis was carried out using Kratos Ultraviolet photoelectron spectrometer. He I (21.22 eV) source was used as an excitation source. The PVSK films were coated on ITO substrate and grounded using silver paste to avoid the charging during the measurement. Conductive atomic force microscopic (AFM) measurement was performed by a Bruker Dimension Icon Scanning Probe Microscope equipped with TUNA application module. The TUNA module provides ultra-high tunneling current sensitivity (<1 pA) with high-lateral

resolution. An antimony-doped Si tip (0.01–0.025 Ohm-cm) coated with 20 nm Pt-Ir was used as a probe. To avoid the electrically driven degradation during the measurement, a low bias voltage (100 mV) was applied. The measurement was carried out under either ambient lighting or low intensity illumination provided by the AFM setup. Temperature-dependent conductivity measurement was carried out using a commercial probe station (Lakeshore, TTP4) in which temperature of the device was controlled by thermoelectric plate and flow of liquid nitrogen. The electrical measurement was conducted with a source/measurement unit (Agilent, B2902A).

Device characterization

Current density–voltage (J–V) curves of the devices were measured using Keithley 2401 source meter under simulated one sun illumination (AM 1.5G, 100 mW-cm^{-2}) in ambient atmosphere. The one sun illumination was generated from Oriel Sol3A with class AAA solar simulator (Newport), in which light intensity was calibrated by NREL-certified Si photodiode equipped with a KG-5 filter. Typically, the J–V curves were recorded at 0.1 Vs^{-1} (between 1.2 V and −0.1 V with 65 data points and 0.2 s of delay time per point). During the measurement, the device was covered with a metal aperture (0.100 cm^2) to define the active area. All the devices were measured without pre-conditioning such as light-soaking and applied bias voltage. Steady-state power conversion efficiency was calculated by measuring stabilized photocurrent density under constant bias voltage. The external quantum efficiency (EQE) was measured using a specially designed system (Enlitech) under AC mode (frequency = 133 Hz) without bias light. For electro-luminescence measurements, a Keithley 2400 source meter and silicon photodiode (Hamamatsu

S1133-14, Japan) were used to measure current–voltage–luminance characteristics of PVSK solar cells.

Stability test

Moisture stability of the films was tested by exposing the PVSK films under relative humidity of 80 ± 5% and ambient lighting. Absorbance of the films was measured every 2 hours while the XRD of the films were recorded every 12 hours. For the devices, ex-situ tests were conducted by storing the devices in a desiccator (relative humidity, RH <30%) in a dark environment. The devices were taken out only for measurements in ambient conditions. For the operational stability, the maximum power point (MPP) tracking and continuous light exposure under open-circuit condition were performed in ambient conditions (RH~50%, T~40 °C). For the MPP tracking, the photocurrent density was monitored while the devices were biased at MPP under 1 sun illumination. For light exposure under open-circuit condition, the encapsulated devices were exposed to ca. 0.9 sun (90 ± 5 mW cm^{-2}) generated by halogen lamps under open-circuit condition, where the steady-state PCE was periodically measured with different exposure time under 1 sun illumination. The encapsulation of the device was performed inside a nitrogen-filled glove box filled by using an UV-curable adhesive and glass cover. The glass substrate was superimposed on the active layer and fixed with the UV-curable adhesive.

References

1. Lee, J.-W. *et al.* 2D perovskite stabilized phase-pure formamidinium perovskite solar cells. *Nat. Commun.* **9**, 3021 (2018).

2. Li, N. *et al.* Mixed Cation FAxPEA1–xPbI3 with Enhanced Phase and Ambient Stability toward High-Performance Perovskite Solar Cells. *Adv. Energy Mater.* **7**, n/a-n/a (2017).

3. Zhou, Y. *et al.* Benzylamine-Treated Wide-Bandgap Perovskite with High Thermal-Photostability and Photovoltaic Performance. *Adv. Energy Mater.* **7**, 1701048 (2017).

4. Wang, Z. *et al.* Efficient ambient-air-stable solar cells with 2D–3D heterostructured butylammonium-caesium-formamidinium lead halide perovskites. *Nat. Energy* **2**, 17135 (2017).

Chapter 7. Conclusions and Future Outlook

Hybrid perovskite materials show major promise as a potential industry-competitive PV technology if their limitations in (i) stability and (ii) efficiency can be further improved towards industry standards: >25% PCE with a 25+ year lifetime. These works have demonstrated effective ways to significantly enhance photovoltaic properties of hybrid perovskite thin films by utilizing this family of material's compositional, dimensional, and chemical tunability through (i) guanidinium-based precursors, (ii) a Lewis acid-base adduct method, and (iii) the co-existence of 2D/3D phases in perovskite thin films. Use of these led to an order of magnitude increase in photoluminescence lifetimes, and consequent V_{oc} increases to yield device performance improvements up to >20% PCE. Stability was enhanced via these techniques, ultimately leading to unencapsulated devices with T_{80} lifetimes >1000 hours under continuous illumination and open-circuit conditions. I will discuss how these works can be further built upon to achieve even more substantial improvements in stability and efficiency.

The V_{OC} loss for the record efficiency perovskite solar cell is around 380 mV which is still much higher than the theoretically achievable value of ~220 mV and the best value that has been achieved for GaAs solar cells is ~300 mV.[1] Experimental evidence suggests that this loss in potential originates from non-radiative recombination losses caused by defects, which indicates room for further control over defects to enhance the carrier lifetime and quasi Fermi level splitting.

However, owed to the low-temperature solution-based processing of metal halide perovskites, thin films are inevitably polycrystalline in nature with abundant surface and bulk crystal defects. The formation energy of Schottky disorders in the conventional $CH_3NH_3PbI_3$ perovskite has been calculated to be as low as 0.14 eV, resulting in an equilibrium vacancy concentration of 0.4% at room temperature.[2] The trap densities of such polycrystalline thin films were measured to be within the range of 10^{16}-10^{18} cm^{-3}.[3] This is relatively high compared to conventional high temperature vacuum-processed inorganic semiconductors, where typical defect densities of crystalline silicon and GaAs are ~10^8 and ~10^{13}-10^{14} cm^{-3},[4,5] respectively. Due to the ionic nature of the perovskite materials, the prevalent defects are charged defects of which activation energies for migration range from 0.5 eV to 2.0 eV. Therefore, the charged defects are highly likely to migrate under built-in and/or applied bias voltage, illumination, etc, which can degrade the operational stability of the perovskite solar cells. Thus far, the correlation between the charged defects and transient current-voltage behaviors (e.g. current-voltage hysteresis) has been actively studied. However, hard evidence and a consensus are still lacking in terms of the specific nature of the defects and their effects on performance and hysteresis, and perhaps even more importantly, there is absence of fundamental understanding of the correlations between the defects and long-term operational stability of the device. Thus, the nature of these defects and their associated physical models are still ambiguous, which has created difficulty in effectively handling defects in perovskites.

The next level of efficiency and stability can be reached by focusing more on the fundamental nature of defects using experimental techniques to extract their identities. These defects can then be correlated to processing conditions, which will then help guide the research community in the proper direction, i.e. to know which defects are detrimental and what

processing parameters can be used to mitigate specific defects. Moreover, an effective strategy to further improve the longevity of these films and devices can be realized through molecular design of small molecules and polymers that can be used to form 2D perovskite phases and also assist in film growth and passivation. These molecules and polymers can be further tailored with more hydrophobic properties such as using fluorinated molecules and understanding which functional groups affect defect formation, passivation, and overall stability of the film. Similarly, new compositions preserving 3D symmetry can also be studied and realized via molecular design and synthesis, such as fluorinated cationic species with appropriate size, dipole moment, and functional groups. In addition, focus must be placed on the other components of the device to improve efficiency and stability, but in this dissertation I focus solely on the perovskite thin film. These types of directions ought to lead to a higher intrinsic stability and efficiency of the perovskite thin film, which will yield more reliable and efficient solar cell devices.

References

1. Tress, W. *et al.* Predicting the Open-Circuit Voltage of CH3NH3PbI3 Perovskite Solar Cells Using Electroluminescence and Photovoltaic Quantum Efficiency Spectra: the Role of Radiative and Non-Radiative Recombination. *Adv. Energy Mater.* **5**, 1400812 (2015).

2. Walsh, A., Scanlon, D. O., Chen, S., Gong, X. G. & Wei, S.-H. Self-Regulation Mechanism for Charged Point Defects in Hybrid Halide Perovskites. *Angew. Chem.* **127**, 1811–1814 (2015).

3. Stranks, S. D. *et al.* Recombination Kinetics in Organic-Inorganic Perovskites: Excitons, Free Charge, and Subgap States. *Phys. Rev. Appl.* **2**, 034007 (November 9).

4. Angelis, F. D. & Petrozza, A. Clues from defect photochemistry. *Nat. Mater.* **17**, 383–384 (2018).

5. Haughn, C. R. *et al.* Quantification of trap state densities in GaAs heterostructures grown at varying rates using intensity-dependent time resolved photoluminescence. *Appl. Phys. Lett.* **102**, 182108 (2013).

Chapter 8. Appendices

A.1. Calculation of solar energy reaching Earth.

*Calculation referenced from: Tsao, J., Lewis, N. & Crabtree, G. Solar FAQs. (2006)

The solar constant (S_0), also known as the total solar irradiance, is approximately 1370 W/m^2 or 1.37 kW/m^2 as measured by satellites in space.

This implies that the Sun is an emitting blackbody with a temperature, T_{sun}, of about 5800K.

The cross-sectional area of the Earth irradiated by the Sun is:

$$A_{cross} = \pi r^2$$

The surface area of the Earth is:

$$A_{surf} = 4\pi r^2$$

Thus, the fraction of the solar constant received by Earth is:

$$\frac{A_{cross}}{A_{surf}} \cdot S_0 = \frac{\pi r^2}{4\pi r^2} \cdot S_0 \;=\; \frac{1}{4} \cdot 1370 \; \frac{W}{m^2} \;=\; \mathbf{342} \; \boldsymbol{\frac{W}{m^2}}$$

However, about 30% of this flux is scattered and 19% absorbed by the Earth's atmosphere and clouds. Therefore, the available amount reaching the Earth's surface is:

$$342 \cdot (1 - 0.49) = \mathbf{174.4} \; \boldsymbol{\frac{W}{m^2}}$$

Integrating this average flux over the surface area of the Earth gives the total theoretical solar power received on Earth's surface:

$$P_{total} = \left(174.4\ \frac{W}{m^2}\right) \cdot (4\pi r^2)$$

$$= \left(174.4\ \frac{W}{m^2}\right) \cdot 4\pi(6378000\ m)^2 = \mathbf{89,300\ TW}$$

This means that in just 1.25 hours the Earth could supply all the energy needed for the entire year of 2018 (400.05 EJ)!

If we have 10% efficient solar PV panels and 15 TW global power production requirements, then theoretically we would only need to cover a surface area 0.168% of Earth:

$$Energy\ harvested\ using\ 10\%\ efficient\ solar\ panels\ =\ 0.10 \cdot (89{,}300\ TW) = 8{,}930\ TW$$

$$Fraction\ of\ Earth's\ surface\ needed\ to\ be\ covered\ by\ solar = \frac{15\ TW}{8{,}930\ TW} = 0.168\%$$

Therefore, the surface area needed would be:

$$A_{surf,req} = (0.168\%) \cdot (4\pi r^2) =\ (0.17\%) \cdot 4\pi(6{,}378\ km)^2 = \mathbf{858,792\ km^2}$$

This is roughly the size of Venezuela (882,050 km^2).

However, this assumes that all solar radiation is received 24 hours per day and does not take into account the number of peak solar hours seen per day. Thus, if we estimate a global average of 5 hours of peak sunlight per day, we have:

$$\frac{5}{24} \cdot (89{,}300\ TW) = 18{,}601\ TW$$

Now using a more realistic and appropriate 20% efficient panels, we get:

$$Energy\ harvested\ using\ 20\%\ efficient\ solar\ panels\ =\ 0.20 \cdot (18{,}601\ TW) = 3{,}720\ TW$$

$$Fraction\ of\ Earth's\ surface\ needed\ to\ be\ covered\ by\ solar = \frac{15\ TW}{3{,}720\ TW} = 0.4032\%$$

Therefore, the surface area needed would be:

$$A_{surf,req} = (0.4032\%) \cdot (4\pi r^2) =\ (0.4032\%) \cdot 4\pi(6{,}378\ km)^2 = \mathbf{2{,}061{,}101\ km^2}$$

This is roughly the size of Saudi Arabia (~2,000,000 km^2).